DYNAMIC ANALYSIS, DESIGN AND PRACTICAL APPLICATIONS OF AN OVERCONSTRAINED MECHANICAL FORCE GENERATOR

A THESIS SUBMITTED TO
THE GRADUATE SCHOOL OF NATURAL AND APPLIED SCIENCES
OF
MIDDLE EAST TECHNICAL UNIVERSITY

BY

UMUR ERDİNÇ

IN PARTIAL FULFILLMENT OF THE REQUIREMENTS
FOR
THE DEGREE OF MASTER OF SCIENCE
IN
MECHANICAL ENGINEERING

DECEMBER 2017

Approval of the thesis:

DYNAMIC ANALYSIS, DESIGN AND PRACTICAL APPLICATIONS OF AN OVERCONSTRAINED MECHANICAL FORCE GENERATOR

Submitted by **UMUR ERDİNÇ** in partial fulfillment of the requirements for the degree of **Master of Science in Mechanical Engineering, Middle East Technical University** by,

Prof. Dr. Gülbin Dural Ünver ________________
Dean, Graduate School of **Natural and Applied Sciences**

Prof. Dr. Mehmet Ali Sahir Arıkan ________________
Head of Department, **Mechanical Engineering**

Prof. Dr. Reşit Soylu ________________
Supervisor, **Mechanical Engineering Dept., METU**

Examining Committee Members:

Prof. Dr. S. Turgut Tümer ________________
Mechanical Engineering Dept., METU

Prof. Dr. Reşit Soylu ________________
Mechanical Engineering Dept., METU

Prof. Dr. Sıtkı Kemal İder ________________
Mechanical Engineering Dept., Çankaya University

Assoc. Prof. Dr. Ergin Tönük ________________
Mechanical Engineering Dept., METU

Assist. Prof. Dr. Ulaş Yaman ________________
Mechanical Engineering Dept., METU

Date: *25.12.2017*

I hereby declare that all information in this document has been obtained and presented in accordance with academic rules and ethical conduct. I also declare that, as required by these rules and conduct, I have fully cited and referenced all materials and results that are not original to this work.

Name, Last Name	: Umur Erdinç
Signature	:

ABSTRACT

DYNAMIC ANALYSIS, DESIGN AND PRACTICAL APPLICATIONS OF AN OVERCONSTRAINED MECHANICAL FORCE GENERATOR

Erdinç, Umur
M.Sc., Department of Mechanical Engineering
Supervisor : Prof. Dr. Reşit Soylu

December 2017, 216 pages

In this thesis, dynamical characteristics of existing machines are improved by coupling mechanical force generators to the machine. In short, mechanical force generators (MFG) are energy efficient, overconstrained, shaking force and shaking moment free planar mechanisms which can be used to generate a desired periodic force profile; store excess energy and release it when needed. They can reduce the energy consumption of an existing machine, or optimize other dynamical characteristics of a machine.

In chapter 2, dynamic analysis of an overconstrained parallelogram mechanism is performed. For this overconstrained mechanism, the "closest" equivalent regular mechanism, in terms of a predetermined dynamical feature, is obtained. Since it is not overconstrained, dynamic analysis of this equivalent mechanism can be performed analytically. This analysis sheds light on the dynamic analysis of mechanical force generators.

In the following chapter, dynamic analyses of mechanical force generators are performed using two different methods. The first method is analytical, whereas

the second method utilizes a computer simulation software. The results of the two methods are compared.

For a given task of an existing machine, the total energy consumption and/or the required maximum actuator power/torque can be minimized by coupling a mechanical force generator to the existing machine. An algorithm, which determines the force to be generated by the MFG for the aforementioned optimizations, is introduced. The design of the MFG which generates this desired force is then realized by utilizing a novel, iterative algorithm. Besides the kinematic and inertial parameters of the MFG, this design yields the slot profiles of the MFG, as well. Effects of certain design parameters are investigated and several recommendations regarding practical implementation of mechanical force generators are presented.

The case studies that have been performed in this thesis show that energy consumption or maximum actuation power/torque of existing machines can be substantially reduced by the utilization of mechanical force generators. Thus, it is possible to reduce the initial cost and/or running cost of existing machines.

Keywords: Mechanical Force Generators, Energy Efficient Mechanisms, Shaking Force and Moment, Dynamical Performance Optimization, Overconstrained Mechanisms

ÖZ

FAZLA KISITLI MEKANİK KUVVET JENERATÖRÜNÜN DİNAMİK ANALİZİ, DİZAYNI VE PRATİK UYGULAMALARI

Erdinç, Umur
Yüksek Lisans, Makina Mühendisliği Bölümü
Tez Yürütücüsü: Prof. Dr. Reşit Soylu

Aralık 2017, 216 sayfa

Bu çalışmanın amacı; mevcut makinelerin dinamik özelliklerinin, mekanik kuvvet jeneratörleri (MKJ) kullanılarak iyileştirilmesidir. Mekanik kuvvet jeneratörleri; enerji verimliliğine sahip, fazla kısıtlı düzlemsel mekanizmalardır ve yere iletilen sarsma kuvvetleri ile sarsma momentleri sıfırdır. Mekanik kuvvet jeneratörleri, istenilen bir periyodik kuvvet profilini üretebilmekte; bir makinede anlık olarak fazlalık olan enerjiyi saklayıp, ihtiyaç anında makineye enerji sağlayabilmektedir. Bağlandıkları makinenin enerji tüketimini azaltabileceği gibi, seçilen bir dinamik özelliğinin iyileştirilmesinde de kullanılabilir.

Bu çalışmanın ilk aşamasında, mekanik kuvvet jeneratörlerinin kuvvet analizinde kullanılmak üzere ön bilgi edinmek için, fazla kısıtlı düzlemsel bir paralel kenar mekanizmasın dinamik analizi yapılmıştır. Fazla kısıtlı bir paralel kenar mekanizmasına seçilen dinamik özellik bakımından "en yakın" fazla kısıtlı olmayan özdeş paralel kenar mekanizması tespit edilmiştir. Bulunan özdeş mekanizma fazla kısıtlı olmadığı için, dinamik analizi analitik yollarla kolaylıkla yapılabilmektedir.

Çalışmanın ilerleyen aşamalarında, mekanik kuvvet jeneratörlerinin dinamik analizleri hem analitik yöntemlerle, hem de mühendislik yazılımlarıyla yapılıp elde edilen sonuçlar karşılaştırılmıştır. Mevcut bir makinenin toplam enerji tüketimi ve/veya maksimum motor torku/gücü, makineye bir MKJ bağlanarak düşürülebilir. Bu amaçla üretilmesi gereken kuvvet profili hesaplanmış ve bu kuvvet profilini üretecek MKJ'yi tasarlamak için bir algoritma önerilmiştir. Önerilen algoritma ile MKJ'nin kinematik ve atalet parametrelerinin yanı sıra slot profili de elde edilebilmektedir. MKJ'nin çeşitli tasarım parametrelerinin etkisi incelenmiş ve pratikteki uygulamalarıyla ilgili önerilerde bulunulmuştur.

Mekanik kuvvet jeneratörleri kullanılarak mevcut makinelerin enerji tüketimi, maksimum motor torku/gücü gibi çeşitli değerlerinin ciddi oranda düşürülebileceği gözlemlenmişir. Bu sayede, ilk yatırım maliyeti ve/veya işletme giderini büyük oranda azaltmak mümkündür.

Anahtar Kelimeler: Mekanik Kuvvet Jeneratörleri, Enerji Verimli Mekanizmalar, Sarsma Kuvveti ve Momenti, Dinamik Performans Optimizasyonu, Fazla Kısıtlı Mekanizmalar

ACKNOWLEDGEMENTS

Firstly, I would like to express my deepest gratitude to my supervisor, Prof. Dr. Reşit Soylu, for his valuable guidance, endless patience, encouragement, and advice throughout the course of this work. His supervision helped me in all the time of research and writing of this thesis. I could not have imagined having a better advisor and mentor for my master study. Thanks to his supervision, I was able to gain great experience on problem-solving and working independently. I also thank the members of my thesis defense jury, Prof. Dr. S. Turgut Tümer, Prof. Dr. Sıtkı Kemal İder, Assoc. Prof. Dr. Ergin Tönük, and Assist. Prof. Dr. Ulaş Yaman for their valuable contributions to this thesis.

I am particularly grateful for the software support of METU Biomaten Center of Excellence in Biomaterials and Tissue Engineering (METU BIOMATEN) and Bias Mühendislik. METU BIOMATEN supplied the computer software for the analyses and Bias Mühendislik helped me regarding the software whenever I needed.

I would like to express my special thanks to Mehmet Uğur Güdelek, Cihat Duru and Cansu Yumuşak for their valuable supports and contributions.

Last but not least, I would like to thank my family who have always been there for me; to my wife Direniş Erdinç for her endless patience, love, trust and encouragement; to my mother Serpil Erdinç and my father Zeyneddin Erdinç for their unconditional love, endless understanding and support, to my sister Hande Erdinç who was my other half; my young siblings Ayşe İdil Çaylı and Canyoldaş Çaylı who made me feel I was not alone.

TABLE OF CONTENTS

LIST OF TABLES

TABLES

LIST OF FIGURES

FIGURES

LIST OF ABBREVIATIONS

Symbols

k	:	Spring constant
$O_i x_i y_i$	:	Coordinate system attached to link i
$s_o(t)$	:	Output displacement
$s_i(t)$	:	Input displacement
$F_R(s_o)$	:	Generated MFG force at right hand side
$F_L(s_o)$	:	Generated MFG force at left hand side
λ	:	Degree of freedom of the space
f_i	:	Number of degree of freedom of link i
m	:	Mass
I_{Gi}	:	Inertia of link i around point G_i
F	:	Force
M	:	Moment
T	:	Torque
ω	:	Angular velocity
K	:	Contact stiffness
μ_s	:	Coefficient of friction (static)
μ_d	:	Coefficient of friction (dynamic)
V_s	:	Stiction transition velocity
V_d	:	Friction transition velocity
α	:	Angular acceleration
t	:	Time
t_{ini}	:	Initial time
t_{fin}	:	Final time
Θ	:	Angular position
r	:	Radius
ρ	:	Density
E	:	Modulus of elasticity
ν	:	Poission’s ratio
M	:	Material
e_{rms}	:	Root mean square error
R	:	Reaction force
a_i	:	i^{th} coefficient of slot shape curve
b_i	:	Dimension related with link i
y_u	:	Free length of the upper spring
y_l	:	Free length of the lower spring
f_i	:	Friction force related with i^{th} link

s_i	:	Displacement of i^{th} link
v_i	:	Velocity of i^{th} link
a_i	:	Acceleration of i^{th} link
I	:	Current
R	:	Resistance
K	:	Constant related with motor efficiency
η	:	Motor efficiency
P_{out}	:	Output power
P_{in}	:	Input power
n	:	Transmission ratio
f_{min}	:	Cost function
E	:	Energy
c	:	Weighting coefficient
T	:	Period
ξ	:	Variable that defines quality of the optimization
U	:	Work done by all external forces
T	:	Kinetic energy of MFG
l_{free}	:	Free length of the spring
W	:	Work
$\overrightarrow{DV}$	:	Design variables vector
σ	:	Parameter that defines the contact surface
θ_t	:	Angle that defines the slope of the slot
r_f	:	Radius of friction
$E_{\sigma=i}$	:	Envelope with $\sigma = i$
$\hat{\mathbf{t}}$	:	Unit vector that defines the slot shape
$\hat{\boldsymbol{e}}$	:	Unit vector that defines the slot shape
σ_{θ_i}	:	Parameter that defines the rolling direction
ϵ	:	Limiting error to stop the iterations

Abbreviations

MFG	:	Mechanical force generator
DOF	:	Degree of freedom
P	:	Prismatic joint
R	:	Revolute joint
C_P	:	Cam joint
PKE	:	Permanently kinematically equivalent
eqMFG	:	Equivalent mechanical force generator
OC	:	Overconstrained
reg	:	Regular
RPM	:	Regular parallelogram mechanism
OPM	:	Overconstrained parallelogram mechanism
INL	:	In-line primitive joint
INP	:	In-plane primitive joint

PERP	:	Perpendicular primitive joint
REV	:	Revolute joint
PRIS	:	Prismatic joint
PoC	:	Point on curve constraint
SOLD	:	Solid to solid contact
CURV	:	Curve to curve contact
rms	:	Root mean square
ave	:	Average
Rel	:	Relative
KE	:	Kinetic energy
SE	:	Spring energy
ME	:	Mechanical energy

CHAPTER 1

INTRODUCTION

Mechanisms are utilized for motion, force, moment or energy transmission [1]. One ultimate aim of mechanical engineering is to improve the performance of machines most of which will employ some sort of a mechanism.

Performance of machines can be increased by:

1. Reducing energy consumption,
2. Reducing maximum torque of the actuator,
3. Reducing shaking forces and moments,
4. Reducing friction.

Recently, Soylu proposed a novel mechanism called “Mechanical Force Generator” (MFG) [2] which is an overconstrained, one degree of freedom, planar mechanism. In this study, various applications of mechanical force generators will be presented in detail.

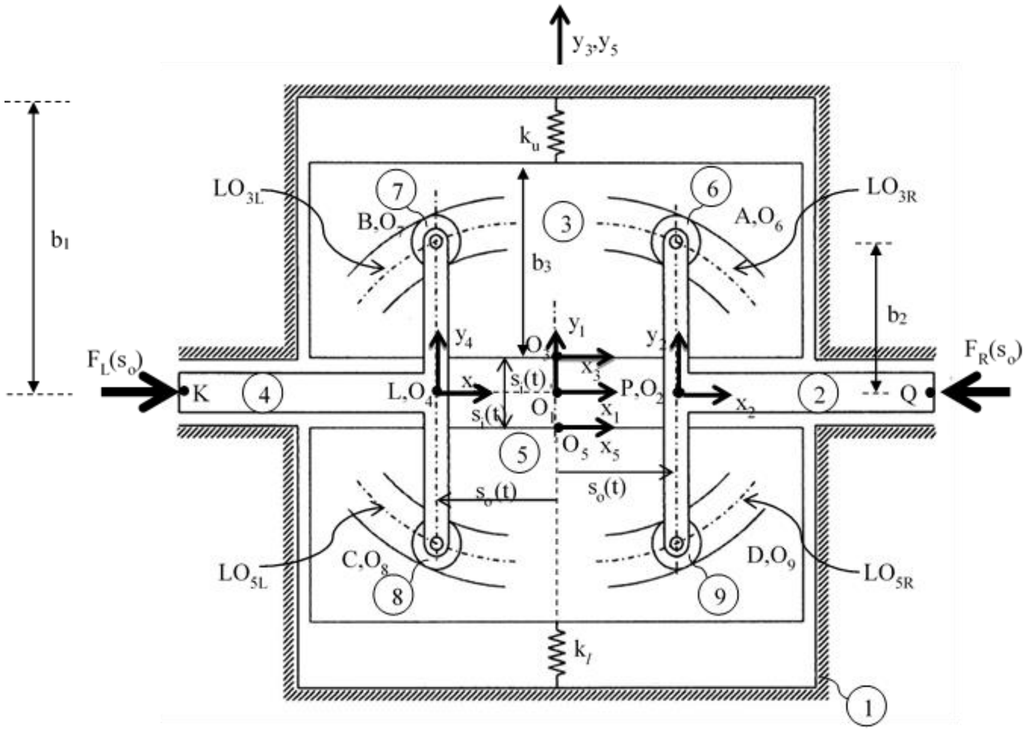

Figure 1: Mechanical Force Generator [3]

1.1 Balancing of Mechanisms

When an unbalanced mechanism runs at high speeds, and when it has heavy links, shaking forces and shaking moments transmitted to the ground create major problems. Firstly, dynamic performance decreases due to unsmooth working conditions. Secondly, the life of the mechanism decreases due to fatigue. Thirdly, vibration and noise problems appear [4]. In order to solve such problems, balancing of the mechanisms comes into prominence.

It is proper to inspect static balancing first. Static balancing is aimed at obtaining a constant potential energy in the system and it is used for a wide range of mechanisms. These mechanisms can be either translational or rotational systems. The most popular approach for static balancing is to add counterweights and pulleys. By utilizing counterweights, translational systems such as double hung windows, elevators etc. are balanced. Some rotational systems such as garage doors, dishwasher doors, anglepoise study lamps [5], robotic manipulators [6], [7]; Steadicams [8], arm support orthoses [9], [10]; passive exoskeletons [11], on the other hand, are balanced by utilizing springs. In general, one can use the aforementioned methods (counterweights and springs) to both translational and rotational systems. Adding springs generally has the advantage of adding a small amount of mass to the system [12]. Note that, springs are practically weightless, while counterweights may be heavier than the payload itself [13].

Nathan [14] proposed a spring mechanism that generates a constant force. Streit and Gilmore [12] utilized (1 to 4) springs to balance rotatable bodies by using energy methods. Perfect balancing means that system is balanced at every position throughout the range of the motion. Schenk and Herder [15] used energy free adjustment for gravity equilibrator by adjusting spring stiffness. Therefore, adjusting the mechanism (in order to balance different loads) does not require external energy. Gravity equilibrator is a statically balanced system which is designed to balance a load or a mass. The spring stiffness is adjusted by changing the effective spring length (i.e., number of active coils). Herder et al. [16] utilized a storage spring to adjust the balancer spring (that balances a specific load) in an energy free manner. Yang and Lan [13] utilized two planar springs (one extension spring and one compression spring) to obtain the required torque curve for balancing. Their mechanism is also adjustable. Planar springs are used to obtain the same effect of large stiffness linear springs within a limited space. Herder [17], for instance, used a spring force compensation technique to balance the unwanted elasticity (parasitic spring forces).

For high speed mechanisms, balancing of shaking forces and shaking moments are crucial. A mechanism is “reactionless” or “dynamically balanced” if the reaction forces (excluding gravity) and the reaction moments at the ground joints (shaking forces and moments) are equal to zero at all times (for any motion of the mechanism) [18]. In the literature, various methods are proposed to achieve this goal. The most obvious one is mass redistribution of the links. If the total center of mass of the mechanism can be made stationary, then shaking force balance is achieved. Berkof and Lowen [19] use the “Method of Linearly Independent Vectors” for complete shaking force balancing of planar four bar and six bar linkages. They redistribute link masses so that the time dependent terms in the center of mass equation vanishes. Tepper and Lowen [20] also studied this method and further improved it.

Another alternative for balancing shaking forces and shaking moments is addition of gear trains and cams. Feng [21] used mass redistribution together with geared inertia counterweights. Kochev [22] used noncircular (cam like) gear drives to balance the shaking moments. Arakelian and Briot [23] used a cam mechanism carrying a counterweight to cancel the shaking forces and moments.

In order to balance a mechanism, one may also add extra linkages to the existing mechanism. Briot and Arakelian [24] added class two Assur groups to planar inline four bar linkages with constant input speed. Bagci [4] used idler parallelogram loops to balance the shaking moments. Arakelian and Smith [25] used pantograph like linkages to balance the shaking forces and moments.

Mendoza-Trejo et al. [26] minimized the magnitude of the acceleration of the center of mass to reduce the shaking forces. Chaudhary and Saha [27] introduced equimomental systems for rigid bodies (in plane motion) by using three point masses. Moore et al. [28] used complex variables to model the linkages and found the complete set of shaking force and shaking moment balanced planar four bar linkages.

A comprehensive literature survey regarding the balancing of mechanisms can be found in [23], [29]. Comparison of several balancing methods applied to a rotatable link can be found in [30].

Up to this point, planar and single degree of freedom mechanisms have been discussed. However, dynamic balancing of spatial multi degree of freedom mechanisms also needs attention. In the literature, there are only a few studies about balancing of spatial multi degree of freedom mechanisms due to their complexity. Gosselin et al. [31] synthesized 3 DOF reactionless parallel mechanisms using dynamically balanced four bar linkages. Fattah and Agrawal [32] used auxiliary parallelograms to balance 3 DOF planar parallel mechanisms. Arakelian and Smith [33] used inertia flywheels or planetary gear trains to balance 3 DOF parallel manipulators. Wu and Gosselin [18] synthesized reactionless 6 DOF parallel manipulators using 3 DOF parallelepiped mechanisms.

1.2 Overconstrained Mechanisms

Overconstrained mechanisms are mechanisms that do not obey the Chebychev–Grübler–Kutzbach criterion. In other words, their actual degree of freedom is larger than the one obtained from the Chebychev–Grübler–Kutzbach criterion. Researchers have focused on analyzing such mechanisms for quite a long time, and there are lots of studies regarding overconstrained mechanisms. Although there are infinitely many overconstrained mechanisms, it is also possible to classify overconstrained mechanisms as in [34]. A comprehensive list of contributions regarding overconstrained mechanisms can be found in [35] and [36].

Dynamical analysis of overconstrained mechanisms leads to indeterminate problems. Hence, it is required to consider the flexibility of the links and compatibility of the displacements. Finite element methods can be utilized to handle these indeterminate problems as in [37] and [38].

In case of mechanisms with redundant constraints, if all the joints are frictionless; and if only position, velocity, acceleration analyses are needed, then there is no need to calculate the joint reaction forces. However, in many cases, friction must also be considered. Therefore, calculation of the joint reaction forces is necessary [39].

In [40], the mobility equation is modified and the solvability of joint forces/torques of spatial mechanisms is investigated. Wojtyra [39], on the other hand, used a rigid body model and presented three different techniques of Jacobian matrix analysis to find reaction forces in an overconstrained mechanism. Furthermore, Fraczek and Wojtyra included the effects of Coulomb friction in the joints [41] and compared three different approaches to handle redundant constraints in [42]. Xu et al. [43] proposed a novel method for force analysis of the overconstrained lower mobility parallel mechanisms. They used flexible links together with rigid links and compared theoretical calculations with simulation results by using MSC Adams software.

1.3 Mechanical Force Generators

Equations of equilibrium obtained solely from rigid body dynamics are not sufficient for the dynamic analysis of overconstrained mechanisms. Since MFG is also an overconstrained mechanism, one should consider the flexibility of the links for its dynamic analysis. Alternatively, one can use an equivalent mechanism for its dynamic analysis, which will be discussed later.

A schematic view of the MFG is shown in Figure 1. MFG has 9 links which are listed below.

Link 1	: ground link (fixed)
Links 2 and 4	: T shaped links (2 identical links)
Links 3 and 5	: plate-like links with slots (2 identical links)
Links 6, 7, 8 and 9	: rollers (4 identical links)

LINK NUMBER	1	2	3	4	5	6	7	8	9
1		P	P	P	P				
2	P					R			R
3	P					C_P	C_P		
4	P						R	R	
5	P							C_P	C_P
6		R	C_P						
7			C_P	R					
8				R	C_P				
9		R			C_P				

Figure 2: Joints of the MFG [3]

The joints of the MFG are listed in the table in Figure 2. The abbreviations that are utilized are given below.

R : revolute joint

P : prismatic joint

C_P : cam joint

Links 2, 3, 4, 5 are connected to the ground by means of prismatic joints. Links 6, 7, 8, 9 are rollers and connected to links 2 and 4 by revolute joints. These rollers are also connected to links 3 and 5 by means of cam joints. The slots on links 3 and 5 are labelled as LO_{ik} where i is the link number and k is either L (for left hand side) or R (for right hand side).

Links 3 and 5 are also connected to the ground by means of springs with spring constants of k_u and k_l, where u denotes “upper” and l denotes “lower”.

The output links of the MFG are links 2 and 4. The output displacement is shown with $s_o(t)$. $F_R(s_o)$ and $F_L(s_o)$ are the forces generated by the MFG.

In the MFG, one may obtain $s_o(t)$ as any desired function of $s_i(t)$, by properly designing the link dimensions and the slot shapes.

In each link of MFG, an $O_ix_iy_i$ coordinate system is attached, where “i” denotes the link number.

The Chebychev–Grübler–Kutzbach criterion, in other words, the mobility formula, yields the degree of freedom of a general mechanism via the following equation [44].

$$DOF = \lambda * (l - j - 1) + \sum_{i=1}^{j} f_i \qquad (1)$$

where

DOF is the degree of freedom of a mechanism,

λ is degree of freedom of the space (which is 6 for spatial mechanisms and 3 for planar mechanism),

l is number of links (including the fixed link),

j is number of joints,

f_i is the number of degree of freedom of the i^{th} joint.

MFG has 4 revolute joints ($f_i = 1$), 4 prismatic joints ($f_i = 1$) and 4 cam joints ($f_i = 2$). Hence, one obtains:

$$\sum_{i=1}^{j} f_i = 4*1+4*1+4*2 = 16 \qquad (2)$$

For practical purposes, the MFG mechanism shown in Figure 1 has 0 degrees of freedom according to the mobility formula. Since $\lambda = 3$ (planar mechanism), $l = 9$, $j = 12$, $\sum_{i=1}^{j} f_i = 16$; equation (1) yields

$$DOF = 3*(9-12-1)+16 = 4 \qquad (3)$$

These 4 degrees of freedom are the rotations of the rollers around the axes of the 4 revolute joints (which are considered to be insignificant for a practical application). However, the real degree of freedom of the MFG is 5, due to its special dimensions. Hence, it is an overconstrained mechanism. The aforementioned special dimensions are as follows:

$$\angle Q_2P_2A_2 = \angle Q_2P_2D_2 = \pi/2 \qquad (4)$$

$$\angle K_4L_4B_4 = \angle K_4L_4C_4 = \pi/2 \qquad (5)$$

$$\overline{P_2A_2} = \overline{P_2D_2} = \overline{L_4B_4} = \overline{L_4C_4} \qquad (6)$$

$$(\ x_2 \text{ axis }) \Leftrightarrow (\ x_1 \text{ axis }) \qquad (7)$$

$$(\ x_4 \text{ axis }) \Leftrightarrow (\ x_1 \text{ axis }) \qquad (8)$$

$$(\ y_3 \text{ axis }) \Leftrightarrow (\ y_1 \text{ axis }) \qquad (9)$$

$$(\ y_5 \text{ axis }) \Leftrightarrow (\ y_1 \text{ axis }) \qquad (10)$$

$$r_6 = r_7 = r_8 = r_9 \qquad (11)$$

$$x_{LO3R} = f(p) \qquad (12)$$

$$x_{LO3R} = g(p) \qquad (13)$$

$$x_{LO3L} = -f(p) \qquad (14)$$

$$y_{LO3L} = g(p) \qquad (15)$$

$$x_{LO5R} = f(p) \qquad (16)$$

$$y_{LO5R} = -g(p) \qquad (17)$$

$$x_{LO5L} = -f(p) \qquad (18)$$

$$y_{LO5L} = -g(p) \qquad (19)$$

Here, "⇔" symbol means "coincident". r_i stands for radius of the i^{th} joint. x_{LOik} and y_{LOik} are the x and y coordinates of the center of a roller that lies on the curve LO_{ik}. f(p) and g(p) are 2 functions that define the slot shapes.

If the above requirements are satisfied, the following conditions are also satisfied:

$$\overline{O_1O_2} = \overline{O_1O_4} = s_o(t) \tag{20}$$

$$\overline{O_1O_3} = \overline{O_1O_5} = s_i(t) \tag{21}$$

There are also some constraints on the masses and inertias of the links. These constraints are given below.

$$m_2 = m_4 \tag{22}$$

$$m_3 = m_5 \tag{23}$$

$$m_6 = m_7 = m_8 = m_9 \tag{24}$$

$$x_{G3} = 0 \tag{25}$$

$$x_{G5} = 0 \tag{26}$$

$$x_{G6} = 0 \tag{27}$$

$$x_{G7} = 0 \tag{28}$$

$$x_{G8} = 0 \tag{29}$$

$$x_{G9} = 0 \tag{30}$$

$$y_{G2} = 0 \tag{31}$$

$$y_{G4} = 0 \tag{32}$$

$$y_{G6} = 0 \tag{33}$$

$$y_{G7} = 0 \tag{34}$$

$$y_{G8} = 0 \tag{35}$$

$$y_{G9} = 0 \tag{36}$$

$$I_{G6} = I_{G7} = I_{G8} = I_{G9} \tag{37}$$

Here,

G_i : mass center of the i^{th} link

m_i : mass of the i^{th} link

x_{Gi} : x coordinate of mass center of the i^{th} link

y_{Gi} : y coordinate of mass center of the i^{th} link

Lastly, the constraints on the applied external forces are as follows:

$$\text{(upper spring)} \Leftrightarrow (y_1 \text{ axis}) \tag{38}$$

$$\text{(lower spring)} \Leftrightarrow (y_1 \text{ axis}) \tag{39}$$

$$\overrightarrow{F_{k_u}} = -\overrightarrow{F_{k_l}} \tag{40}$$

$$F_R(s_o) \Leftrightarrow (x_1 \text{ axis}) \tag{41}$$

$$F_L(s_o) \Leftrightarrow (x_1 \text{ axis}) \tag{42}$$

$$F_L(s_o) = F_R(s_o) \tag{43}$$

Equations (4) to (43) are taken from [3].

As long as

- Equations (4) to (43) are satisfied,
- Gravitational acceleration is taken as 0,
- Frictional properties of the 4 revolute joints in the rollers are identical to each other,
- Frictional properties of the 4 cam joints in the slots are identical to each other,

all reaction forces and moments at the ground joints will always be zero.

The aforementioned feature of the MFG implies that the shaking forces and moments of the MFG that are transmitted to the ground are all zero and the MFG is balanced. [45]

MFG can be used for the following applications as described in [46]:

1. MFG can be used as energy efficient energy storage device for regulating the power requirement of an existing machine. By this way, it can minimize the energy requirement for a specific task. For multiple tasks, multiple MFGs can be used with an appropriate clutch system.

2. MFG can be used as an energy efficient mechanical force generator for improving the dynamic characteristics (shaking force/moment, actuator force/torque etc.) of an existing machine.
3. MFG can be used as all-in-one actuator which includes energy storage system and/or mechanical transmission system and/or actuator.
4. MFG can be used as a stand-alone mechanism for replacing any existing planar mechanism with 1 degree of freedom.

MFG can be connected to either twin machines (as in Figure 3) or a single machine (as in Figure 4). Here, twin machines are two identical machines that operate synchronously [46].

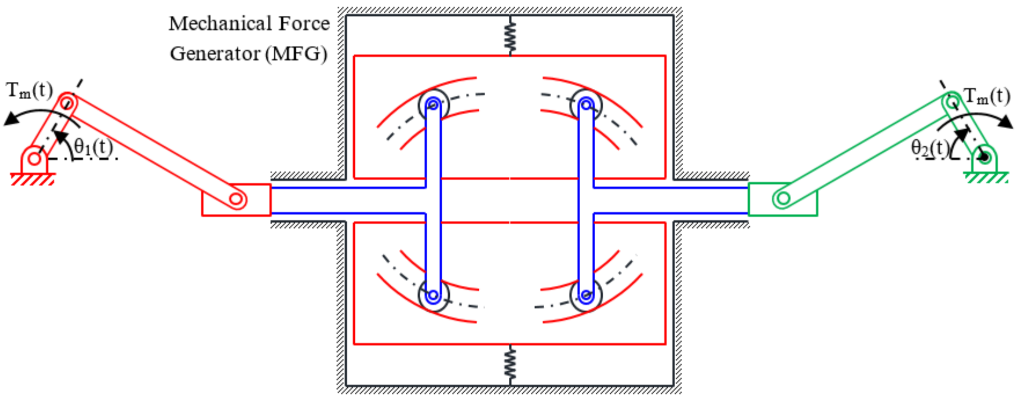

Figure 3: MFG Connected to Twin Mechanisms [46]

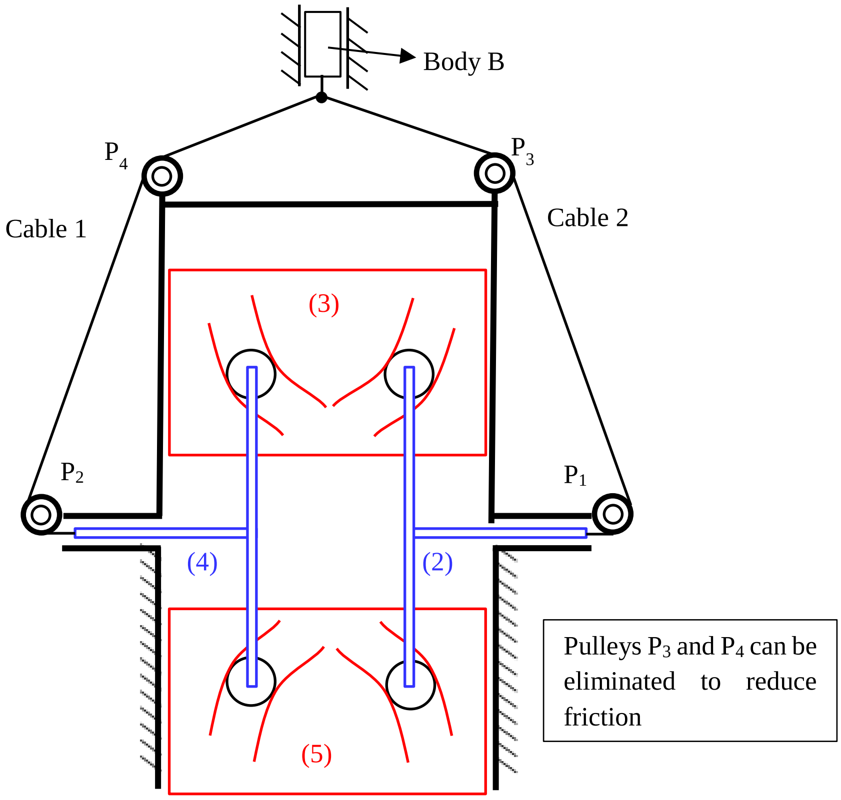

Figure 4: MFG connected to a Single Mechanism [46]

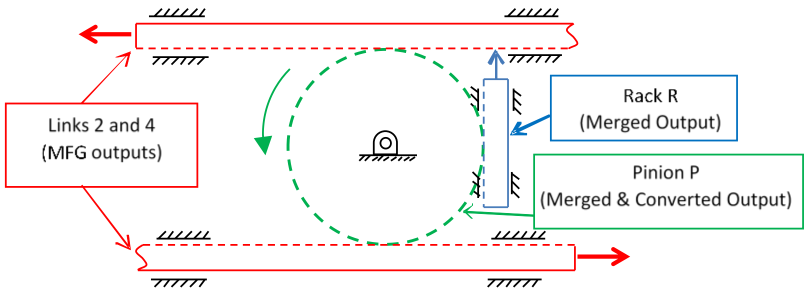

Figure 5: Output Merging (and Converting) System [46]

It is also possible to convert the translating outputs of the MFG to rotational outputs; and/or merging the two outputs to a single output by means of an output merging (and converting) system as shown in Figure 5 [46].

Indeed, there may be other ways to merge or convert the outputs and connect the MFG to existing machines. However, they will not be discussed here.

Since MFG is proposed very recently by Soylu [2], the literature on MFG is very scarce. The only study other than [3], [45] and [46] is [47]. In this study kinematic and dynamic analyses of the MFG are performed. Applications and connection possibilities of the MFG are also discussed.

In [47], performance optimization of four bar mechanisms (in terms of actuating torque and shaking forces and moments) are inspected and compared by

- connecting a rotational adjusting mechanism to the rocker link of a four bar mechanism,
- connecting a translational adjusting mechanism to the rocker link of a four bar mechanism,
- connecting an MFG to the rocker link of a four bar mechanism

Performance optimization of slider crank mechanisms are also inspected and compared. In this case, an MFG is connected to the slider link. The original slider crank and the MFG connected slider crank is inspected in terms of actuating torque and shaking forces and moments [47].

MFG can act as a double slider mechanism, since both of them have translational inputs and translational outputs. Mencek has also compared the performances of the MFG and the double slider mechanism, by considering different types of motors [47].

A physical prototype of the MFG is designed and manufactured by Mencek. This MFG prototype is connected to two identical slider crank mechanisms. Main aim here is to compare the energy consumptions of the original slider crank mechanisms with the MFG connected slider crank mechanisms. However, due to some manufacturing problems, this comparison couldn’t be completed successfully [47].

1.3.1 Dynamic Analysis of MFG

Since MFG is an overconstrained mechanism, the number of equations and the number of unknowns are not equal in the dynamic analysis. Hence, one obtains an indeterminate problem. Therefore, it is convenient to introduce a regular (in other words, not overconstrained) MFG which is permanently kinematically equivalent (PKE) to the original (overconstrained) MFG [3]. An overconstrained mechanism and a regular mechanism are PKE mechanisms if the motions of two mechanisms are identical, when the input motions are identical for both mechanisms. Furthermore, their dynamic analyses will also be identical under certain conditions. More detailed explanations regarding PKE mechanisms can be found in [3].

MFG can have several PKE mechanisms, in other words, equivalent MFGs (eqMFG). "Equivalent mechanical force generator - 1 & 3 ($EqMFG_{1\&3}$)" is obtained by replacing the prismatic joint between links 1 and 3 in the original MFG. In $EqMFG_{1\&3}$, this prismatic joint is replaced with a cylinder in slot joint as shown in Figure 6. Curve C_{13} of link 3 lies on a circle with radius d_1 and center U_3. $EqMFG_{1\&3}$ and MFG are identical except for the joint between links 1 and 3. As opposed to to MFG, $EqMFG_{1\&3}$ is a regular mechanism, not an overconstrained mechanism. Hence its degree of freedom is 5. 4 of these degrees of freedoms are due to the rotations of the rollers. The remaining 1 degree of freedom is due to the motions of all links together. [3]

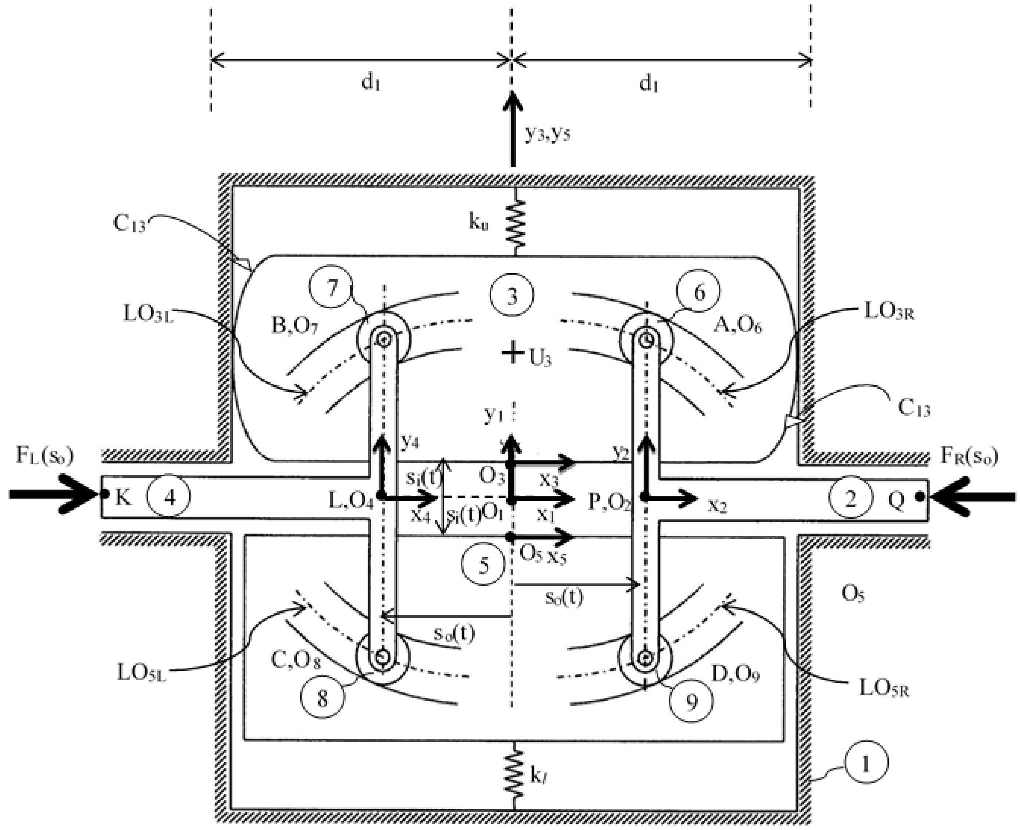

Figure 6: $EqMFG_{1\&3}$ Mechanism [46]

Similarly, $EqMFG_{1\&2}$ can be obtained by replacing the prismatic joint of MFG between links 1 and 2 with a cylinder in slot joint.

More detailed information about eqMFG mechanisms and other versions of eqMFG mechanisms can be found in [46].

4 algorithms are proposed by Soylu for the dynamic analysis of the EqMFGs [45]. Two of these algorithms are for the inverse dynamic analyses, and the remaining two are for the forward dynamic analyses. For both the inverse and forward dynamic analyses, two cases are considered:

1. There exists slippage at the slots.
2. There exists no slippage at the slots.

Hence by including the above two cases for both forward and inverse dynamic analyses, there are a total of four algorithms. These algorithms are developed for $EqMFG_{1\&2}$, but they can also be applied to other versions of EqMFGs, such as $EqMFG_{1\&3}$. The inverse dynamic analysis algorithm when there exists no slippage at the slots is summarized in Chapter 3.

1.4 Mechanical Presses and Actuators

In this study, the MFG will be connected to a mechanical press. Hence, it is necessary to review the mechanical press literature. In [48], a comprehensive review of the existing press machines are presented. Servo presses and their advantages are explained, and mechanisms of presses are classified. To take full advantage of the MFG, servo presses are more appropriate. In [49], characteristic features of mechanical servo presses and their advantages over other types of presses are explained; furthermore, applications of presses are presented. In [50], mechanical press types and the press nomenclature are explained. In [51], design rules of presses are explained in a detailed fashion.

In the literature, it is possible to find sample load data for the press machines for various works. For example, one can use [52] for deep drawing, [53] for forging, [54] for stamping and [55] for bending sample load data. In this study, MFG will be connected to a forging press and the load data given in [53] will be used.

It is also important to include a motor efficiency model in the analyses of the MFG. The main losses in electric motors may be classified as copper losses, iron losses, stray load losses and mechanical losses. Among these, the copper losses are the most dominant losses [56]. Hence, in this study, a simple efficiency model that only includes copper losses will be used.

In the literature, the efficiency maps of electric motors are obtained by using four different methods. These methods are listed below.

1. In order to obtain the efficiency map, one can make physical tests. In other words, one can change the input voltage and current of a motor and measure the output torque and speed of the motor, at a limited number of points. Then, one can create a contour plot for efficiency. Some experimental tests are presented in [56], [57] and [58].
2. In order to obtain the efficiency map, one can virtually model the motor by using finite element analysis techniques which are readily available in commercial software such as ANSYS Maxwell, etc. [59]
3. In order to obtain the efficiency map, one can model certain major losses and thus create approximate efficiency maps. In [58], two of these approximate models are compared with experimental results.
4. In [59], losses in electric motors are modelled for different $T^m\omega^n$ products where, T is the motor torque and ω is the motor speed. "m" and "n" are constants which can be any integer from 0 to 3.

1.5 Scope of the Thesis

Mechanical force generator is a recently introduced novel concept, and there are very few studies related to it. In this study, dynamic analyses of these mechanisms will be realized by means of the computer software, MSC Adams; and the results will be compared with the results obtained by the dynamic analysis algorithm developed in [45]. In order to optimize the dynamic performance of an existing mechanism, the optimal force to be applied by an MFG will be determined. A simplified dynamic analysis of the MFG will also be presented and the slot shape of the MFG will be obtained by an iterative algorithm.

The author believes that, MFG will be very beneficial for the dynamic optimization of various widely used industrial mechanisms, such as press machines, etc. Dynamic optimization can be related to shaking forces/moments, the maximum power demand, or the total energy consumption. By utilization of

MFG in such industrial machines, one can reduce the size of the actuator and/or reduce the energy consumption of the machine.

The organization of the thesis is given below.

- In Chapter 2, in order to obtain a preliminary know-how information (regarding the dynamic analysis of overconstrained mechanism), the parallelogram mechanism will be studied. Dynamic analysis of a parallelogram mechanism requires one to consider the flexibilities of the links because dynamical analyses of overconstrained mechanisms lead to indeterminate problems. Hence, dynamic analysis of the parallelogram mechanism will be performed by including the flexibilities of the links. Then, by increasing the degree of freedom of an appropriate joint, dynamic analysis will be repeated by using only rigid links. An extra translational degree of freedom will be added for this purpose. The angle of this translational axis will be changed and the effect of different angles will be studied.
- In Chapter 3, dynamic analysis of MFG will be realized by using a commercial software, MSC Adams. Secondly, an algorithm proposed by Soylu [45] will be implemented by means of a commercial software, MATLAB. Results of the two solution methods will then be compared.
- In Chapter 4, as an example, a press mechanism is studied. Dynamic analysis of the press mechanism is performed for various types of loads and the force to be provided by an MFG rigidly coupled to the press is included as an optimization parameter. When an appropriate MFG is coupled to the press, it will be shown that, the energy consumption of the press and the maximum power requirement of the actuator of the press may be reduced extensively.
- In Chapter 5, an algorithm, which yields the slot profile of the MFG, for a given motion and generated force, is introduced. Effects of link masses, inertias and spring properties on slot profile are discussed. Approximate

dynamic analysis of the MFG is performed, by including only two links. As an output, the contact surface of the slot is obtained.

CHAPTER 2

COMPARISON OF REGULAR PARALLELOGRAM MECHANISMS AND OVERCONSTRAINED PARALLELOGRAM MECHANISM

2.1 Introduction

In this chapter, an overconstrained parallelogram mechanism which is shown in Figure 7 and a regular parallelogram mechanism which is shown in Figure 8 will be compared in terms of their dynamic properties. Here, a “regular” mechanism refers to a mechanism, which is not overconstrained.

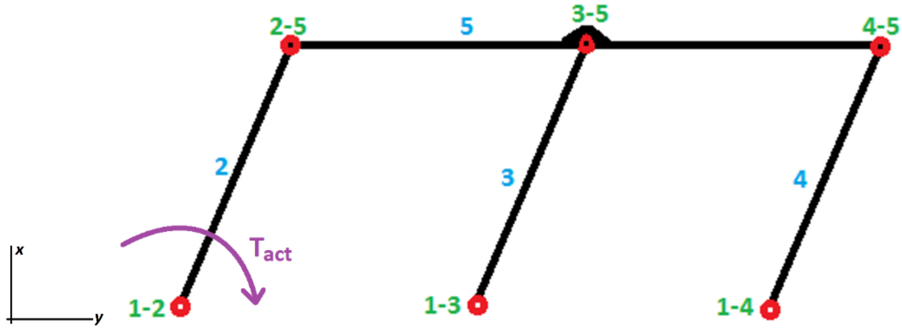

Figure 7: An Overconstrained Parallelogram Mechanism

In Figure 7, blue numbers refer to the link labels. Note that ground is labeled as link 1. Green numbers, on the other hand, refer to joint labels. Joint i-j, for instance, refers to the joint between link i and link j. Here, link 5 has 3 joints;

with link 2, link 3, and link 4. Other links have 2 joints. Links 2, 3 and 4 are directly connected to the ground via the joints 1-2, 1-3, and 1-4. All of the joints are revolute joints (R), which have only 1 degree of freedom.

For the parallelogram mechanism shown in Figure 7 with $\lambda = 3$, $l = 5$, $j = 6$, $f_i = 1$ for all joints, the degree of freedom equation yields

$$DOF_{oc} = 3 * (5 - 6 - 1) + 6 * 1 = 0 \quad (44)$$

Here, DOF_{oc} refers to the degree of freedom of the parallelogram mechanism shown in Figure 7. However, the actual degree of freedom of the system is 1, due to the special dimensions. Hence, it is an overconstrained mechanism, and "oc" in the subscript stands for "overconstrained". The aforementioned special dimensions are as follows:

- Link lengths of link 2, 3 and 4 are equal.
- Link 2, 3 and 4 are parallel.
- Distance between joints 1-2 and joint 1-3 is equal to distance between joint 2-5 and 3-5.
- The line passing through joint 1-2 and joint 1-3 is parallel to the line passing through joint 2-5 and joint 3-5.
- Distance between joints 1-3 and joint 1-4 is equal to distance between joint 3-5 and 4-5.
- The line passing through joint 1-3 and joint 1-4 is parallel to the line passing through joint 3-5 and joint 4-5.
- Joints 1-2, 1-3 and 1-4 are on the same straight line.
- Joints 2-5, 3-5 and 4-5 are on the same straight line.

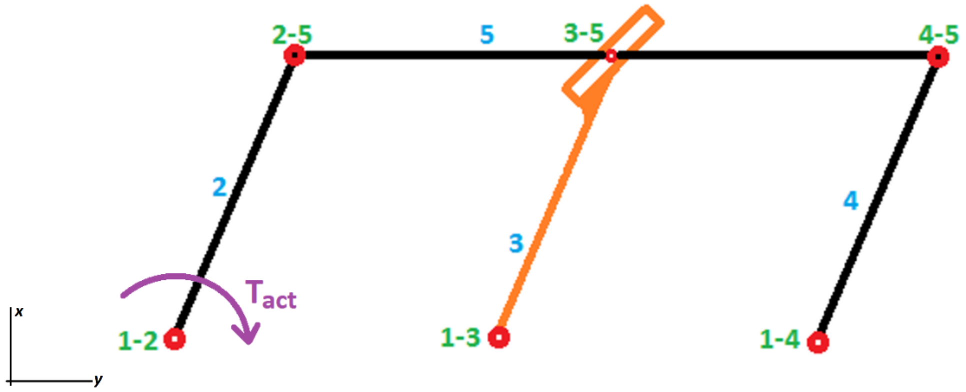

Figure 8: A Regular Parallelogram Mechanism

In Figure 8, a regular parallelogram mechanism is shown. Here, joint 3-5 (which was a revolute joint) is changed with a cylinder in slot joint (C_s).

For the parallelogram mechanism shown in Figure 8 with $\lambda = 3$, $l = 5$, $j = 6$ and $f_i = 1$ for all 5 R joints and $f_i = 2$ for the C_s joint, the degree of freedom equation yields

$$DOF_{reg} = 3 * (5 - 6 - 1) + (5 * 1 + 2) = 1 \qquad (45)$$

Here, DOF_{reg} refers to the degree of freedom of the parallelogram mechanism shown in Figure 8. Hence, it is a regular mechanism, and "reg" in the subscript stands for "regular".

For the sake of simplicity, after this point, the regular parallelogram mechanism will be called as "RPM" and the overconstrained parallelogram mechanism will be called as "OPM".

For both the RPM and the OPM, there are 12 equations which are listed below.

<u>Equations</u>

1. Force equilibrium of body 2 in the x direction
2. Force equilibrium of body 2 in the y direction
3. Moment equilibrium of body 2

4. Force equilibrium of body 3 in the x direction
5. Force equilibrium of body 3 in the y direction
6. Moment equilibrium of body 3
7. Force equilibrium of body 4 in the x direction
8. Force equilibrium of body 4 in the y direction
9. Moment equilibrium of body 4
10. Force equilibrium of body 5 in the x direction
11. Force equilibrium of body 5 in the y direction
12. Moment equilibrium of body 5

An actuating torque is applied to both mechanisms, in order to obtain the predetermined motion. Here, the motion is known, and the actuating torque is unknown.

For the OPM, there are 13 unknowns which are listed below.

Unknowns for the OPM

1. Joint reaction force in joint 1-2 in the x direction
2. Joint reaction force in joint 1-2 in the y direction
3. Joint reaction force in joint 1-3 in the x direction
4. Joint reaction force in joint 1-3 in the y direction
5. Joint reaction force in joint 1-4 in the x direction
6. Joint reaction force in joint 1-4 in the y direction
7. Joint reaction force in joint 2-5 in the x direction
8. Joint reaction force in joint 2-5 in the y direction
9. Joint reaction force in joint 3-5 in the x direction
10. Joint reaction force in joint 3-5 in the y direction
11. Joint reaction force in joint 4-5 in the x direction
12. Joint reaction force in joint 4-5 in the y direction
13. Actuating torque which is applied to link 2

For the RPM, there are 12 unknowns which are listed below.

Unknowns for the RPM

1. Joint reaction force in joint 1-2 in the x direction
2. Joint reaction force in joint 1-2 in the y direction
3. Joint reaction force in joint 1-3 in the x direction
4. Joint reaction force in joint 1-3 in the y direction
5. Joint reaction force in joint 1-4 in the x direction
6. Joint reaction force in joint 1-4 in the y direction
7. Joint reaction force in joint 2-5 in the x direction
8. Joint reaction force in joint 2-5 in the y direction
9. Joint reaction force in joint 3-5 (there is a single reaction force for joint 3-5, which is perpendicular to the slot axis)
10. Joint reaction force in joint 4-5 in the x direction
11. Joint reaction force in joint 4-5 in the y direction
12. Actuating torque which is applied to link 2

Therefore, the number of unknowns and the number of equations are equal for the RPM. However, the number of unknowns and the number of equations are not equal for the OPM. Hence, the equations can be solved only in terms of a selected unknown. Alternatively, one may model the links as flexible (rather than rigid). In this case, all 13 unknowns of the OPM can be solved using the rigid body dynamic equilibrium equations and the equations arising due to consistency of the displacements in the flexible links. This can be realized by using a finite element method.

In this chapter, the objective is to examine the two permanently kinematically equivalent mechanisms, namely OPM and RPM, in terms of their dynamic characteristics.

2.2 Method

The OPM and the RPM will be analyzed by using the commercial software MSC Adams. Two mechanisms will be completely equivalent in terms of their link lengths, materials, external loads, friction etc.

Dynamic analysis of OPM will be realized by using flexible links. Dynamic analysis of RPM, on the other hand, will be realized by using rigid links.

Here, the goal is to determine the RPM which is “closest” to the OPM in terms of a given dynamic characteristics. In order to achieve this goal, the angle α (see Figure 9) will be used as the design parameter. It should be noted that there exists infinitely many RPM mechanisms, with different α values, which are permanently kinematically equivalent to a given OPM. Hence, there are many dynamic characteristics (such as the actuating torque, joint reactions, work done in one cycle, etc.) which are affected by the value of α. In this chapter, a primary objective will be to compare the actuating torque of an OPM with the actuating torque of an RPM for different values of α. In this comparison, the input motions of the OPM and RPM; and other parameters that affect the dynamic force analysis will be kept to be the same for the OPM and RPM. The effect of α on the joint reaction forces of an RPM will also be investigated. Similarly, the effect of α on the work done (in one cycle) by an RPM will also be investigated.

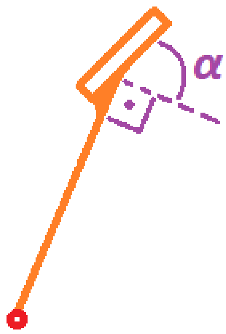

Figure 9: Angle α, Design Parameter for RPM

Before going into the details, some preliminary information, regarding MSC Adams will be given. This information will be used in chapters 2 and 3.

2.2.1 Joints & Constraints in MSC Adams Environment

In MSC Adams, by default, each body has 6 degrees of freedom in space. One can also constrain a body as a "planar part" in a selected plane. With this option, 2 rotational and 1 translational degrees of freedom become constrained.

In order to construct systems, bodies should be somehow connected to each other. There are mainly 3 ways of connecting bodies to each other in MSC Adams:

1. Idealized Joints: Joints that have physical counterparts, such as a revolute joint or a translational joint.
2. Joint Primitives: Joints that place restrictions on a relative motion, such as restricting one part to always move on a specified line on another part. Unlike the idealized joints, the joint primitives don't have physical counterparts.
3. Higher Pair Constraints: Constraints that restrict a curve or a point defined on the first part to remain in contact with another curve defined on a second part.

The aforementioned constrains restrict several degrees of freedom of the related parts. Depending on the type of joint used, one to six degrees of freedom may be removed. In order to restrict the motion of a part with respect to another part, one can also define a contact between two bodies. In this case, no degrees of freedoms are removed. However, the contact forces between the two parts restrict the relative motion.

In the following sections, some of the above mentioned joints (and their specifications in MSC Adams) will be introduced briefly.

2.2.1.1 Idealized Joints

2.2.1.1.1 Revolute Joint

Revolute joints remove 2 rotational and 3 translational degrees of freedom. Hence, only one rotational degree of freedom remains. Friction can be added easily. They cannot be used with planar parts to restrict only in-plane translations. If they are used with planar parts with λ=3, out of plane rotations and translation become restricted two times for each, which results in redundant constraints.

2.2.1.1.2 Translational Joint

Translational joints remove 3 rotational and 2 translational degrees of freedom. Hence, only one translational degree of freedom remains. Friction can be added easily. They cannot be used with planar parts to restrict only in-plane translation and rotation. If they are used with planar parts with λ=3, out of plane rotations and translation become restricted two times for each, and results redundant constraints.

2.2.1.2 Joint Primitives

2.2.1.2.1 In-Plane Primitive Joint

In-plane primitive joints constrain one translational degree of freedom of a body. In other words, a specified point on the first part always moves on a plane defined on the second part as shown in Figure 10. This type of joint can be used also in planar parts with λ=3. Friction cannot be added from the menu. It should be introduced and defined as an external force/torque.

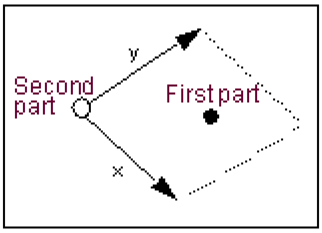

Figure 10: In-Plane Primitive Joint [60]

2.2.1.2.2 In-Line Primitive Joint

In-line primitive joints constrain two translational degrees of freedom of a body. In other words, a specified point on the first part always moves on a line defined on the second part as shown in Figure 11. This type of joint can be used also in planar parts with λ=3. Friction cannot be added from the menu. It should be introduced and defined as an external force/torque.

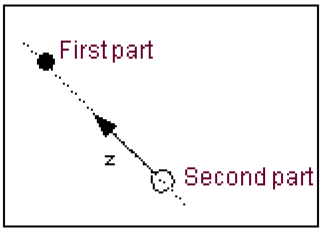

Figure 11: In-Line Primitive Joint [60]

For planar parts with λ=3, by using in-line primitive joint, one can compose a joint that is equivalent to a revolute joint. Here, the line described for the revolute joint is the axis of rotation of the revolute joint and it is perpendicular to the plane of the planar part. Being planar part constrains out of plane translation and rotations (in total, 1 translation+2 rotations). In-line primitive joint constrains 2 translations on the plane. Hence, a total of 5 degrees of freedom become constrained as in the revolute joint.

2.2.1.2.3 Perpendicular Primitive Joint

Perpendicular primitive joints constrain one rotational degree of freedom of a body. In other words, a specified line on the first part always stays perpendicular to another line defined on the second part as shown in Figure 12. This type of joint can also be used in planar parts with λ=3. Friction cannot be added from the menu. It should be introduced and defined as an external force/torque.

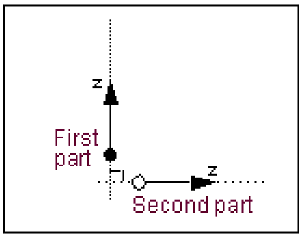

Figure 12: Perpendicular Primitive Joint [60]

For planar parts with $\lambda=3$, by using an in-plane primitive joint and a perpendicular primitive joint together, one can compose a joint that is equivalent to a translational joint. Here, being planar part constrains out of plane translation and rotations (in total, 1 translation+2 rotations). In-plane primitive joint restricts one translational degree of freedom. Perpendicular primitive joint restricts one rotational degree of freedom. By using all of these together in a proper manner, the only remaining degree of freedom is one translational degree of freedom. Hence, a total of 5 degrees of freedom become constrained (like as in the translational joint).

If a perpendicular primitive joint is not added, the degree of freedom of the part increases to 2, as in the cylinder in slot joint, which possesses an in-plane rotation and an in-plane translation. By this way, one can compose a joint between link 3 and link 1 (ground joint) in the balanced $EqMFG_{1\&3}$. (See section 3.2)

2.2.1.3 Higher Pair Constraints

Although there are other types of higher pair constraints, here, only the point on curve constraint will be introduced.

2.2.1.3.1 Point on Curve Constraint

Point on curve constraints constrain two translational degrees of freedom of a body. In other words, a specified point on the first part always moves on a curve defined on the second part as shown in Figure 13. The first part is free to slide and roll on the curve specified on the second part. This curve can be planar, spatial, open or closed. The first part cannot lift off the second part, in other words, it must always lie on the curve. This type of joint can be used also in planar parts with $\lambda=3$. Friction cannot be added from the menu. It should be introduced and defined as an external force/torque.

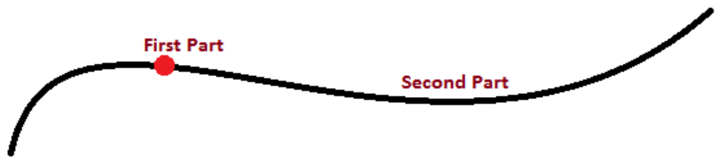

Figure 13: Point on Curve Constraint

Although point on curve constraint looks similar to an in-line primitive joint, they are not the same. In an in-line primitive joint, the constraint should be described over a straight line. However, in point on curve constraint, the curve doesn’t need to be a straight line. Moreover, the curve can be defined in 3 dimensional space. The advantage of an in-line primitive joint is that it can be constructed easily.

2.2.1.4 Contact

By using contacts, defining complex joints like a cylinder in slot joint or a cam joint and introducing friction to them is possible. Contacts can restrict the motion of a part with respect to another part by creating contact forces, without directly removing degree of freedom of a body.

In contacts, two parts do not need to touch each other necessarily. If there is an external effect like gravity, external force or a specific geometry (like a cylinder in slot), they may touch each other. If there is no such force, they may not touch each other, or they may touch each other only for some specific time interval.

Although more sophisticated usages are also possible, only the related content will be introduced here. In this study, for defining a cylinder in slot joint with friction, curve to curve and solid to solid contacts will be used.

2.2.1.4.1 Contact Force and Contact Detection Algorithm

The contact algorithm can be thought as a nonlinear spring-damper system.

As an example, consider the contact between a sphere and a rectangular prism, as shown in Figure 14.

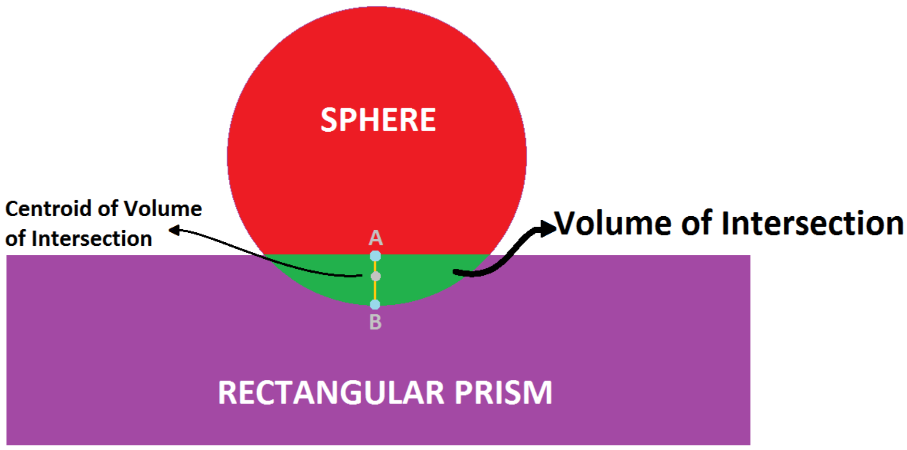

Figure 14: Illustration of Contact Detection Algorithm

Although it is exaggerated for illustration purposes, the green volume is the volume of intersection. Gray point is the centroid of the volume of intersection. Point A is the closest point in the sphere to the centroid of the volume of intersection. Point B is the closest point in the rectangular prism to the centroid of the volume of intersection. Length of the line AB is defined as the "penetration depth". Contact forces act in the direction of line AB.

The contact force is defined as follows:

$$F = K * (penetration\ depth)^n \tag{46}$$

where

K: contact stiffness

n: exponent

n should be larger than 1, for stiffening spring characteristics. This exponent should normally be set to a number higher than 1.5. According to design studies, models run better with $n>2.1$. Hence its default value is 2.2 in MSC Adams, and thus, in this study 2.2 will be used.

In general, higher stiffness means more rigid contact. But higher stiffness values lead to difficulties in integrations.

By default, K is 10^5 N/mm for the parts whose mass is in the order of 1 kg and which are made of steel. Since, for the system to be analyzed, masses are in the order of 1 kg, K will be taken* as 10^5 N/mm.

Note that, frictional forces and damping forces may also exist in a contact. Again, for the parts whose mass is in the order of 1 kg and which are made of steel, damping coefficient can be taken* as 10 (N*s)/mm which is the default value.

MSC Adams solver uses a cubic STEP function to increase the damping coefficient from zero, at zero penetration, to full damping when the penetration reaches a predefined value. The penetration depth at which MSC Adams solver turns on full damping is specified as 10^{-3} mm.

* *only for curve to curve contact*

2.2.1.4.2 Contact Friction

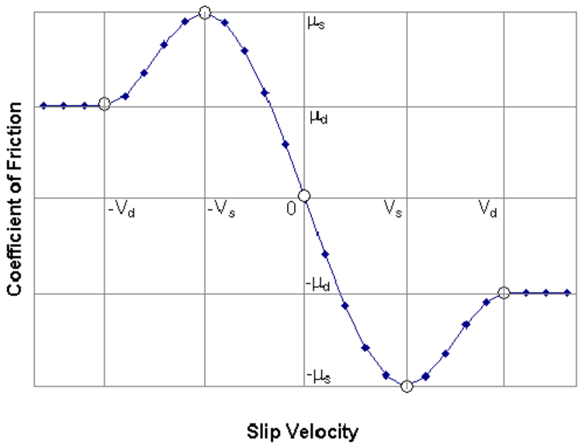

Figure 15: Slip Velocity vs Coefficient of Friction [60]

In Figure 15, slip velocity vs coefficient of friction is shown, where;

μ_s : Coefficient of friction (Static)

μ_d : Coefficient of friction (Dynamic)

V_s : Stiction transition velocity

V_d : Friction transition velocity

Note that, one should have $0 \leq V_s \leq V_d$ and $0 \leq \mu_d \leq \mu_s$. Furthermore, both V_s and V_d should be 5 times larger than integrator error, which is the requested accuracy of the integrator. This error is 10^{-3} by default.

There is no contact stiction in MSC Adams, unlike the friction models in the idealized joints. Hence, a slip velocity is necessary to generate frictional forces and it is used to compute a coefficient of friction. As the slip velocity decreases below the friction transition velocity, the coefficient of friction gradually increases from μ_d to μ_s. At the stiction transition velocity, the coefficient of friction becomes equal to μ_s. Between the stiction transition velocity and the zero slip velocity, the coefficient of friction decreases gradually to zero, as the slip velocity decreases. Therefore, even the no slip condition for contacts includes a small slip. If the slip velocity is smaller than the stiction transition velocity, it is safe to claim that there is no slip.

2.2.1.4.3 Contact Types

Although there are other types of contact, only the "curve to curve" and "solid to solid" contacts will be discussed here.

2.2.1.4.3.1 Curve to Curve Contact

Contact detection is analytic. Hence solution time is shorter than solid to solid contact. The contact forces are also smoother.

2.2.1.4.3.2 Solid to Solid Contact

Solid to solid contact is limited to external contact surfaces. Contact detection is not analytic. The surfaces are tessellated as in Figure 16.

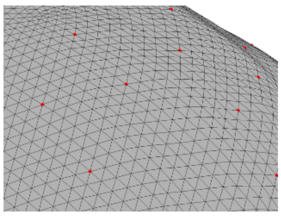

Figure 16: Tessellation [60]

If it is possible, preferring the curve to curve contact is more meaningful and advantageous because of the above mentioned benefits. However, for complex geometries, solid to solid contact may be necessary.

Table 1: Summary of Constraint Types

Abbreviation	Joint Type	Usable for Planar Parts (λ=3)?	Constrained DOF'S	Total Constrained DOF's
INL	In-Line Primitive Joint	YES	2T	2
INP	In-Plane Primitive Joint	YES	1T	1
PERP	Perpendicular Primitive Joint	YES	1T	1
REV	Revolute Joint	NO	3T+2R	5
PRIS	Prismatic Joint	NO	2T+3R	5
PoC	Point on Curve Constraint	YES	2T	2
SOLD	Solid to Solid Contact	YES		0
CURV	Curve to Curve Contact	YES		0

For convenience, all types of constraints that will be utilized in this study are presented in Table 1.

2.3 Model

The notation to be used in the developed model is presented below.

μ : friction coefficient between two contact surfaces for all types of joints

k_L : spring constant of the load

α : angle of the slot in link 3 (see Figure 9)

t : time

t_{ini} : initial time

t_{fin} : final time

$\Theta_{in}(t)$: angular position of link 2 (input) (see Figure 17)

$T_{act}(t)$: actuating torque acting on link 2 (see Figure 17)

r_{pin} : pin radius of the revolute joints

ρ : density of the material

E : modulus of elasticity

ν : Poisson's ratio

M : material

Steel will be used as the link material. Properties of steel are given below.

E = 207 GPa

ρ = 7801 kg/m^3

ν = 0.29

In Figure 17, the front view of the OPM which is connected to a compression spring, is shown. In the same figure, the "working grid" is also shown. Working grid in MSC Adams is an imaginary grid that lies in the x-y plane. In this model, the spacing between each point of the working grid is 100 mm. Therefore, the length of link 5 is 800 mm. All other dimensions may be determined using the working grid.

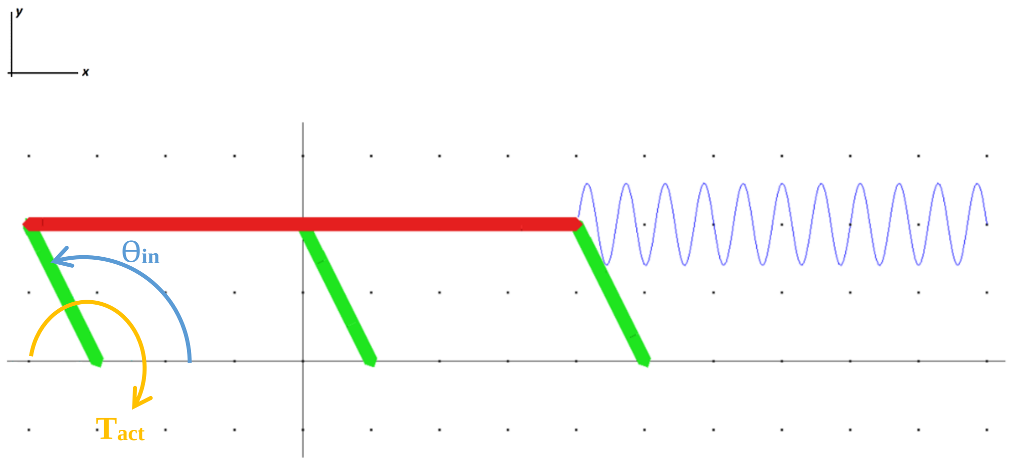

Figure 17: Front View of the OPM

Width of all links are 20 mm. Depth of link 2, 3 and 4 is 10 mm, depth of link 5 is 30 mm. Depth of the links are defined as the length that is perpendicular to the front view shown in Figure 17. Width of the links, on the other hand, can be directly seen from the front view in Figure 17. In Figure 18, an isometric view of the OPM is shown.

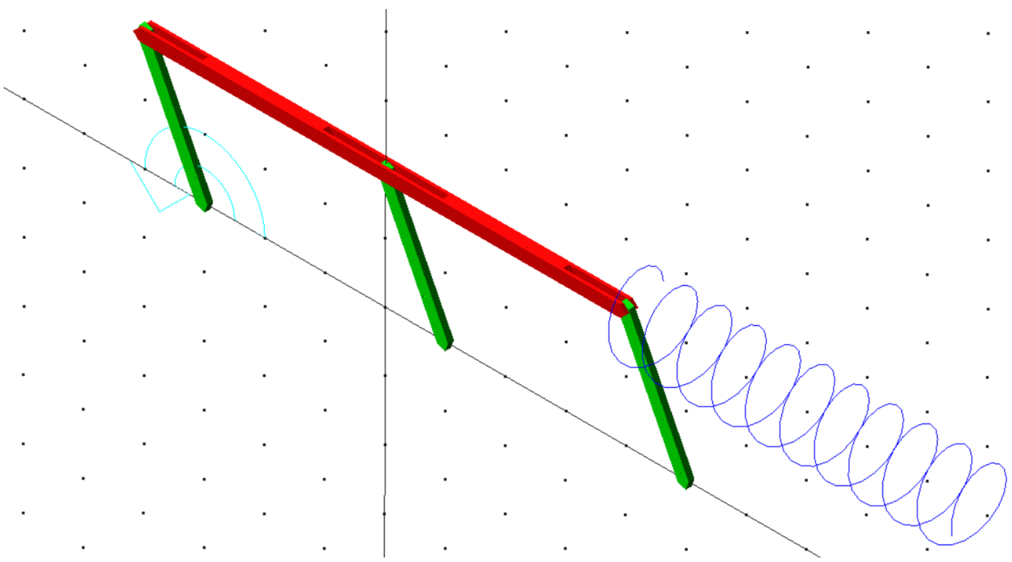

Figure 18: Isometric View of the OPM

Here, the spring simulates an external load. In reality, instead of the spring, any external load could be applied to the mechanism. The spring constant of the spring, k_L, is 0.5 N/mm. The length of the spring shown in Figure 17 is the free length, which is 600 mm.

OPM is located in a vertical plane, and gravity acts in the –y direction as shown in Figure 17. OPM is perfectly symmetrical with respect to the x-y plane. Hence, there exists no out-off plane forces.

OPM is modelled as **flexible** and all joints are revolute joints with friction. The friction coefficient μ is 0.1 (between steel and steel, lubricated). For lubricated steel to steel contact, taking μ larger than 0.2 is not reasonable. Pin radius of the revolute joints are taken 5 mm.

Transition velocity is taken as 10^{-5} mm/s, which is very small. Hence, only sliding friction is considered, whereas, static friction is not taken into account.

Motion of the OPM is specified via joint 1-2, as shown with a blue arrow in Figure 17. The specified motion of the OPM is defined by the 4 equations given below.

$\ddot{\theta}_{in}(t) = -10^o/s^2$

$\dot{\theta}_{in}(0) = 0^o/s$

$\theta_{in}(0) = 0^o$ (assume θ_{in} shown in Figure 17 is 0^o, in other words, initial position)

$t_{fin}=4$ s

Analysis is done in 201 discrete time steps.

The model for OPM with visible icons is shown in Figure 19. Icons are shown for frictions, joints, actuating torque, etc. are shown for better understanding of the model.

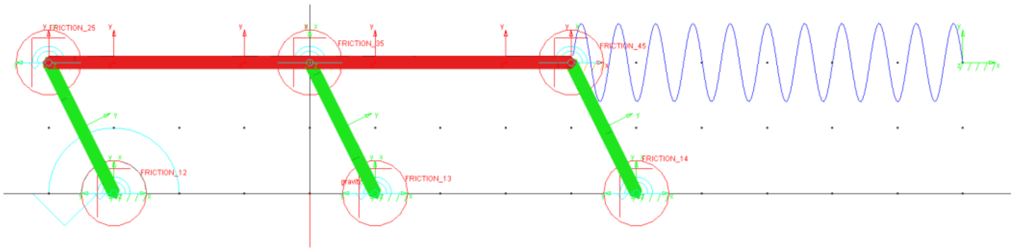

Figure 19: OPM with Visible Icons

RPM is also modelled in a similar manner as shown in Figure 20.

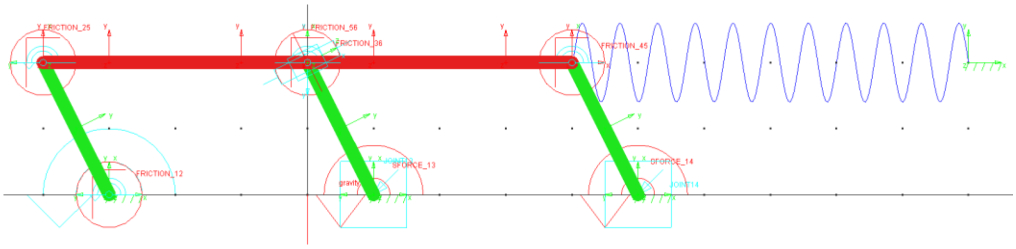

Figure 20: RPM with Visible Icons

It should be noted that, there are 3 key differences between PRM and OPM:

- RPM is modelled as **rigid**, whereas, OPM is modelled as **flexible**.
- In OPM, joint 3-5 is revolute joint. In RPM, joint 3-5 is a cylinder in slot joint. In MSC Adams, there is no readily available cylinder in slot joint. Hence, the cylinder in slot joint is modelled as explained below.

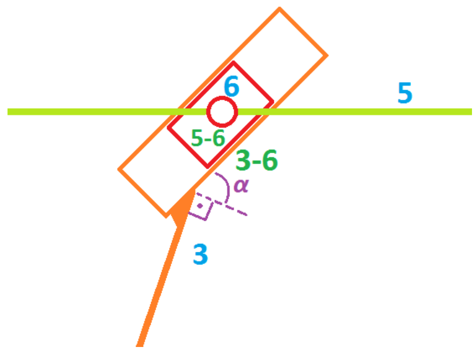

Figure 21: Modeling Cylinder in Slot Joint

Firstly, an imaginary link, link 6, is introduced as shown in Figure 21. A revolute joint is used between link 6 and link 5 (joint 5-6). A prismatic joint is used between link 3 and link 6 (joint 3-6). Hence, joint 3-5 is modeled as combination of 2 one degree of freedom joints. The model will be much more accurate if the mass of link 6 is negligible. In this model, density of link 6 is 10^6 times smaller than the density of steel, which implies that mass of link 6 is negligible.

- In OPM, all revolute joints are modeled as revolute joints. In RPM, however, joint 1-3 and joint 1-4 are modeled as in-line primitive joints ($f_i = 4$). This is because, in MSC Adams, there is no revolute joint type for planar mechanisms. Revolute joints always remove 5 degrees of freedom even if the mechanism is planar. This is due to the fact that MSC Adams always takes λ to be 6 (while calculating the degree of freedom), even if the mechanism is a planar mechanism with $\lambda = 3$. Alternatively, one can introduce a body as a planar link and restrict the 3 degrees of freedom of the body, without changing the degree of freedom of space, λ. Note that, differences between in-line primitive joints and revolute joints have already been explained in section 2.2.1. Recall that for in-line primitive joints, friction is introduced as an external force, i.e., there is no built-in friction choice for primitive joints.

Remember that, in the RPM model of MSC Adams, $l = 6$, $j = 7$, $f_i = 1$ for all 4 revolute joints and the prismatic joint. $f_i = 4$ for in-line primitive joints.
With 2 in-line primitive joints rather than revolute joints:

$$DOF_{reg} = 6 * (6 - 7 - 1) + (5 * 1 + 2 * 4) = 1 \qquad (47)$$

If revolute joints are used for joints 1-3 and 1-4:

$$DOF_{reg} = 6 * (5 - 6 - 1) + (7 * 1) = -5 \qquad (48)$$

In that case, MSC Adams arbitrarily removes some constraints which is not desired.
Note that, in RPM, one could model each link as a planar link and use only in-line primitive joints. However, all friction forces should be modelled as external torque/forces for this model. Hence, one should use, as much as possible, revolute joint models in order to take advantage of the built-in friction model of the revolute joints.
In OPM, there is no degree of freedom problem, because it is modeled as flexible. Each joint can be modelled as a revolute joint (which restricts 5 degrees of freedom), and the degree of freedom of space, λ, is taken as 6.

Recall that, the design parameter is angle α, which is the angle of the slot in link 3, as explained before.

2.4 Results

The error at any time t, $e(t)$, between 2 functions $f_1(t)$ and $f_2(t)$, can be described as follows:

$$e(t) = f_1(t) - f_2(t) \qquad (49)$$

The root mean square error between the initial time t_{ini} and final time t_{fin}, on the other hand, can be defined as follows:

$$e_{rms} = \sqrt{\frac{\int_{t=t_{ini}}^{t=t_{fin}} e^2(t) * dt}{t_{fin} - t_{ini}}} \tag{50}$$

In general, the smaller e_{rms} is, the "closer" the curves $f_1(t)$ and $f_2(t)$ in the interval $t_{ini} \leq t \leq t_{fin}$. Note that the units of e_{rms} is the same as the units of $f_1(t)$ and $f_2(t)$.

The non-dimensional, normalized, form of the root mean square error, on the other hand, is defined via the equation

$$e_{nrms} = \frac{e_{rms}}{\max\big(f_1(t), f_2(t)\big) - \min\big(f_1(t), f_2(t)\big)} \tag{51}$$

where $\max\big(f_1(t), f_2(t)\big)$ is the maximum value of the functions $f_1(t)$ and $f_2(t)$ in the interval $t_{ini} \leq t \leq t_{fin}$. Similarly, $\min\big(f_1(t), f_2(t)\big)$ is the minimum value of the functions $f_1(t)$ and $f_2(t)$ in the interval $t_{ini} \leq t \leq t_{fin}$. Therefore, $\max\big(f_1(t), f_2(t)\big) - \min\big(f_1(t), f_2(t)\big)$ may be considered to represent the "size" of the union of the ranges of the functions $f_1(t)$ and $f_2(t)$. In this study, percent e_{nrms}, which is obtained by multiplying e_{nrms} by 100, will be used.

Let the root mean square error of the actuating torque be $e_{T,rms}$. Clearly, $e_{T,rms}$=f[α, μ, k_L, Θ_{in}(t); M, t_{ini}, t_{fin}]. In other words, $e_{T,rms}$ is a function of α, μ, k_L, Θ_{in}(t); M, t_{ini}, t_{fin}. Here, [α, μ, k_L, Θ_{in}(t)] are continuous parameters, whereas, [M, t_{ini}, t_{fin}] are discrete parameters. One can obtain plots of $e_{T,rms}$ or $e_{T,nrms}$ vs 1 or 2 continuous parameters, while keeping the remaining parameters constant. Firstly, T_{act} of OPM and RPM is compared for several α values, while keeping the remaining parameters constant. The remaining parameters are given below.

[α, μ, k_L, Θ_{in}(t); M, t_{ini}, t_{fin}]=[α, 0.1, 0.5 N/mm, (-5° * t^2); steel, 0 s, 4 s]

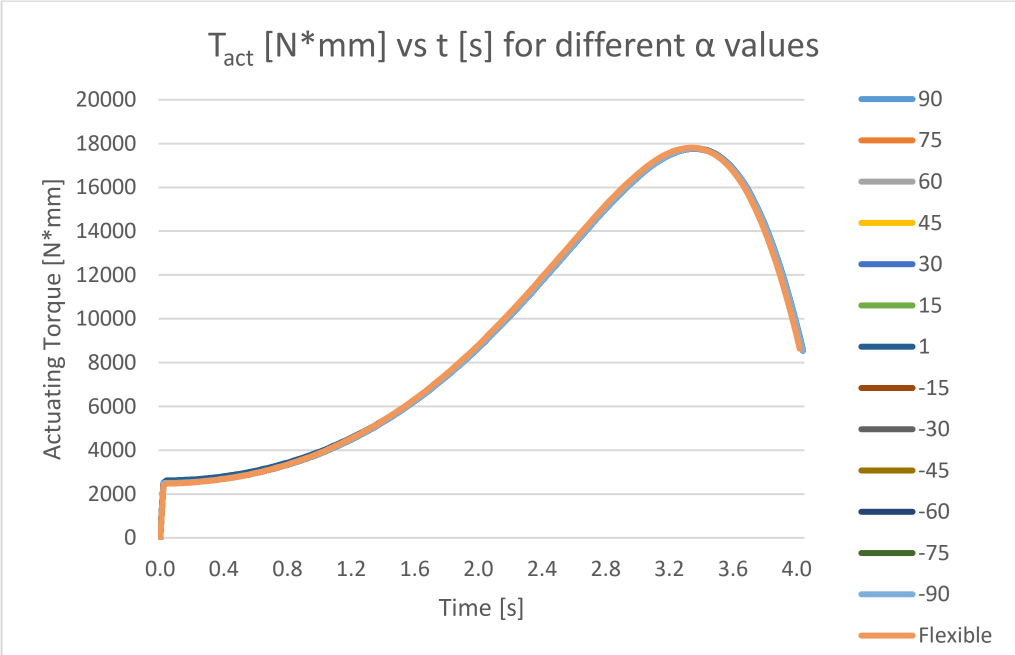

Figure 22: T_{act} [N*mm] vs t [s] for different α values

As can be seen from Figure 22, for all α values, actuating torques are quite close to each other. When one zooms into the plots, the differences become more observable (see Figure 23).

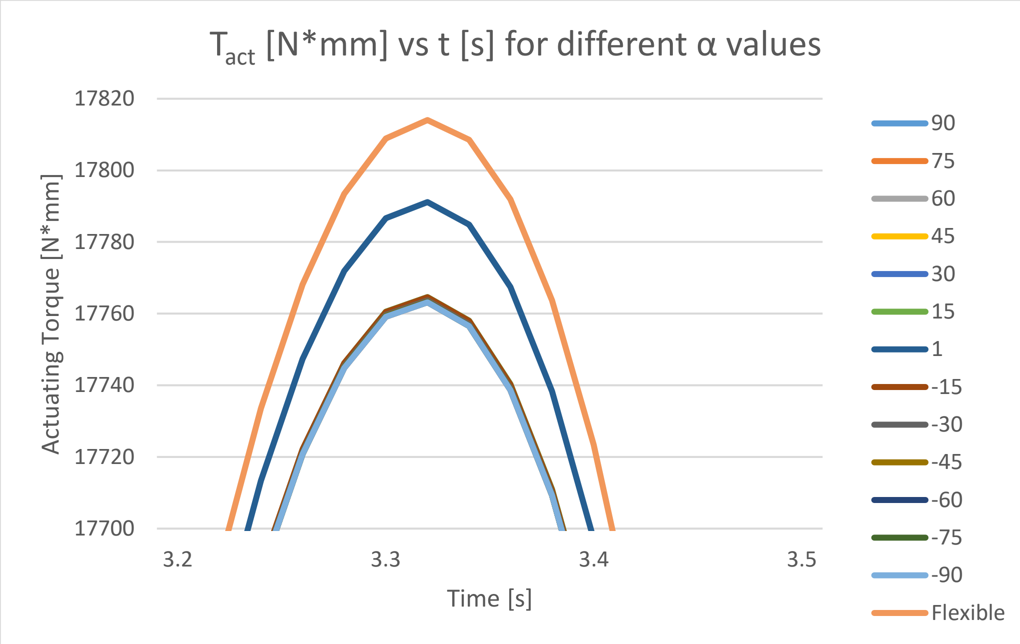

Figure 23: A Closer Look to T_{act} [N*mm] vs t [s] Graph Between t=3.2 and t=3.5

When friction exists, these graphs will differ from each other. Since the pin diameter of the revolute joints are much smaller than the lengths of the links, one expects that the plots for different α values are close to each other. If the pin diameters are comparable to the link lengths, then T_{act} graphs would be much more different.

Next, the "closeness" of OPM and RPM will be assessed in regard to $T_{act,OPM}(t)$ and $T_{act,RPM}(t)$.

Here, $T_{act,OPM}(t)$ is the actuating torque of the OPM, and $T_{act,RPM}(t)$ is the actuating torque of the RPM. Firstly, the error e_T is defined by replacing $f_1(t)$ and $f_2(t)$ with $e_{act,RPM}$ and $e_{act,OPM}$ in equation (49), i.e.,

$$e_T = e_{act,RPM} - e_{act,OPM} \tag{52}$$

Using e_T, $e_{T,rms}$ can be defined in accordance with equation (50), i.e.,

$$e_{T,rms} = \sqrt{\frac{\int_{t=t_{ini}}^{t=t_{fin}} e_T(t) * dt}{t_{fin} - t_{ini}}} \qquad (53)$$

Since time is discrete in the MSC Adams model, the integration in equation (53) is replaced by a summation, yielding

$$e_{T,rms} = \sqrt{\frac{\sum_{t_{ini}}^{t_{fin}} e_T(t) * \Delta t}{t_{fin} - t_{ini}}} \qquad (54)$$

with

$$\Delta t = \frac{4\ s}{201}$$

$$t_{ini} = 0\ s$$

$$t_{fin} = 4\ s$$

“201” in Δt, stands for number of discrete time steps used in the MSC Adams analysis.

Finally, $e_{T,nrms}$ can be defined as shown below:

$$e_{T,nrms} = \frac{e_{T,rms}}{\max(T_{act}) - \min(T_{act})} \qquad (55)$$

In Figure 25, $e_{T,nrms}$ [N*mm] vs angle α [°] graph is shown. The plot is obtained by taking α to be 90°, 75°, 60°, 45°, 30°, 15°, 1°, -15°, -30°, -45°, -60°, -75° and -90°. α=0° is not taken as a data point. This is because, at α=0°, $T_{act,RPM}(t)$ goes to infinity.

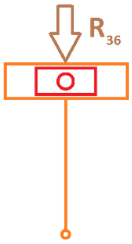

Figure 24: α=0° case for link 3

As shown in Figure 24, the joint reaction force of joint 3-6 (R_{36}) cannot create a moment which would rotate link 3 for α=0° (see Figure 8). So R_{36} goes to infinity at α=0°. Hence, the friction force also goes to infinity in joints 3-6 and 1-3. Hence, at α=0°, $T_{act,RPM}(t)$ goes to infinity. Therefore, instead of α=0°, α=1° is utilized.

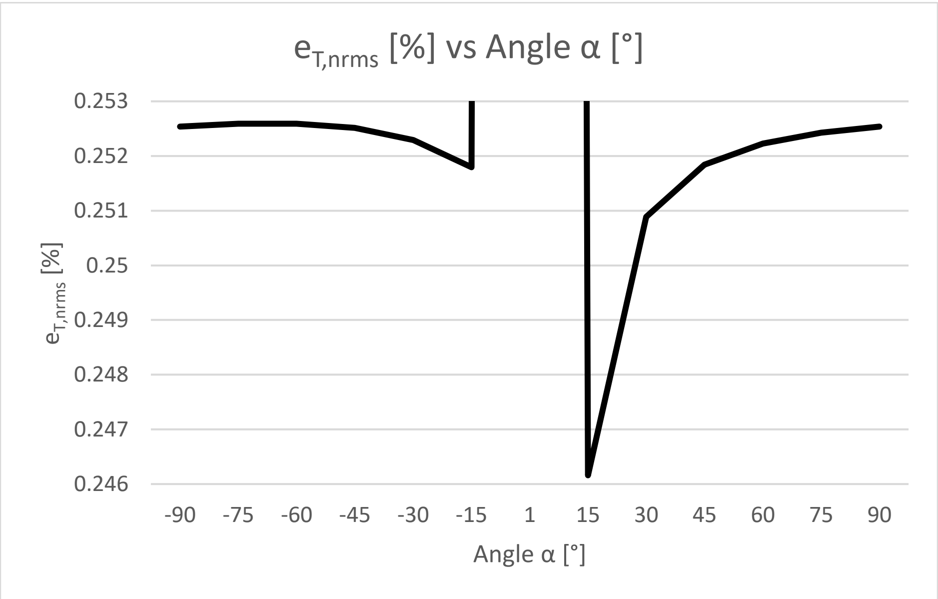

Figure 25: $e_{T,nrms}$ [%] vs Angle α [°]

According to Figure 25, minimum $e_{T,nrms}$ is achieved at α=15°, yielding $e_{T,nrms}$=0,246%. Therefore, RPM with α=15° is the closest regular mechanism to

OPM (as far as the actuator torques are concerned) when α takes the values 90°, 75°, 60°, 45°, 30°, 15°, 1°, -15°, -30°, -45°, -60°, -75° and -90°.

Note that in evaluating $e_{T,nrms}$, the first data point (t=0 s) is omitted, since in the two different models (namely OPM and RPM), the initial behavior of the systems are different. (In OPM, initial data starts from 0.)

In Figure 26, work vs angle α graph is shown for the RPM. As angle α goes to 0°, work is increasing. Minimum work is achieved at α= ±90°.

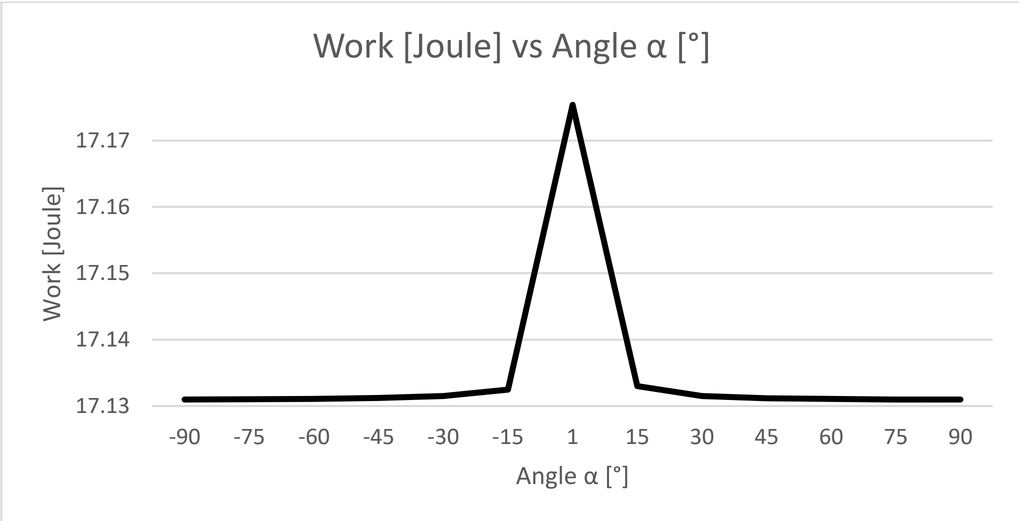

Figure 26: Work [Joule] Done by RPM vs Angle α [°]

In Figure 27, the x component of the joint reaction force of joint 1-3, in other words, R_{13x} is compared between OPM and RPM for α=[90°, 75°, 60°, 45°, 30°, 15°, 10°, 5°, 1°, -1°, -5°, -10°, -15°, -30°, -45°, -60°, -75°, -90°], while keeping the other parameters constant. Again, α=0° is avoided, because of the reason that has been explained before. Yet, the data points around α=0° are more intensive this time, since they need special attention.

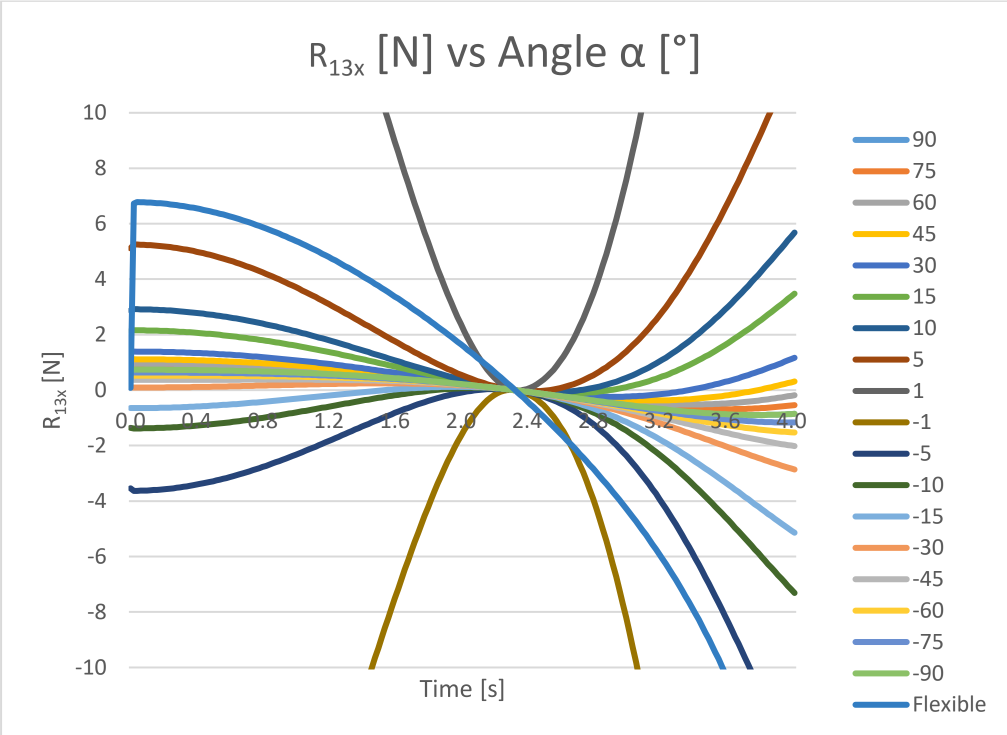

Figure 27: R_{13x} [N] vs t [s] for different α values

$e_{13x,nrms}$ [N] vs angle α [°] graph is shown in Figure 28.

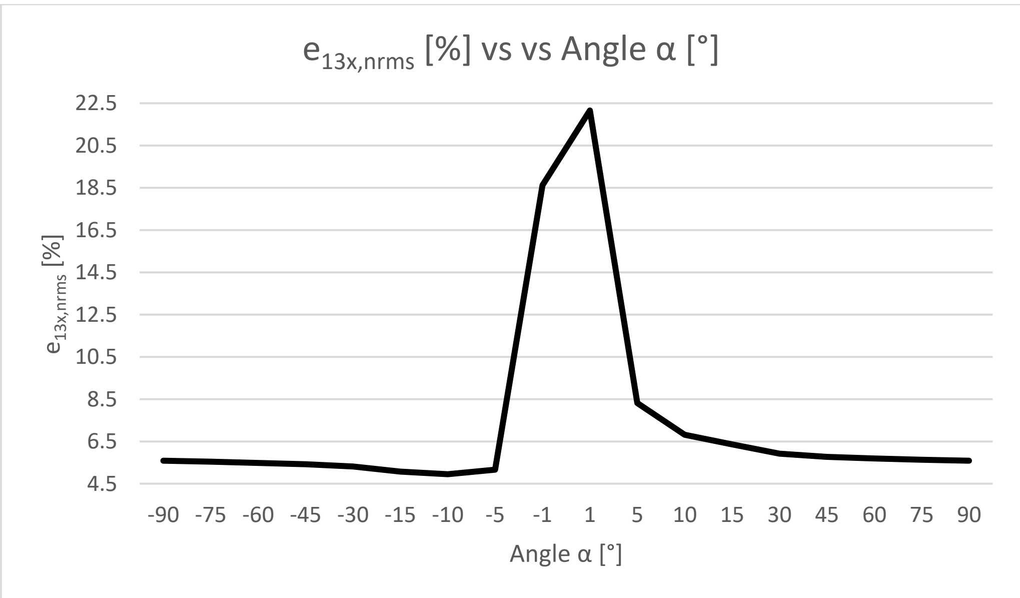

Figure 28: $e_{13x,nrms}$ [%] vs Angle α [°]

The minimum $e_{13x,nrms}$ which is $e_{13x,rms}$=4,95%, is achieved at α=-10°. Therefore, RPM with α=-10° is the closest one to OPM (in terms of R_{13x}) when α takes the values 90°, 75°, 60°, 45°, 30°, 15°, 10°, 5°, 1°, -1°, -5°, -10°, -15°, -30°, -45°, -60°, -75°, -90°.

As it can be seen from Figure 27, as opposed to the $T_{act}(t)$ values, R_{13x} values for different α angles differ significantly from each other. In other words, although angle α has no significant effect on the actuation torque, it has significant effects regarding the joint reaction forces, shaking forces and shaking moments. Note that, if α approaches to 0°, R_{13x} values increase substantially.

So far, the effects of α on $e_{T,nrms}$ have been investigated. Next, the combined effects of α and revolute joint friction on $e_{T,nrms}$ will be investigated.

For revolute joints, the friction torque can be found as below:

$$T_f = \mu * r_{pin} * F_{reaction} \tag{56}$$

where $F_{reaction}$ is the magnitude of the reaction force developed in the revolute joint [44]. Therefore, different friction characteristics can be obtained by changing $\mu * r_{pin}$. In this investigation, 8 different friction cases will be considered. These cases are listed below.

Case 1: $\mu * r_{pin}$ =0

Case 2: $\mu * r_{pin}$= 0,25 mm

Case 3: $\mu * r_{pin}$= 0,5 mm

Case 4: $\mu * r_{pin}$= 0,75 mm

Case 5: $\mu * r_{pin}$= 1 mm

Case 6: $\mu * r_{pin}$= 1,25 mm

Case 7: $\mu * r_{pin}$= 1,5 mm

Case 8: $\mu * r_{pin}$= 1,75 mm

Note that, in the previous analyses the friction characteristics was identical with case 3, since μ and r_{pin} were taken to be 0.1 and 5 mm, respectively.

In Figure 29, the variation of $e_{T,nrms}$ [%] with respect to angle α [°] and friction (μ* r_{pin}) [mm] is shown. At α=1°, $e_{T,nrms}$ increases rapidly and dominates the graph provided that friction increases. Therefore, as angle α goes to 0°, the error between RPM and OPM goes beyond acceptable limits.

In Figure 30, α=1° is omitted to see the rest of the graph more clearly. The minimum error is obtained for the frictionless case (case 1). The expected result is 0% error. However, since OPM is constructed with flexible links and RPM is constructed with rigid links, a small error occurs. It should be noted that, all errors for all slot angles (even for α=1° and α=0°) are the same with case 1, which is 0,2215%.

Second smallest error is obtained at α=15° and μ* r_{pin}=0.75 mm, which is 0.2358%. Actually, in all friction cases, minimum errors are obtained at α=15°, which shows that, the results obtained in Figure 25 are quite similar for all friction cases.

The numerical data that leads to Figure 29 and Figure 30 are shown in Table 2.

Table 3: $e_{T,nrms}$ [%] vs Angle α [°] vs Friction (μ* r_{pin}) [mm]

		Friction Case (μ* r) [mm]							
		0	**0.25**	**0.5**	**0.75**	**1**	**1.25**	**1.5**	**1.75**
Angle α [deg]	**90**	0.221505	0.276384	0.242149	0.245813	0.265787	0.278707	0.293423	0.309715
	75	0.221505	0.276334	0.242042	0.245660	0.265582	0.278463	0.293141	0.309398
	60	0.221505	0.276256	0.241848	0.245350	0.265166	0.277924	0.292483	0.308620
	45	0.221505	0.276118	0.241482	0.244741	0.264334	0.276833	0.291119	0.306984
	30	0.221505	0.275771	0.240565	0.243207	0.262251	0.274095	0.287705	0.302882
	15	0.221505	0.273995	0.236033	0.235817	0.252448	0.261448	0.272181	0.284480
	1	0.221505	0.290404	0.388601	0.638869	1.094076	1.936163	3.864241	11.08184
	-15	0.221505	0.276465	0.241435	0.243625	0.262554	0.273608	0.286171	0.300083
	-30	0.221505	0.276430	0.241911	0.245024	0.264578	0.276772	0.290647	0.306005
	-45	0.221505	0.276443	0.242126	0.245578	0.265393	0.278016	0.292379	0.308271
	-60	0.221505	0.276437	0.242197	0.245798	0.265731	0.278545	0.293132	0.309271
	-75	0.221505	0.276417	0.242200	0.245861	0.265838	0.278738	0.293429	0.309683
	-90	0.221505	0.276384	0.242149	0.245813	0.265787	0.278707	0.293423	0.309715

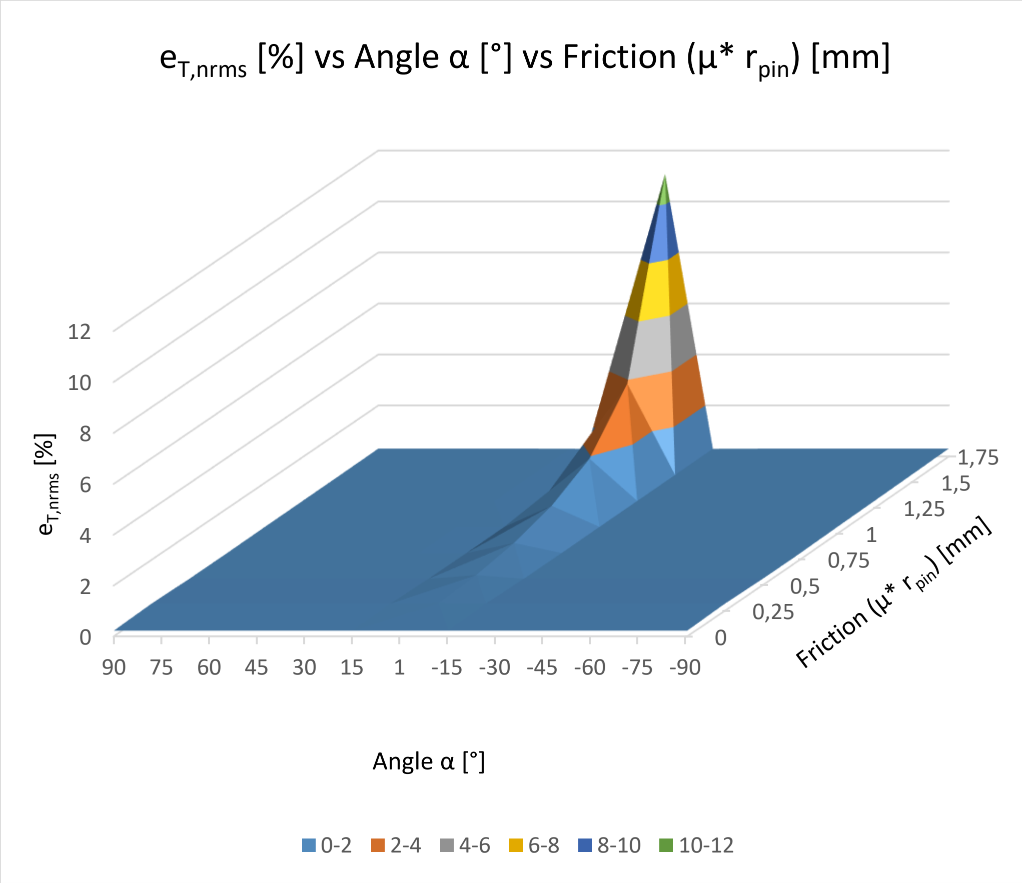

Figure 29: $e_{T,nrms}$ [%] vs Angle α [°] vs Friction (μ* r_{pin}) [mm]

As it can be seen from Figure 29, around α=0°, when friction increases, the difference between OPM and RPM increases substantially.

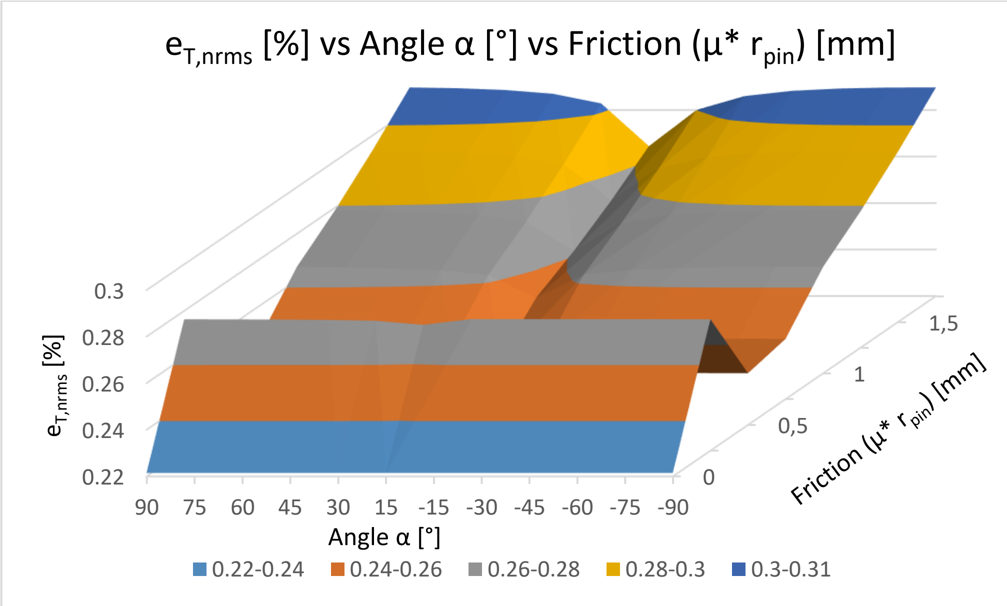

Figure 30: $e_{T,nrms}$ [%] vs Angle α [°] vs Friction (μ* r_{pin}) [mm] (excluding α=1)

Figure 31 shows variation of $e_{T,nrms}$ with respect to friction when α is kept constant at α=15°.

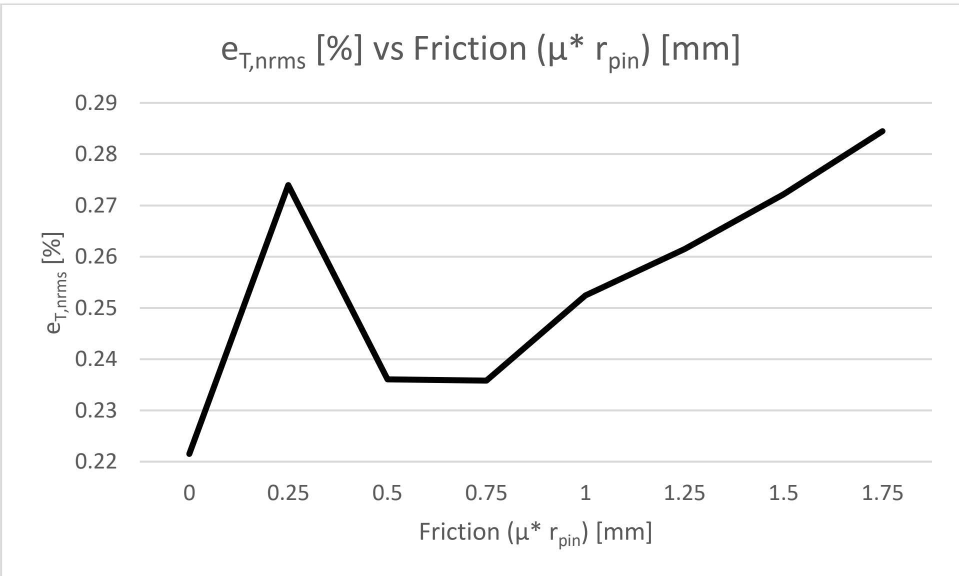

Figure 31: $e_{T,nrms}$ [%] vs Friction (μ* r_{pin}) [mm] (for α=15)

- Compared to the dynamic analysis of the RPM, the dynamic analysis of the OPM is much more difficult, because, besides the rigid body dynamic equlibrium equations, it is also necessary to consider the displacements that arise due to the flexibilities of the links. Clearly, dynamic analysis of the OPM can be solved by using a finite element analysis program. Alternatively, by using rigid body dynamic equlibrium equations solely, one could solve the dynamic analysis of an RPM, with a suitable α value; and thus obtain an approximate solution to the dynamic analysis of the OPM. The results obtained in this chapter indicate that such an approximation is quite valid, at least in the preliminary design stage. Hence, in the following chapters, the dynamic analysis of the $EqMFG_{1\&3}$ mechanism will be used to approximate the dynamic analysis of the MFG mechanism.
- In this chapter, T_{act} and R_{13x} values are compared for the RPM and the OPM. For these 2 dynamic properties, RPM with α=15° and RPM with α=-10° are the closest mechanisms to OPM respectively, among the considered set of α values. However, for different dynamic properties (R_{13y}, R_{14x}, $|R_{13}|$ etc.) another α might give closer results to the OPM. Hence, for optimization purposes, taking all ground joint reactions together (with or without different weighting factors) may be a more proper choice, rather than taking only one joint reaction.
- Besides α, other parameters (such as friction) can also be changed in order to obtain the closest RPM to a given OPM.
- Besides preliminary analysis purposes, one can also use an RPM in order to improve one or more of the dynamic properties of a given OPM. For example, if one needs to decrease R_{13x}, one can use an RPM with α=90°. As can be seen from Figure 27, in this case, the magnitude of R_{13x} decreases noticeably.

CHAPTER 3

COMPARISON OF DYNAMIC ANALYSES OF MFG

3.1 Introduction

In this chapter, inverse dynamic analysis of the balanced $EqMFG_{1\&3}$ mechanism (necessary conditions to be balanced is explained in section 1.3) will be performed by using two methods and the results will be compared and discussed.

First, a MATLAB code of the algorithm for the inverse dynamic analysis of the balanced $EqMFG_{1\&3}$ mechanism will be written as suggested in [45]. This algorithm (when there exist no slippage at the slots) is summarized below.

1. Make certain assumptions regarding the contact face (either the upper face or the lower face of the slot).
2. Determine the angular displacements of the rollers by using input displacement of links 2 and 4.
3. Solve F_R (and F_L) and the joint reaction forces between links 2 and 6. If found joint reaction forces are smaller than zero, it means that there is a conflict in the assumptions, so go to the step 1 and make new assumptions.
4. Find normal forces acting on the rollers. If found normal forces are in conflict with the assumptions, go to the step 1 and make new assumptions.
5. Determine friction force in between slots and rollers. If found friction forces are in conflict with the assumptions, go to the step 1 and make new assumptions.
6. STOP!

Then, the dynamic analysis of the balanced $EqMFG_{1\&3}$ will be performed by using the MSC Adams software. In MSC Adams, several models will be constructed, and the most meaningful model will be chosen for the comparison with the MATLAB algorithm.

3.2 Virtual Model of $EqMFG_{1\&3}$

In this section, modeling of the balanced $EqMFG_{1\&3}$ will be presented.

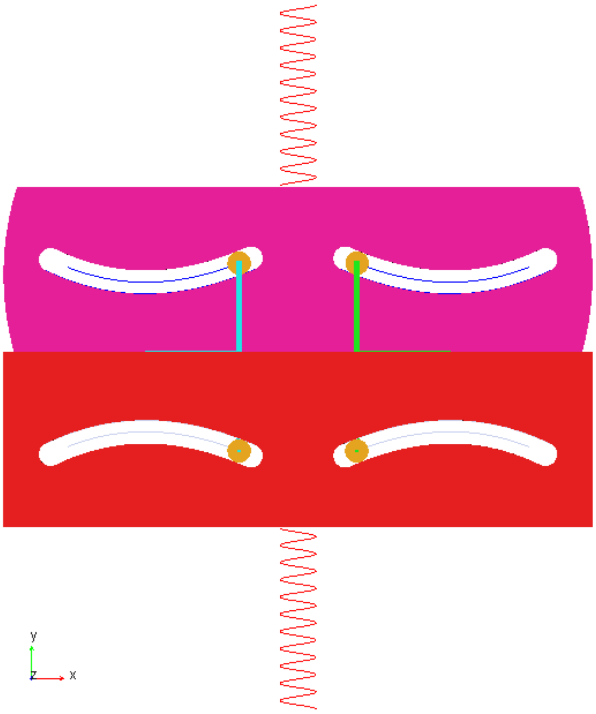

Figure 32: Front View of the Balanced $EqMFG_{1\&3}$

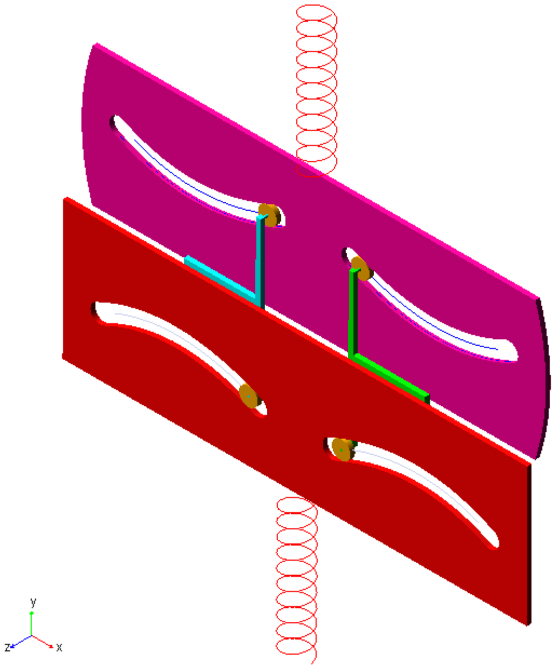

Figure 33: Isometric View of the Balanced $EqMFG_{1\&3}$

Front view of the balanced $EqMFG_{1\&3}$ is shown in Figure 32. Isometric view of the balanced $EqMFG_{1\&3}$ is shown in Figure 33. For the sake of simplicity, ground is not shown in these figures.

In MSC Adams, three different models are constructed. The most successful one is chosen for the comparison of the results of the MATLAB algorithm for the inverse dynamic analysis of the balanced $EqMFG_{1\&3}$ mechanism (which will be called as "*algorithm*" shortly) and the MSC Adams model.

The dimensions, inertial parameters and other parameters of the balanced $EqMFG_{1\&3}$ (that will be used for the comparison) are given below after introducing the notation to be used.

m_x : mass of link x

I_x : mass moment of inertia of roller link x about axis of rotation at center of mass

b_1, b_2, b_3 : dimensions of links 1, 2, 4 which are shown in Figure 1

r_x : radius of roller link x

k_u : spring stiffness of the upper spring which is connected to link 3

k_l : spring stiffness of the lower spring which is connected to link 5

y_u : free length of the upper spring

y_l : free length of the lower spring

a_0, a_1, a_2, a_3 : coefficients of the curve that describes the slot shapes

r_b : common bearing radius of the revolute joints at the centers of the rollers

μ_s : coefficient of friction between slot and rollers

μ_r : coefficient of friction at revolute joint bearings

The numerical values of the data to be used are taken from [47] and given below.

m_2=1.824 kg

m_4=1.824 kg

m_3=3 kg

m_5=3 kg

m_6=0.004 kg

m_7=0.004 kg

m_8=0.004 kg

m_9=0.004 kg

$I_6=2*10^{-7}$ kg*m^2

$I_7=2*10^{-7}$ kg*m^2

$I_8=2*10^{-7}$ kg*m^2

$I_9=2*10^{-7}$ kg*m^2

$b_1=0.3$ m

$b_2=0.08$ m

$b_3=0.15$ m

$r_6=0.01$ m

$r_7=0.01$ m

$r_8=0.01$ m

$r_9=0.01$ m

$k_l=275$ N/m

$k_u=275$ N/m

$y_l=0.115$ m

$y_u=0.115$ m

$a_0=0.11$

$a_1=-0.605$

$a_2=1.916$

$a_3=2.177$

$r_b=0.00125$ m

$\mu_s=0.1$

$\mu_r=0.1$

Note that, in MSC Adams model, links 2, 3, 4 and 5 are connected to the ground from their centers of mass by means of prismatic joint.

Slot shapes are defined via the equation $y(x) = a_0 + a_1 * x + a_2 * x^2 + a_3 * x^3$ which is a third order polynomial where $50 \text{ mm} \leq x \leq 175 \text{ mm}$. For the given coefficients above, the slot shape is shown in Figure 34. Note that, slot shape is taken from [47].

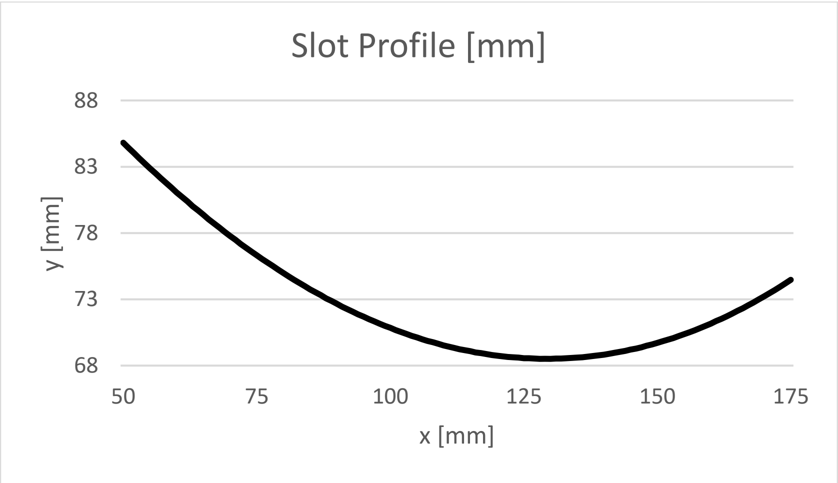

Figure 34: Slot Profile

Parameters that are of interest are given below:

s_2 : Input displacement of link 2 as shown in Figure 35

s_4 : Input displacement of link 4 as shown in Figure 35

s_3 : Output displacement of link 3 as shown in Figure 35

θ_6 : Angular position of roller link 6

F_{26} : Reaction force between link 2 and link 6

F_R : Actuating force applied to link 2 as shown in Figure 1, $F_R = F_L$

F_L : Actuating force applied to link 4 as shown in Figure 1, $F_R = F_L$

F_{N6} : Normal force between roller link 6 and the slot of link 3

F_{N7} : Normal force between roller link 7 and the slot of link 3

F_{N8} : Normal force between roller link 8 and the slot of link 5

F_{N9} : Normal force between roller link 9 and the slot of link 5

f_6 : Friction force between roller link 6 and the slot of link 3

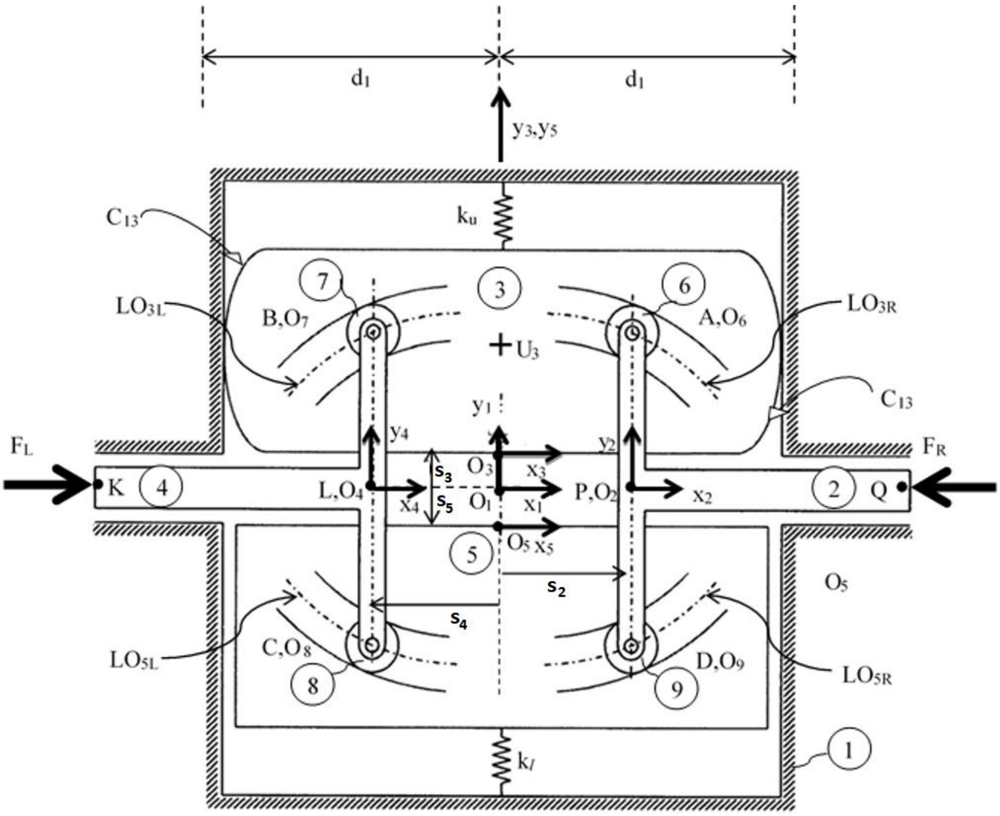

Figure 35: EqMFG$_{1\&3}$ Mechanism [46]

Input is given as <u>displacement between link 2 and link 4</u>. Hence, the only input is specified as s_{24} which is the summation of s_2 and s_4 ($s_2 = s_4$).

$$s_{24} = s_2 + s_4 \tag{57}$$

$$s_2 = 0.02 * t^2 \tag{58}$$

s_2 [mm] vs time [s] graph is also given in Figure 36.

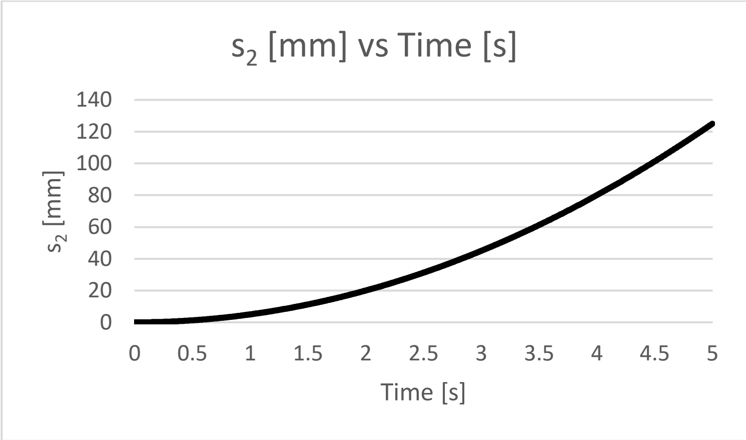

Figure 36: s_2 [mm] vs Time [s]

Gravity is not taken into consideration. Total time duration is taken as 5 seconds which is divided into 1000 increments.

Modeling the cylinder in slot joint is troublesome in MSC Adams. To this purpose, 3 different models are suggested.

3.2.1 Model 1 with Point on Curve Constraint

In this model, center of mass of the rollers 6, 7, 8 and 9 are restricted to move on the curves which are at the middle of the slots. This is achieved by imposing point on curve constraints. All bodies are selected to be planar links with λ=3. So, translation of the rollers in the z direction (shown in Figure 32 and Figure 33) are restricted 2 times. Obviously, one of the constraints is redundant, and hence should be removed. MSC Adams automatically detects this situation and removes the redundant constraints. Although there are other alternatives which do not introduce redundant constraints, modeling all parts as planar links is the most meaningful and simple model when the point on curve constraint is used.

Joints used in model 1 are presented in Table 3. In each row, the connection of a link with the remaining links (located on the columns) are presented. In the second column, the degree of freedom of the corresponding link is shown. If a link is selected to be a "planar" link with λ=3, it is shown in green.

Each joint is shown only once in black. If any joint is shown for the second time, it is shown in red. Hence, the joints in black represent all of the joints without any repetitions. Under the abbreviation of each joint, the degree of freedom restricted by that joint is given.

Table 3: Summary of Joints of Model 1

LINK	SPACE DOF	1		2	3	4	5	6	7	8	9
2	3	INP 1	PERP 1					INL 2			INL 2
3	3	INP 1						PoC 1	PoC 1		
4	3	INP 1	PERP 1						INL 2	INL 2	
5	3	INP 1	PERP 1							PoC 1	PoC 1
6	3			INL 2	PoC 1						
7	3				PoC 1	INL 2					
8	3					INL 2	PoC 1				
9	3			INL 2			PoC 1				

Point on curve constraints normally remove 2 degrees of freedom. However, according to the explanation in the first paragraph, they remove only 1 degree of freedom here. In order to emphasize this point, their restricted degrees of freedom are shown with blue in Table 3.

In Table 4, the degree of freedom calculation of model 1 is shown. In this table, the degree of freedom of bodies, joints and constraints are displayed.

Table 4: Degree of Freedom Calculation of Model 1

Item	Number	DOF per item	Resulting DOF
3 DOF Body	8	3	24
INL	4	-2	-8
INP	4	-1	-4
PERP	3	-1	-3
PoC	4	**-1**	**-4**
		TOTAL	**5**

By summing the degree of freedom values in the last column, the degree of freedom of model 1 is found to be 5. 4 of these degree of freedoms are associated with the rotations of the rollers along their centroidal axes (which are practically redundant). The remaining 1 degree of freedom is the actual degree of freedom of the mechanism.

In this model, friction is not included. Hence, rotations of the rollers are completely arbitrary.

3.2.2 Model 2 with Solid to Solid Contact

In this model, the joints between links 3, 5 and the rollers 6, 7, 8, 9 are modelled by solid to solid contact and link 3 is selected to be planar link with λ=3. A summary of the joints of model 2 are presented in Table 5.

Table 5: Summary of Joints of Model 2

LINK	SPACE DOF	1	2	3	4	5	6	7	8	9
2	6	PRIS 5					REV 5			REV 5
3	3	INP 1					SURF	SURF		
4	6	PRIS 5						REV 5	REV 5	
5	6	PRIS 5							SOLD	SOLD
6	6		REV 5	SURF						
7	6			SURF	REV 5					
8	6				REV 5	SOLD				
9	6		REV 5			SOLD				

In Table 6, degree of freedom calculation of model 2 is shown.

Table 6: Degree of Freedom Calculation of Model 2

Item	Number	DOF per item	Resulting DOF
3 DOF Body	1	3	3
6 DOF Body	7	6	42
INP	1	-1	-1
REV	4	-5	-20
PRIS	3	-5	-15
SOLD	4	0	0
		TOTAL	**9**

As can be seen in Table 6, the degree of freedom of model 1 is found as 9. 4 of these degree of freedoms are associated with the rotations of the rollers along their centroidal axes (which are practically redundant). 4 of the degree of freedoms seem to be free, but since the contacts restrict the translational motions perpendicular to the slots, they are actually not free. Here, the contacts do not directly decrease the degree of freedom, but still restrict the motion. The remaining 1 degree of freedom is the actual degree of freedom of the mechanism.

In this model, there exists friction between the rollers and the slots; and between the rollers and links 2, 4. Hence, the rotation of rollers are not arbitrary (they depend on the friction forces).

The data used in the Coulomb friction model is given below.

$\mu_s = 0.1$

$\mu_d = 0.1$

$V_s = 0.1$ mm/s

$V_d = 0.1$ mm/s

Equality of the transition velocities implies that; in Figure 15, for velocities greater than V_s, the graph is a straight line parallel to the x axis. This is because in the MATLAB algorithm, static friction is not taken into consideration.

Using too small V_s and V_d values leads to integrator difficulties. Here, moderately small values are used. In the results, it is observed that, the slip velocities do not even come close to these values.

For the revolute joint friction, stiction transition velocity is taken as 10^{-3} mm/s, which is very small. Hence, only sliding friction is considered (similar to the MATLAB algorithm), i.e., static and dynamic friction coefficients are taken to be equal to each other.

Initially, contact stiffness was taken to be 10^5 N/mm and the contact damping coefficient was taken to be 10 (N*s)/mm. However, because of the integrator difficulties in solid to solid contact, they have been changed to 10 N/mm and 1 (N*s)/mm respectively which are small enough to make the mathematical model easier to handle. If large values are used, oscillatory results are obtained. Using small values, on the other hand, makes the contact less rigid and increases the amount of penetration.

3.2.3 Model 3 with Curve to Curve Contact

In this model, the contact between links 3, 5 and the rollers 6, 7, 8, 9 is modelled via curve to curve contact. Furthermore, links 3 and 5 are selected to be planar links with λ=3. A summary of the joints used in model 3 are presented in Table 7.

Table 7: Summary of Joints of Model 3

LINK	SPACE DOF	1	2	3	4	5	6	7	8	9
2	6	PRIS 5					REV 5			REV 5
3	3	INP 1					CURV	CURV		
4	6	PRIS 5						REV 5	REV 5	
5	3	INP 1 PERP 1							CURV	CURV
6	6		REV 5	CURV						
7	6			CURV	REV 5					
8	6				REV 5	CURV				
9	6		REV 5			CURV				

In Table 8, degree of freedom calculation of model 3 is shown.

Table 8: Degree of Freedom Calculation of Model 3

Item	Number	DOF per item	Resulting DOF
3 DOF Body	2	3	6
6 DOF Body	6	6	36
INP	2	-1	-2
PERP	1	-1	-1
REV	4	-5	-20
PRIS	2	-5	-10
CURV	4	0	0
		TOTAL	**9**

The degree of freedom of model 1 is found as 9. 4 of these degree of freedoms are associated with the rotations of the rollers along their centroidal axes (which are practically trivial). 4 of the degree of freedoms seem to be free, but since the contacts restrict the translational motions perpendicular to the slots, they are actually not free. Here, the contacts do not directly decrease the degree of freedom, but still restrict the motion. The last 1 degree of freedom is the actual degree of freedom of the mechanism.

In this model, there exists friction between the rollers and the slots; and between the rollers and links 2, 4. Hence, the rotation of the rollers are not arbitrary, but depend on the friction forces.

The parameters used in the Coulomb friction model are given below.

$\mu_s = 0.1$

$\mu_d = 0.1$

$V_s = 0.1$ mm/s

$V_d = 0.1$ mm/s

These parameters are the same as the values that are used in model 2.

3.3 Results & Discussion

In this section, the result obtained by using the three models and the algorithm will be compared with each other. Firstly, the correctness of each MSC Adams model will be checked. For this purpose, the output displacements (s_3) will be compared.

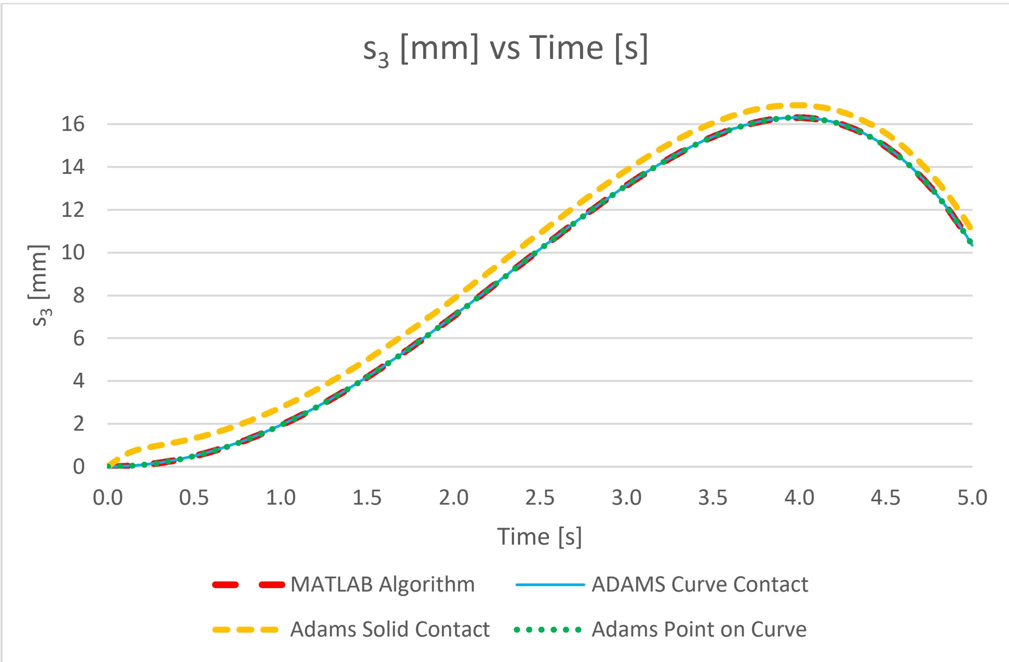

Figure 37: s_3 [mm] vs Time [s]

In Figure 37, output displacement s_3 vs time graph is shown. As can be observed from the figure, solid to solid contact is significantly different from the remaining three. This is because of the large penetration in the solid to solid contact model. The penetration reaches to 0.7 mm, which is quite large. Normally, it should be much smaller. However, since small contact stiffness value is used for the solid to solid contact model, a large penetration is needed in order to create the necessary contact force.

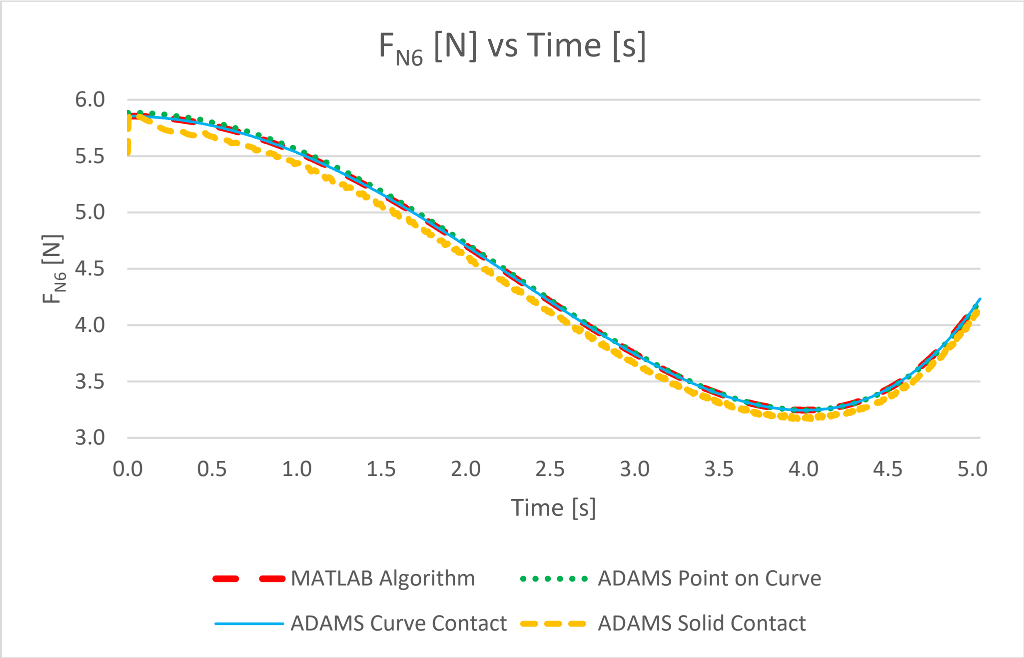

Figure 38: F_{N6} [N] vs Time [s]

Secondly, the normal forces acting between the slots and the rollers are compared. In Figure 38, F_{N6} vs time graph is shown. Solid to solid contact is, again, significantly different from the others. So, the solid to solid contact model deserves a closer attention.

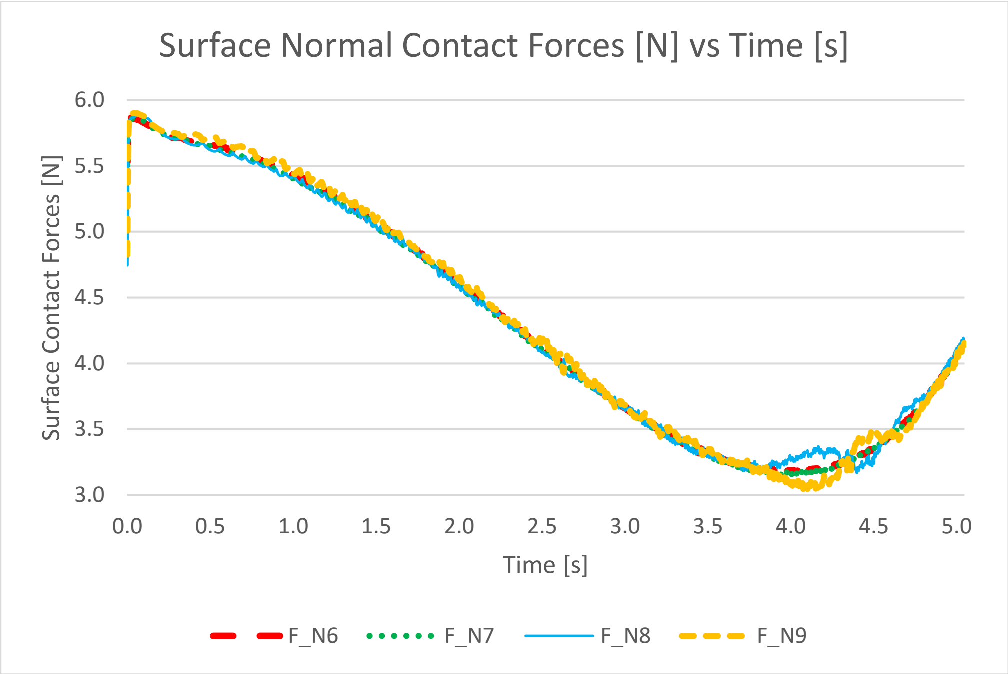

Figure 39: Surface Normal Contact Forces [N] vs Time [s] for Solid to Solid Contact

In Figure 39, the normal contact force vs time graph is shown (for all of the rollers) for the solid to solid contact model. The normal forces for the rollers 8 and 9 are too oscillatory, although their averages are comparable with the normal forces of rollers 6 and 7. This oscillation can be seen easily at t=4 sec. In solid to solid contact, contact detection is not analytic as explained before and the surfaces are tessellated as in Figure 16. Even in the small contact stiffness case, oscillations can be observed. If the contact stiffness is increased, the normal forces will become closer to the other models and the difference in Figure 38 will decrease (at the cost of a significant increase in the amount of oscillations).

In Figure 40, actuating force vs time graph is shown. Until 4th second, a negative actuating force is obtained. This means that, energy will be either consumed due to the motor braking or generated due to the regenerative braking. It is because of the relation between slot shape and spring. Slots are formed such that, until 4th second, they help link 2 and link 4 to move with the same direction with the input such that tension springs shrink. After 4th second, springs apply counter force to the input.

As expected, point on curve model generates (if regenerative braking is used in the motors) larger force until 4th second, and consumes less force after 4th second, since it doesn't involve friction. On the other hand, solid to solid contact model generates smaller force until 4th second, and consumes larger force after 4th second. Lastly, actuation forces for MATLAB algorithm and MSC Adams curve to curve contact model are similar.

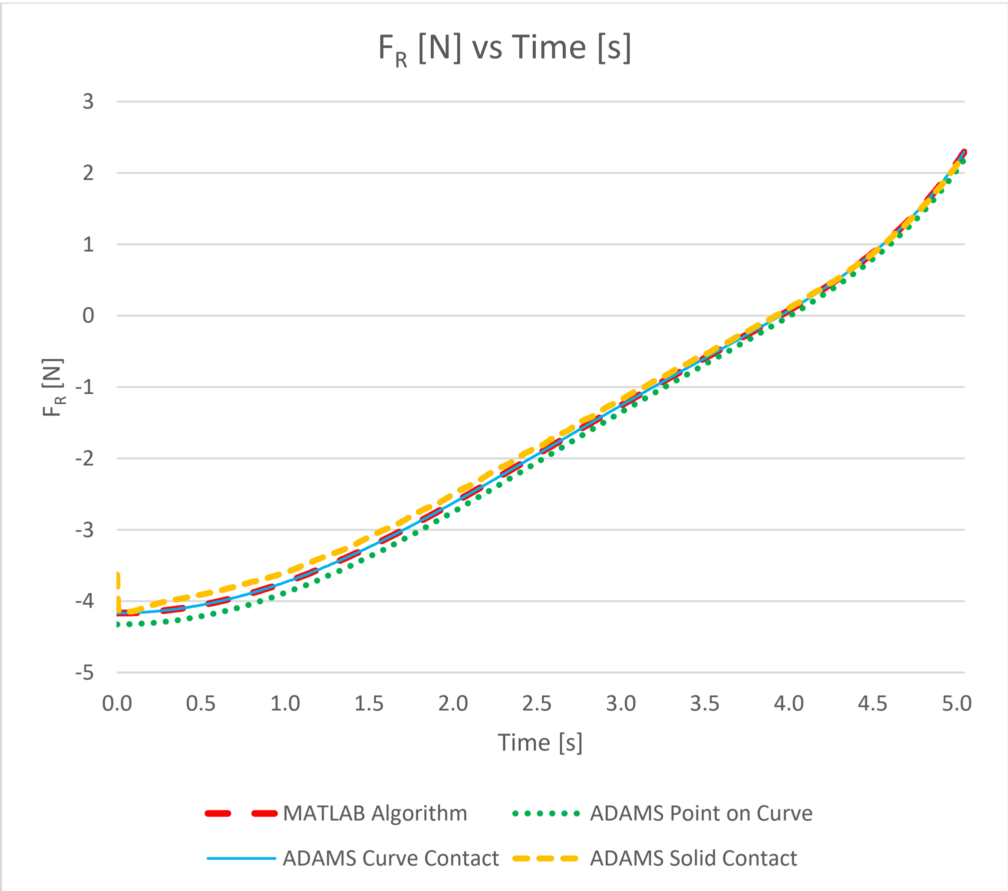

Figure 40: F_R [N] vs Time [s]

The results presented up to this point indicate that the solid to solid contact model is not accurate. Hence, the results related to the solid to solid contact model will not be presented after this point.

Point on curve model, on the other hand, is formed for being a rough guide for the other 2 models. Since it does not include friction, it gives approximate results. Hence, the results for the point on curve model will also be excluded after this point for the sake of conciseness.

Therefore, in the following graphs, only the MATLAB algorithm and the MSC Adams curve to curve contact model will be included. Curve to curve contact model seems accurate and easy to handle mathematically, since contact is defined analytically.

In Figure 41, the angular position of roller 6 vs time is shown. For both of the models, the angular positions are similar. Hence, it can be concluded that the no slip assumption that is used in the MATLAB algorithm is correct, since the rotations of the rollers are similar with the MSC Adams model.

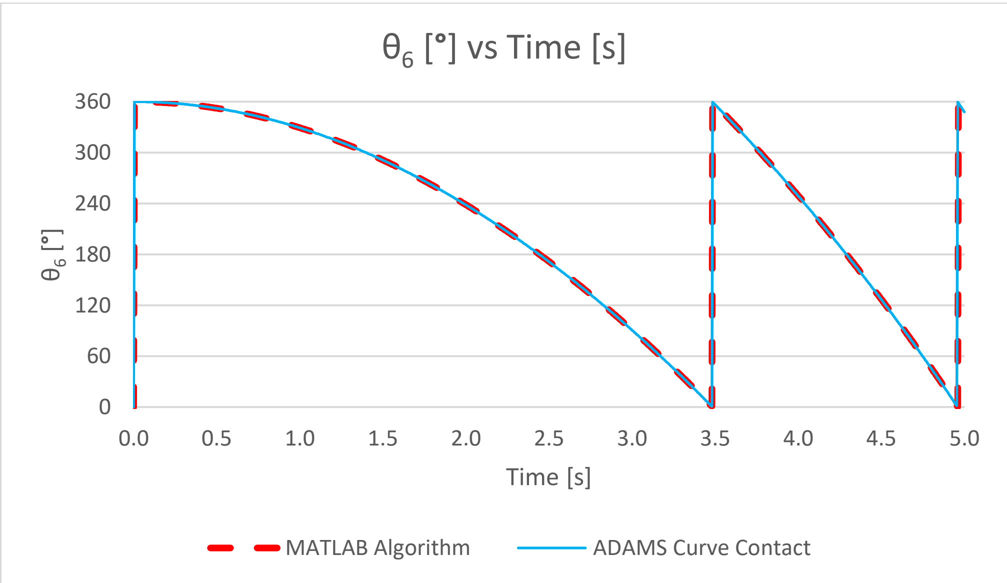

Figure 41: θ_6 [°] vs Time [s]

In Figure 42, the reaction force between link 2 and link 6 vs time graph is shown. For both the MATLAB algorithm and the MSC Adams curve to curve contact model, the reaction forces are similar. In fact, F_{26} is very close to F_{N6}, since f_6 (friction force between roller 6 and slot of link 3) is very small compared to F_{N6}.

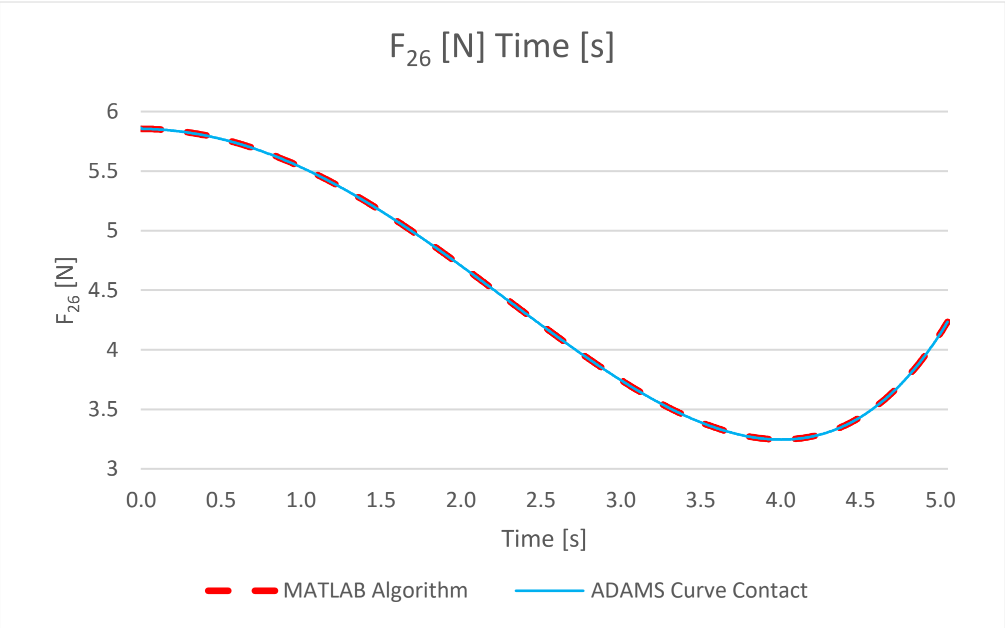

Figure 42: F_{26} [N] Time [s]

In Figure 43, spring force vs time graph is shown. For both the MATLAB algorithm and the MSC Adams curve to curve contact model, the graphs are similar.

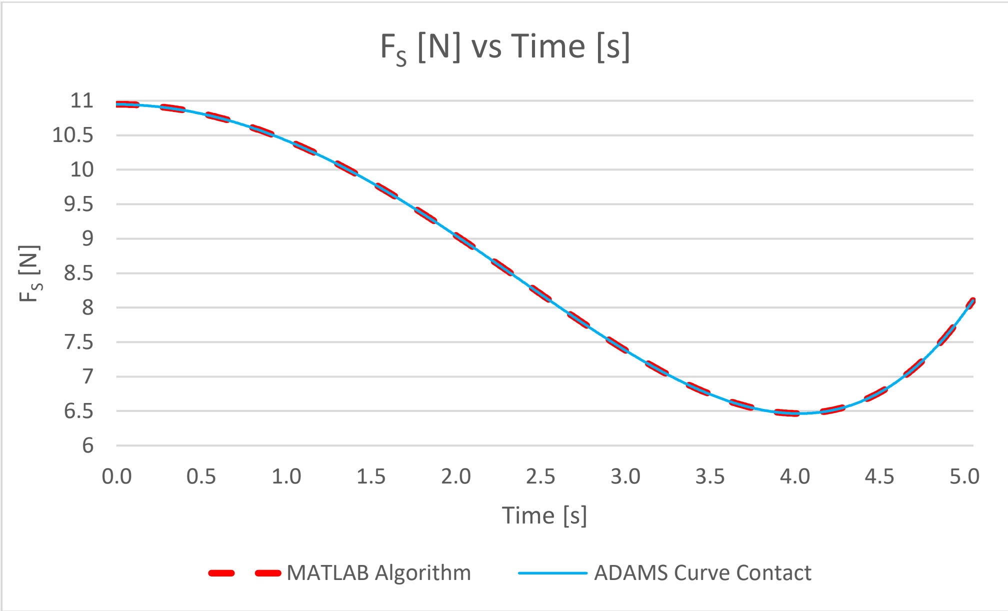

Figure 43: F_S [N] vs Time [s]

In Figure 44, power consumption vs time graph is given. For both the MATLAB algorithm and the MSC Adams curve to curve contact model, the graphs are similar.

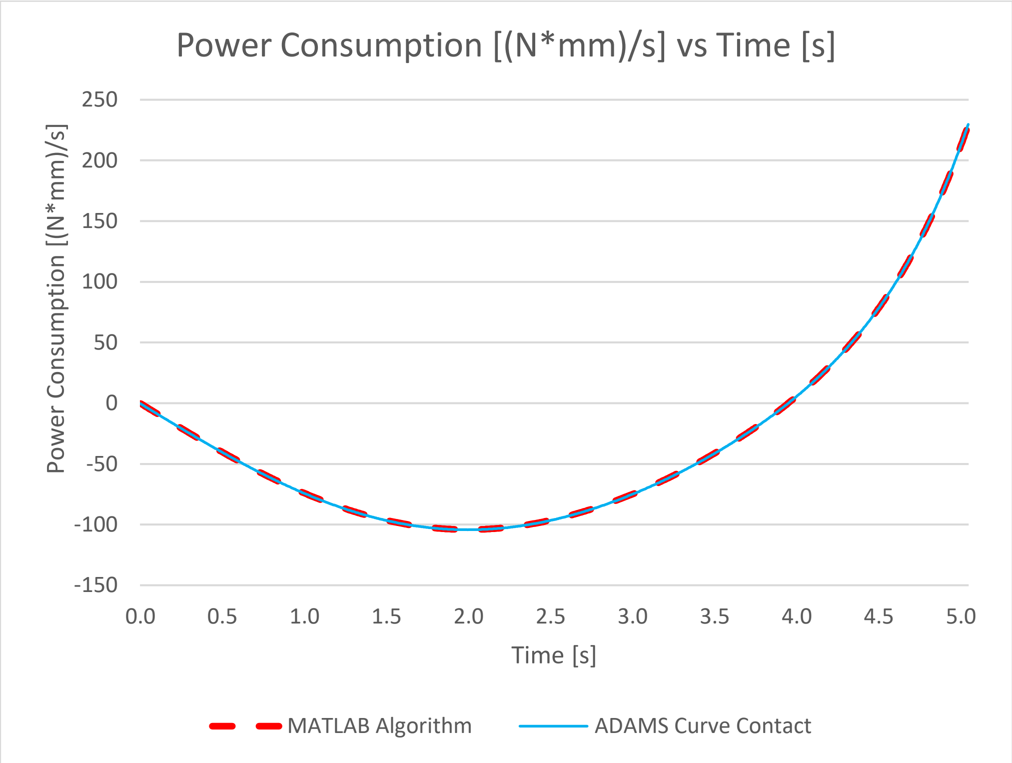

Figure 44: Power Consumption [(N*mm)/s] vs Time [s]

It is observed that, until the 4th second, the power consumption is negative, implying that work is done by the mechanism. After the 4th second, the power consumption is positive. Hence, work is done on the system. Note that the power consumption of the MATLAB algorithm is found via the equation

$$Power\ Consumption = \frac{2 * \Delta s_2 * F_R}{Time\ Step\ Size} \tag{59}$$

where, time step size is 0.005 s. Note that time is discrete, not continuous in the analyses. Calculations are made in each 0.005 seconds.

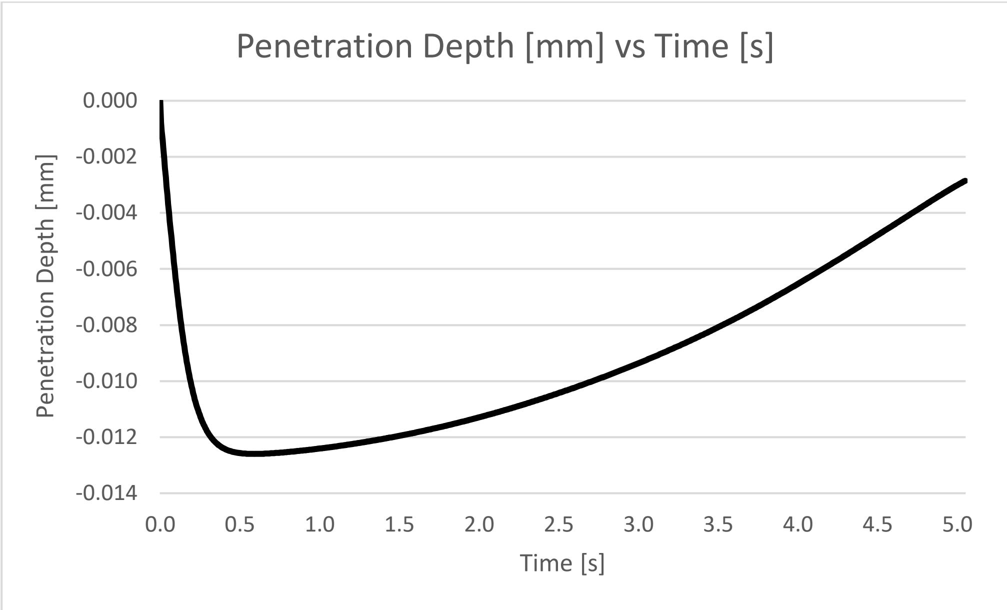

Figure 45: Penetration Depth [mm] vs Time [s]

In Figure 45, the penetration depth of the curve to curve contact vs time graph is shown. The maximum penetration does not exceed 0.013 mm, which is considered to be acceptable.

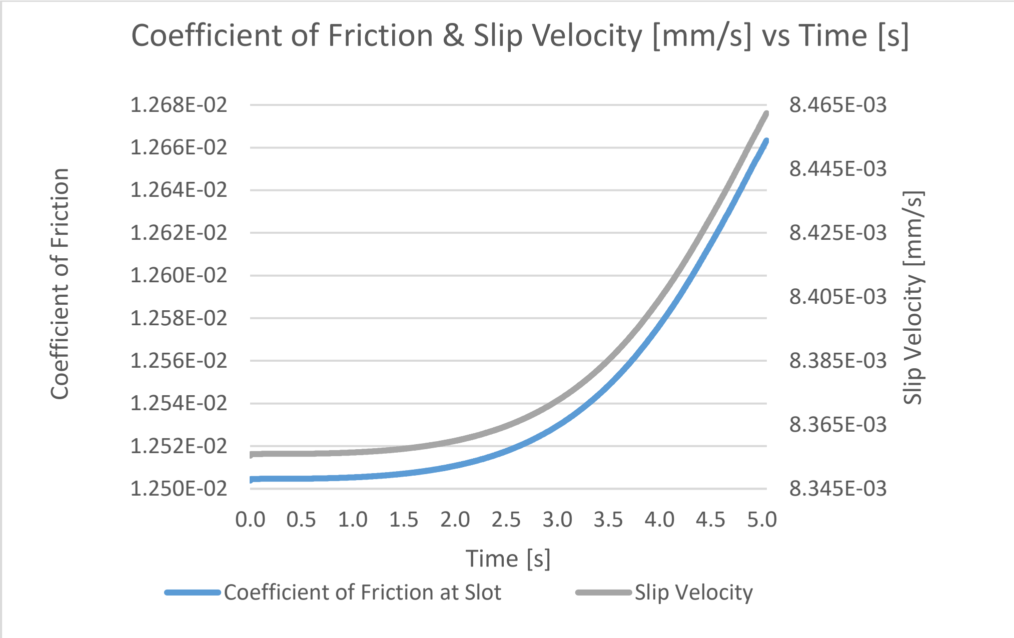

Figure 46: Coefficient of Friction & Slip Velocity [mm/s] vs Time [s]

In Figure 46, the coefficient of friction and the slip velocity vs time graphs are shown. They are shown together, because the coefficient of friction is directly related to the slip velocity in MSC Adams (see Figure 15). Recall that V_s and V_d have been specified to be $V_s = V_d = 0.1$ mm/s.

Hence the slip velocity doesn't even approach to the specified value. Therefore, it is safe to say that there is no slip. Moreover, the coefficient of friction is also too small. Recall that μ_s and μ_d have been specified to be $\mu_s = \mu_d = 0.1$.

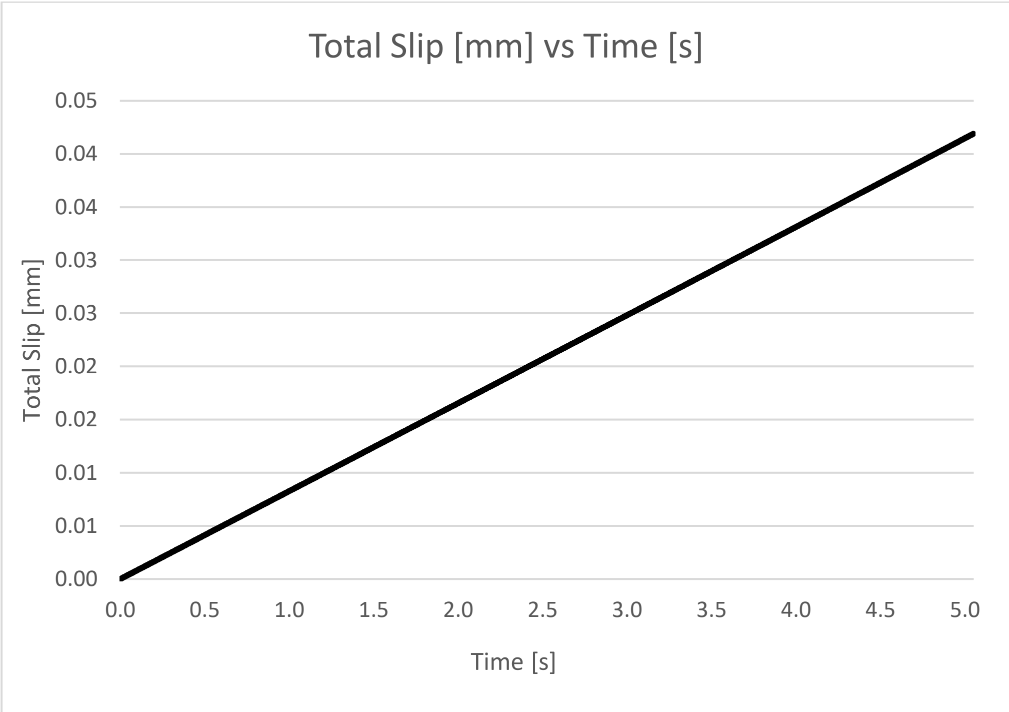

Figure 47: Total Slip [mm] vs Time [s]

In Figure 47, total slip vs time graph is shown. Total slip doesn't exceed 0.05, although the roller moves more than 125 mm. Hence, as concluded before, it is safe to say that there is no slip. Remember that this very small amount of slip is necessary to create the friction force in MSC Adams.

In Figure 48, friction force acting on the rollers vs time graph is shown. For both the MATLAB algorithm and the MSC Adams curve to curve contact model, the graphs are similar. Remember that, F_{26} is very close to F_{N6}, since f_6 (friction force between roller 6 and slot of link 3) is very small comparing to F_{N6}.

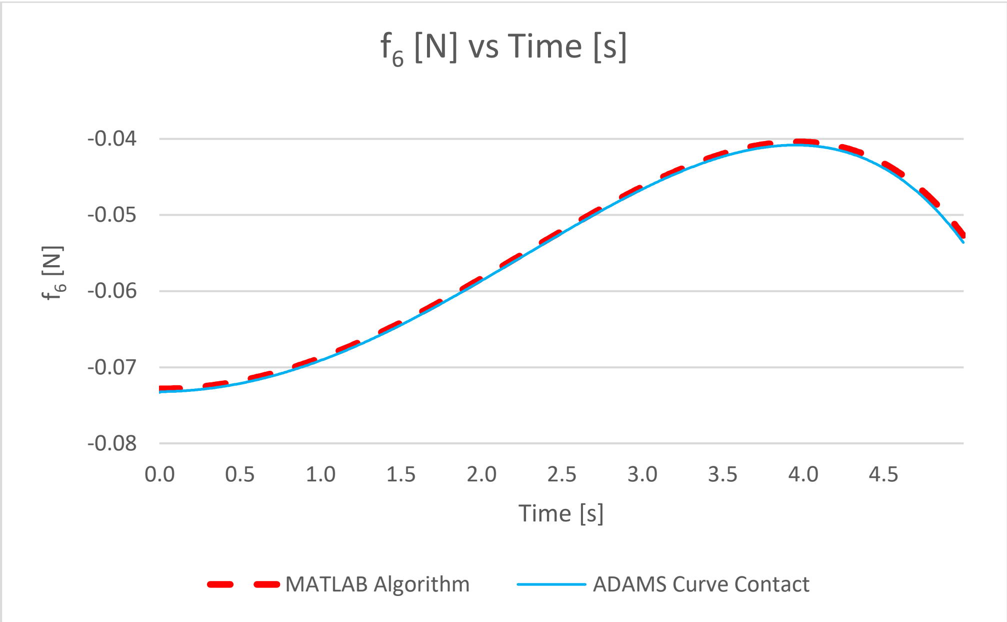

Figure 48: f_6 [N] vs Time [s]

In Figure 49, revolute joint friction torque vs time graph is given. The graph is obtained from the output of the MSC Adams curve to curve contact model. It will be used to calculate the frictional loses.

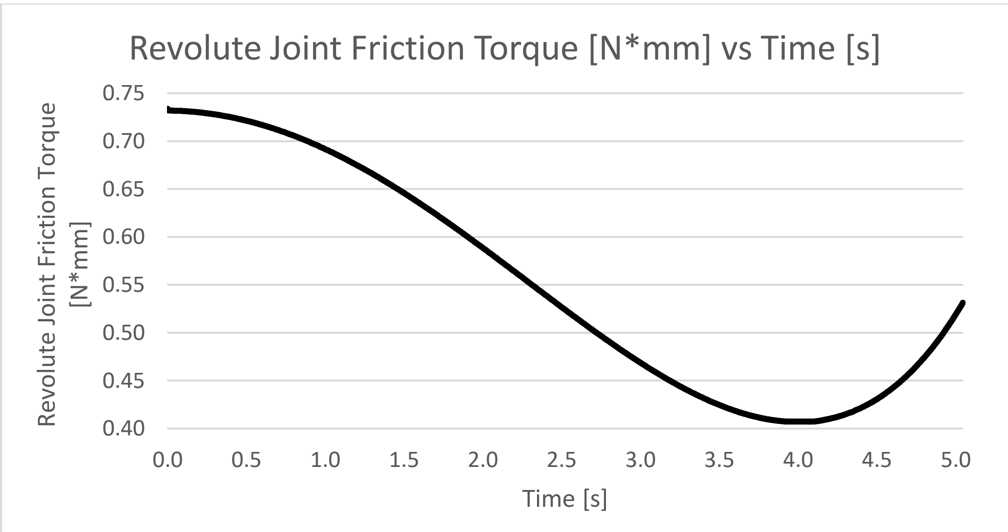

Figure 49: Revolute Joint Friction Torque [N*mm] vs Time [s]

In Figure 50, power consumptions of the motion and friction vs time graph is shown. Power consumption due to the friction at the 4 revolute joints is obtained via the equation

$$Power\ Consumption = \frac{4 * \Delta\theta_6 * T_{f6}}{Time\ Step} \qquad (60)$$

where time step size is taken to be 0.005 s and T_{f6} is the revolute joint friction torque as shown in Figure 49. There is no power consumption due to the friction between the slots and the rollers, since there is no slip at these contacts. Furthermore, since the mechanism is balanced, the reaction forces at the ground joints are all zero. Hence, there is no frictional losses at these joints as explained in section 1.3.

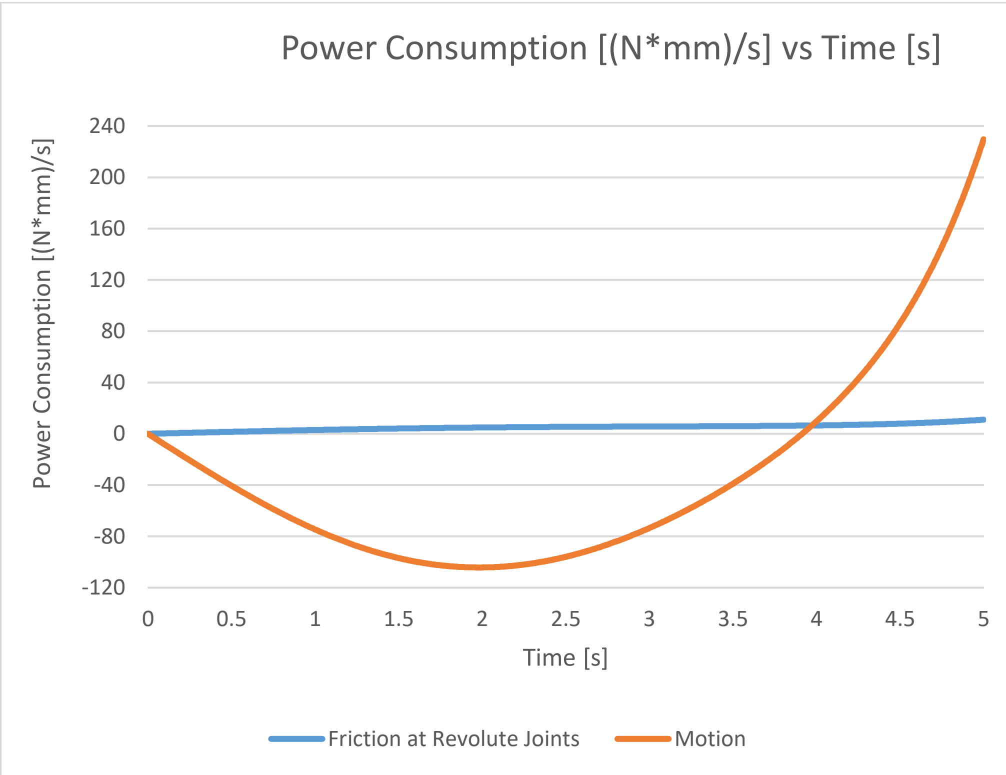

Figure 50: Power Consumption [(N*mm)/s] vs Time [s]

As it can be seen from Figure 50, power consumed by the friction is very small compared to power consumption or generation of the motion.

To obtain meaningful results, examine this graph by dividing into two parts:

1. [0 s, 4 s] part at which power consumption is negative. (energy is consumed due to braking or regenerated due to regenerative braking)

2. [4 s, 5 s] part at which power consumption is positive.

At the first part, friction consumed 6.2% of the energy generated due to regenerative braking. At the second part, friction consumes 8.9% of the total energy consumed.

In another task that is inspected by Mencek [47, p. 231], friction consumes 11.60% of the total energy consumed. Hence, results of this study and Mencek's study are compatible. In Mencek's study, the double slider mechanism which performs a similar task with the MFG (with translating input and translating output), the friction losses are 22.35%. Therefore, one may replace a double slider mechanism with an MFG and save energy.

3.4 Conclusive Remarks

To conclude, in chapter 3, inverse dynamic analysis of the $EqMFG_{1\&3}$ is made with both algorithm proposed by Soylu [45] and MSC Adams model. Results of them are in great agreement with each other. So, both of them are verified.

Curve on curve constraint is the most suitable constraint to model the slots of MFG. Hence, one can use curve on curve constraint to simulate the MFG in MSC Adams.

Constructing MSC Adams model is quite harder and more complex than the MATLAB algorithm. Hence, one should use the algorithm for simulating MFG in general.

However, to get more sophisticated results, or to get visual results, one can use MSC Adams for simulating MFG. In more complicated cases (for example by introducing gravitational acceleration, etc.), MSC Adams can be preferred to deal with the complexity.

CHAPTER 4

OPTIMIZATION OF DYNAMIC PROPERTIES OF A PRESS MACHINE

4.1 Introduction

In this chapter, MFG will be used to improve the dynamical behavior of a press machine by connecting it to the ram of the press. Note that the MFG can be used to

1. Reduce the overall energy consumption of the press,
2. Reduce the maximum motor torque or maximum motor power of the press,
3. Increase the minimum motor torque or minimum motor power of the press (when they are negative, in other words, when the system is storing energy),
4. Reduce the motor torque or motor power (throughout the motion in a root mean square sense),
5. Reduce any one of the reaction forces/moments at the joints of the press.

Throughout these analyses, a divide and conquer method will be used. Firstly, the kinematic and dynamic analyses of the press machine will be performed. Using these analyses, the required force (to be applied by the MFG) to optimize one of the above mentioned properties will be determined. Secondly, the slot profile of the MFG will be determined together with its inertial parameters and dimensions.

Throughout the analyses, the sample crank press data given in [53] will be used. The nominal force of this press is 16 MN. In Figure 51, the compression versus force graph for forging a connecting rod is shown. In this graph, 2 lines are fitted to the data points (which are obtained by finite element analysis). Note that the end of the compression zone corresponds to the bottom dead center.

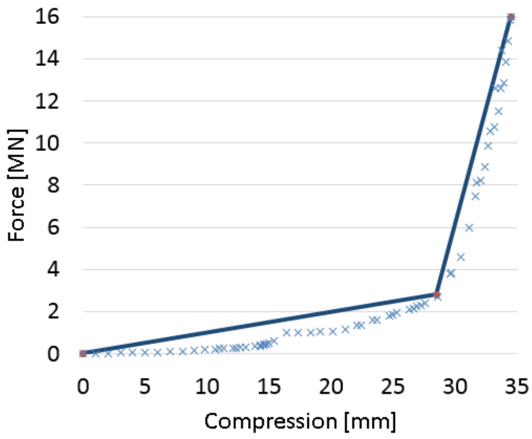

Figure 51:Compression vs Force Graph [53]

The specifications of the crank press are taken as listed below.

density of the links : 7850 kg/m^3

crank length : 128.5 mm

coupler length : 771 mm

forging stroke : 34.5 mm

crank speed : 60 rpm (constant)

Link thicknesses are determined by considering buckling of the beams. The safety factor is taken as 1.5 for the load described in Figure 51. For all loads and tasks, the same link dimensions will be used.

4.1.1 Model of the Electric Motor

As stated before, MFG may be used to reduce the energy consumption of the press. Reduction of the energy consumption can be realized in two different ways.

1. By storing energy when the required actuating torque is negative (i.e., when there is a need for braking),
2. By forcing the electric motor to run in its most efficient zone.

In order to simulate the second case, one needs to include a model of an electric motor with a variable efficiency.

By making tests, or by using finite element analysis, one can obtain the efficiency map of an electric motor on the torque vs speed plane (see section 1.4). In general, the efficiency map of an electric motor looks like the one in Figure 52.

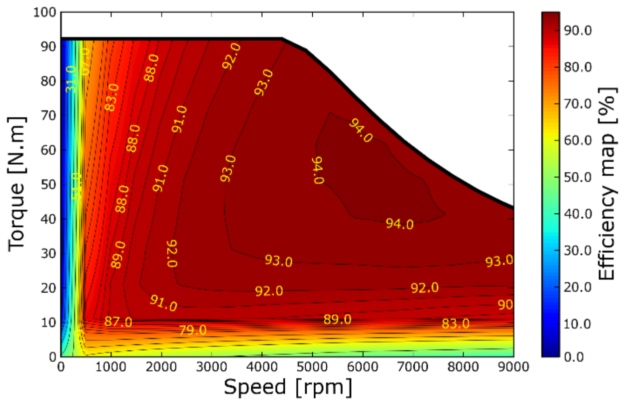

Figure 52: A Typical Efficiency Map for an Electric Motor [61]

In this study, in order to obtain the efficiency map, a simplified approach will be used. In this approach, only the copper losses of the motor will be taken into account. Possible errors due to this simple model will be discussed in the results and discussion section.

Copper loss can be simply described as below: [59]

$$Copper\ loss = [I(t)]^2 * R = K * [T_m(t)]^2 \tag{61}$$

where

$I(t)$: current drawn by the motor at time t

R : resistance of the motor

K : a constant $[(\Omega * A^2)/(N^2 * m^2)]$

$T_m(t)$: motor torque at time t

In equation (61), it has been noted that $T_m(t) = K_T * I(t)$ where K_T is the torque constant of the motor. Hence, the constant K can be obtained in terms of R and K_T, yielding $K = {}^{R}/_{K_T^2}$. Alternatively, K could be solved from equation (61), yielding

$$K = \frac{[I(t)]^2 * R}{[T_m(t)]^2} \tag{62}$$

Efficiency of an electric motor, on the other hand, is given via the equation

$$\eta(t) = \frac{P_{out}(t)}{P_{in}(t)} = \frac{T_m(t) * \omega_m(t)}{T_m(t) * \omega_m(t) + K * [T_m(t)]^2} \tag{63}$$

where

$\omega_m(t)$: angular speed of the motor shaft

$P_{out}(t)$: output power

$P_{in}(t)$: input power

Dividing the right hand side of Equation (63) by $T_m(t)$, one obtains,

$$\eta(t) = \frac{\omega_m(t)}{\omega_m(t) + K * T_m(t)} \qquad (64)$$

where

$\eta(t)$: efficiency of the electric motor

Hence, efficiency is obtained as a function of angular speed and torque. In Figure 53, efficiency graphs (in the $\omega_m T_m$ plane) for 2 different K values are shown. The K values used in Figure 53 are arbitrarily selected, in order to see the effect of K on the efficiency. Clearly, as K increases, the efficiency decreases at all points in the $\omega_m T_m$ plane.

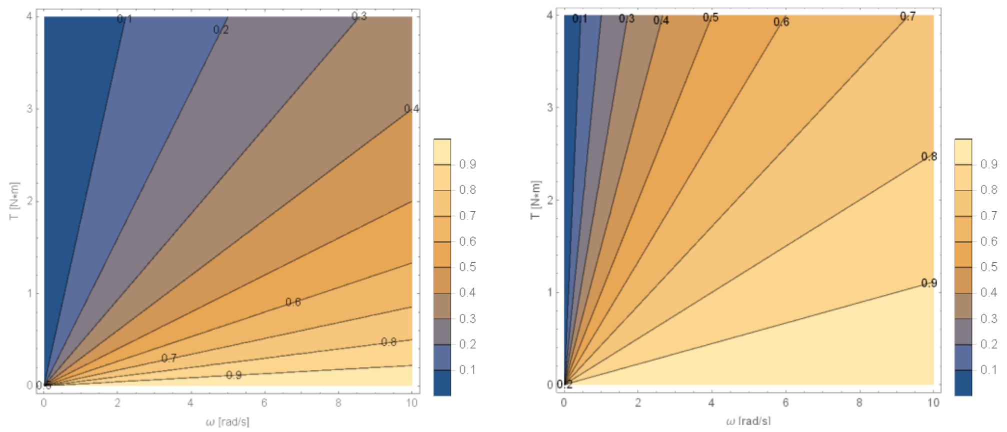

K=5 K=1

Figure 53: Efficiency Graphs on Rotational Speed vs Torque Plane for 2 Different K Values

From equation (63);

$$P_{in}(t) * \eta(t) = P_{out}(t) = T_m(t) * \omega_m(t) \qquad (65)$$

Solving P_{in} from equation (65), one obtains

$$P_{in}(t) = T_m(t) * \omega_m(t) * \frac{1}{\eta(t)} \qquad (66)$$

which, upon substituting equation (64) yields

$$P_{in}(t) = T_m(t) * \omega_m(t) + K * [T_m(t)]^2 \tag{67}$$

Now, define the transmission ratio, *n*, via the equation

$$n = \frac{\omega_m(t)}{\omega(t)} \tag{68}$$

Alternatively

$$n = \frac{T(t)}{T_m(t)} \tag{69}$$

where

ω : rotational speed of the crank shaft

T : torque on the crank shaft

Substituting equations (68) and (69) into equation (67), one obtains

$$P_{in}(t) = T(t) * \omega(t) + [T(t)]^2 * K * \frac{1}{n^2} \tag{70}$$

Now, define a new constant, K^*, via the equation

$$K^* = K * \frac{1}{n^2} \tag{71}$$

Hence, by substituting equation (62) into equation (71), one obtains

$$K^* = \frac{[I(t)]^2 * R}{[T_m(t)]^2 * n^2} \tag{72}$$

By substituting equation (71) into (70), one obtains

$$P_{in}(t) = T(t) * \omega(t) + [T(t)]^2 * K^* \tag{73}$$

Note that equations (71) and (64) yield

$$\eta(t) = \frac{\omega_m(t)}{\omega_m(t) + K^* * n^2 * T_m(t)} \tag{74}$$

The power of the selected motor should be more than the maximum power requirement, which can be found via equation (73), where K^* is defined in equation (72). The efficiency of the motor (at any point), on the other hand, can be obtained from equation (74).

4.2 Kinematic and Dynamic Analyses of the Press Machine

In this chapter, in order to optimize a dynamic feature of the press, the required MFG force profile will be determined. For this purpose, it is necessary to perform kinematic and dynamic analyses of the press. The kinematic dimensions and the free body diagrams of the links of the press to be analyzed are shown in Figure 54. In Figure 54.a, the link numbers are shown with orange. Kinematic dimensions are shown with blue. Linear and angular displacements are shown with green. The links are shown with black. At the bottom right corner, the reference coordinate system is also shown.

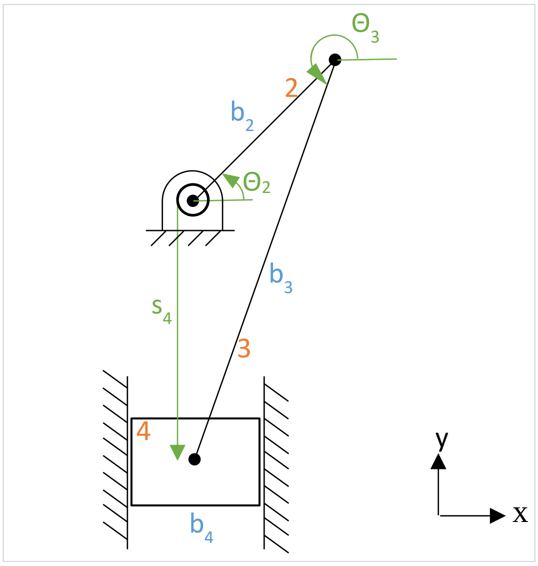

a: Dimensions of the Press Machine

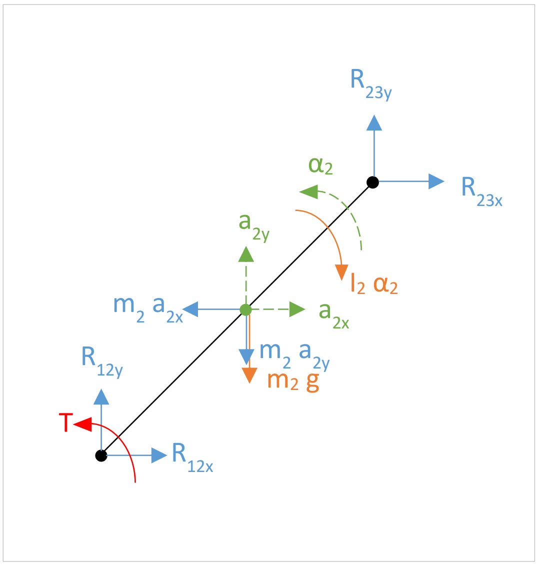

b: Free Body Diagram of Link 2 (Crank)

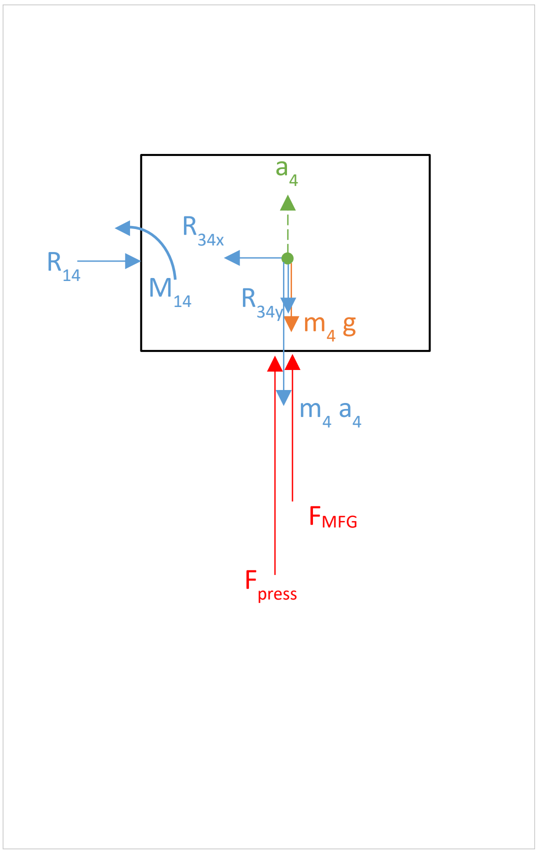

c: Free Body Diagram of Link 4 (Slider/Ram)

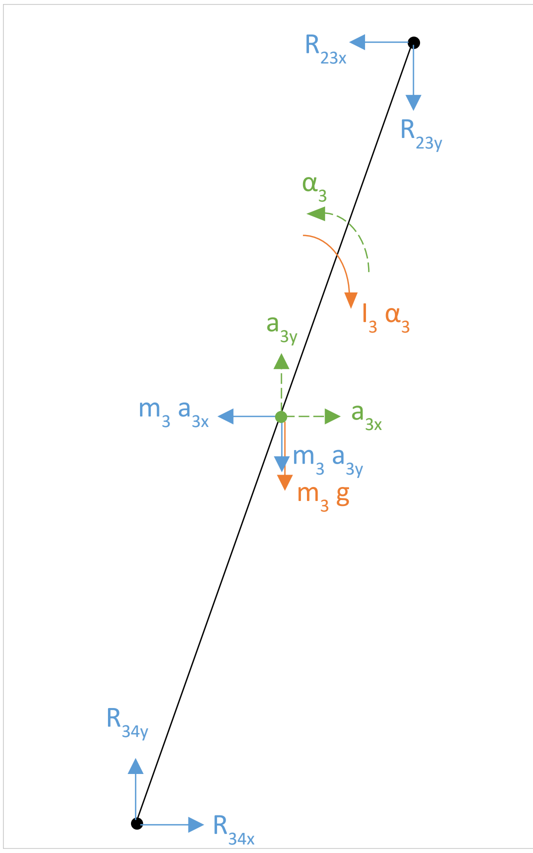

d: Free Body Diagram of Link 3 (Coupler)

Figure 54: Press Machine

4.2.1 Kinematic Analysis of the Press Machine

The details of the kinematic analysis will not be given here, since it is quite trivial to perform the kinematic analysis of a press machine (which is actually a slider crank mechanism). Hence, only the results of the kinematic analysis will be presented. The displacement, velocity and acceleration of the links are given below.

$$\theta_3 = -\arccos\left(-\frac{b_2}{b_3}\cos(\theta_2)\right) \tag{75}$$

$$s_4 = b_2 \sin(\theta_2) + b_3 \sin(\theta_3) \tag{76}$$

$$\omega_3 = -\frac{b_2 \sin(\theta_2)}{b_3 \sin(\theta_3)}\omega_2 \tag{77}$$

$$v_4 = -b_2 \frac{\sin(\theta_2 - \theta_3)}{\sin(\theta_3)}\omega_2 \tag{78}$$

$$\alpha_3 = -\frac{b_2}{b_3 \sin(\theta_3)}\left\{\frac{[\cos(\theta_2)\sin(\theta_3)\,\omega_2 - \sin(\theta_2)\cos(\theta_3)\omega_3]\omega_2}{\sin(\theta_3)} + \sin(\theta_2)\,\alpha_2\right\} \tag{79}$$

$$a_4 = \left\{\frac{[(\omega_3 - \omega_2)\cos(\theta_3 - \theta_2)\sin(\theta_3) - \omega_3 \sin(\theta_3 - \theta_2)\cos(\theta_3)]\omega_2}{\sin(\theta_3)} + \sin(\theta_3 - \theta_2)\alpha_2\right\}\frac{b_2}{\sin(\theta_3)} \tag{80}$$

$$a_{2x} = -\frac{b_2}{2}{\omega_2}^2\cos(\theta_2) - \frac{b_2}{2}\alpha_2 \sin(\theta_2) \tag{81}$$

$$a_{2y} = -\frac{b_2}{2}{\omega_2}^2\sin(\theta_2) + \frac{b_2}{2}\alpha_2 \cos(\theta_2) \tag{82}$$

$$a_{3x} = \frac{b_3}{2}{\omega_3}^2\cos(\theta_3) + \frac{b_3}{2}\alpha_3 \sin(\theta_3) \tag{83}$$

$$a_{3y} = a_4 + \frac{b_3}{2}{\omega_3}^2\sin(\theta_3) - \frac{b_3}{2}\alpha_3 \cos(\theta_3) \tag{84}$$

where

θ_3 : angular displacement of link 3 (see Figure 54.a)

s_4 : displacement of link 4 (see Figure 54.a)

ω_3 : angular velocity of link 3

v_4 : velocity of link 4

α_3 : angular acceleration of link 3 (see Figure 54.d)

a_4 : acceleration of the link 4 (see Figure 54.c)

a_{2x} : x component of the acceleration of the mass center of link 2 (see Figure 54.b)

a_{2y} : y component of the acceleration of the mass center of link 2 (see Figure 54.b)

a_{3x} : x component of the acceleration of the mass center of link 3 (see Figure 54.d)

a_{3y} : y component of the acceleration of the mass center of link 3 (see Figure 54.d)

Note that the positive x and y directions are shown in the coordinate system in Figure 54.a. The positive direction for the angular measurements, on the other hand, is the counter clockwise direction.

4.2.2 Dynamic Analysis of the Press Machine

Free body diagrams of the press machine are shown in Figure 54.b, Figure 54.c, Figure 54.d. In the free body diagrams, frictional effects are neglected since it is assumed that the revolute joint bearing radii are small and a well lubricated slider is used. Hence, in the force analysis, one obtains a linear set of equations which can be solved in closed form. Gravity is in the –y direction.

In the free body diagrams, external forces and torques (such as the motor torque, press force and MFG force) are shown with red. The reaction forces and inertia forces are shown with blue. Inertia moments and gravitational forces are shown with orange. Linear and angular accelerations are shown with green. The inertia forces and moments are shown with dashed lines. The center of masses of the links are shown with green points.

The 8 dynamic equilibrium equations corresponding to link 2, 3 and 4 are given by equations (85) - (92).

Equation (85) is the force equilibrium of link 2 in the x direction. Equation (86) is the force equilibrium of link 2 in the y direction. Equation (87) is the moment equilibrium of link 2 around its center of mass. Equation (88) is the force equilibrium of link 3 in the x direction. Equation (89) is the force equilibrium of link 3 in the y direction. Equation (90) is the moment equilibrium of link 3 around its center of mass. Equation (91) is the force equilibrium of link 4 in the x direction. Equation (92) is the force equilibrium of link 4 in the y direction.

The moment equilibrium of link 4, which is the 9th dynamic equilibrium equation, is utilized to determine the prismatic joint reaction moment, M_{14}, which is found to be zero. Hence, only 8 equilibrium equations are listed.

$$R_{12x} + R_{23x} - m_2 a_{2x} = 0 \tag{85}$$

$$R_{12y} + R_{23y} - m_2 a_{2y} - m_2 g = 0 \tag{86}$$

$$T - I_2 \alpha_2 - (R_{23x} - R_{12x}) \frac{b_2}{2} \sin(\theta_2) + \left(R_{23y} - R_{12y}\right) \frac{b_2}{2} \cos(\theta_2) = 0 \tag{87}$$

$$R_{34x} - R_{23x} - m_3 a_{3x} = 0 \tag{88}$$

$$R_{34y} - R_{23y} - m_3 a_{3y} - m_3 g = 0 \tag{89}$$

$$-I_3\alpha_3 - (R_{23x} + R_{34x})\frac{b_3}{2}\sin(\theta_3) + (R_{34y} + R_{23y})\frac{b_3}{2}\cos(\theta_3) = 0 \quad (90)$$

$$R_{14} - R_{34x} = 0 \quad (91)$$

$$F_{press} + F_{MFG} - R_{34y} - m_4a_4 - m_4g = 0 \quad (92)$$

Assuming that the motion of the press is specified, the 8 dynamic equilibrium equations involve the 8 unknowns $T, R_{12x}, R_{12y}, R_{23x}, R_{23y}, R_{34x}, R_{34y}$ and R_{14}. Here, T is the actuation torque and $R_{\mathrm{ab}k}$ denotes the reaction force (in the *k* direction) between bodies *a* and *b*. Furthermore, F_{press} denotes the applied force on the ram due to the pressing process and F_{MFG} denotes the applied force by the MFG.

4.3 Method

For programming purposes, a commercial software, MATLAB, is used. In order to differentiate and integrate easily, v_4 and F_{MFG} are expressed using Fourier series. v_4 is written as a 4th order Fourier series since it is observed that a 4th order series is sufficient to approximate a given v_4.

There are several objective functions that can be minimized. These objective functions can be combined into a single objective function, f_{min}, which is defined below.

$$f_{min} = c_{max} * \max(P) - c_{min} * \min(P) + c_{energy} * E_{total} + c_{rms} * \sqrt{\frac{\sum_{i=1}^{steps}\left(P_i - c_{average} * P_{ave}\right)^2}{steps}} \quad (93)$$

where

P : instantaneous power

E_{total} : total consumed energy

$steps$: number of discrete time steps used

c_{max} :weighting coefficient for minimizing the maximum instantaneous power

c_{min} :weighting coefficient for maximizing the minimum instantaneous power

c_{energy} : weighting coefficient for minimizing the total consumed energy

c_{rms} : weighting coefficient for minimizing, in a root mean square sense, the deviation of the instantaneous power from its average value

$c_{average}$: user selected coefficient that multiplies the average of power, P_{ave}

One can change the values of c_{max}, c_{min}, c_{energy}, c_{rms} to change the weights in the objective function. By changing $c_{average}$, one can change P_{ave}. In general, $c_{average}$ should be taken as 1.

Note that, since the specified angular speed of the motor will be constant, power is proportional to the actuation torque. Hence, minimization or maximization of power corresponds to minimization or maximization of actuator torque.

Although maximizing the minimum power doesn't seem to be reasonable, maximizing a negative power consumption corresponds to minimizing the braking power.

F_{MFG} can be expressed in terms of a Fourier series of any order. In this study, the optimal order will be determined iteratively by considering the 3rd, 4th, 5th, 6th and 7th order Fourier series given below.

$$F_{MFG_3} = a_0 + a_1 * \cos\left(\frac{2\pi t}{T}\right) + b_1 * \sin\left(\frac{2\pi t}{T}\right) + a_2 * \cos\left(\frac{4\pi t}{T}\right) + b_2 * \sin\left(\frac{4\pi t}{T}\right) + a_3 * \cos\left(\frac{6\pi t}{T}\right) + b_3 * \sin\left(\frac{6\pi t}{T}\right) \quad (94)$$

$$F_{MFG_4} = a_0 + a_1 * \cos\left(\frac{2\pi t}{T}\right) + b_1 * \sin\left(\frac{2\pi t}{T}\right) + a_2 * \cos\left(\frac{4\pi t}{T}\right) + b_2 * \sin\left(\frac{4\pi t}{T}\right) + a_3 * \cos\left(\frac{6\pi t}{T}\right) + b_3 * \sin\left(\frac{6\pi t}{T}\right) + a_4 * \cos\left(\frac{8\pi t}{T}\right) + b_4 * \sin\left(\frac{8\pi t}{T}\right) \quad (95)$$

$$F_{MFG_5} = a_0 + a_1 * \cos\left(\frac{2\pi t}{T}\right) + b_1 * \sin\left(\frac{2\pi t}{T}\right) + a_2 * \cos\left(\frac{4\pi t}{T}\right) + b_2 * \sin\left(\frac{4\pi t}{T}\right) + a_3 * \cos\left(\frac{6\pi t}{T}\right) + b_3 * \sin\left(\frac{6\pi t}{T}\right) + a_4 * \cos\left(\frac{8\pi t}{T}\right) + b_4 * \sin\left(\frac{8\pi t}{T}\right) + a_5 * \cos\left(\frac{10\pi t}{T}\right) + b_5 * \sin\left(\frac{10\pi t}{T}\right) \quad (96)$$

$$F_{MFG_6} = a_0 + a_1 * \cos\left(\frac{2\pi t}{T}\right) + b_1 * \sin\left(\frac{2\pi t}{T}\right) + a_2 * \cos\left(\frac{4\pi t}{T}\right) + b_2 * \sin\left(\frac{4\pi t}{T}\right) + a_3 * \cos\left(\frac{6\pi t}{T}\right) + b_3 * \sin\left(\frac{6\pi t}{T}\right) + a_4 * \cos\left(\frac{8\pi t}{T}\right) + b_4 * \sin\left(\frac{8\pi t}{T}\right) + a_5 * \cos\left(\frac{10\pi t}{T}\right) + b_5 * \sin\left(\frac{10\pi t}{T}\right) + a_6 * \cos\left(\frac{12\pi t}{T}\right) + b_6 * \sin\left(\frac{12\pi t}{T}\right) \quad (97)$$

$$F_{MFG_7} = a_0 + a_1 * \cos\left(\frac{2\pi t}{T}\right) + b_1 * \sin\left(\frac{2\pi t}{T}\right) + a_2 * \cos\left(\frac{4\pi t}{T}\right) + b_2 * \sin\left(\frac{4\pi t}{T}\right) + a_3 * \cos\left(\frac{6\pi t}{T}\right) + b_3 * \sin\left(\frac{6\pi t}{T}\right) + a_4 * \cos\left(\frac{8\pi t}{T}\right) + b_4 * \sin\left(\frac{8\pi t}{T}\right) + a_5 * \cos\left(\frac{10\pi t}{T}\right) + b_5 * \sin\left(\frac{10\pi t}{T}\right) + a_6 * \cos\left(\frac{12\pi t}{T}\right) + b_6 * \sin\left(\frac{12\pi t}{T}\right) + a_7 * \cos\left(\frac{14\pi t}{T}\right) + b_7 * \sin\left(\frac{14\pi t}{T}\right) \quad (98)$$

Firstly, F_{MFG} will be expressed in terms of a 3rd order Fourier series which will be named as F_{MFG_3}. A 3rd order Fourier series (see equation (94)) has 7 unknown coefficients to be determined. However, one of the coefficients (namely, b_1) is used to satisfy the following condition:

$$\int_{t=0}^{t=T} (F_{MFG} * v_4) dt = 0 \quad (99)$$

where

t : time

T : period of motion

Assuming that there are no frictional losses in the MFG, the net work done, in one period of motion, by F_{MFG} will always be zero, which leads to equation (99). Equation (99) is satisfied by solving for coefficient b_1 in terms of other coefficients. Hence, b_1 becomes a known parameter in terms of other coefficients.

Hence, only 6 of the coefficients of F_{MFG_3} are available as design parameters. These 6 design parameters will be used to minimize the objective function f_{min} given by equation (93). For the numerical minimization, “fminsearch” command of MATLAB, which uses Nelder-Mead simplex algorithm (see [62]

[63]), is used. Using 100 arbitrary selected initial guesses, the optimal values of a_0, a_1, a_2, a_3, b_2, b_3 (which are designated by a_0', a_1', a_2', a_3', b_2', b_3') are determined. Next, F_{MFG} is represented as a 4th order series (see equation (95)), which is designated as F_{MFG_4}. In order to determine the optimal values of the 8 design parameters, (namely a_0', a_1', a_2', a_3', a_4', b_2', b_3', b_4') 200 initial guesses are utilized. 100 of these guesses are obtained by using the optimal design parameters that have been already determined for F_{MFG_3} plus 100 arbitrarily selected a_4', b_4' pairs. In this manner, the result of the optimization via F_{MFG_3} is taken advantage of. The remaining 100 initial guesses for the 8 design parameters are arbitrarily selected. The minimum of f_{min} obtained from the 200 initial guesses is taken to be the new minimum of f_{min} (by using F_{MFG_4}). The same procedure is repeated to determine more accurate f_{min} values by considering F_{MFG_5}, F_{MFG_6} and F_{MFG_7} (see Figure 55). At the end of the procedure, the minimum of f_{min} is taken to be the minimum obtained via F_{MFG_7}.

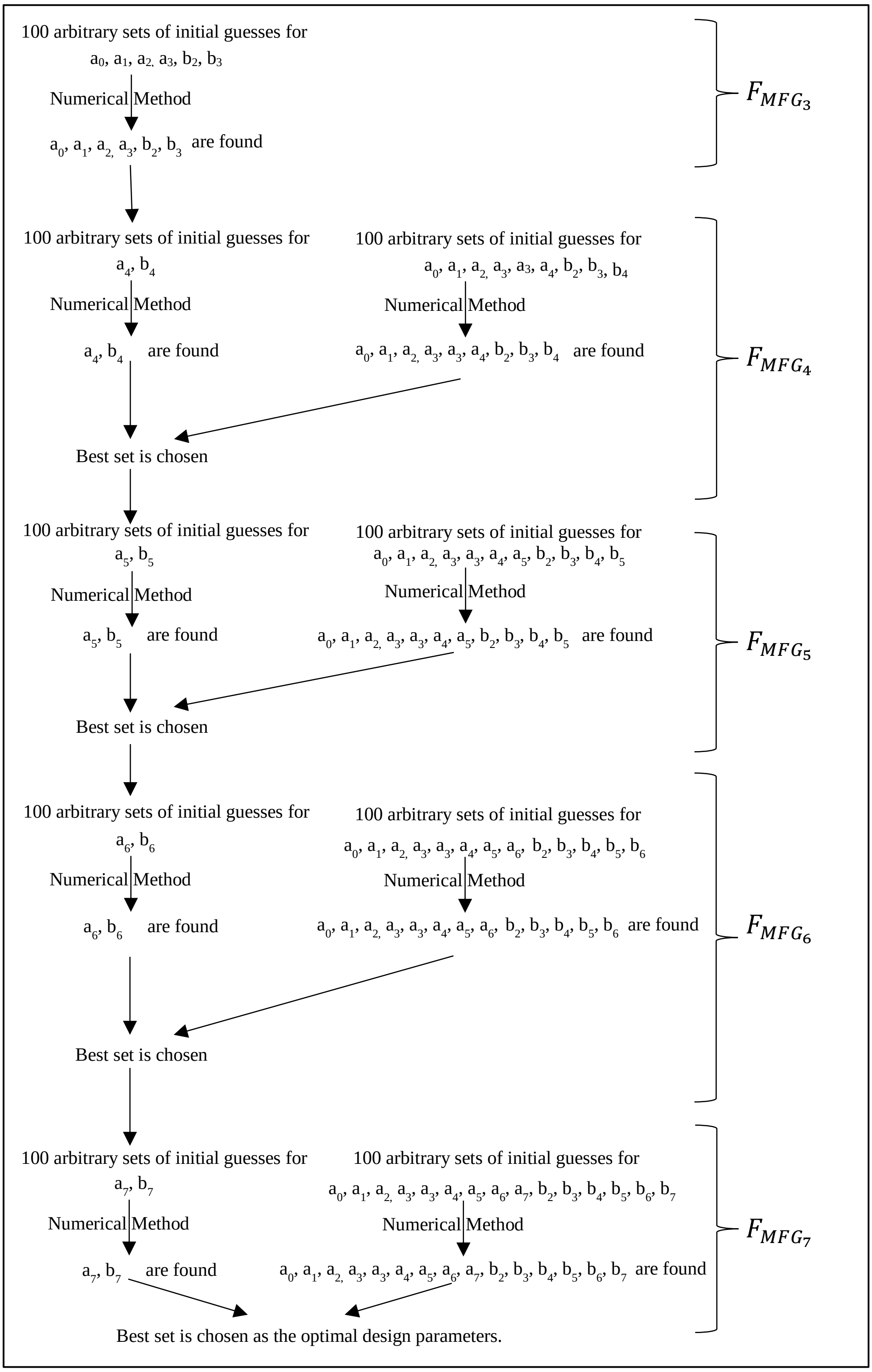

Figure 55: Iterative Method to Find F_{MFG}

4.3.1 Sample Work Cases

In this section, 5 different tasks will be considered. Force vs compression distance graph of Task-A is shown in Figure 51.

Force vs compression distance graph of Task-B is shown in Figure 56. Between 0-29 mm penetration, the force in Task-B is 100 times smaller than the force in Task-A. After 29 mm penetration, the slope doesn't change in Task-B (unlike Task-A). In other words, slope is constant in Task-B.

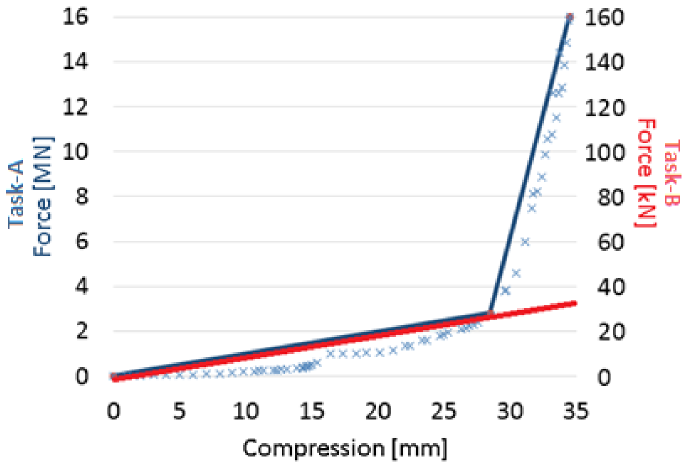

Figure 56: Force vs Compression Graph for Task-A & Task-B

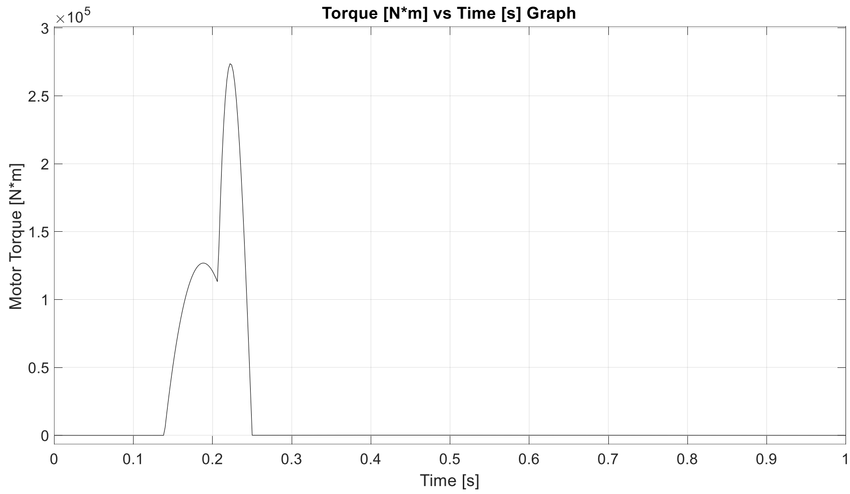

Figure 57: Motor Torque vs Time Graph for Task-A

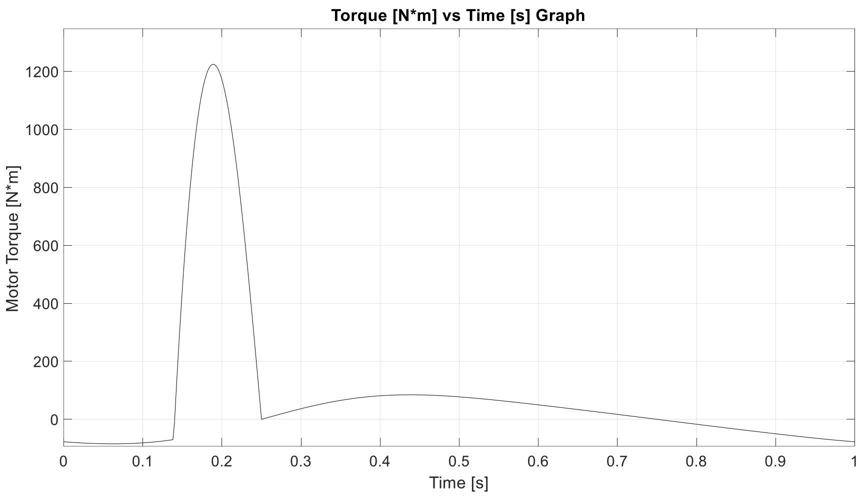

Figure 58: Motor Torque vs Time Graph for Task-B

In Figure 57 and Figure 58, motor torque vs time graphs are shown for Task-A and Task-B. Note that inertial parameters and motor speed was introduced in section 4.1 (Remember that motor speed is 60 rpm, i.e., constant.). As can be observed from the graphs, in Task-A, the inertial and gravitational forces are too small with respect to the press force. Hence, except for the press compression zone, the motor torque is nearly a straight line. However, in Task-B, the inertial and gravitational forces are somewhat comparable with the press compression forces.

In the third task, there is no press force. Hence, the only forces that are taken into account are the inertial and gravitational forces. This scenario will be named as "Task-C". Motor torque vs time graph for Task-C is given in Figure 59.

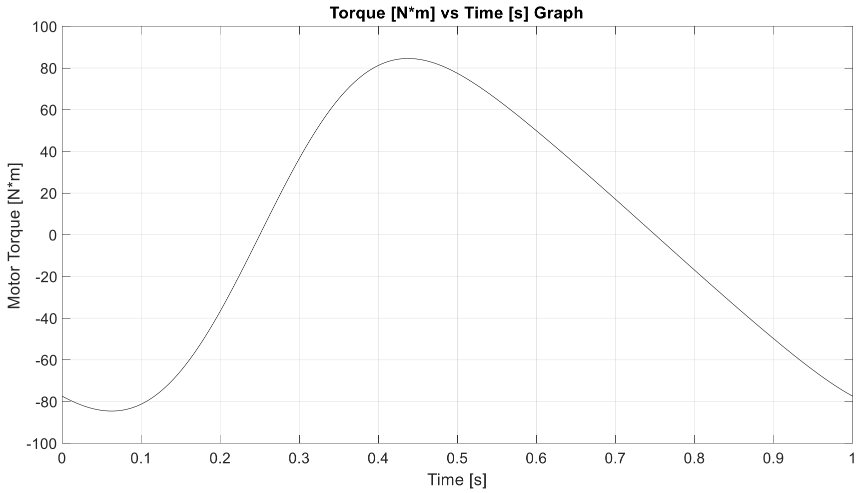

Figure 59: Motor Torque vs Time Graph for Task-C

These three scenarios are distinct as far as the ratio of work forces to the inertial and gravitational forces are concerned. For Task-A, this ratio is very large. For Task-B, this ratio is small. For Task-C, on the other hand, this ratio is 0.

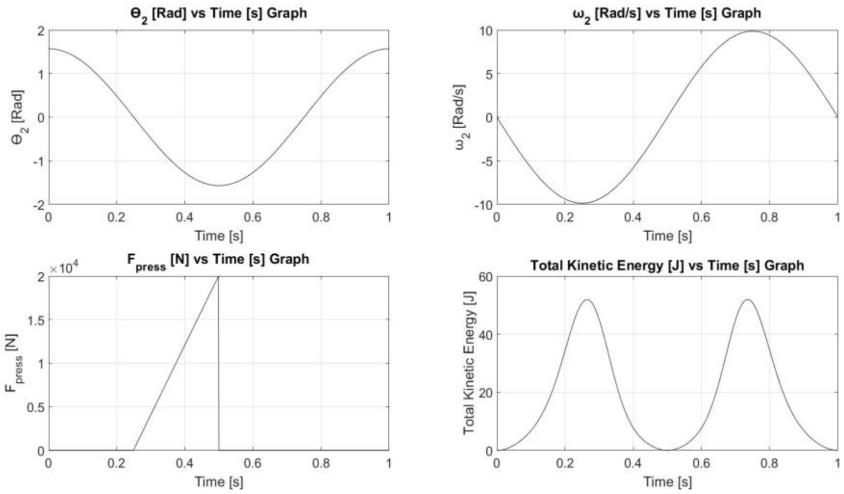

Figure 60: Angular Position, Angular Velocity, Press Force and Kinetic Energy Graphs for Task-D

4th task is defined with variable crank speed. In this task, crank starts to rotate with zero angular velocity and makes half turn rotation (180°). Then it stops and comes back to initial position by rotating in the opposite direction. Press force, crank angle, crank angular velocity and total kinetic energy graphs are given in Figure 60. This task is named as Task-D and it demonstrates a general servo motor case, since it has variable speed. Moreover, it is possible to store the kinetic energy in the MFG, rather than losing it during braking.

Finally, 5th task is defined by changing only the press force of Task-D, i.e., except for the press force, they are defined as completely same. Press force, crank angle, crank angular velocity and total kinetic energy graphs are given in Figure 61. This task is named as Task-E.

In Task-E, the inertial and gravitational forces are too small with respect to the press force. However, in Task-D, the inertial and gravitational forces are comparable to the press force.

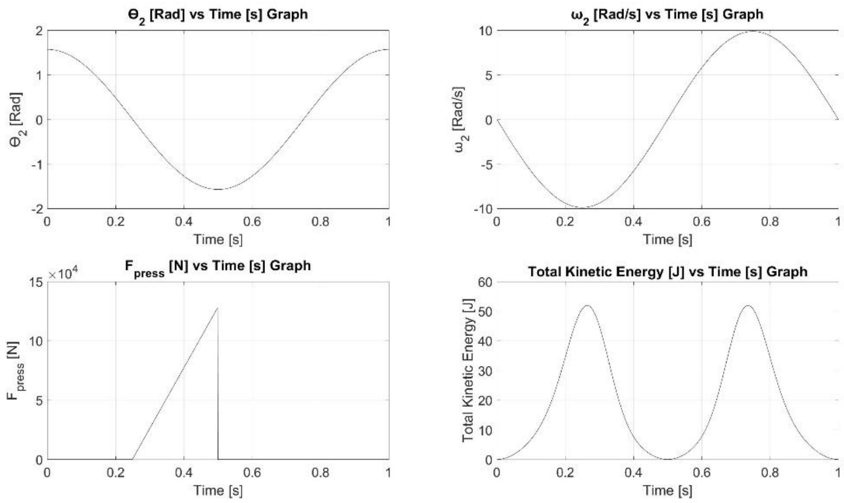

Figure 61: Angular Position, Angular Velocity, Press Force and Kinetic Energy Graphs for Task-E

4.3.2 Motor Selection

4.3.2.1 Motor Selection for Task-A

Maximum power consumption in Task-A is 1.72 MW. Hence, the electric motor that will be used for this task should be chosen accordingly. It is assumed that this press is a servo crank press, and no flywheel is used. There are 2 reasons for not using a flywheel in these analyses:

1. In servo presses, there are no flywheels, electric motor is directly connected to the gearbox.
2. MFG can replace a flywheel since it can store mechanical energy in an efficient manner.

For the given task, a DC motor from Siemens DC motor catalogue, namely, the 1GG5 635-5EV40-2XV5 motor, is selected [64, p. 3.76] This motor has a rated power of 1.61 MW. Hence, it is assumed that it can deliver 1.72 MW instantaneously. The properties of the motor at the rated point and the resistance, R, of the motor are listed below.

$I = 2350$ A

$T_m = 41200$ Nm

$\omega_m = 374$ rpm

$R = 12.3$ mΩ

Since $\omega = 60$ rpm = constant for the task, equation (68) yields

$$n = \frac{374}{60} = 6.23$$

Hence equation (72) yields

$$K^*_{1.61MW} = \frac{2350^2 * 12.3 * 10^{-3}}{41200^2 * 6.23^2} = 1.0299 * 10^{-6} \frac{\mathrm{A}^2 * \Omega}{\mathrm{Nm}^2}$$

The rated efficiency of this motor according to the motor catalogue is:

$$\eta_{1.61MW,catalogue} = 94\%$$

However, since a simple efficiency model is used to determine the efficiency map, efficiency at the rated point should also be calculated according to this simple efficiency model. Hence, from equation (74) one obtains

$$\eta_{1.61MW,rated} = 96.1\%$$

Clearly, $\eta_{1.61MW,rated}$ is quite close to $\eta_{1.61MW,catalogue}$. Therefore, it can be concluded that the simplified efficiency mapping model is reasonable to use. Note that at 1.72 MW power (with 60 RPM speed), the efficiency decreases to 95.8% (according to the equation (74)), i.e.,

$$\eta_{1.61MW@1.72MW} = 95.8\%$$

For Task-A the same press machine will now be actuated by 2 identical and smaller motors. Note that, for high capacity presses, multiple servo motors can be used [48]. In general, the efficiency of "small" motors are less than the efficiency of "large" motors. Hence, the effects of the efficiency of the motor on the results will be investigated. From the same Siemens catalogue [64, p. 3.73], the motor 1GG5 634-5EG40-2XV5 is chosen. This motor has rated power of 860 kW. Hence, the two motors provide 1.72 MW power, which is exactly the desired value. K^* and the efficiency values of the motor are given below.

$$K^*_{860kW} = 3.1313 * 10^{-6} \frac{\mathrm{A}^2 * \Omega}{\mathrm{Nm}^2}$$

$$\eta_{860kW,catalogue} = 92\%$$

$$\eta_{860kW,rated} = 93.6\%$$

As can be seen from the comparison of $\eta_{1.61MW@1.72MW}$ and $\eta_{860kW,rated}$, the first motor (1GG5 635-5EV40-2XV5) is more efficient than the second motor (1GG5 634-5EG40-2XV5).

Efficiency maps of the two motors are shown in Figure 62 and Figure 63. For the sake of simplicity, only rotational speeds between 6 rad/s and 7 rad/s are shown. The black dotted lines indicate the working zone. Since the rotational speed is fixed at 60 RPM, the working zone is a line, not a curve. Note that, for the 860 kW motor, the maximum torque value is half of the maximum torque value of 1.61 MW motor, since 2 motors are used.

As can be observed from these graphs, the optimization algorithm will basically try to decrease the actuating torque; since the lower the torque is, the higher the efficiency will be.

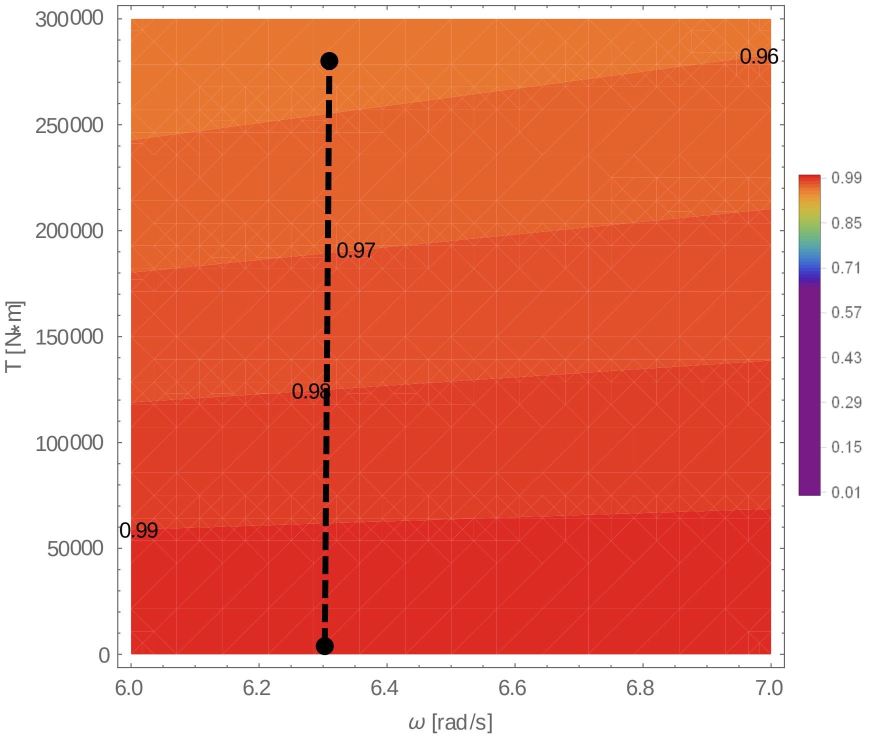

Figure 62: Efficiency Map of 1.61 MW Motor

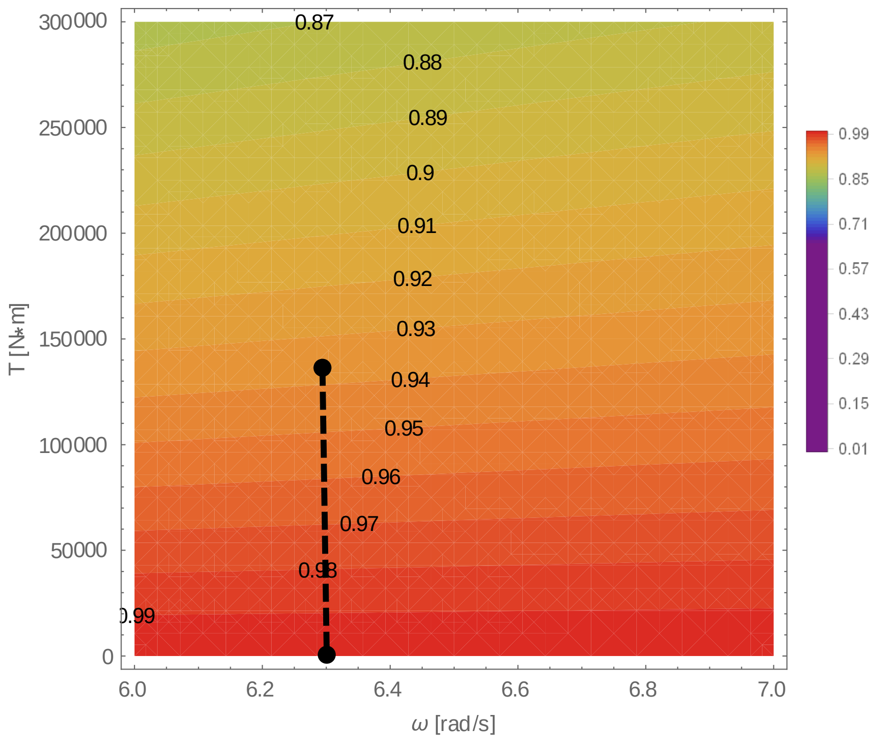

Figure 63: Efficiency Map of 860 kW Motor

Since torque is supplied by 2 motors, equation (73) should be modified for the 860 kW motors, yielding

$$P_{in,total} = 2 * P_{in,motor} \tag{100}$$

where

$P_{in,total}$: total input power

$P_{in,motor}$: input power for single motor

Since each motor supplies half of the required torque, the input power for a single motor is defined as:

$$P_{in,motor} = \frac{T}{2} * \omega + \left(\frac{T}{2}\right)^2 * K^* \tag{101}$$

Hence, equations (100) and (101) yield

$$P_{in,total} = T * \omega + T^2 * \frac{K^*}{2} \quad (102)$$

Now, defining K^{**} via the equation

$$K^{**} = \frac{K^*}{2} \quad (103)$$

Equation (102) yields

$$P_{in,total} = T * \omega + T^2 * K^{**} \quad (104)$$

Hence, throughout the analysis,

$$K^{**}_{860kW} = \frac{K^*_{860kW}}{2} = 1.56565 * 10^{-6} \frac{\mathrm{A}^2 * \Omega}{\mathrm{Nm}^2}$$

will be used.

4.3.2.2 Motor Selection for Task-B

Maximum power consumption of Task-B is 7.69 kW. The first motor to be used is the 1.61 MW motor that is used for Task-A (1GG5 635-5EV40-2XV5). The second motor is chosen to be LSK 1124 M 03 from the Leroy Somer catalogue [65, p. 87]. This motor has a rated power of 8 kW at 440 V.

K^* and the efficiency values of the motor are given below.

$$K^*_{8kW} = 1.2925 * 10^{-3} \frac{\mathrm{A}^2 * \Omega}{\mathrm{Nm}^2}$$

$$\eta_{8kW,catalogue} = 78\%$$

$$\eta_{8kW,rated} = 79.3\%$$

However, since the maximum power consumption of Task-B is 7.69 kW, rather than 8 kW, the efficiency of the 8 kW motor at the maximum torque point is:

$$\eta_{8kW@7.69kW} = 79.9\%$$

Clearly, this motor is much smaller and less efficient than the large 1.61 MW motor (1GG5 635-5EV40-2XV5). Its efficiency map and working zone is shown in Figure 64.

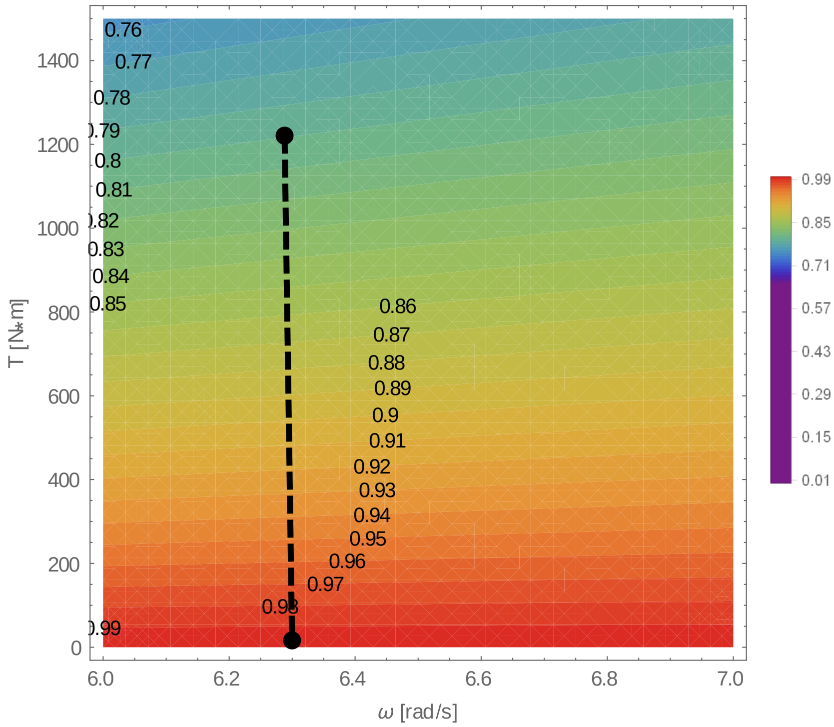

Figure 64: Efficiency Map of 8 kW Motor

As it can be seen from Figure 62; the 1.61 MW motor will work with a very large efficiency (larger than 99%), hence there is no need to show its efficiency map for Task-B.

4.3.2.3 Motor Selection for Task-C

Maximum power consumption of Task-C is 534 W, hence the 8 kW motor (LSK 1124 M 03) is suitable for Task-C. A smaller motor will not be selected for this task, because, the aim of analyzing Task-C is to see the energy storage capability of the MFG, rather than forcing the motor to run at more efficient points.

4.3.2.4 Motor Selection for Task-D

Maximum power consumption of Task-E is 4.95 kW, hence the 8 kW motor (LSK 1124 M 03) is also suitable for this task. Note that plugging type braking (see section 4.3.3) is assumed for this motor. Hence, the motor is always consuming energy and never regenerates energy.

4.3.2.5 Motor Selection for Task-E

Maximum power consumption of Task-D is 36.6 kW. The 8 kW motor (LSK 1124 M 03) will be used for this task. The aim here is to decrease the maximum power requirement of the task and to see that this motor would be enough for Task-D. Note that plugging type braking is assumed for this motor. Hence, the motor is always consuming energy and never regenerates energy.

4.3.3 Types of Electric Motors

In the simulations, three different kinds of electric motors will be used.

4.3.3.1 Regenerating Braking Electric Motor

During braking (in other words, when power is generated or power consumption is negative), the motor operates as a generator. During the electric energy generation, there may be some losses. Hence, the regeneration efficiency is described as:

$$\eta_{regeneration} = \frac{Generated\ Electrical\ Energy}{Absorbed\ Mechanical\ Energy\ During\ Braking} \quad (105)$$

In the simulations, $\eta_{regeneration}$ will be taken as 50% and 90%. By using 2 different values, it will be possible to see the effect of $\eta_{regeneration}$.

4.3.3.2 Dynamic Braking

During braking, excessive mechanical energy is converted to heat. Hence power consumption is zero during braking. For programming purposes, the regeneration efficiency for dynamic braking will be defined as;

$$\eta_{regeneration} = 0$$

4.3.3.3 Plugging Type Braking

During braking, motor tends to operate in the reverse direction and draws additional current. Hence, during braking motor consumes energy. For programming purposes, the regeneration efficiency will be defined for plugging type braking as;

$$\eta_{regeneration} = -1$$

4.4 Results & Discussion

4.4.1 Minimizing the Maximum Power Consumption

By minimizing the maximum instantaneous power consumption, one can use smaller electric motors and decrease the amount of capital investment.

For the aim for minimizing the maximum power consumption, c_{max} in equation (93) will be taken as 1, and the remaining weighting coefficients will be taken as 0. For minimizing the maximum power consumption, only Task-A will be considered.

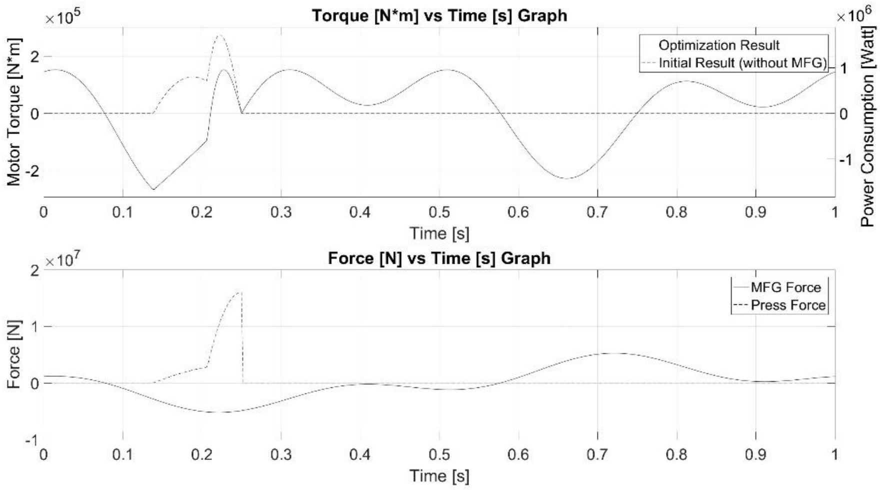

Figure 65: Torque & Power Consumption vs Time Graph for 3rd Order Fourier Series for Minimizing Maximum Power

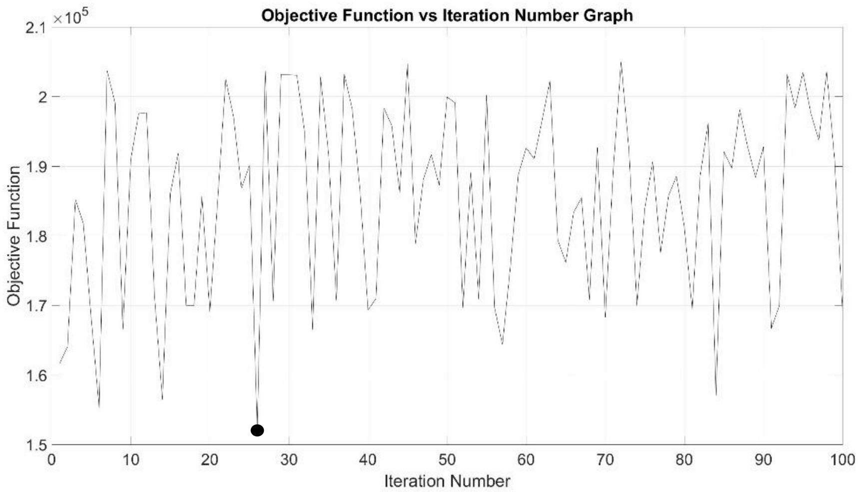

Figure 66: Objective Function vs Iteration Number Graph for 3rd Order Fourier Series for Minimizing Maximum Power

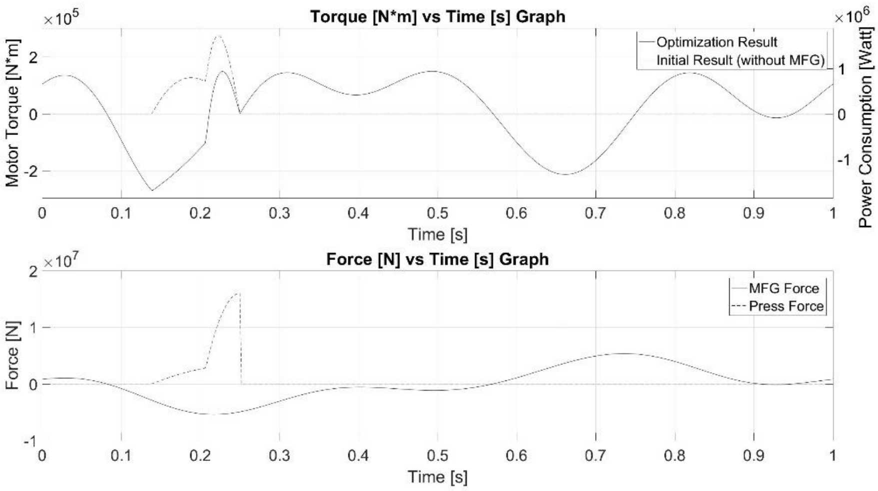

Figure 67: Torque & Power Consumption vs Time Graph for 4th Order Fourier Series for Minimizing Maximum Power

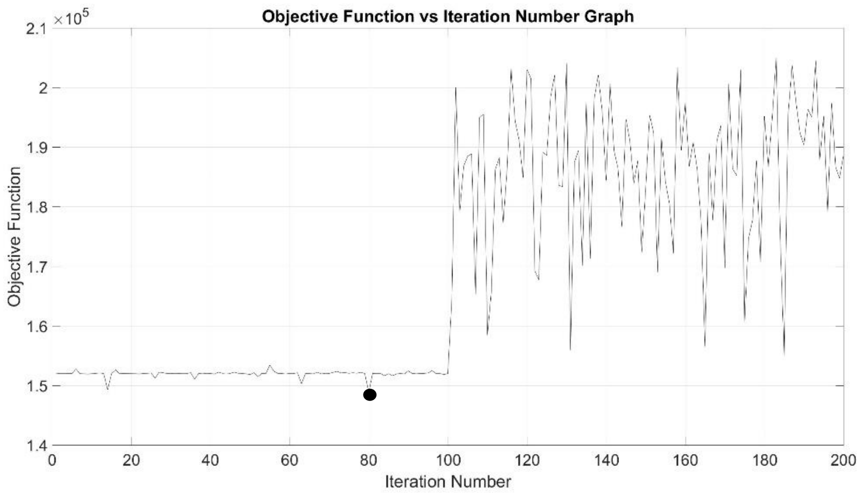

Figure 68: Objective Function vs Iteration Number Graph for 4th Order Fourier Series for Minimizing Maximum Power

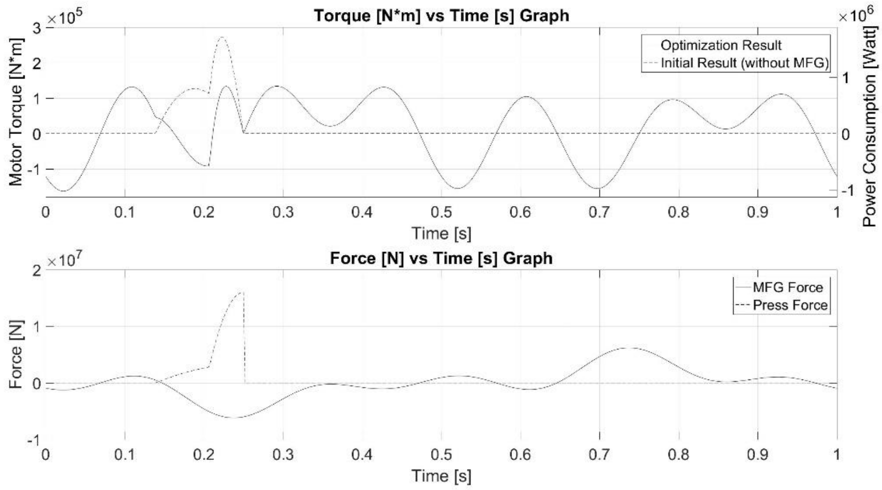

Figure 69: Torque & Power Consumption vs Time Graph for 5th Order Fourier Series for Minimizing Maximum Power

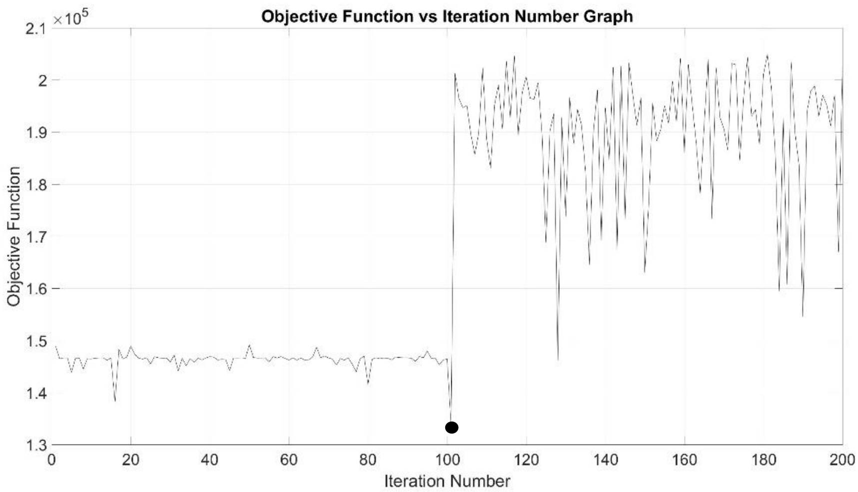

Figure 70: Objective Function vs Iteration Number Graph for 5th Order Fourier Series for Minimizing Maximum Power

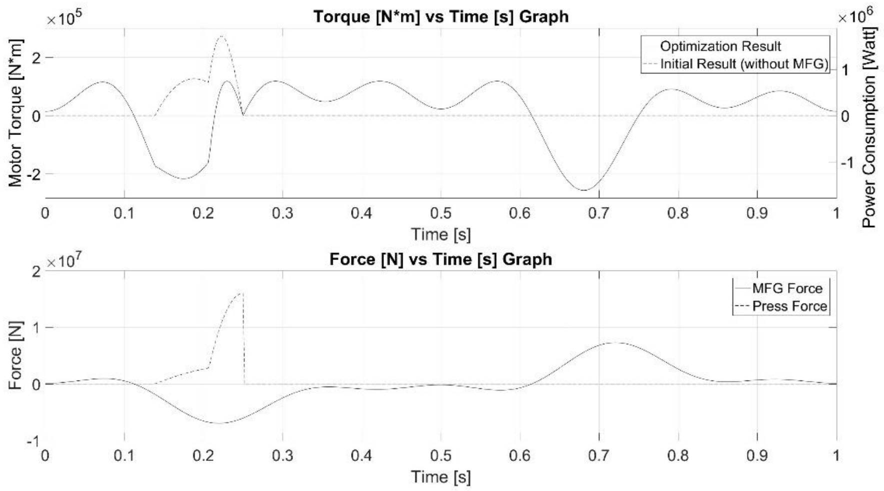

Figure 71: Torque & Power Consumption vs Time Graph for 6th Order Fourier Series for Minimizing Maximum Power

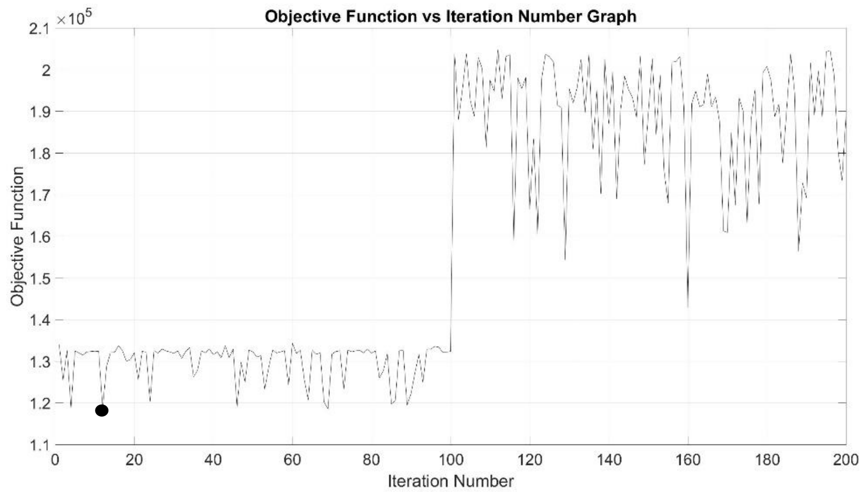

Figure 72: Objective Function vs Iteration Number Graph for 6th Order Fourier Series for Minimizing Maximum Power

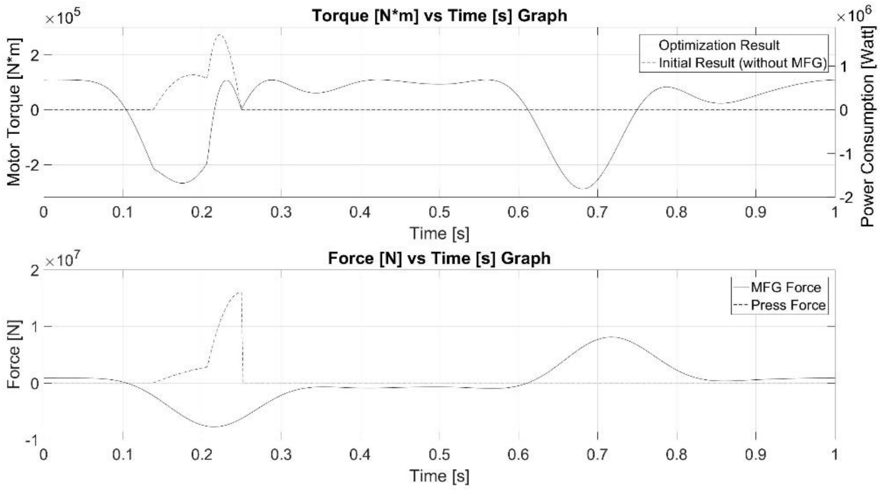

Figure 73: Torque & Power Consumption vs Time Graph for 7th Order Fourier Series for Minimizing Maximum Power

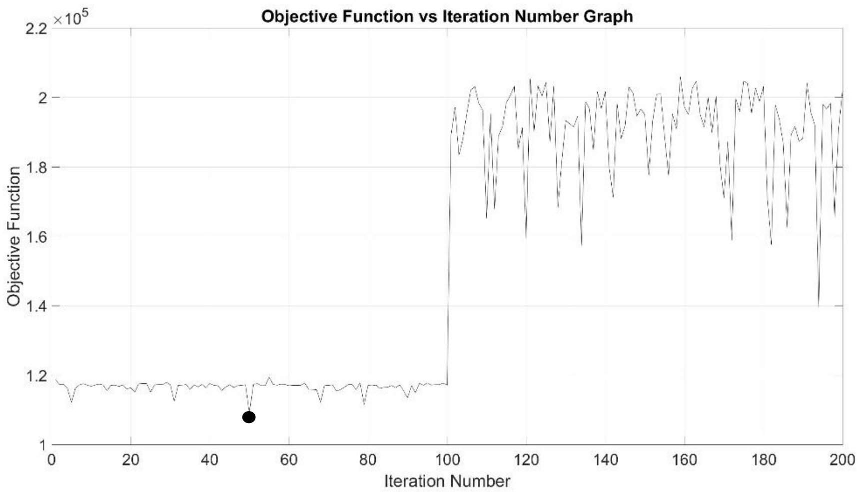

Figure 74: Objective Function vs Iteration Number Graph for 7th Order Fourier Series for Minimizing Maximum Power

In Figure 65, Figure 67, Figure 69, Figure 71 and Figure 73; torque vs time, power consumption vs time and MFG force vs time graphs (for Fourier series of orders 3, 4, 5, 6 and 7) are shown for the aim of minimizing the instantaneous maximum power consumption. As it can be seen from the figures, torque and power consumption graphs are exactly same, the only change being in the units. Power is 2π times larger than the torque where 2π rad/s (=60 rpm) is the constant angular speed of the crankshaft.

In Figure 66, Figure 68, Figure 70, Figure 72, Figure 74; objective function vs iteration number graphs are shown for the aim of minimizing the maximum power consumption.

In Figure 66, there are 100 iterations since there are 100 initial guesses for finding F_{MFG_3}. The smallest value of the objective function is shown with a black dot. Hence, that result is the best among all other initial guesses (in terms of minimizing the maximum power consumption). Therefore, as described in Figure 55; a_0, a_1, a_2, a_3, b_2, b_3 that correspond to the dotted point are the optimal values of the design parameters. F_{MFG_3} is found by using these optimal design parameters. Note that b_1 is dictated by the condition that is given in equation (99). Hence, it is not a free parameter to choose.

As described in Figure 55, for finding F_{MFG_4}, there are 100 initial guesses (the first 100 initial guesses in Figure 68) that use the same a_0, a_1, a_2, a_3, b_2, b_3 values as in F_{MFG_3}; and 100 other initial guesses (the second 100 initial guesses in Figure 68) that are completely arbitrary. As shown in Figure 68, the best result is achieved by using the first 100 initial guesses, implying that a_0, a_1, a_2, a_3, b_2, b_3 coefficients of the optimal F_{MFG_3} are useful since they lead to the minimum value of the objective function. That is quite reasonable, since the numerical algorithm starts with the 6 coefficients that are already tested and found to be the best in the previous run, and searches for only 2 extra coefficients. In the second 100 initial guesses, the numerical algorithm searches for 8 coefficients, the optimal values of which are more difficult to determine.

The same method is used for finding F_{MFG_5}, F_{MFG_6} and F_{MFG_7}. Referring to Figure 70, one notes that the best result is found in the second 100 initial guesses. In other words, this time completely arbitrary set of initial guesses leads to the minimum of the objective function. This, in fact, justifies the necessity of the second 100 initial guesses (which are completely arbitrary).

Note that, execution time to find F_{MFG_3} is around 2 minutes and execution time to find F_{MFG_7} is around 25 minutes.

In order to evaluate the quality of the optimization, the parameter ξ, defined via the equation

$$\xi = \frac{f_{min}\ with\ MFG\ connected}{f_{min}\ without\ MFG\ connected} \tag{106}$$

will be used. Hence, as ξ decreases, the quality of the optimization increases.

Table 9: ξ Values for Different Fourier Series Orders for Minimizing Maximum Power

Fourier Series Order	ξ
3	0.5556
4	0.5441
5	0.4897
6	0.4333
7	0.3989

In Table 9 and Figure 75, ξ values for different Fourier series orders are shown. As expected, ξ decreases as the order of the Fourier series increases. In other words, the optimization quality increases. Using a 3rd order Fourier series, the maximum power consumption decreases to 55.56% of the original power consumption. On the other hand, if a 7th order Fourier series is employed, the maximum power consumption decreases to 39.89% of the original power consumption. Hence, a much smaller electric motor can be used for the same operation.

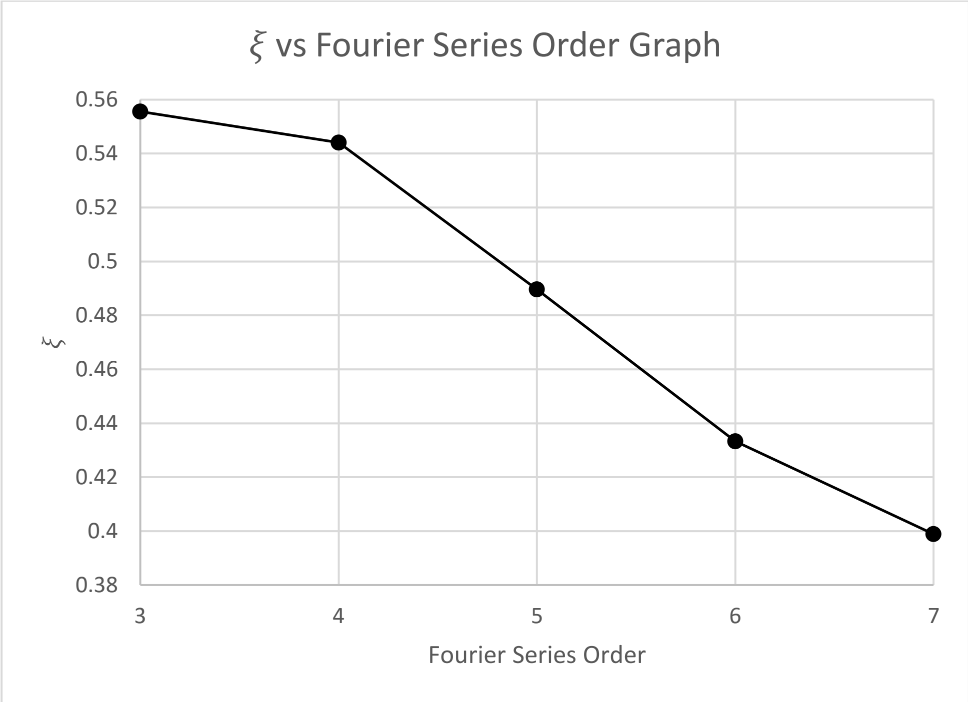

Figure 75: ξ vs Fourier Series Order Graph

It should be noted that, as the order of the Fourier series increases, ξ is expected to decrease until the graph becomes tangent to a horizontal asymptote.

4.4.2 Minimizing the Total Energy Consumption

Another objective of the optimization is minimizing the total energy consumption. In order to realize this objective, c_{energy} in equation (93) will be taken as 1, and the remaining weighting coefficients will be taken as 0.

MFG can minimize the total energy consumption in the following two ways.

- By forcing the electric motor to run at the more efficient points (in the efficiency map),

  and/or

- By storing the mechanical energy in the MFG when there is a need for "braking" the system, and by releasing this energy to the system (press machine in this case) when it is consumed.

Note that, lower limit for the energy consumption is the energy demand of the task. In other words, energy consumption of the electric motor cannot be decreased below the energy demand of the task. Moreover, total energy consumption of the electric motor for 1 period of the task will be investigated throughout this chapter.

In order to minimize the total energy consumption, 4 cases will be considered. In each case, several electric motors (with different efficiencies) will be utilized.

For minimizing the total energy consumption, the number of initial guesses are increased in order to get better results. 500, 500, 200, 100, 100 initial guesses are used for Fourier series of orders 3, 4, 5, 6, 7 respectively. Recall that 100 initial guesses have been utilized, for Fourier series of any order, for minimizing the maximum instantaneous power.

ξ values for each task and motor type; and for each Fourier series order are presented in Table 10. The 7^{th} order Fourier series results are written in bold characters. Note that the properties of the fictitious motor used for task A will be given later.

Table 10: ξ Values for Different Fourier Series Orders for Minimizing Total Energy Consumption

Motor & Task Type	Regeneration Efficiency				Fourier Order
	-1.0	0.0	0.5	0.9	
	Plugging Type Braking	Dynamic Braking	Regenerative Braking		
1610 kW Task-A	0.9972	0.9986	0.9993	0.9999	3
	0.9972	0.9986	0.9993	0.9997	4
	0.9972	0.9986	0.9993	0.9960	5
	0.9972	0.9986	0.9990	0.9920	6
	0.9972	**0.9986**	**0.9936**	**0.9894**	7
2 x 860 kW Task-A	0.9972	0.9986	0.9993	0.9999	3
	0.9972	0.9986	0.9993	0.9980	4
	0.9972	0.9986	0.9993	0.9910	5
	0.9972	0.9986	0.9993	0.9861	6
	0.9972	**0.9986**	**0.9989**	**0.9830**	7
Fictitious Motor Task-A	0.9973	0.9987	0.9994	0.9966	3
	0.9973	0.9987	0.9994	0.9857	4
	0.9973	0.9987	0.9965	0.9736	5
	0.9973	0.9975	0.9846	0.9653	6
	0.9973	**0.9830**	**0.9739**	**0.9599**	7
1610 kW Task-B	0.6804	0.8108	0.8962	0.9787	3
	0.6799	0.8099	0.8957	0.9786	4
	0.6796	0.8098	0.8956	0.9785	5
	0.6795	0.8097	0.8955	0.9785	6
	0.6795	**0.8097**	**0.8955**	**0.9785**	7
8 kW Task-B	0.7256	0.8453	0.9187	0.9365	3
	0.7244	0.8443	0.8916	0.8996	4
	0.7240	0.8211	0.8573	0.8767	5
	0.7119	0.7950	0.8341	0.8584	6
	0.6820	**0.7778**	**0.8212**	**0.8518**	7
8 kW Task-C	0.008733	0.002331	0.004474	0.011569	3
	0.002889	0.000999	0.001055	0.000605	4
	0.002146	0.000117	0.000774	0.000387	5
	0.001354	0.000085	0.000317	0.000234	6
	0.000190	**0.000079**	**0.000157**	**0.000144**	7
8 kW Task-D	**0.8542**				7
8 kW Task-E	**0.6318**				7

To visualize the results, each task will be investigated on bar graphs. Torque and force graphs (as in section 4.4.1) will not be given for each task in this section for the sake of readability. Only ξ results will be discussed for each task.

4.4.2.1 Task-A

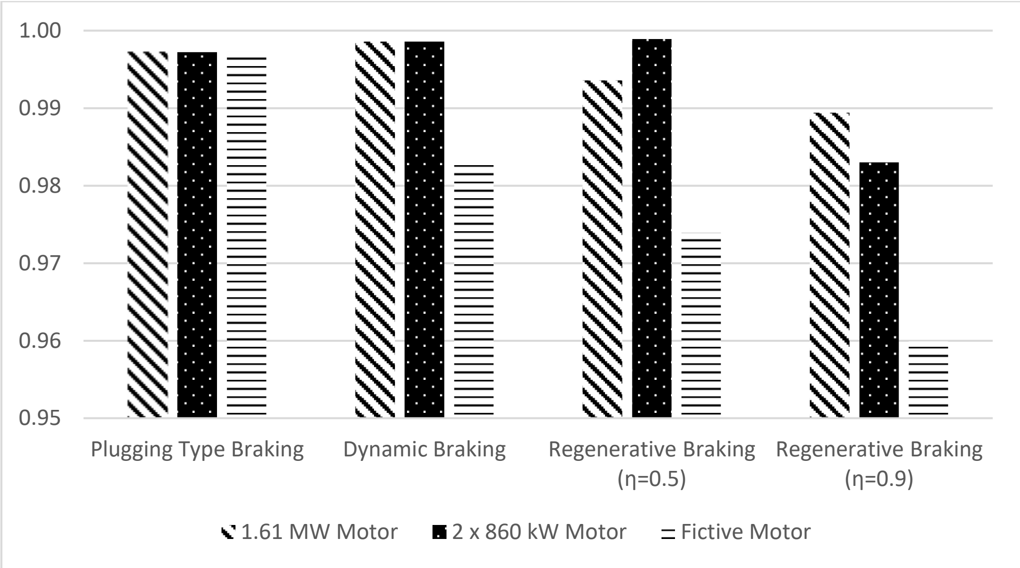

Figure 76: ξ Values for Different Types of Motors & Regeneration Efficiencies for Task-A

In Figure 76, ξ values for different types of motors and regeneration efficiencies for Task-A are shown. As it is explained in section 4.3.2.1, the 1.61 MW motor is more efficient than the 860 kW motors. Their K^{*}, K^{**} and efficiencies at 1.72 MW (60 RPM) are:

$$K^{*}_{1.61MW} = 1.0299 * 10^{-6}\frac{\mathrm{A}^2 * \Omega}{\mathrm{Nm}^2}$$

$$\eta_{1.61MW@1.72MW} = 95.8\%$$

$$K^{**}_{860kW} = 1.56565 * 10^{-6}\frac{\mathrm{A}^2 * \Omega}{\mathrm{Nm}^2}$$

$\eta_{860kW,rated} = 93.6\%$

It should be noted that, the results are not easily distinguishable since their K^* and K^{**} values are too close to each other. So, a fictitious motor with

$$K^*_{fictive} = 3.1313 * 10^{-6} \frac{\mathrm{A}^2 * \Omega}{\mathrm{Nm}^2}$$

$$\eta_{fictive@1.72MW} = 88\%$$

is also included into the analyses. This fictitious motor has distinctly less efficiency than the other two motors. By introducing such a motor, the effect of motor efficiency can be seen clearly. K^* of this fictitious motor is equal to K^*_{860kW} (which is for single motor). So, one can consider the fictitious motor as the same 860 kW motor (in terms of electrical parameters like current or resistance), but can run at 1.72 MW for an instant as a single motor.

Among these three motors, 1.62 MW motor is the most efficient one. 860 kW motor with a double motor arrangement is the second efficient one. Fictitious motor is the least efficient one.

From Figure 76, it is obvious that, for plugging type braking motors, decrease in power consumption is very small for all 3 motors. Power saving is as small as 0.28%. Another important observation is that, the decrease in energy consumption is nearly the same for all 3 motors.

For the fictitious motor, as the regeneration efficiency increases, ξ decreases, i.e., energy saving increases. This trend is also valid for higher efficiency motors (1.61 MW motor and 2 x 860 kW), but it is barely distinguishable.

As a summary, for the tasks that necessitate much larger load forces (than inertial and gravitational forces), i.e., as in high tonnage presses;

- Utilization of the MFG saves more energy for less efficient motors. This is an expected result. If a high efficiency motor is used, utilization of the MFG would save less energy. Because, even without the utilization of MFG, the motor runs in an efficient zone.

- Efficiency of “bigger” (high power) motors are generally high. Hence, utilization of the MFG would save more energy in “smaller” motors.
- For plugging type braking motors, energy saving is low.
- As the regeneration efficiency of the motor increases, ratio of the energy saving increases.

4.4.2.2 Task-B

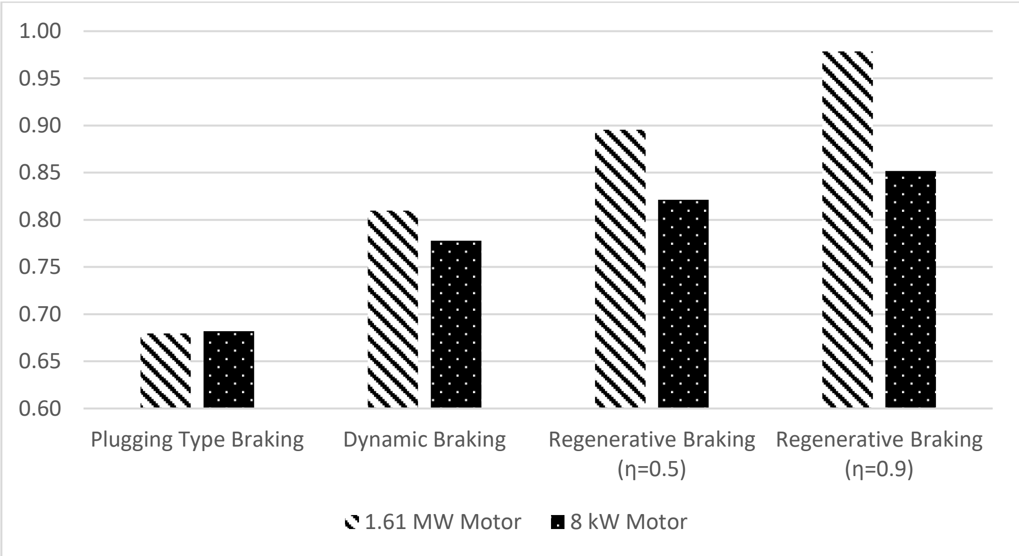

Figure 77: ξ Values for Different Types of Motors & Regeneration Efficiencies for Task-B

In Figure 77, ξ values for different types of motors and regeneration efficiencies for Task-B are shown. As it is explained in section 4.3.2.2, the 1.61 MW motor is much more efficient than the 8 kW motor, for this task. Actually, using the 1.61 MW motor is unnecessary for such a task, since maximum power demand is much less than the motor’s power. However it is still a reasonable example, since it is always possible to perform a relatively small task on a large capacity press.

For Task-B, which includes comparable, yet larger forces than inertial and gravitational forces (like general industrial applications), the following comments can be made.

- For plugging type braking, energy savings are close for both high and low efficiency motors and the saving is more than 30%.
- For dynamic braking, energy savings are 19.03% and 22.22% for high efficiency and low efficiency motors respectively.
- As the regeneration efficiency increases, ratio of the energy savings decreases.
- In general, if low efficiency motors are used, energy saving is larger. Note that, this comment is similar to the comment that has been made for Task-A.

4.4.2.3 Task-C

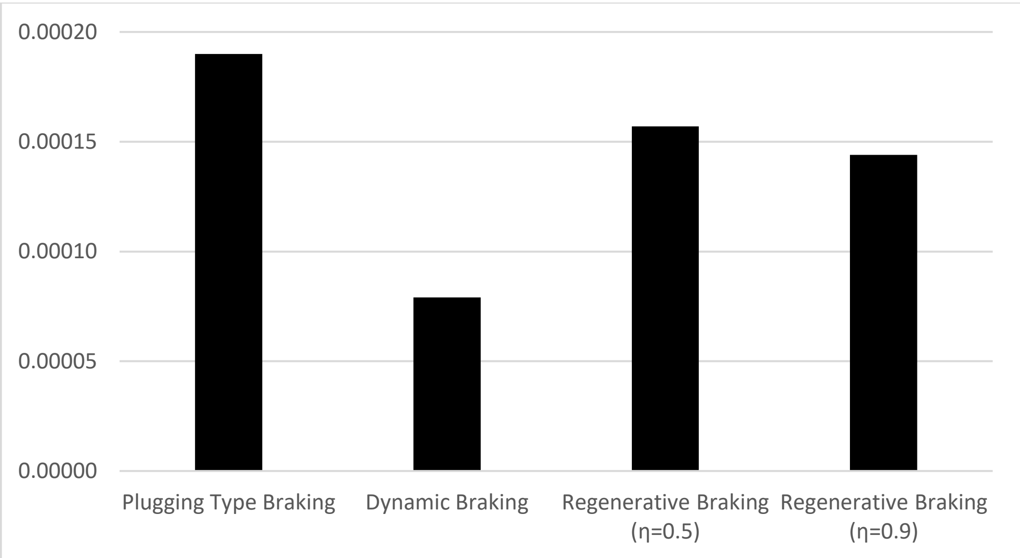

Figure 78: ξ Values for Different Regeneration Efficiencies for Task-C (8 kW Motor)

In Figure 78, ξ values for different types of motors and regeneration efficiencies for Task-C are shown. In this task, only the 8 kW motor is used. As it is obvious, all ξ values are very small. Hence, more than 99.9% of energy is saved for all motor types. Remember that friction is neglected. Hence if friction exists at the press mechanism, some energy would be consumed for friction, meaning that energy saving would be less. However, even with friction, a great amount of energy would be saved.

Considering the second graph of Figure 79, it seems that the power requirement of the task is nearly equally distributed to the positive and negative sides of the x-axis. Hence, the excessive energy at power generation (i.e., negative power consumption) can be stored in the MFG. This stored energy can be released when power input is needed (during the positive power consumption zone). After connecting the MFG, actuating torque is decreased drastically, as it can be seen from first graph of Figure 79.

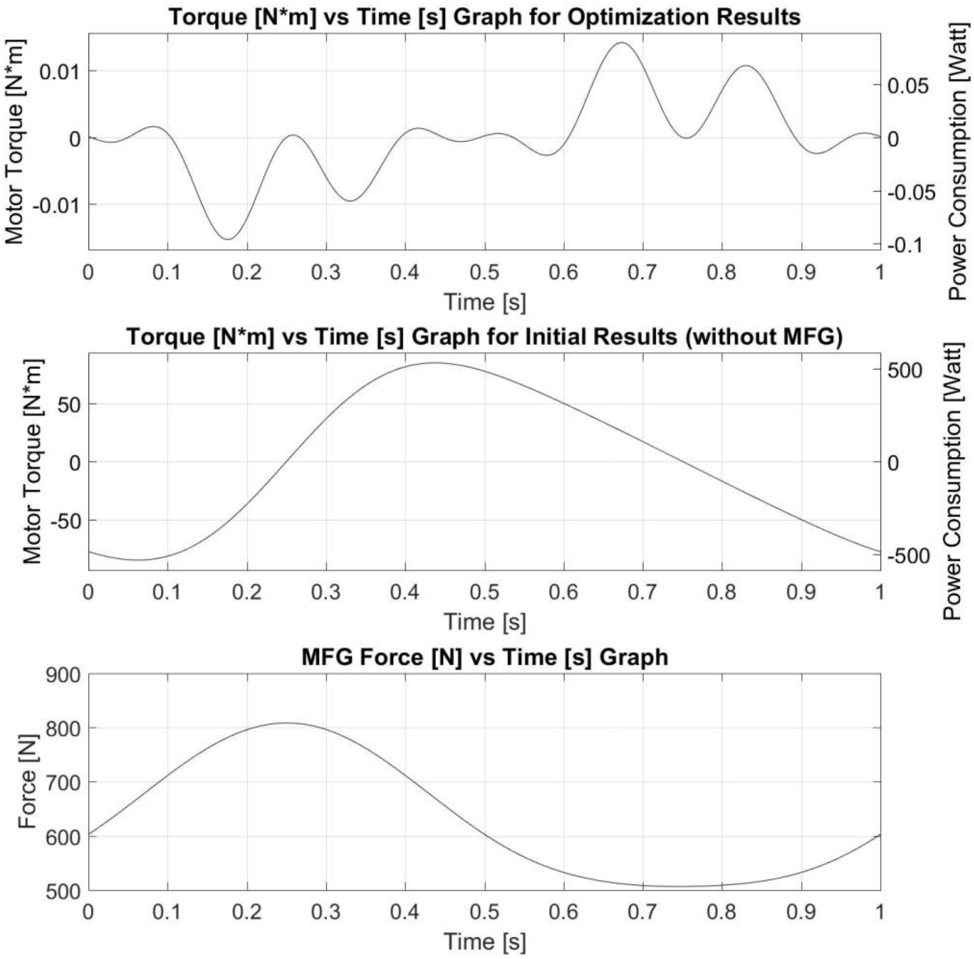

Figure 79: Torque & Power Consumption vs Time Graph for 7th Order Fourier Series for Minimizing Energy Consumption (Dynamic Braking 8 kW Motor)

For this kind of a task (i.e., for tasks with a high percentage of negative power consumption), MFG can be used to store the braking energy in order to release it whenever needed. Flywheels can also store excessive mechanical energy, but they introduce a lot of practical constraints, and they have few design parameters. MFG’s, on the other hand, have many design parameters. Hence, they may be designed for the exact need. Furthermore, with variable speeds, flywheels are difficult to use. Gearboxes should be introduced into the system to realize a limited number of speeds. With MFG's, infinitely many number of speeds can be achieved. In this sense, MFG's are ideal candidates (in order to improve the dynamic characteristics of the machine) to use with servo motors with variable speeds.

4.4.2.4 Task-D

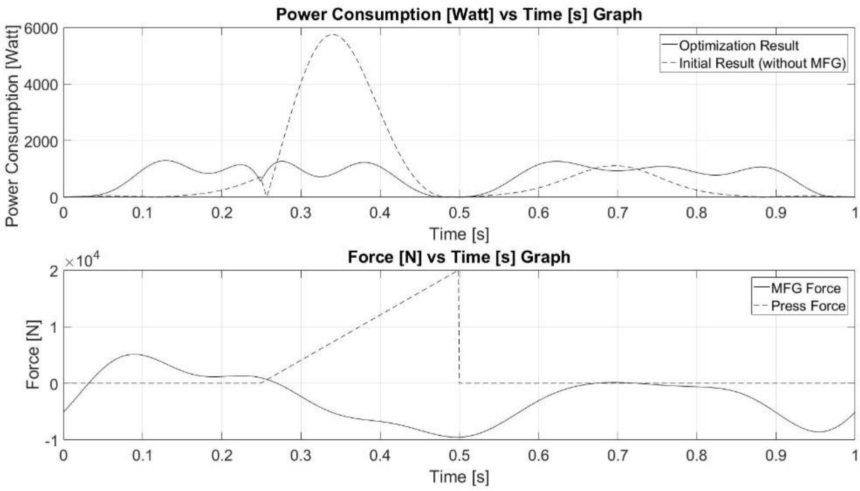

Figure 80: Power Consumption vs Time and Generated MFG Force vs Time Graph for Task-D

In Figure 80, power consumption vs time and generated MFG force vs time graphs are shown for Task-D. Recall that velocity is not constant in Task-D. The crank makes a half rotation and then returns to its initial position. Hence, the total kinetic energy increases to its maximum value and decreases to zero for 2 times in each period, as shown in Figure 60. Clearly, this kinetic energy is dissipated. However, this energy can be stored with the utilization of an MFG. The amount of potentially storable energy is 51.9 J * 2 = 103.8 J for each period. Total potential energy of the press also changes. Maximum potential energy is 161.8 J and maximum mechanical energy achieved in one period is 165.3 J. Potential, kinetic and total mechanical energy of the press is shown in Figure 81.

Total energy consumption during one period, on the other hand, is 874 J. Here, energy consumption can be decreased due to three reasons:

- The electric motor can be forced to run at a more efficient point by the MFG.
- Excessive kinetic energy can be stored in the MFG.
- Potential energy can be stored in the MFG.

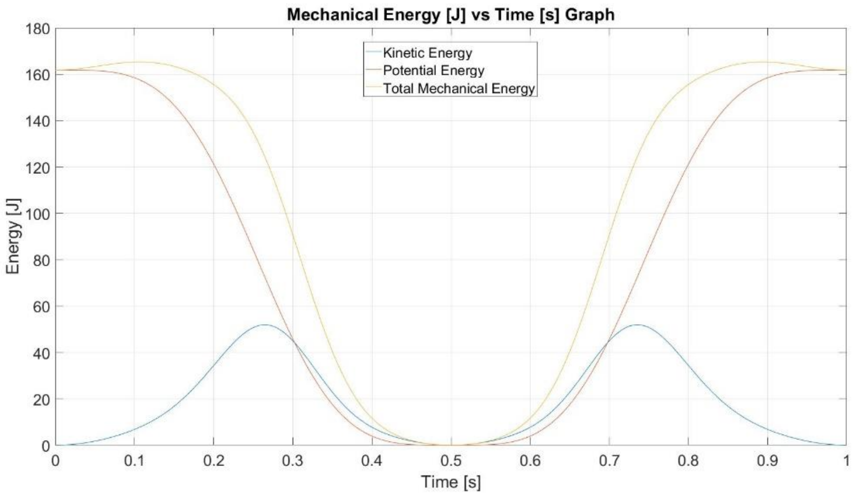

Figure 81: Mechanical Energy vs Time Graph for Task-D and Task-E

Table 11: Energy Table for Task-D

	without MFG	with MFG	Difference
Energy Consumed in the Motor due to the Losses [J]	77.0	22.5	54.5
Mechanical Energy Output of the Motor [J]	797.0	724.0	73
Total Electrical Energy Input [J]	874.0	746.5	127.5
Efficiency for 1 Period	91.19%	96.98%	

After utilization of the MFG, the total energy consumption is decreased by 14.58%. In this case, most of the energy (73 J) is saved due to the reduction in the mechanical energy demand. In other words, a significant amount of kinetic energy and/or potential energy is stored in the MFG. At the same time, the motor is forced to run at a more efficient zone and the efficiency for 1 period is increased from 91.19% to 96.98%. The maximum power consumption of the motor is also reduced (from 4.95 kW to 1.25 kW).

The difference in the energy consumption for the cases with and without utilizing the MFG is 127.5 Joule for 1 second. Hence, if one assumes that this task is performed continuously for 1 year (24 hours x 365 days), 1.1169 megawatt-hours of energy saving is achieved.

To conclude, it is shown that, MFG may be used to store the excessive kinetic and potential energy and thus, it decreases the energy consumption significantly.

4.4.2.5 Task-E

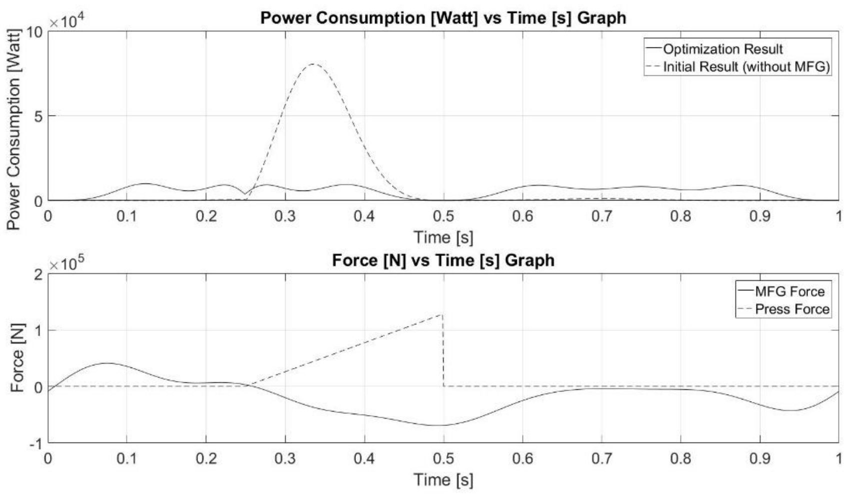

Figure 82: Power Consumption vs Time and Generated MFG Force vs Time Graph for Task-E

In Figure 82, power consumption vs time and generated MFG force vs time graphs are shown for Task-E. The total energy consumption during one period is 8.77 kJ.

Table 12: Energy Table for Task-E

	without MFG	with MFG	Difference
Energy Consumed in the Motor due to the Losses [J]	4069.7	916.1	3153.561
Mechanical Energy Output of the Motor [J]	4700.6	4624.8	75.8
Total Electrical Energy Input [J]	8770.3	5540.9	3229.4
Efficiency for 1 Period	53.60%	83.47%	

After utilization of the MFG, total energy consumption is decreased by 36.82%. In this case, most of the energy is saved due to the fact that the motor runs at more efficient zone (after the utilization of the MFG). Efficiency for 1 period is increased from 53.60% to 83.47%. However, some amount of energy is also saved due to the savings in the mechanical energy consumption. This mechanical energy is very close to the mechanical energy saving in Task-D. This is because, for both tasks, the same press is used with the same velocity profiles.

Without utilization of an MFG, of course, using the aforementioned 8 kW motor (LSK 1124 M 03) is not meaningful, since its efficiency is quite low for this task and the initial maximum power demand is 36.60 kW. However, with the utilization of an MFG, the maximum power consumption reduces to 7.89 kW, and hence, using this motor becomes reasonable. Furthermore, there is a major energy saving.

4.4.3 Conclusion

In this section, a general conclusion will be given for all tasks.

In Figure 78, there is no exact trend regarding the regeneration efficiencies. This is because of the numerical minimization that is used. Since a limited number of initial guesses are used, it is not possible to obtain the exact trend because the objective function has many local minima and each time, the optimization algorithm converges to one of these local minima.

Clearly, as the number of initial guesses increases, the results would be more accurate, revealing the exact trend. In this study, the number of initial guesses have not been increased any further, since the execution time required grows too much. Furthermore, the trend between different regeneration efficiencies for Task-C is not important. Because, in all cases, the energy saving is very close to 100%.

Again, in Figure 76, the trend between the 860 kW motor and the 1.61 MW motor is not clear. For $\eta_{regeneration} = 0.5$, MFG with a 1.61 MW motor saved more energy. For $\eta_{regeneration} = 0.9$, MFG with 860 kW motors saved more energy. However, the energy savings are close to each other. So the trend is not clear and the relationship between the two arrangements is not dependable, due to the limited number of initial guesses. As the number of initial guesses increases, the exact trend may become clear. Without increasing the number of initial guesses, another motor (fictitious motor), with distinguishably less efficiency, is added to get the exact trend.

Note that, for the aforementioned cases, using a low order Fourier series may be another reason for not obtaining the exact trend. When the order of the Fourier series is increased, one will obtain more dependable results.

In all cases, friction is neglected to get a linear set of equations. By this way, analytic results are found. Friction may be introduced and an iterative method may be used for the dynamic analysis. But it will make optimization much harder as far as the execution time is concerned. This is why friction is neglected. This assumption in such a press mechanism is quite reasonable. Because, friction in revolute joints can be neglected since the bearing radii are small. The only remaining and significant friction is the slider friction. Since coupler to crank ratio is large (It is larger than 4 for crank presses [51, p. 51] and for this case, it is taken as 6.), the lateral force on the slider is small. Hence, with the help of a good lubrication, it would not create large frictional forces.

In this chapter, the required MFG force profile (to improve any one of the dynamic characteristics of the press machine) is determined. As an outcome, the success rate of this improvement is measured. In order to obtain the derivatives and the integrals easily, the MFG force is expressed as a Fourier series. The order is increased up to 7. If the order is increased more, different (possibly more successful) results may be obtained.

As mentioned in section 4.1.1, the efficiency map of an electric motor is similar to the one shown in Figure 52. Since, obtaining this efficiency map is out of the scope of this study, a simple efficiency model is used.

For small rotational speeds of the motor (near the vertical axis of the efficiency map), efficiency is low in both efficiency models. However for small torque values (near the horizontal axis of the efficiency map), the efficiency decreases in the real case (see Figure 52), but it increases in the proposed simple model (see Figure 53). Hence, in the energy consumption optimization, algorithm tries to decrease the actuation torque in order to increase the motor efficiency. However, this is not in accordance with the real case. In reality, the motor torque may be decreased until a certain point (to increase the efficiency); but after a certain torque value, a decrease in torque will result in reduction in the efficiency. Therefore, an optimum torque value (rather than a minimum torque value) should be reached in reality.

Nevertheless, the energy saving percentages indicate the success of the MFG in energy saving. Moreover, if the real efficiency data is supplied by means of tests or finite element models, further realistic optimizations may be performed. Hence, regardless of the accuracy of the simplified efficiency model of the electric motors, it is obvious that MFG may have a great impact on the energy saving.

Besides the tasks with constant speeds (Tasks A, B, C), tasks with variable speed (Tasks D, E) have also been introduced. It is observed that the excessive potential and kinetic energy can be stored in the MFG and a significant amount of energy saving can be obtained.

To conclude, MFG may be used to;

1. Decrease the size (and cost) of the electric motor by decreasing the maximum power requirement of the motor,
2. Decrease the total energy consumption.

MFG can also be used for decreasing the RMS value of the actuating torque, for decreasing the shaking forces or moments; or for a combination of the aforementioned objectives.

CHAPTER 5

DYNAMIC ANALYSIS OF MFG & SLOT PROFILE DETERMINATION

5.1 Introduction

In this chapter, the slot shape of the MFG will be determined for a specified $F_2(t)$ and $s_2(t)$ (see Figure 83). Contact envelope of the slot will be identified via force analysis. Factors affecting the slot shape will also be discussed.

5.2 Determination of the MFG Slot Profile

Throughout the analysis, the following assumptions will me made:

1. Gravity is into the paper as shown in Figure 83. So, it will not appear in the calculations.
2. There exists no slippage between the rollers and the slots. Hence, the degree of freedom of the MFG is 1; and the frictional forces between the slots and the rollers do no work.
3. Friction at the 4 revolute joints (connecting the 4 rollers to links 3 and 5) are negligible.
4. F_2, which is the force applied on links 2 and 4, satisfies the following condition:

$$\int_{t=0}^{t=T} [F_2(t) * \dot{s}_2(t)]dt = 0 \qquad (107)$$

where T is the period of the cyclic motion of the MFG.

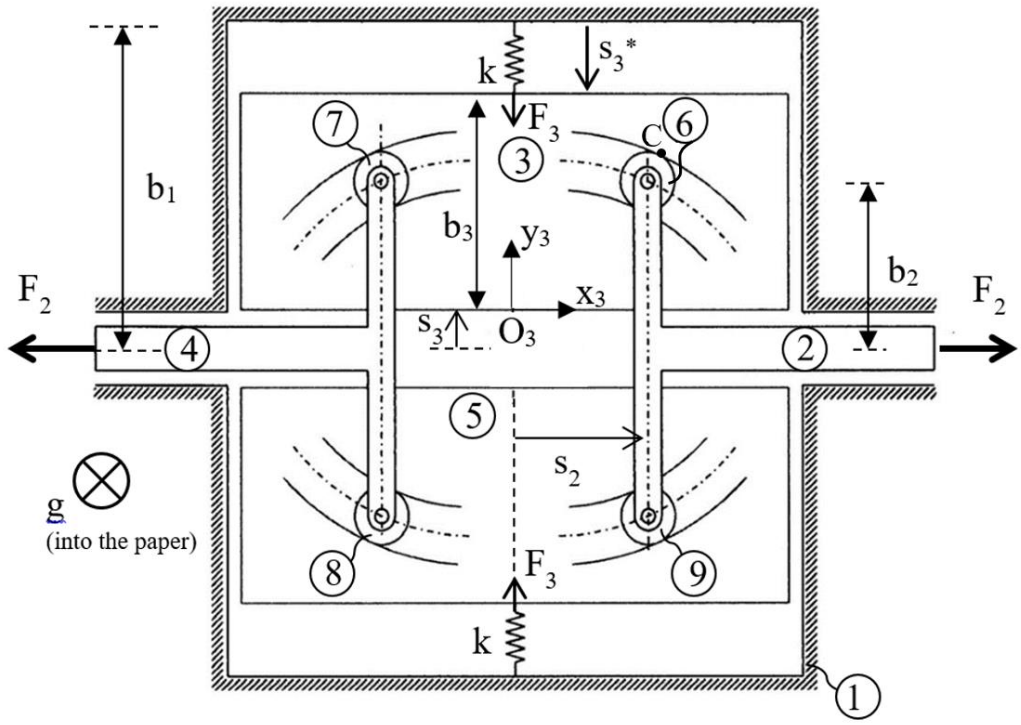

Figure 83: Mechanical Force Generator [3]

Work-energy equation for the MFG shown in Figure 83 is given by the equation

$$U_{i-a} = T_a - T_i = \Delta T \qquad (108)$$

where

i : initial position of the MFG, i.e., position at time=0

a : any position of the MFG, i.e., position at time=t

U_{i-a} : work done, on the MFG, by all external forces acting on the system from time=0 to time=t, i.e., work done by the spring force F_3 and the applied force F_2. Here, it should be recalled that frictional effects at the 4 revolute joints are neglected.

T_a , T_i : kinetic energies of the MFG at time=t and t=0, respectively

Here, it is important to note that, regardless of the motion of the MFG, the mass center of the MFG is stationary, i.e., it is always located at O_1 (see Figure 1). Hence, regardless of the direction of the gravitational acceleration, the change in potential energy of the MFG (due to gravity) will always be zero for any 2 positions of the MFG.

Since only $F_3(t)$ and $F_2(t)$ contribute to U_{i-a}, one can express U_{i-a} as in the following form.

$$U_{i-a} = (U_{i-a})_{F_3} + (U_{i-a})_{F_2} \tag{109}$$

where

$(U_{i-a})_{F_3}$: work done on the MFG by F_3

$(U_{i-a})_{F_2}$: work done on the MFG by F_2

$$(U_{i-a})_{F_3} = -2 * \int_{s_3=(s_3)_0}^{s_3=s_3(t)} F_3(t) ds_3 \tag{110}$$

where $(s_3)_0$ is defined to be initial value of s_3 at $t = 0$, in other words, $s_3(0)$. In equation (110), there is a minus, because directions of F_3 and ds_3 are opposite. Again in equation (110), the multiplier 2 exists, because there are 2 springs. The spring force $F_3(t)$ is modelled to be compressive and is given via the equation

$$F_3(t) = k * [L + s_3(t)] \tag{111}$$

where k is the spring constant and L is defined by the equation

$$L = l_{free} - b_1 + b_3 \tag{112}$$

Here, l_{free} is the free length of the springs.

Substituting equations (111) and (112) into (110), one obtains

$$(U_{i-a})_{F_3} = -2 * \int_{s_3=(s_3)_0}^{s_3=s_3(t)} k * [L + s_3(t)] ds_3 \quad (113)$$

which yields

$$(U_{i-a})_{F_3} = -2 * [(k * L) * s_3(t) + (0.5 * k) * s_3(t)^2 - (k * L) * (s_3)_0 - (0.5 * k) * (s_3)_0^2] \quad (114)$$

$(U_{i-a})_{F_2}$, on the other hand, is given by

$$(U_{i-a})_{F_2} = 2 * \int_{t=0}^{t=t} [F_2(t) * \dot{s}_2(t)] dt \quad (115)$$

The multiplier "2" exists in equation (115), because there are two F_2 forces (applied to links 2 and 4).

By substituting equations (114) and (115) into equation (109), one obtains

$$U_{i-a} = 2 * \left\{ \int_{t=0}^{t=t} [F_2(t) * \dot{s}_2(t)] dt - [(k * L) * s_3(t) + (0.5 * k) * s_3(t)^2 - (k * L) * (s_3)_0 - (0.5 * k) * (s_3)_0^2] \right\} \quad (116)$$

The kinetic energies, T_a and T_i, on the other hand, can be computed as follows:

$$T_a = 2 * (T_2)_a + 2 * (T_3)_a + 4 * (T_6)_a \quad (117)$$

where

$2 * (T_2)_a$: total kinetic energy of links 2 and 4 at time=t

$2 * (T_3)_a$: total kinetic energy of links 3 and 5 at time=t

$4 * (T_6)_a$: total kinetic energy of the 4 rollers at time=t

Hence,

$$T_a = 2 * \left\{\frac{1}{2} * m_2 * [\dot{s}_2(t)]^2\right\} + 2 * \left\{\frac{1}{2} * m_3 * [\dot{s}_3(t)]^2\right\} + 4 * \left\{\frac{1}{2} * m_6 * [\dot{s}_2(t)]^2 + \frac{1}{2} * I_6 * \left[\dot{\theta}_6(t)\right]^2\right\} \quad (118)$$

which, upon simplification, yields

$$T_a = [m_2 + 2 * m_6] * [\dot{s}_2(t)]^2 + [m_3] * [\dot{s}_3(t)]^2 + [2 * I_6] * \left[\dot{\theta}_6(t)\right]^2 \quad (119)$$

where

m_2, m_3, m_6 : masses of links 2, 3, 6 (note the symmetry of the links)

I_6 : mass moment of inertia of link 6 with respect to its center of mass

Similar to equation (119), one obtains T_i as follows:

$$T_i = [m_2 + 2 * m_6] * [(\dot{s}_2)_0]^2 + [m_3] * [(\dot{s}_3)_0]^2 + [2 * I_6] * \left[\left(\dot{\theta}_6\right)_0\right]^2 \quad (120)$$

where

$(\dot{s}_2)_0$: value of $\dot{s}_2(t)$ at time=0, i.e., $\dot{s}_2(0)$

$(\dot{s}_3)_0$: value of $\dot{s}_3(t)$ at time=0, i.e., $\dot{s}_3(0)$

$\left(\dot{\theta}_6\right)_0$: value of $\dot{\theta}_6(t)$ at time=0, i.e., $\dot{\theta}_6(0)$

Substituting equations (116), (119), (120) into equation (108) the work-energy equation yields

$$2 * \left\{ \int_{t=0}^{t=t} [F_2(t) * \dot{s}_2(t)]dt - [(k * L) * s_3(t) + (0.5 * k) * s_3(t)^2 - (k * L) * (s_3)_0 - (0.5 * k) * (s_3)_0^2] \right\} = [m_2 + 2 * m_6] * [\dot{s}_2(t)]^2 + [m_3] * [\dot{s}_3(t)]^2 + [2 * I_6] * \left[\dot{\theta}_6(t)\right]^2 - [m_2 + 2 * m_6] * [(\dot{s}_2)_0]^2 - [m_3] * [(\dot{s}_3)_0]^2 - [2 * I_6] * \left[\left(\dot{\theta}_6\right)_0\right]^2 \tag{121}$$

which may be arranged as:

$$\int_{t=0}^{t=t} [F_2(t) * \dot{s}_2(t)]dt + [0.5 * m_2 + m_6] * \{[(\dot{s}_2)_0]^2 - [\dot{s}_2(t)]^2\} + [0.5 * m_3] * \{[(\dot{s}_3)_0]^2 - [\dot{s}_3(t)]^2\} + [I_6] * \left\{ \left[\left(\dot{\theta}_6\right)_0\right]^2 - \left[\dot{\theta}_6(t)\right]^2 \right\} = [(k * L) * s_3(t) + (0.5 * k) * s_3(t)^2 - (k * L) * (s_3)_0 - (0.5 * k) * (s_3)_0^2] \tag{122}$$

Now, define the left hand side of equation (122) as $W(t)$. Hence, the work-energy equation can be written in the following form:

$$W(t) = [(k * L) * s_3(t) + (0.5 * k) * s_3(t)^2 - (k * L) * (s_3)_0 - (0.5 * k) * (s_3)_0^2] \tag{123}$$

In equation (123), $W(t)$ is defined as:

$$W(t) \triangleq \int_{t=0}^{t=t} [F_2(t) * \dot{s}_2(t)]dt + [0.5 * m_2 + m_6] * \{[(\dot{s}_2)_0]^2 - [\dot{s}_2(t)]^2\} + [0.5 * m_3] * \{[(\dot{s}_3)_0]^2 - [\dot{s}_3(t)]^2\} + [I_6] * \left\{ \left[\left(\dot{\theta}_6\right)_0\right]^2 - \left[\dot{\theta}_6(t)\right]^2 \right\} \tag{124}$$

which, after taking time derivatives, yields

$$\dot{W}(t) = [F_2(t) * \dot{s}_2(t)] - [m_2 + 2 * m_6] * [\dot{s}_2(t) * \ddot{s}_2(t)] - [m_3] * [\dot{s}_3(t) * \ddot{s}_3(t)] - [2 * I_6] * [\dot{\theta}_6(t) * \ddot{\theta}_6(t)] \quad (125)$$

$$\ddot{W}(t) = [\dot{F}_2(t) * \dot{s}_2(t) + F_2(t) * \ddot{s}_2(t)] - [m_2 + 2 * m_6] * \{[\ddot{s}_2(t)]^2 + \dot{s}_2(t) * \dddot{s}_2(t)\} - [m_3] * \{[\ddot{s}_3(t)]^2 + \dot{s}_3(t) * \dddot{s}_3(t)\} - [2 * I_6] * \{[\ddot{\theta}_6(t)]^2 + \dot{\theta}_6(t) * \dddot{\theta}_6(t)\} \quad (126)$$

Now rewrite $W(t)$ in the following form:

$$W(t) = W_2(t) + W_3(t) + W_6(t) \quad (127)$$

where

$$W_2(t) \triangleq \int_{t=0}^{t=t} [F_2(t) * \dot{s}_2(t)]dt + [0.5 * m_2 + m_6] * \{[(\dot{s}_2)_0]^2 - [\dot{s}_2(t)]^2\} \quad (128)$$

$$W_3(t) \triangleq [0.5 * m_3] * \{[(\dot{s}_3)_0]^2 - [\dot{s}_3(t)]^2\} \quad (129)$$

$$W_6(t) \triangleq [I_6] * \left\{ \left[(\dot{\theta}_6)_0\right]^2 - [\dot{\theta}_6(t)]^2 \right\} \quad (130)$$

It should be noted that $F_2(t)$ and $s_2(t)$ are specified. Hence, the unknown functions to be found are:

- a periodic function $s_3(t)$ with period T
- a periodic function $\theta_6(t)$ with period T

The ultimate aim, on the other hand, is to find the slot coordinates $x_s(t)$ and $y_s(t)$ which are the coordinates of the center of roller 6 with respect to $O_3x_3y_3$ the coordinate system shown in Figure 83. Using the loop closure equations, $x_s(t)$ and $y_s(t)$ can be found as:

$$x_s(t) = s_2(t) \quad (131)$$

$$y_s(t) = b_2 - s_3(t) \quad (132)$$

First and second time derivatives of $x_s(t)$ and $y_s(t)$, on the other hand, are:

$$\dot{x}_s(t) = \dot{s}_2(t) \quad (133)$$

$$\dot{y}_s(t) = -\dot{s}_3(t) \quad (134)$$

$$\ddot{x}_s(t) = \ddot{s}_2(t) \quad (135)$$

$$\ddot{y}_s(t) = -\ddot{s}_3(t) \quad (136)$$

Here, it should be noted that since $F_2(t)$ and $s_2(t)$ are known, and since they are expressed by using Fourier series, the integral in equation (124) can always be evaluated in closed form.

The work-energy equation given by equation (123) can be rearranged in the form

$$(0.5 * k) * s_3(t)^2 + (k * L) * s_3(t) + c(t) = 0 \quad (137)$$

where

$$c(t) = -(k * L) * (s_3)_0 - (0.5 * k) * (s_3)_0^2 - W(t) \quad (138)$$

Clearly, equation (137) is a quadratic equation in $s_3(t)$. Hence, the two roots of this equation can be obtained via the equation:

$$[s_3(t)]_{1,2} = \frac{-k * L \pm \sqrt{k^2 * L^2 - 2 * k * c(t)}}{k} \quad (139)$$

Since the spring constant k is larger than 0, equation (139) yields

$$[s_3(t)]_{1,2} = \frac{-k * L \pm \sqrt{k} * \sqrt{k * L^2 - 2 * c(t)}}{k} \quad (140)$$

which, when simplified, becomes

$$[s_3(t)]_{1,2} = -L \pm \frac{\sqrt{k * L^2 - 2 * c(t)}}{\sqrt{k}} \quad (141)$$

In order to determine which of the 2 solutions corresponds to the given initial condition $(s_3)_0$, one may proceed as follows:

$$[s_3(0)]_1 = -L + \frac{\sqrt{k * L^2 - 2 * c(0)}}{\sqrt{k}} \quad (142)$$

Substitute equation (138) into (142) to get:

$$[s_3(0)]_1 = -L + \frac{\sqrt{k * L^2 + 2 * (k * L) * (s_3)_0 + (k) * (s_3)_0^2 + 2 * W(0)}}{\sqrt{k}} \quad (143)$$

By substituting t=0 into equation (124);

$$W(0) = 0 \quad (144)$$

Now, substitute equation (144) into (143) and simplify, to get

$$[s_3(0)]_1 = s_3(0) \quad (145)$$

Similarly, it can be shown that

$$[s_3(0)]_2 = -2 * L - s_3(0) \quad (146)$$

Hence, $[s_3(0)]_1$ always satisfies the initial condition, whereas $[s_3(0)]_2$ does not. Hence, the solution for $s_3(t)$ is given by $[s_3(t)]_1$, yielding

$$s_3(t) = -L + \frac{\sqrt{k * L^2 - 2 * c(t)}}{\sqrt{k}} \quad (147)$$

Substituting $c(t)$ from equation (138) and simplifying, one obtains:

$$s_3(t) = -L + \frac{\sqrt{R(t)}}{\sqrt{k}} \quad (148)$$

where

$$R(t) \triangleq k * [L + (s_3)_0]^2 + 2 * W(t) \quad (149)$$

Now, define R_{min} as follows:

$$R_{min} \triangleq k * [L + (s_3)_0]^2 + 2 * W_{min} \quad (150)$$

where

$$W_{min} = \underset{0 \le t \le T}{\text{Min}}[W(t)] \quad (151)$$

From equation (148), it is clear that in order for $s_3(t)$ to be a real number, $R(t)$ must be greater than or equal to zero. This must be true for all t values in the interval $0 \le t \le T$. Hence, $s_3(t)$ will always be a real number in the interval $0 \le t \le T$ if and only if

$$R_{min} \geq 0 \tag{152}$$

Equation (152) is the condition to be satisfied by the design variables k, L, $(s_3)_0$, m_2, m_3, m_6, I_6, r_6 such that $s_3(t)$ given by equation (148) is real valued for all times.

First and second time derivatives of $s_3(t)$ can be found as follows:

$$\dot{s}_3(t) = \frac{\dot{W}(t)}{\sqrt{k} * \sqrt{R(t)}} \tag{153}$$

$$\ddot{s}_3(t) = \frac{\ddot{W}(t) * R(t) - \left[\dot{W}(t)\right]^2}{\sqrt{k} * [R(t)]^{\frac{3}{2}}} \tag{154}$$

Using equation (148) in equation (111), one can also find the spring force $F_3(t)$ as:

$$F_3(t) = \sqrt{k} * \sqrt{R(t)} \tag{155}$$

Once $s_3(t)$ is determined for a specified $s_2(t)$, $\dot{s}_3(t)$ can be obtained by differentiation (see equation (153)). $\dot{s}_2(t)$ can also be obtained by taking derivative of the specified $s_2(t)$. Hence, once $\dot{s}_2(t)$ and $\dot{s}_3(t)$ are known, $\dot{\theta}_6(t)$ can be determined by using the fact that there exists no slippage between the rollers and the slots. Next, the method used to determine $\dot{\theta}_6(t)$ will be given.

When there is no slippage between rollers and the slots, one must have [45]:

$$\left[V_{c_6}^t(t)\right]_{rel} = 0 \tag{156}$$

Here, $\left[V_{c_6}^t(t)\right]_{rel}$ is the relative velocity of the contact point C on the roller with respect to the contact point C on the slot (see Figure 83).

But from equation (10) of [45]:

$$\left[V_{c_6}^t(t)\right]_{rel} = \cos(\theta_t(t)) * \dot{s}_2(t) + r_6 * \dot{\theta}_6(t) * \sigma - \sin\big(\theta_t(t)\big) * \dot{s}_3(t) \tag{157}$$

where the parameter σ, which is +1 or -1, defines whether the contact between the roller and the slot is at the outer envelope or the inner envelope. $\theta_t(t)$, on the other hand, is described in Figure 84.

It is clear that

$$\tan\left(\theta_t(t)\right) = \frac{\dot{y}_s(t)}{\dot{x}_s(t)} \tag{158}$$

Substituting equations (133) and (134) into (158), one obtains

$$\tan\left(\theta_t(t)\right) = \frac{-\dot{s}_3(t)}{\dot{s}_2(t)} \tag{159}$$

Hence, $\theta_t(t)$ can be found via the equation

$$\theta_t(t) = atan2[\dot{s}_2(t), -\dot{s}_3(t)] \tag{160}$$

Substituting equation (157) into equation (156) and solving for $\dot{\theta}_6(t)$ one obtains:

$$\dot{\theta}_6(t) = \frac{1}{r_6 * \sigma} * \left[\sin\left(\theta_t(t)\right) * \dot{s}_3(t) - \cos(\theta_t(t)) * \dot{s}_2(t)\right] \tag{161}$$

5.2.1 Iterative Algorithm to Determine the MFG Slot Profile

When $F_2(t)$ and $s_2(t)$ are specified, the slot profiles of the MFG may be obtained by using an iterative, but efficient, algorithm. The notation to be used in the iterative algorithm is as follows:

$s_{3@i}(t)$: $s_3(t)$ at the ith iteration

$\theta_{6@i}(t)$: $\theta_6(t)$ at the ith iteration

$(\dot{s}_{3@i})_0$: $\dot{s}_{3@i}(t)\,|_{t=0}$, in other words, initial value of $\dot{s}_{3@i}(t)$ at the ith iteration

$\left(\dot{\theta}_{6@i}\right)_0$: $\dot{\theta}_{6@i}(t)\,\Big|_{t=0}$, in other words, initial value of $\dot{\theta}_{6@i}(t)$ at the ith iteration

$W_{@i}(t)$: $W(t)$ at the ith iteration

$W_{3@i}(t)$: $W_3(t)$ at the ith iteration

$W_{6@i}(t)$: $W_6(t)$ at the ith iteration

$$\overrightarrow{DV}_{@i} \triangleq [\{k_{@i}, L_{@i}, (s_{3@i})_0\}, \{m_{2@i}, m_{3@i}, m_{6@i}, I_{6@i}\}, \{r_{6@i}, \sigma_{@i}\}] \quad (162)$$

where

$\overrightarrow{DV}_{@i}$	:design variables vector at the ith iteration
$k_{@i}$	:spring constant at the ith iteration
$L_{@i}$	:value of L at the ith iteration (see equation (112))
$(s_{3@i})_0$	:value of $(s_3)_0$ at the ith iteration
$m_{2@i}, m_{3@i}, m_{6@i}, I_{6@i}$	:values of m_2, m_3, m_6, I_6 at the ith iteration
$r_{6@i}$	:value of roller radius r_6 at the ith iteration
$\sigma_{@i}$	:value of σ at the ith iteration where σ is either +1 or -1. Later on, it is shown that, $\sigma_{@i}$ may be taken to be +1 without any loss of generality (see equation (179)).

Next, the equations that will be utilized in the iterative algorithm are introduced.

Referring to equation (127):

$$W_{@i}(t) = W_2(t) + W_{3@i}(t) + W_{6@i}(t) \quad (163)$$

Referring to equation (129):

$$W_{3@i}(t) = [0.5 * m_{3@i}] * \{[(\dot{s}_{3@i})_0]^2 - [\dot{s}_{3@i}(t)]^2\} \quad (164)$$

Referring to equation (130):

$$W_{6@i}(t) = [I_{6@i}] * \left\{ \left[\left(\dot{\theta}_{6@i} \right)_0 \right]^2 - \left[\dot{\theta}_{6@i}(t) \right]^2 \right\} \quad (165)$$

Referring to equation (148):

$$s_{3@(i+1)}(t) = -L_{@i} + \frac{\sqrt{R_{@i}(t)}}{\sqrt{k_{@i}}} \tag{166}$$

Referring to equation (153):

$$\dot{s}_{3@(i+1)}(t) = \frac{\dot{W}_{@i}(t)}{\sqrt{k_{@i}} * \sqrt{R_{@i}(t)}} \tag{167}$$

where $\dot{W}_{@i}(t)$ can be found by numerically derivating $W_{@i}(t)$ with respect to time or analytically (see equation (125)).

Referring to equation (160):

$$\theta_{t@i}(t) = atan2[\dot{s}_2(t), -\dot{s}_{3@i}(t)] \tag{168}$$

Referring to equation (161):

$$\dot{\theta}_{6@i}(t) = \frac{1}{r_{6@i} * \sigma_{@i}} * \left[\sin\left(\theta_{t@i}(t)\right) * \dot{s}_{3@i}(t) - \cos(\theta_{t@i}(t)) * \dot{s}_2(t)\right] \tag{169}$$

Referring to equation (149):

$$R_{@i}(t) = k_{@i} * [L_{@i} + (s_{3@i})_0]^2 + 2 * W_{@i}(t) \tag{170}$$

The root mean square error $(e_{3@i})_{rms}$ is defined via the equation

$$(e_{3@i})_{rms} \triangleq \sqrt{\frac{\int_0^T [e_{3@i}(t)]^2 dt}{T}} \tag{171}$$

where

$$e_{3@i}(t) \triangleq s_{3@(i+1)}(t) - s_{3@i}(t) \tag{172}$$

for $0 \leq t \leq T$.

Next, the steps of the algorithm are given.

1. Define discrete time vector t as " $\coloneqq 0{:}\,\Delta t{:}\,t_{final}$ ". Here, Δt is the step size for discrete time values and t_{final} is the final value of the time which is the period, *T*.
2. Set iteration number "i:=0".
3. Set " $condition \coloneqq true$ ". (Note that " $condition$ " is a variable which is assigned as either " $true$ " or " $false$ ".)
4. Define $\dot{s}_{3@0}(t)$ and $\dot{\theta}_{6@0}(t)$ via the equations

$$\dot{s}_{3@0}(t) = 0 \tag{173}$$

$$\dot{\theta}_{6@0}(t) = 0 \tag{174}$$

Note that $\dot{s}_{3@0}(t)$ and $\dot{\theta}_{6@0}(t)$ are defined for $t = 0{:}\,\Delta t{:}\,t_{final}$. Hence, they are vectors of size $\left(\frac{t_{final}}{\Delta t} + 1\right)$.

5. Make a selection for $\overrightarrow{DV}_{@0}$ where $\overrightarrow{DV}_{@i}$ is defined via the equation (162).
6. Find $R_{@0}(t)$ from equation (170).
7. While " $condition = true$ " apply steps 7.1 to 7.10.

   7.1. If

$$(R_{@i})_{min} < 0 \tag{175}$$

modify $\overrightarrow{DV}_{@i}$ to get $\overrightarrow{DV}_{@i}^{mod}$ (where superscript "mod" denotes modified") such that;

$$\left(R_{@i}^{mod}\right)_{min} \geq 0 \tag{176}$$

where $\left(R_{@i}^{mod}\right)_{min}$ is found by using $\overrightarrow{DV}_{@i}^{mod}$. Once equation (176) is satisfied, set $(R_{@i})_{min}$ and $\overrightarrow{DV}_{@i}$ as follows:

$$(R_{@i})_{min} = \left(R_{@i}^{mod}\right)_{min} \tag{177}$$

$$\overrightarrow{DV}_{@i} = \overrightarrow{DV}_{@i}^{mod} \tag{178}$$

while finding $\overrightarrow{DV}_{@i}^{mod}$, it seems reasonable that one changes (or modifies) the value of $k_{@i}$ and/or $L_{@i}$, although any component of $\overrightarrow{DV}_{@i}$ could be changed. Also, one would like to satisfy equation (175

) or (176) such that $(R_{@0})_{min}$ or $\left(R_{@0}^{mod}\right)_{min}$ is "as small as possible". Because a smaller $(R_{@0})_{min}$ value yields a "smaller" MFG mechanism.

7.2. Determine $W_2(t)$, $W_{3@i}(t)$ and $W_{6@i}(t)$ via equations (128), (164) and (165), respectively.

7.3. Determine $W_{@i}(t)$ via equation (163).

7.4. Determine $R_{@i}(t)$ via equation (170).

7.5. Determine $s_{3@(i+1)}(t)$, which is a vector of size $\left(\frac{t_{final}}{\Delta t}+1\right)$, via equation (166).

7.6. Determine $\dot{s}_{3@(i+1)}(t)$ via equation (167).

7.7. Determine $\theta_{t@i}(t)$ and $\dot{\theta}_{6@i+1}(t)$, which is a vector of size $\left(\frac{t_{final}}{\Delta t}+1\right)$, via equations (168) and (169), respectively. Also, note that $\dot{\theta}_{6@i}(t)$ is always squared (see equation (165)). Hence, $\sigma_{@i}$ which is +1 or -1, does not affect $W_{6@i}(t)$. Hence, one may, without loss of generality, use

$$\sigma_{@i} = +1\ for\ all\ i\ values \tag{179}$$

7.8. Determine $(e_{3@i})_{rms}$ via equation (171).

7.9. If the condition

$$(e_{3@i})_{rms} \leq \epsilon \tag{180}$$

is satisfied, set "$condition \coloneqq false$". The solution has converged. Return $s_{3@(i+1)}(t)$ as the solution for $s_3(t)$ and $\overrightarrow{DV}_{@i}$ as the solution for the design variables vector $\overrightarrow{DV}$. Note that, ϵ is a user specified error limit to stop the iterations.

7.10. If equation (180) is not true,

$$\overrightarrow{DV}_{@i+1} = \overrightarrow{DV}_{@i} \tag{181}$$

and increase i by 1 ($i \coloneqq i+1$). Go the step 7.1.

Once the algorithm converges, one obtains $s_3(t)$ and $\overrightarrow{DV}$. Then by using $s_3(t)$, one can determine $x_s(t)$, $y_s(t)$, $F_3(t)$ via equations (131), (132) and (155), respectively.

5.3 Dynamic Analysis of MFG

In this section, dynamic analysis of the MFG will be realized. This analysis will be more simplified than the dynamic analysis realized by Soylu [45]. In the force analysis, the forces f_6, $F_{26,x}$, $F_{26,y}$ and F_{N6} will be determined (see Figure 84 and Figure 85). Here, f_6 is the friction force developed at the contact point between roller 6 and the slot in body 3; $F_{26,x}$ and $F_{26,y}$ are the reaction forces due to the revolute joint at the center of roller 6; and finally F_{N6} is the normal force developed between roller 6 and the slot in body 3. Once f_6, $F_{26,x}$, $F_{26,y}$ and F_{N6} are determined, the frictional forces, revolute joint reactions and normal forces associated with the remaining rollers (i.e., links 7, 8, 9) can be obtained due to symmetry.

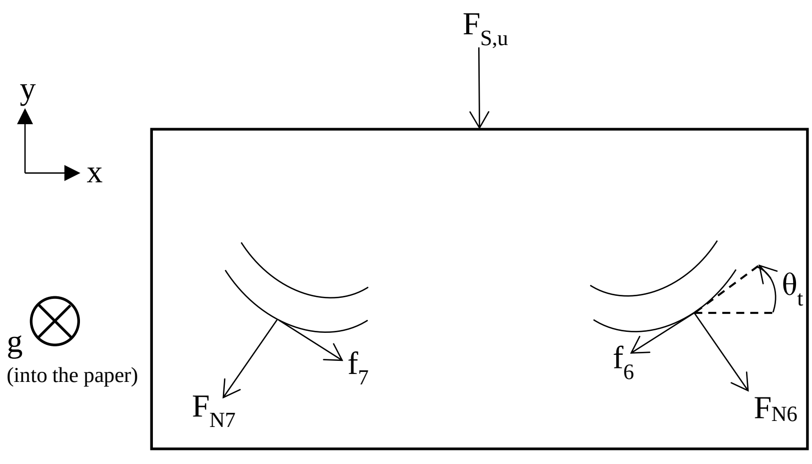

Figure 84: Free Body Diagram of Link 3

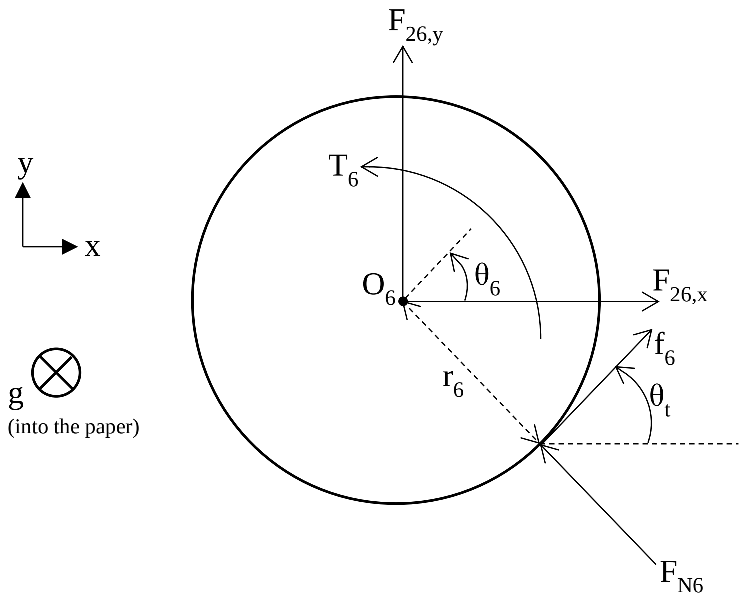

Figure 85: Free Body Diagram of Link 6 (Roller)

In order to solve the 4 unknown forces mentioned in the previous paragraph, it is sufficient to consider the free body diagrams of links 3 and 6 (see Figure 84 and Figure 85). For link 3, only the force equilibrium in the y direction will be considered, since the force equilibrium in the x direction and the moment equilibrium are trivial due to the symmetry of the forces and due to the fact that the 4 joint reactions at the 4 joints that connect the mechanism to the ground are all zero. For link 6 (roller), all 3 equilibrium equations (i.e., force equilibrium in the x and y directions and moment equilibrium) will be written.

For link 3, the force equilibrium equation in the y direction is given below.

$$-F_{S,u} - 2 * F_{N6} * \cos(\theta_t) - 2 * f_6 * \sin(\theta_t) = m_3 * a_3 \qquad (182)$$

Here,

$F_{S,u}$: upper spring force acting on link 3

F_{N6} : normal force between the slot and the roller

θ_t : slope of the slot ($-90° \leq \theta_t \leq +90°$)

f_6 : friction force between the slot and the roller

m_3 : mass of link 3

a_3 : linear acceleration of link 3 (defined as positive in +y direction)

Gravitational forces are not included in the equations since gravity is defined as perpendicular to the paper. In equation (182), only F_{N6} and f_6 are used. F_{N7} and f_7 are not used because they are identical to F_{N6} and f_6, respectively.

For link 6 (roller), the force equilibrium equation the in x direction is given below.

$$F_{26,x} + f_6 * \cos(\theta_t) - F_{N6} * \sin(\theta_t) = m_6 * a_2 \qquad (183)$$

where a_2 is the linear acceleration of link 2 in +x direction, which is identical to the acceleration of the center of mass of link 6 in +x direction; $F_{26,x}$ is the x component of the reaction force between links 2 and 6.

For link 6 (roller), force equilibrium in y direction is given below.

$$F_{26,y} + f_6 * \sin(\theta_t) + F_{N6} * \cos(\theta_t) = 0 \qquad (184)$$

where $F_{26,y}$ is the y component of the reaction force between links 2 and 6. Note that, the right hand side of equation (184) is 0. This is because, the roller does not move in the y direction. Hence, the acceleration of the center of mass of the roller in the y direction is zero. Hence, the corresponding equation has no acceleration term.

T_6 shown in Figure 85 is the friction torque and is defined below.

$$T_6 = \sigma_{\theta_6} * r_f * \sqrt{F_{26,x}^2 + F_{26,y}^2} \quad (185)$$

where r_f is the radius of friction, which is defined below.

$$r_f = r_{pin} * \mu_{pin} \quad (186)$$

r_{pin} is the pin radius in revolute joints which connects rollers with links 2 and 4. μ_{pin} is the friction coefficient in the revolute joints.

σ_{θ_6} used in equation (185) is defined below.

$$\sigma_{\theta_6} = \begin{cases} +1 & if\ \dot{\theta}_6 < 0 \\ & if\ \dot{\theta}_6 = 0, \ddot{\theta}_6 < 0 \\ -1 & if\ \dot{\theta}_6 > 0 \\ & if\ \dot{\theta}_6 = 0, \ddot{\theta}_6 > 0 \\ 0 & if\ \dot{\theta}_6 = 0, \ddot{\theta}_6 = 0 \end{cases} \quad (187)$$

For link 6 (roller), moment equilibrium around point O_6 (center of mass) is as follows:

$$T_6 + \sigma * f_6 * r_{roller} = I_6 * \ddot{\theta}_6 \quad (188)$$

where

r_{roller} : roller radius

I_6 : inertia of the link 6 around point O_6 (center of mass)

$\ddot{\theta}_6$: angular acceleration of link 6 around point O_6 (center of mass)

σ in equation (188) is either +1 (for the case shown in Figure 85) or -1. Its value depends on the side of the contact in the slot. It should be taken as either +1 or -1 at the start of the calculations which will be crosschecked later.

In Figure 86, slot envelopes are shown for both $0° \le \theta_t \le 90°$ and $-90° \le \theta_t \le 0°$ cases. $\hat{\mathbf{t}}_6$ is the unit vector for defining the slope of the slot (θ_t). $\hat{\boldsymbol{e}}_6$ is the unit vector that is obtained by rotating $\hat{\mathbf{t}}_6$ by $-90°$.

First envelope, which will be called "envelope with $\sigma = +1$" and abbreviated to "$\mathrm{E}_{\sigma=+1}$", is located at the $\hat{\boldsymbol{e}}_6$ side. At the opposite side to $\hat{\boldsymbol{e}}_6$ and $\mathrm{E}_{\sigma=+1}$, the second envelope is located, which is "envelope with $\sigma = -1$" and abbreviated to "$\mathrm{E}_{\sigma=-1}$".

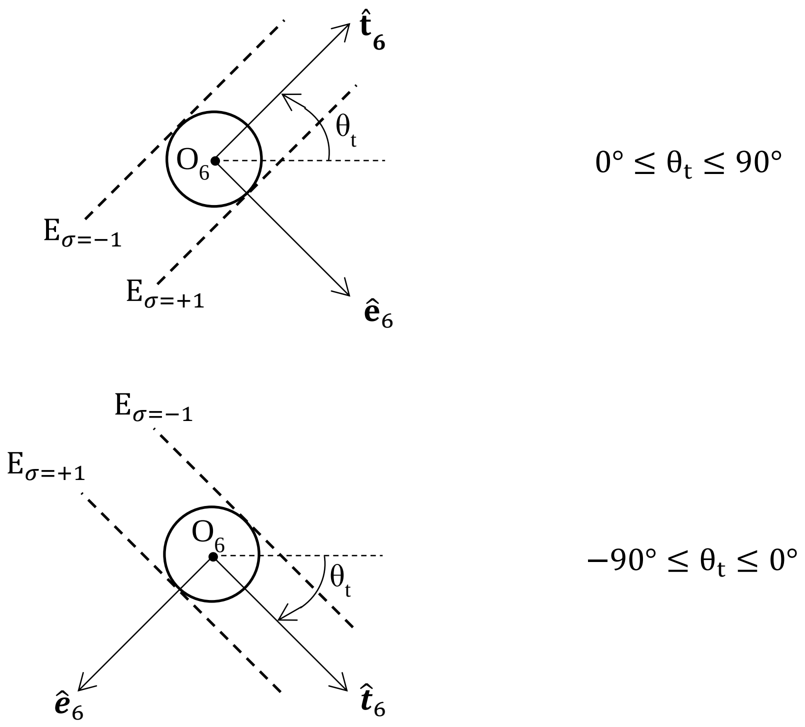

Figure 86: Explanation of Slot Envelopes

For an arbitrary slot shape, two envelopes are shown in Figure 87.

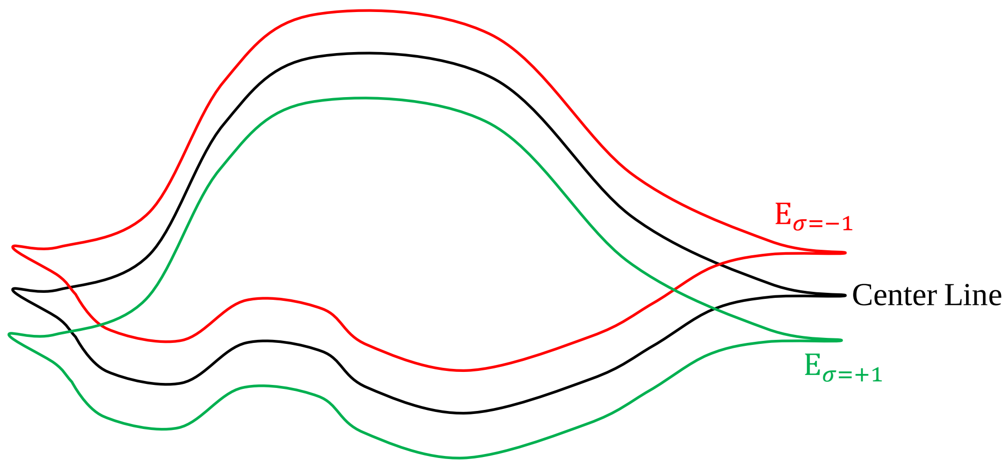

Figure 87: Sketch of Slot Envelopes for an Arbitrary Slot Shape

Substituting equations (185) and (186) into (188);

$$\sigma_{\theta_6} * r_{pin} * \mu_{pin} * \sqrt{F_{26,x}^2 + F_{26,y}^2} + \sigma * f_6 * r_{roller} = I_6 * \ddot{\theta}_6 \qquad (189)$$

There are four equations (equations (182), (183), (184) and (189)) and four unknowns (f_6 , $F_{26,x}$, $F_{26,y}$, F_{N6}) to solve. Hence, this set of equations can be solved analytically.

From equation (182), f_6 can be written in terms of F_{N6}:

$$f_6(F_{N6}) = \frac{-F_{S,u} - 2 * F_{N6} * \cos(\theta_t) - m_3 * a_3}{2 * \sin(\theta_t)} \qquad (190)$$

From equation (183), $F_{26,x}$ can be written in terms of F_{N6} and f_6:

$$F_{26,x}(F_{N6}, f_6) = m_6 * a_2 - f_6 * \cos(\theta_t) + F_{N6} * \sin(\theta_t) \qquad (191)$$

From equation (184), $F_{26,y}$ can be written in terms of F_{N6} and f_6:

$$F_{26,y}(F_{N6}, f_6) = m_6 * a_3 - f_6 * \sin(\theta_t) - F_{N6} * \cos(\theta_t) \qquad (192)$$

Hence, f_6 , $F_{26,x}$ and $F_{26,y}$ can be written in terms of F_{N6}.

Equation (189) can be rearranged as below.

$$F_{26,x}^2 + F_{26,y}^2 = \left(\frac{I_6 * \ddot{\theta}_6 - \sigma * f_6 * r_{roller}}{\sigma_{\theta_6} * r_{pin} * \mu_{pin}}\right)^2 \qquad (193)$$

Equation (193) can be written in terms of only F_{N6}, by using equations (190), (191), (192) as follows:

$$a * F_{N6}^2 + b * F_{N6} + c = 0 \qquad (194)$$

For the ease of readability; coefficients a, b and c will not be written explicitly here, since they are too long to write. However, they have been found by using the Mathematica software and this output is used in the MATLAB software (see APPENDIX).

According to equation (194), one may have two distinct roots, one repeated root, or no roots. Once F_{N6} is found, one can easily find f_6 , $F_{26,x}$ and $F_{26,y}$ by using equations (190), (191), (192).

Once F_{N6} is found, one can crosscheck the following fact:

$$\sigma = sign(F_{N6}) \qquad (195)$$

One should also crosscheck whether equation (187) is fulfilled or not.

5.4 Sample Tasks to Be Used for the Analyses

Slot shapes will be determined for four different tasks. Each dataset includes the force ($F_2(t)$) and the displacement ($s_2(t)$) data).

Firstly, the notation to be used will be introduced.

$F_2(t)$: Force applied <u>on</u> MFG

$F_{MFG}(t)$: Force <u>generated by</u> MFG

Hence, their directions are opposite, i.e.,

$$F_2(t) = -F_{MFG}(t) \qquad (196)$$

$P_{MFG,in}$(t) : Power <u>input</u> to MFG

$P_{MFG}(t)$: Power <u>output</u> of MFG

where

$$P_{MFG,in}(\mathrm{t}) = F_2(t) * \dot{s}_2(t) \quad (197)$$

$$P_{MFG}(t) = F_{MFG}(t) * \dot{s}_2(t) \quad (198)$$

By using equations (196), (197) and (198) together;

$$P_{MFG,in}(\mathrm{t}) = -P_{MFG}(t) \quad (199)$$

Furthermore,

$$\dot{M}E(t) = P_{MFG,in}(\mathrm{t}) = -P_{MFG}(t) \quad (200)$$

where $\dot{M}E(t)$ is the time rate of change of total mechanical energy of the MFG.

The first task (Task-1) corresponds to minimizing the maximum power consumption which is examined in section 4.4.1. Hence, $F_2(t)$ is taken as the opposite of the MFG force that is shown in Figure 73. $s_2(t)$ is obtained by redefining $s_4(t)_{machine}$ as follows:

$$s_2(t) = s_4(t)_{machine} + s_{2,shift} \quad (201)$$

where

$s_4(t)_{machine}$: $s_4(t)$ of the press machine (see equation (76))

$s_{2,shift}$: shift in the displacement

Note that, here, two press machines are used as twin machines. Hence, a single MFG is connected to two press machines from links 2 and 4 of the MFG, as shown in Figure 3. $-F_{MFG}(t)$ is directly taken as $F_2(t)$, according to the equation (196). $s_2(t)$ and $F_2(t)$ graphs of Task-1 are given in Figure 88.

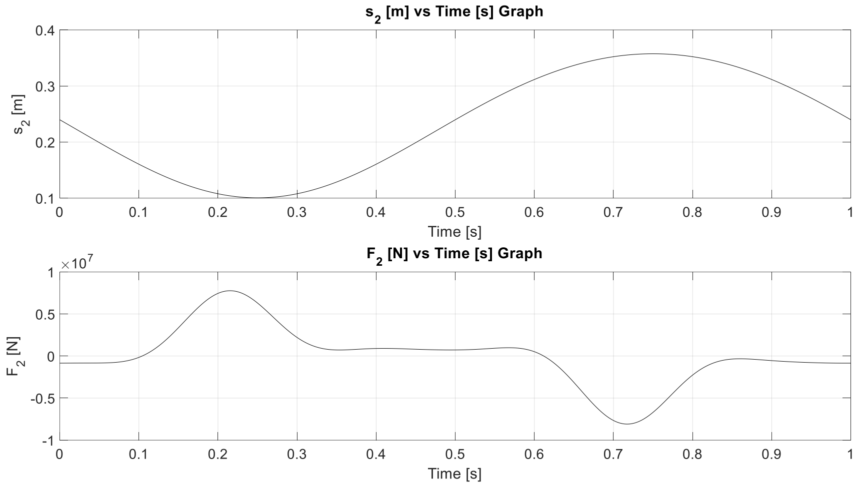

Figure 88: $\mathrm{s}_2(\mathrm{t})$ and $\mathrm{F}_2(\mathrm{t})$ graphs of Task-1

Task-2 is constructed with the same $s_2(t)$ of Task-1 and opposite of $F_2(t)$ of Task-1. In other words, the direction of the applied force is inverted for Task-2. By inverting the direction of the applied force on the MFG, it is possible to see the resulting change in the slot profile. $s_2(t)$ and $F_2(t)$ graphs of Task-2 are given in Figure 89.

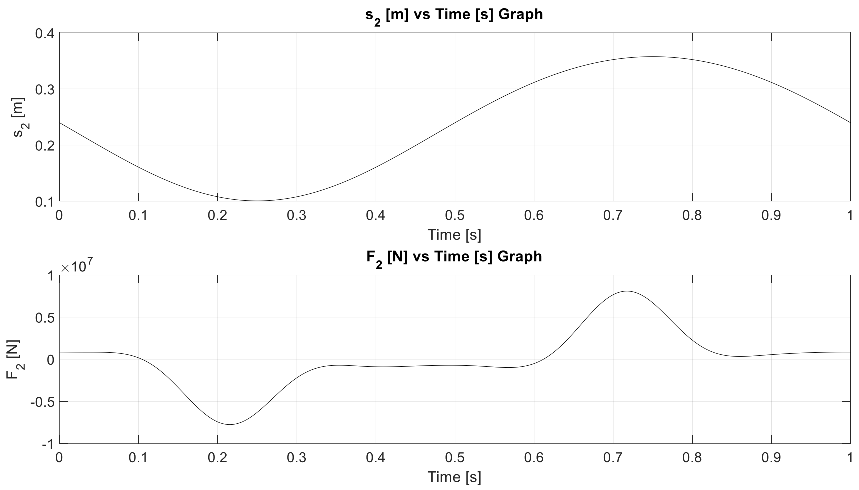

Figure 89: $\mathrm{s}_2(\mathrm{t})$ and $\mathrm{F}_2(\mathrm{t})$ graphs of Task-2

Task-3 is a new and special task. Consider a conveyor as shown in Figure 90. The conveyor always moves in the same direction. The part of the MFG that is shown in Figure 90 may be link 2 of the MFG, or it may be another link that merges the outputs of links 2 and 4 as explained in section 1.3. In this case study, it is either link 2 or link 4 of the MFG. Hence, a single MFG is connected to two different conveyors, which are twin machines like the ones in Figure 3.

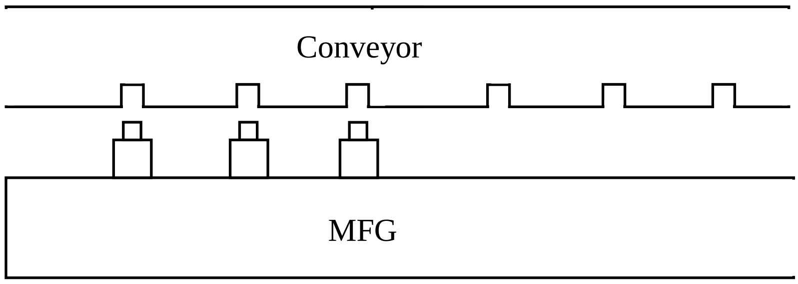

Figure 90: Conveyor & MFG Engagement

The MFG can be engaged to the conveyor by the help of the pins shown in Figure 90. The period of the total motion is 8 seconds. Corresponding displacement vs time graph is shown in Figure 91. In the first 4 seconds, MFG is engaged to the conveyor and the conveyor moves together with the MFG. Between the 4^{th} and 5^{th} seconds, MFG disengages from the conveyor while both the MFG and conveyor are stationary. Between the 5^{th} and 7^{th} seconds, MFG moves back to the initial position while the conveyor is stationary. Between the 7^{th} and 8^{th} seconds, MFG engages to the conveyor while both the MFG and conveyor are stationary. After the 8^{th} second, the period ends and the same motion starts as explained above.

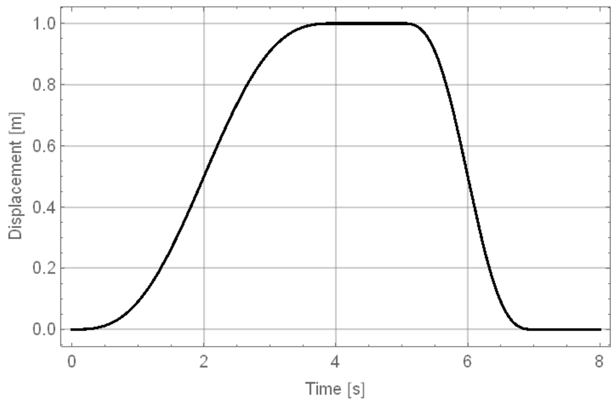

Figure 91: Displacement vs Time Graph

In this study, for the ease of analytic calculations, the displacement $\mathrm{s}_2(\mathrm{t})$ is approximated by a Fourier series of order 20. Hence, its derivatives can be easily found analytically. Furthermore, this $\mathrm{s}_2(\mathrm{t})$ can be used after redefining it by addition of $s_{2,shift}$ (similar to equation (201)).

In Figure 92, mass vs time graph of the overall system is shown.

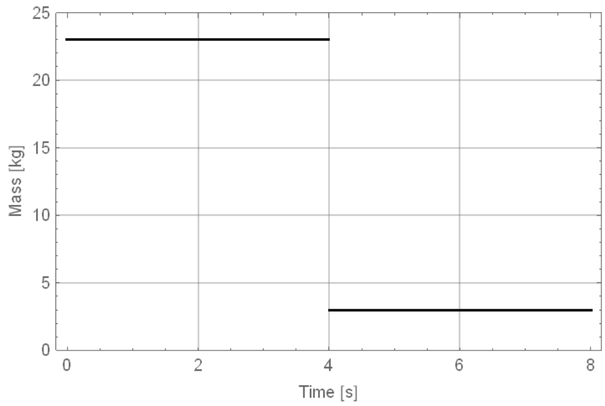

Figure 92: Mass vs Time Graph

Here, the mass of the conveyor is 20 kg, and the mass of the engagement system (pins, etc.) is 3 kg (which excludes the mass of link 2 of MFG). Hence, MFG carries the engagement mass of 3 kg at all times. In the first 4 seconds of each period, MFG also carries the conveyor mass which is 20 kg (yielding a total of 23 kg). The force that should be generated by MFG is found as below.

$$F_{MFG}(t) = \begin{cases} (m_{conveyor} + m_{engagement}) * \ddot{s}_2(t) & for\ 0 \le t < 4 \\ (m_{engagement}) * \ddot{s}_2(t) & for\ 4 \le t < 8 \end{cases} \tag{202}$$

where

$m_{conveyor}$: mass of the conveyor

$m_{engagement}$: mass of the engagement

$\ddot{s}_2(t)$: linear acceleration of link 2 of MFG

$F_{MFG}(t)$ is expressed as a 20th order Fourier series (see Figure 93).

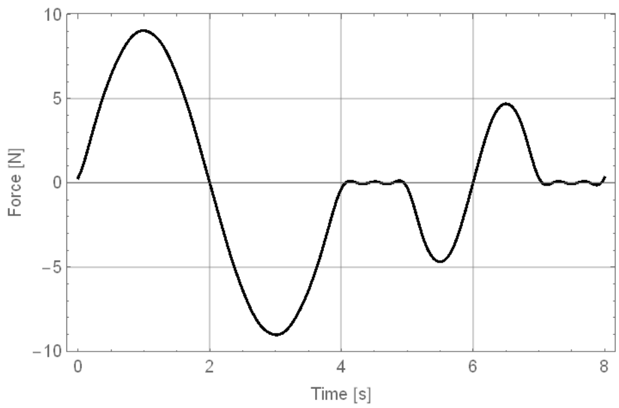

Figure 93: Force vs Time Graph

Corresponding $s_2(t)$ and $F_2(t)$ graphs of Task-3 are given in Figure 94.

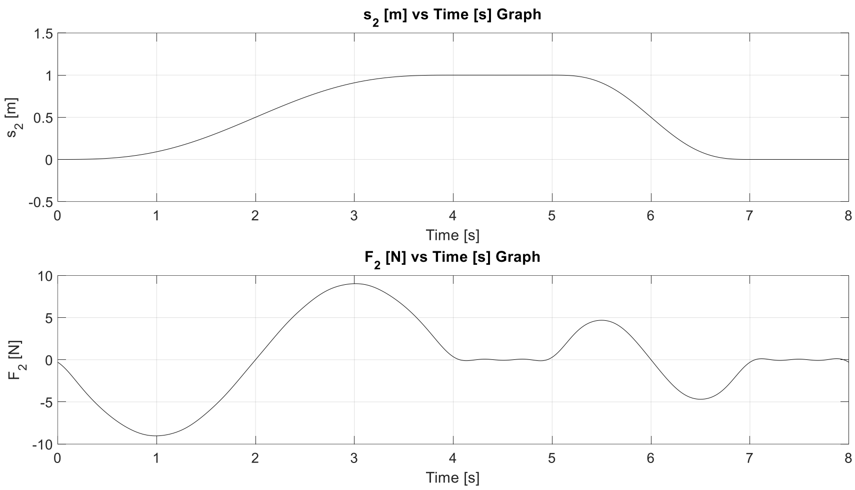

Figure 94: $\mathrm{s_2(t)}$ and $\mathrm{F_2(t)}$ graphs of Task-3

Lastly, Task-4 is constructed with the same $s_2(t)$ of Task-3 and the opposite of the $F_2(t)$ of Task-3. In other words, the direction of the applied force (that is given in Figure 93) is inverted for Task-4. By inverting the direction of the applied force on the MFG, it is possible to see the resulting change in the slot profile. Corresponding $s_2(t)$ and $F_2(t)$ graphs of Task-4 are given in Figure 95.

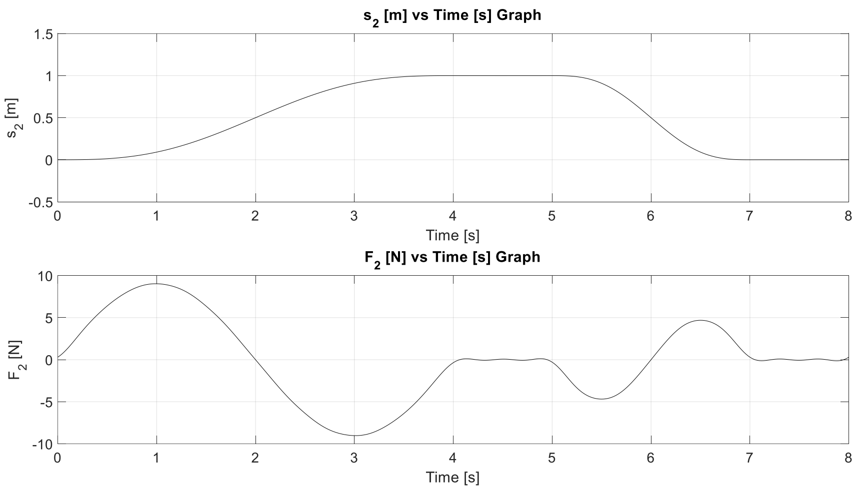

Figure 95: $\mathrm{s_2(t)}$ and $\mathrm{F_2(t)}$ graphs of Task-4

5.5 Results & Discussion

5.5.1 Task-1

For Task-1, the design variables that are obtained via the iterative algorithm are listed below.

$b_1 = 1.5$ m

$b_3 = 0.8$ m

$b_2 = 0.5$ m

$(s_3)_0 = 0.2$ m

$s_{2,shift} = 1$ m

$k = 2000$ N/mm

$l_{free} = 1$ m

$m_2 = 500$ kg

$m_3 = 500$ kg

$m_6 = 2$ kg

$r_6 = 0.005$ m

In order to the stop iterations, $\epsilon = 0.001$ mm must be reached. This value makes the results of the iterations precise enough.

Some of the selected design variables are quite large. However, considering the capacity of the press machine, they are all reasonable. The spring is a compression spring. In Figure 96, the slot profile for Task-1 is shown. The initial point is shown with a dot. The roller moves in the direction which is shown with two arrows. In both ends of the slot profile, the slot slopes are equal for the two tangents (which are shown with two double arrows on the right-hand side of the slot profile; for the sake of simplicity, no arrows are put on the left-hand side). This is due to the smoothness of s_3 and s_2 curves. If one of them was not continuous or non-smooth at any point, there would be sharp edges in the slot shape, and the slopes of two tangent lines would not be equal at the two ends.

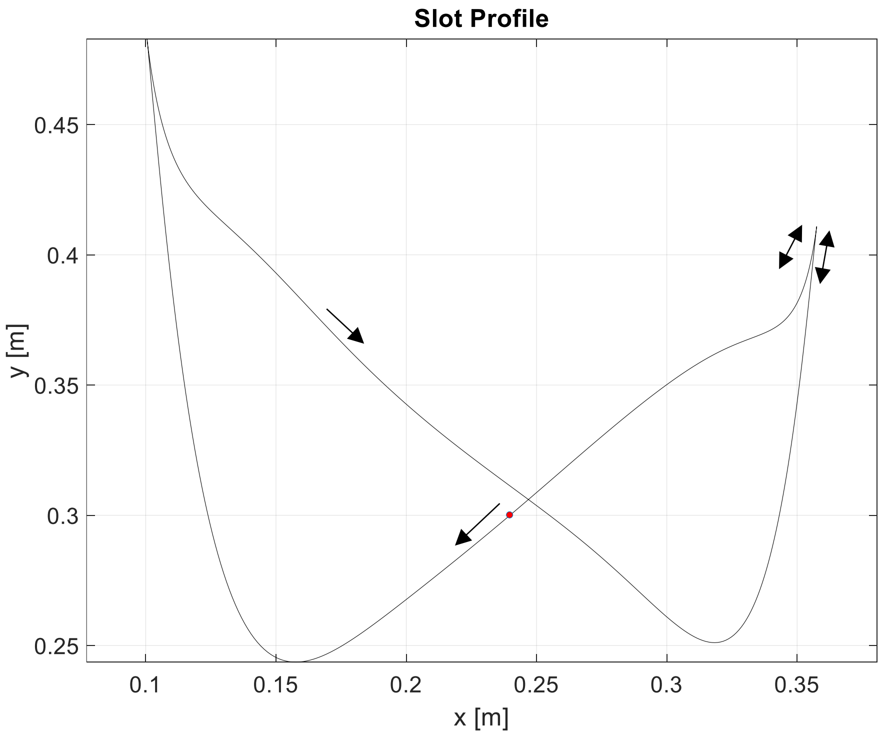

Figure 96: Slot Profile for Task-1

At the end of the 5th iteration, $\epsilon = 0.001$ mm is reached and the slot profile is obtained. In Figure 97, the slot profile with envelopes is shown. The width of the slot is 1 cm, since the roller diameter is 1 cm.

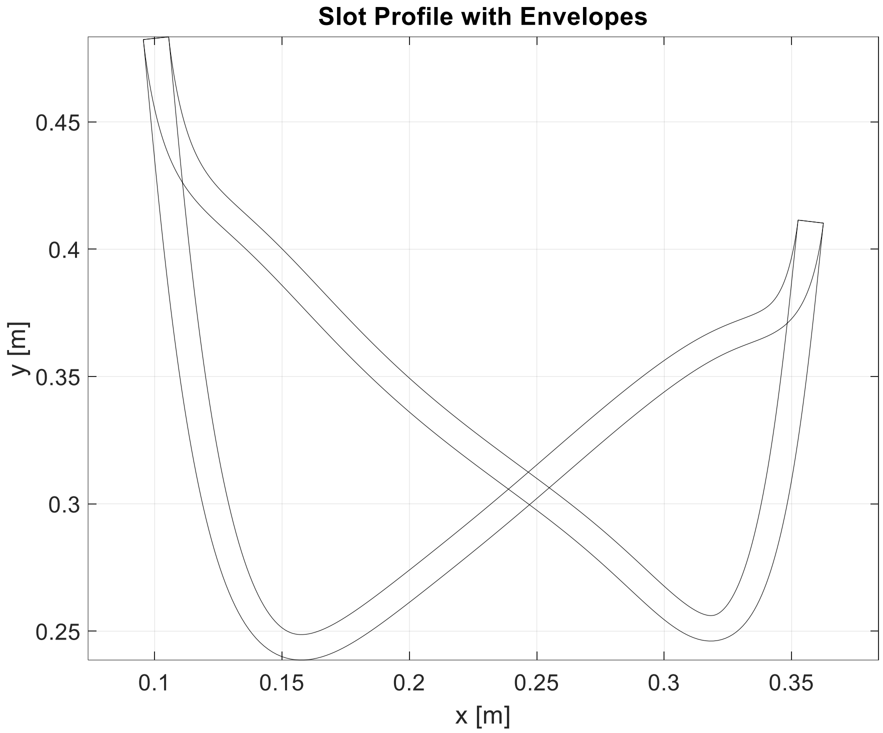

Figure 97: Slot Profile with Envelopes for Task-1

5.5.2 Task-2

Recall that, direction of $F_2(t)$ is the opposite of Task-1. $s_2(t)$ and the magnitude of $F_2(t)$, on the other hand, are the same as Task-1. For Task-2, l_{free} is determined to be 0.8 m. All of the remaining design variables are the same as Task-1.

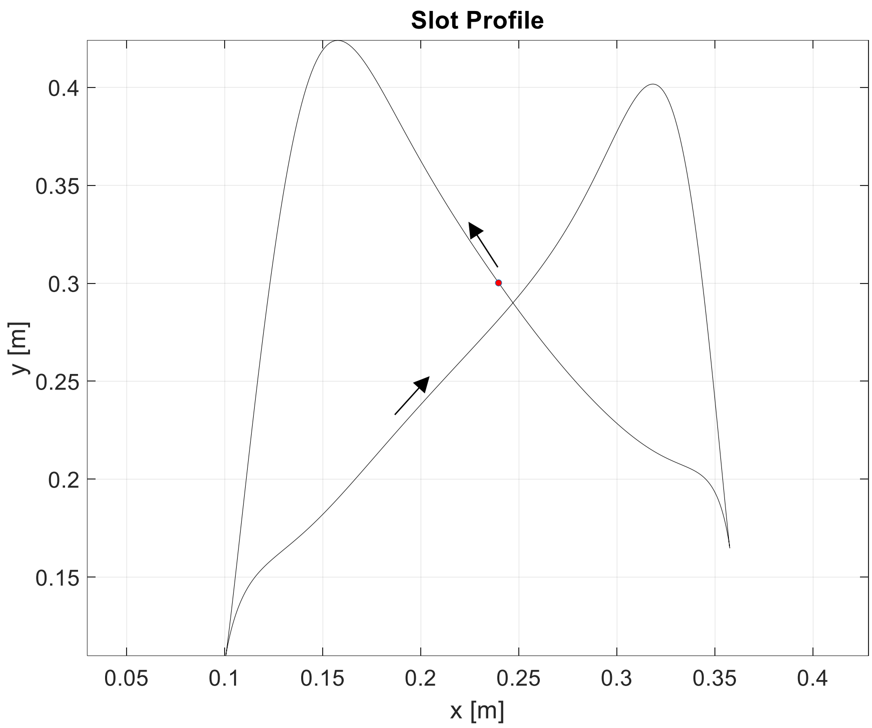

Figure 98: Slot Profile for Task-2

In Figure 98, the slot profile for Task-2 is shown. Initial point is shown with a dot. The roller moves in the direction shown with an arrow.

At the end of the 6th iteration, $\epsilon = 0.001$ mm is reached and the slot profile is obtained. In Figure 99, the slot profile with the envelopes is shown. The width of the slot is 1 cm, since the roller diameter is 1 cm. Note that, the intersection of the two slots (in the middle of the figure) will be investigated later.

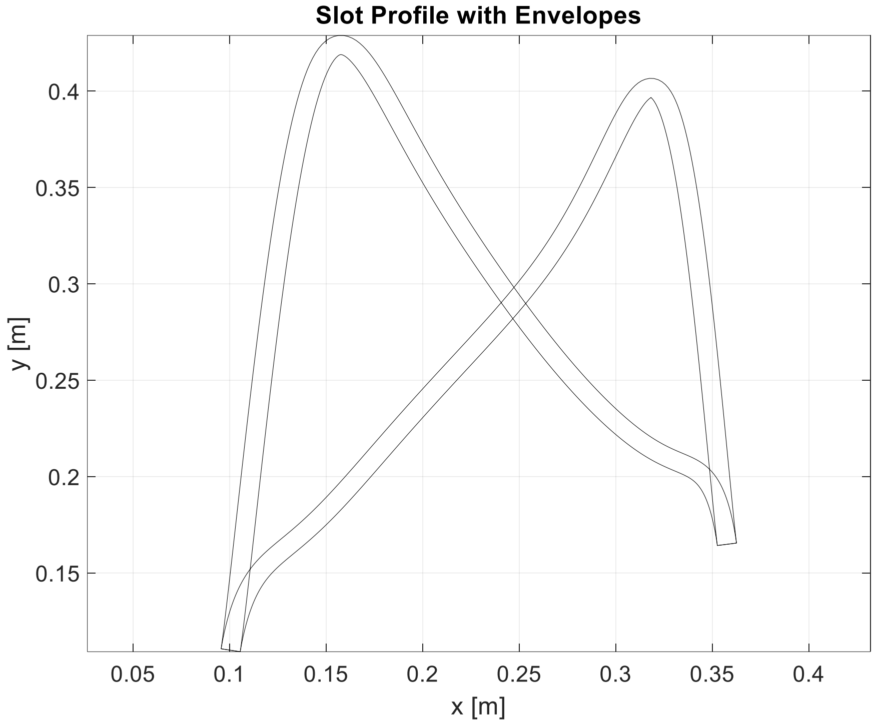

Figure 99: Slot Profile with Envelopes for Task-2

The slot profile of Task-2 is roughly symmetrical with the slot profile of Task-1 (with respect to a horizontal line). This is due to the fact that $F_2(t)$ is inverted.

In Figure 100, the following quantities are plotted:

KE_{24}	: total kinetic energies of links 2 and 4
KE_{35}	: total kinetic energies of links 3 and 5
$KE_{rollers}$	: total kinetic energies of the rollers
SE	: total spring energies of the springs
ME	: total mechanical energies of all links and springs
W_{MFG}	: work done by the MFG

W_{MFG} is defined as below.

$$W_{MFG}(t) = \int_{t=0}^{t=t} [2 * F_{MFG} * \dot{s}_2(t)]dt \quad (203)$$

Clearly,

$$-W_{MFG}(t) = ME(t) - ME(0) \quad (204)$$

where

$$ME(t) = KE_{24}(t) + KE_{35}(t) + KE_{rollers}(t) + SE(t) \quad (205)$$

and

$$KE_{24} = 2 * \left(\frac{1}{2} * m_2 * \dot{s}_2^2\right) \quad (206)$$

$$KE_{35} = 2 * \left(\frac{1}{2} * m_3 * \dot{s}_3^2\right) \quad (207)$$

$$KE_{rollers} = 4 * \left(\frac{1}{2} * m_6 * \dot{s}_2^2 + \frac{1}{2} * I_6 * \dot{\theta}_6^2\right) \quad (208)$$

$$SE = 2 * \left(\frac{1}{2} * k * (L + s_3)\right) \quad (209)$$

As seen in Figure 100, the biggest contributors to the mechanical energy are the springs in Task-2. If the masses of the links are increased, their contributions to the total mechanical energy increase (This aspect will be examined for Task-4 in section 5.5.4.1.).

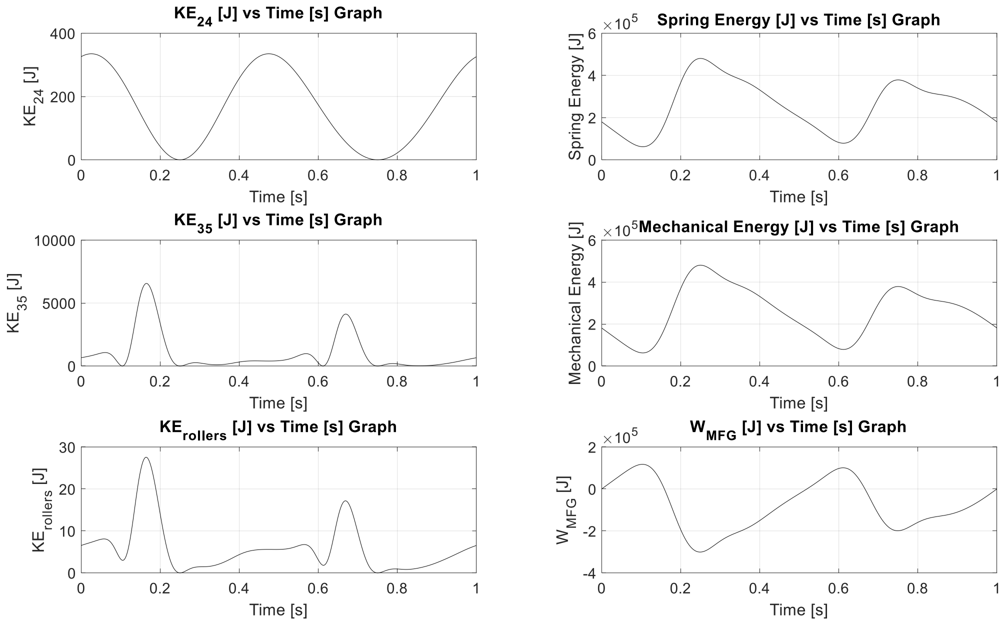

Figure 100: Energy Graphs for Task-2

In Figure 101, time rate of change of energy graphs are shown for Task-2. In Figure 102, the contributions of links to the total mechanical energy are shown. As expected from the results of Figure 100, the springs are by far the biggest contributors. The second biggest contributors are the links 3 and 5. Although their masses are equal to the masses of links 2 and 4; links 3 and 5 contribute to the total mechanical energy much more. This is due to the difference in the velocity profiles (Links 3 and 5 reach higher speeds.). For another MFG, links 2 and 4 may contribute to the mechanical energy more than the contribution made by links 3 and 5. Contribution of the rollers to the mechanical energy are lower than the contributions of all other links, since their masses are too small with respect to the masses of the other links.

Note that, at 0.25 s and 0.75 s (at both ends of the slot), since all the links stop for an instant, kinetic energies of all links decrease to 0. At these instants, energy is stored only in the springs.

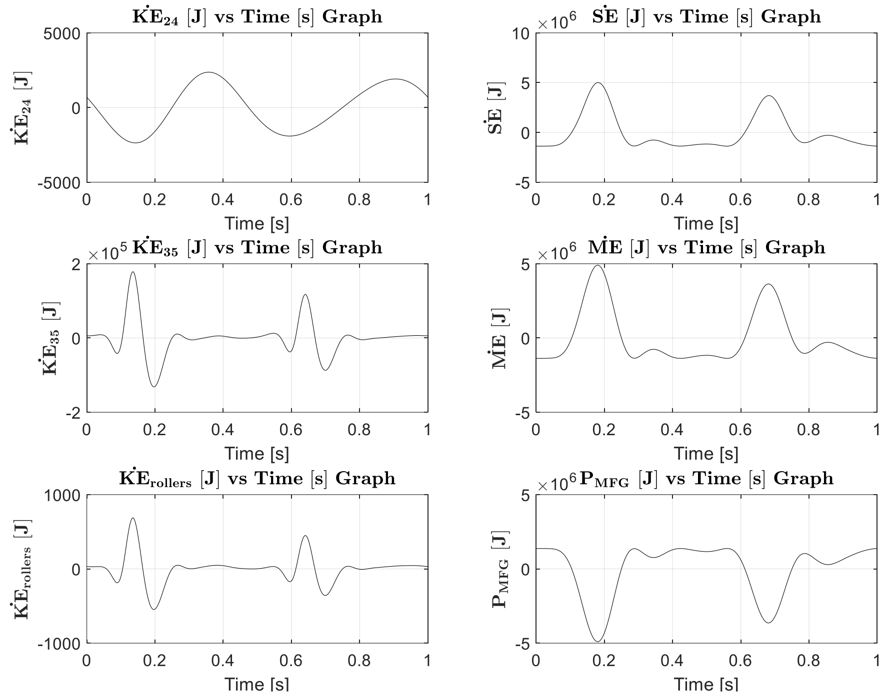

Figure 101: Time Rate of Change of Energy Graphs for Task-2

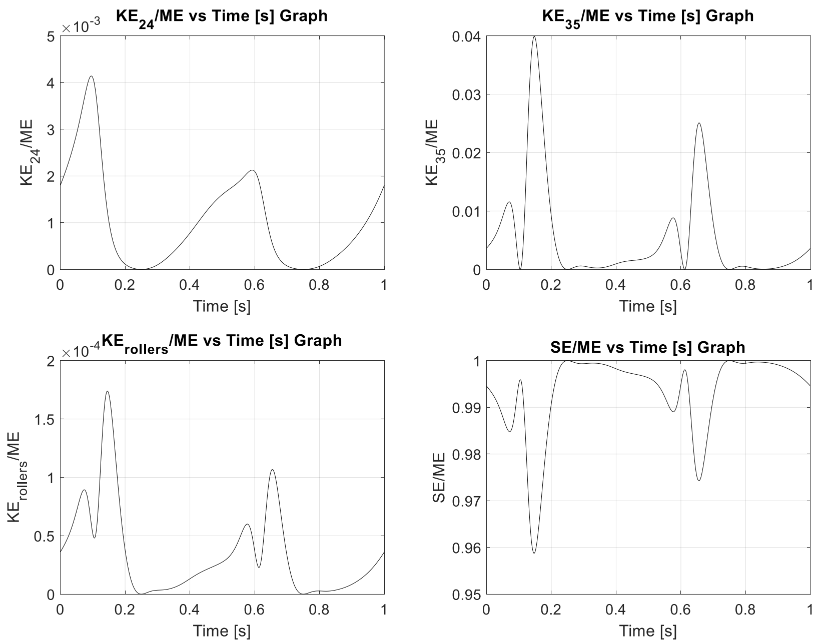

Figure 102: Contributions of Links to Total Mechanical Energy for Task-2

In Figure 103, the ratios of the time rate of change of energies to the time rate of change of the total mechanical energy for Task-2 are shown for all links and springs. Since $\dot{ME}$ is 0 at some points, there are peaks at these points (because of division by 0).

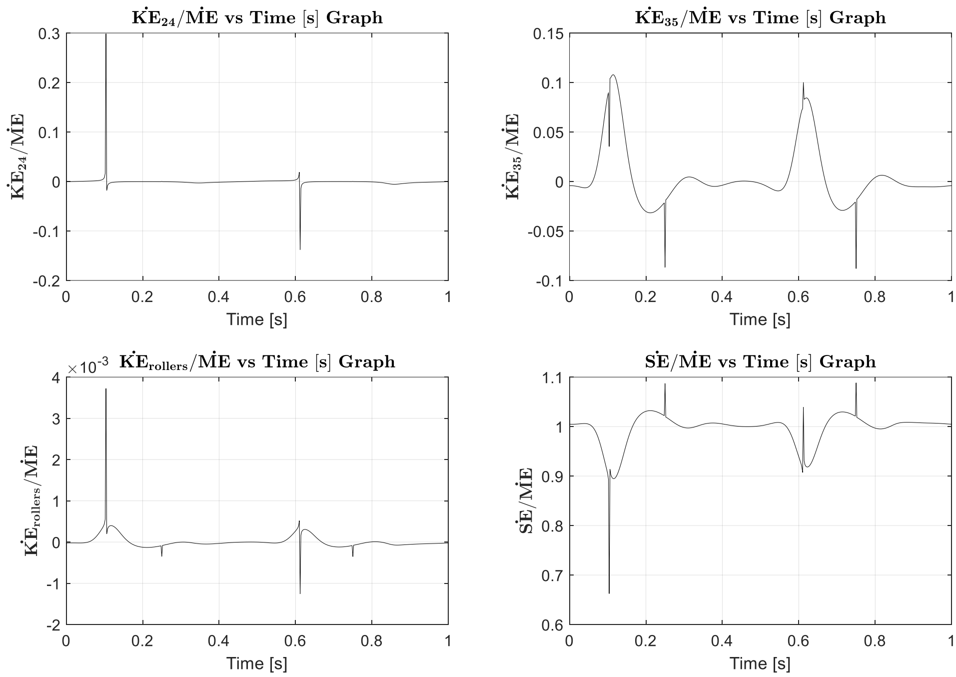

Figure 103: Ratios of the Time Rate of Change of to the Time Rate of Change of the Energies to Total Mechanical Energy for Task-2

The maxima and minima of the energies and the time rate of change of energies for Task-2 are presented in Table 13.

Table 13: Presentation of the Results for Task-2

	Unit	Maximum	Minimum	Total Change
ME	Joule	480471.5	62203.3	418268.2
KE_{24}	Joule	335.0	0.0	335.0
KE_{35}	Joule	6555.6	0.0	6555.6
$KE_{rollers}$	Joule	27.6	0.0	27.6
SE	Joule	480471.5	61950.7	418520.8
P_{MFG}	Watt	4903530.0	-1372744.9	6276274.9
$\dot{KE}_{24}$	Watt	2368.6	-2368.6	4737.2
$\dot{KE}_{35}$	Watt	178397.0	-131561.6	309958.6
$\dot{KE}_{rollers}$	Watt	687.0	-546.6	1233.6
$\dot{SE}$	Watt	5002454.6	-1379273.7	6381728.3

5.5.2.1 Force Analysis for Task-2

Force analysis of MFG for Task-2 is performed according to the explanations in section 5.3.

According to equation (194), one may have two distinct roots for F_{N6}, one repeated root, or no roots at all. However, the F_{N6} values that are obtained should be inserted into equation (189) to see whether they satisfy the equation or not, since there is a square root in this equation.

Equation (189) can be rearranged as follows:

$$\sigma_{\theta_6} * r_{pin} * \mu_{pin} * \sqrt{F_{26,x}^2 + F_{26,y}^2} + \sigma * f_6 * r_{roller} - I_6 * \ddot{\theta}_6 = 0 \qquad (210)$$

In order to satisfy the equation, the right hand side should be equal to zero.

In Figure 104, the left hand side of equation (210) is shown for the two distinct roots of F_{N6}. For every time instant, only one of the roots satisfy the equation. Hence, for each time instant, only one of the roots (which makes equation (210) equal to zero) is taken as the answer.

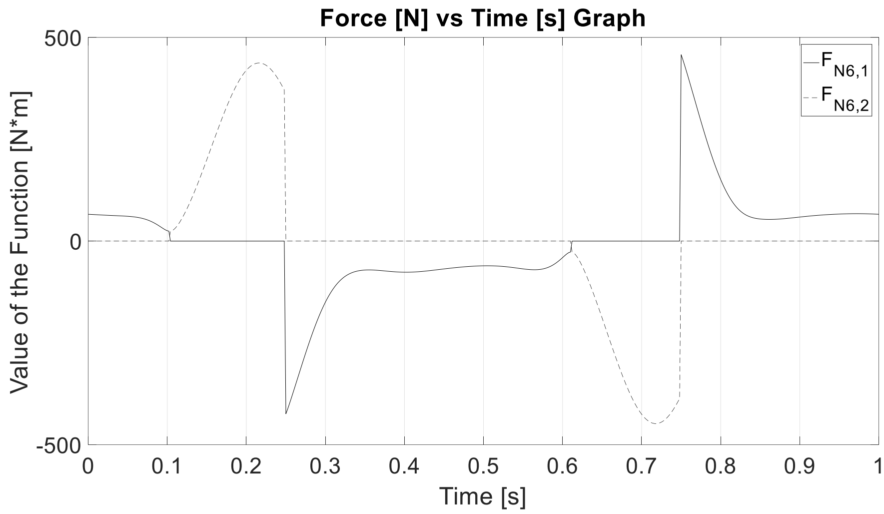

Figure 104: Value of Equation (210)

In Figure 105, F_{N6} vs time graph for the two distinct roots of F_{N6} is shown. As explained above, for each time instant, F_{N6} will be chosen from these two roots which makes equation (210) equal to zero. Once F_{N6} is found, one can determine f_6, $F_{26,x}$ and $F_{26,y}$ by using equations (190), (191) and (192).

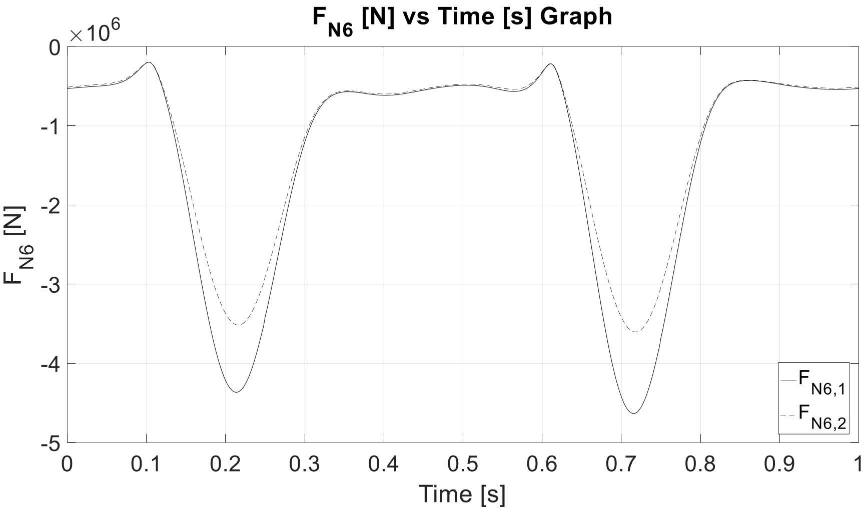

Figure 105: F_{N6} vs Time Graph for the 2 Distinct Roots

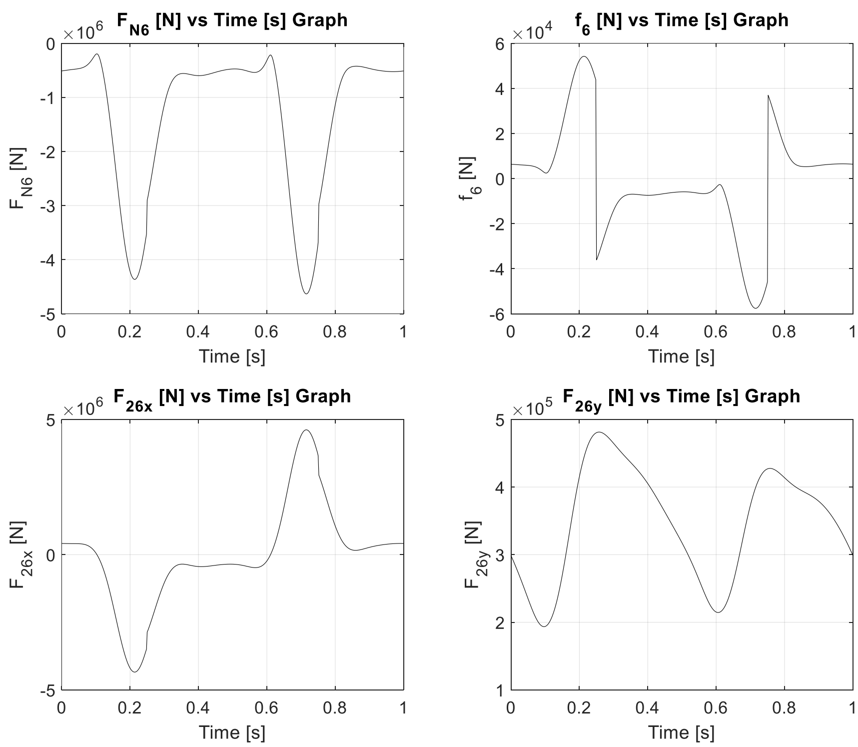

Figure 106: F_{N6}, f_6, F_{26_x}, F_{26_y} vs Time Graphs

In Figure 106, F_{N6}, f$_6$, F_{26_x}, F_{26_y} vs time graphs are shown.

At t=0.25 s and t=0.75 s, the rollers reach the two end points of the slots; stop and change direction. Since the direction of the motion is changed, the direction of the friction force f_6 also changes. That explains the jumps in the F_{N6}, f_6, F_{26_x} graphs. In the F_{26_y} graph, there is no jump, because it is directly correlated with the spring force (and the inertias).

Now, recall the no slip assumption. For no slip, one must have:

$$f_6 \leq F_{N6} * \mu_{slot} \tag{211}$$

where μ_{slot} is the friction coefficient between the slot and the roller.

By rearranging equation (211), one obtains

$$\frac{f_6}{F_{N6}} \leq \mu_{slot} \tag{212}$$

Hence, for the no slip case, equation (212) should be satisfied at all times. For Task-2, it is found that:

$$max\left(\frac{f_6}{F_{N6}}\right) = 0.01263$$

Hence, any μ_{slot} value higher than 0.01228 will be sufficient for the no slip condition. This value is quite small and nearly for all materials, the friction coefficient would be higher than that.

Once F_{N6} is found, one can crosscheck whether equation (195) is satisfied or not. Here, the initial guess was $\sigma = -1$. Hence, $\sigma = sign(F_{N6})$ equality is satisfied (if σ was taken as +1, F_{N6} would be negative, hence it would not satisfy the equality). That means, roller contact is at $E_{\sigma=-1}$ for every time instant (it is an expected result, since the spring is in compression). In other words, roller contact for rollers 6 and 7 is always at the upper side (+y direction side) of the slot (see Figure 87). This information is important in order to design the MFG physically.

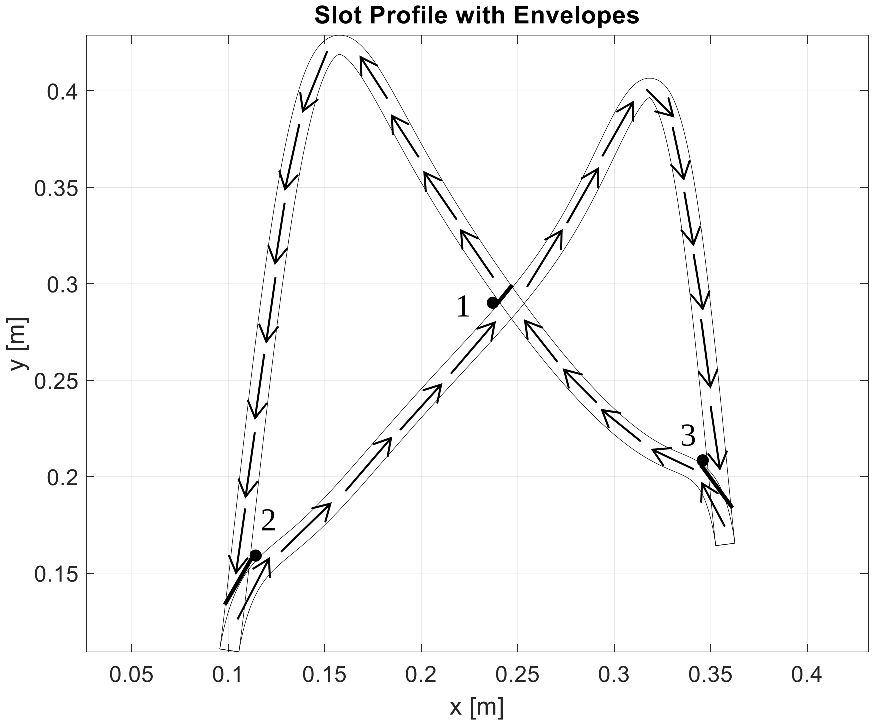

Figure 107: Physical Justification of Slot Profile

Since the roller always contacts the upper side of the slot, at the intersection (marked as point 1), at the left-hand side of the slot (marked as point 2) and at the right-hand side of the slot (marked as point 3) (see Figure 107). The roller can move in the wrong direction. In order to solve this problem, one can locate arms (like "doors", shown with thick lines) and connect them to revolute joints (shown with points). These arms can rotate only in a single direction. In this case, arm 1 and arm 2 can turn counterclockwise around their revolute joints, and arm 3 can turn clockwise around its revolute joint. In Figure 107, these arms are shown at their closed positions. At the revolute joints, one can also employ torsional springs to ensure that these arms will come back to their initial (closed) positions once opened.

Note that, the slot shape may be more complicated with more than one intersections, or it may be simpler, without any intersections.

In Figure 108, a possible slot shape for another task and the direction of motion of the roller is shown. If $\sigma = -1$ at all times (same as Task-2), only one arm at the intersection would be sufficient. At both ends, roller would find its path without the help of an arm.

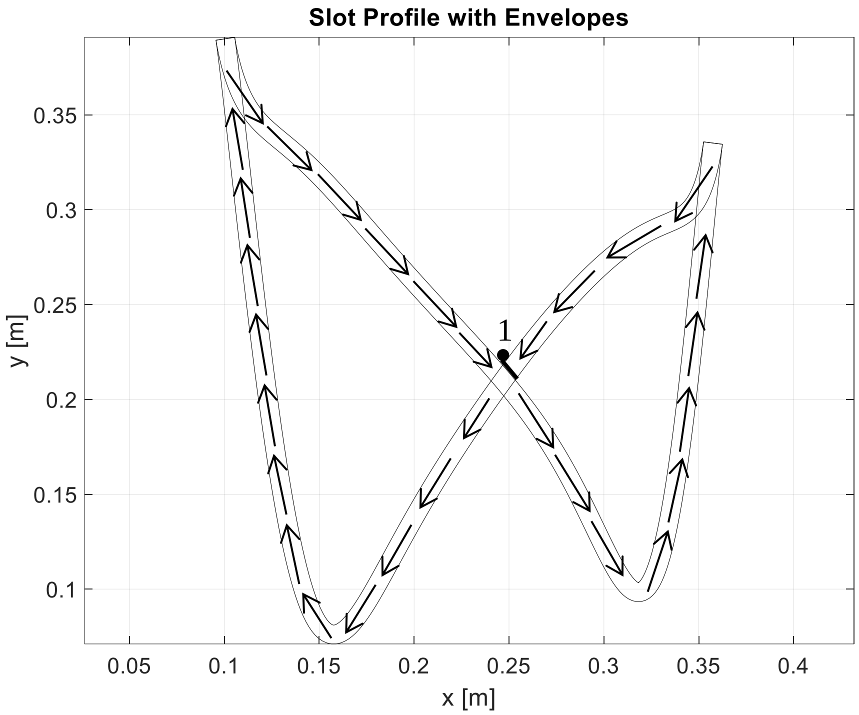

Figure 108: Slot Shape for Another Task

Indeed, there may be other ways for practical implementation of intersecting slots. For example, one can utilize two different slots in parallel, but not coincident, planes.

Note that, the cross check for equation (187) is also fulfilled for Task-2.

5.5.3 Task-3

For Task-3, the design variables that are obtained via the iterative algorithm are listed below.

$b_1 = 0.8$ m

$b_3 = 0.4$ m

$b_2 = 0.3$ m

$(s_3)_0 = 0.15$ m

$s_{2,shift} = 0.2$ m

$k = 120$ N/m

$l_{free} = 0.5$ m

$m_2 = 2$ kg

$m_3 = 2$ kg

$m_6 = 0.1$ kg

$r_6 = 0.005$ m

At the end of the 8th iteration, $\epsilon = 0.001$ mm is reached and the slot profile is obtained. In Figure 109, the slot profile for Task-3 is shown. The initial point is shown with a dot. The roller moves in the direction shown with an arrow.

In Figure 110, the slot profile with the envelopes is shown. The width of the slot is 1 cm, since the roller diameter is 1 cm.

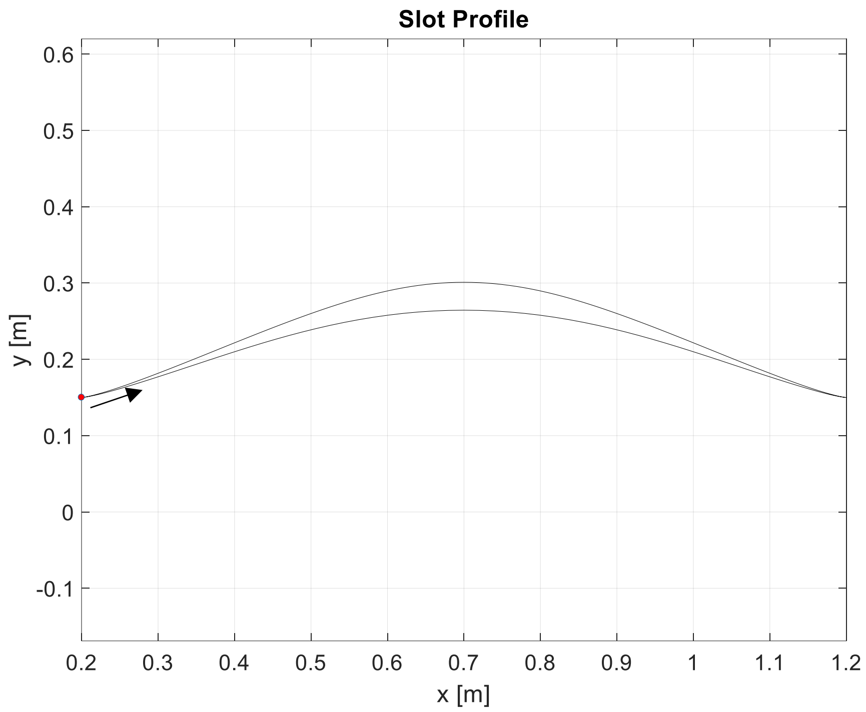

Figure 109: Slot Profile for Task-3

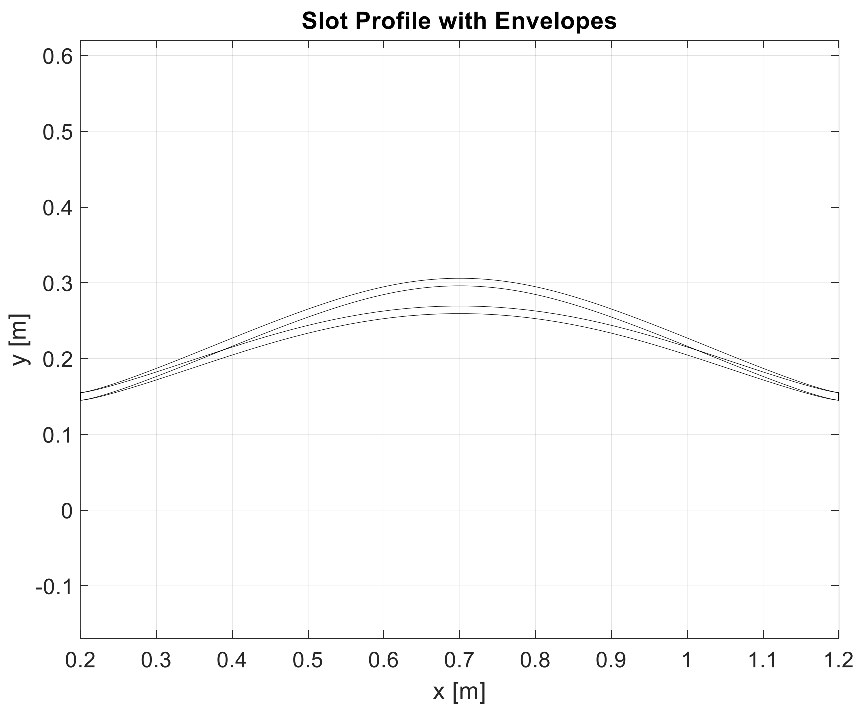

Figure 110: Slot Profile with Envelopes for Task-3

5.5.4 Task-4

Recall that, the direction of $F_2(t)$ is the opposite of Task-3. $s_2(t)$ and the magnitude of $F_2(t)$, on the other hand, are the same as Task-3. For Task-4, l_{free} is selected as 0.3 m and k is selected as 200 N/m. All the remaining design variables are the same as Task-3.

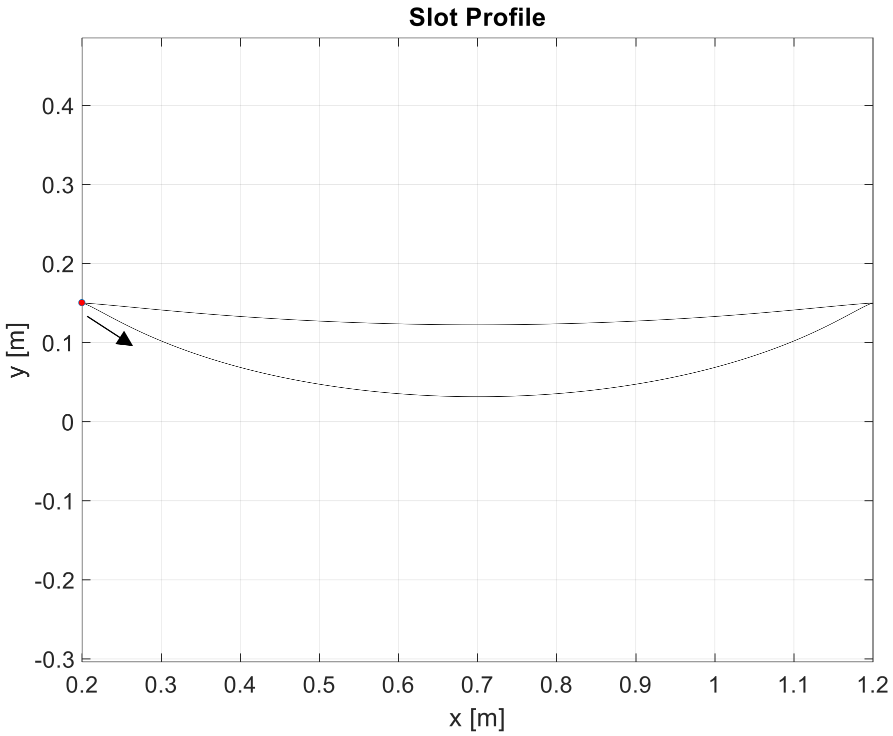

Figure 111: Slot Profile for Task-4

In Figure 111, the slot profile for Task-4 is shown. The initial point is shown with a dot. The roller moves in the direction shown with an arrow.

Table 14:Iteration Number vs RMS Error Table for Task-4

Iteration Number	RMS Error [mm]
1	1.00731
2	0.01708
3	0.00057

This slot profile is obtained at the end of 3 iterations. In other words, at the end of the 3rd iteration, $\epsilon = 0.001$ mm is reached. Note that, in general, the algorithm has a very fast convergence rate (execution time to find the slot shape is around 2 minutes). For instance, for Task-4, the iteration number vs RMS error values are shown in Table 14. The plots of all three slot profiles (which correspond to the three iterations) will not be presented here, since the RMS errors are very small for all iterations and hence, it is not possible to distinguish the difference between the three slots.

In Figure 112, the slot profile with the envelopes is shown. The width of the slot is 1 cm, since the roller diameter is 1 cm.

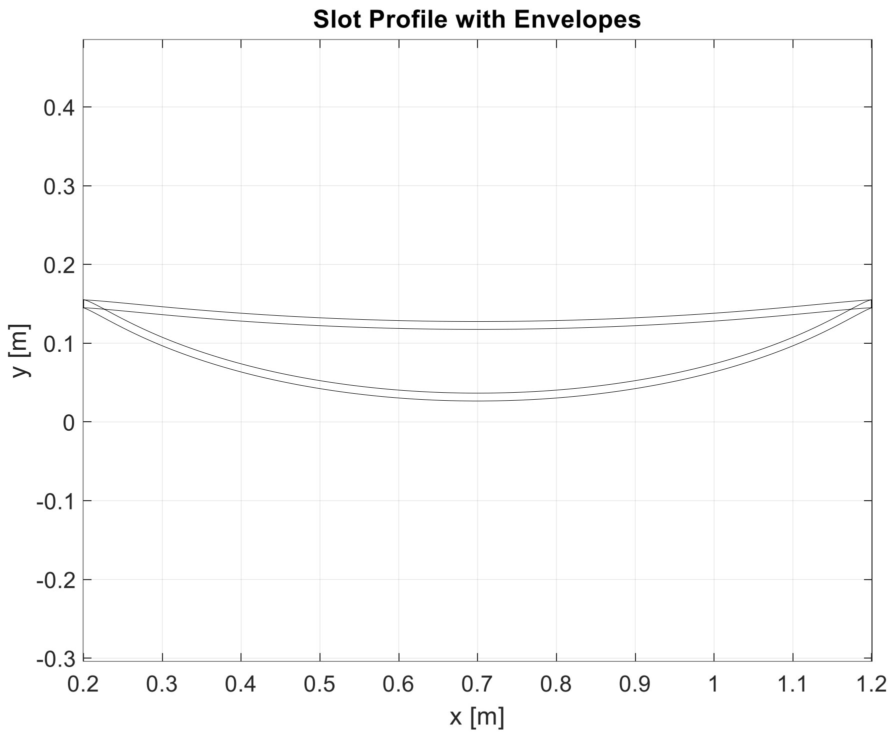

Figure 112: Slot Profile with Envelopes for Task-4

The slot profile of Task-4 is roughly symmetrical with the slot profile of Task-3 (with respect to a horizontal line). This is due to the fact that $F_2(t)$ is inverted. However, due to the change in the spring stiffness, the new slot profile is rescaled in y direction.

Considering undercutting, the radius of curvature of the slot profile should be larger than the radius of the roller [44]. For Task-4, the minimum radius of curvature of the slot is 133 times larger than the roller radius. Hence, undercutting does not occur.

In Figure 113, the roller positions are shown for different time values for Task-4. Between the 4^{th} and 5^{th} seconds; and between the 7^{th} and 8^{th} seconds, the roller does not move. This is expected because Task-4 is a rise-dwell-return-dwell type task (see the displacement profile shown in Figure 91).

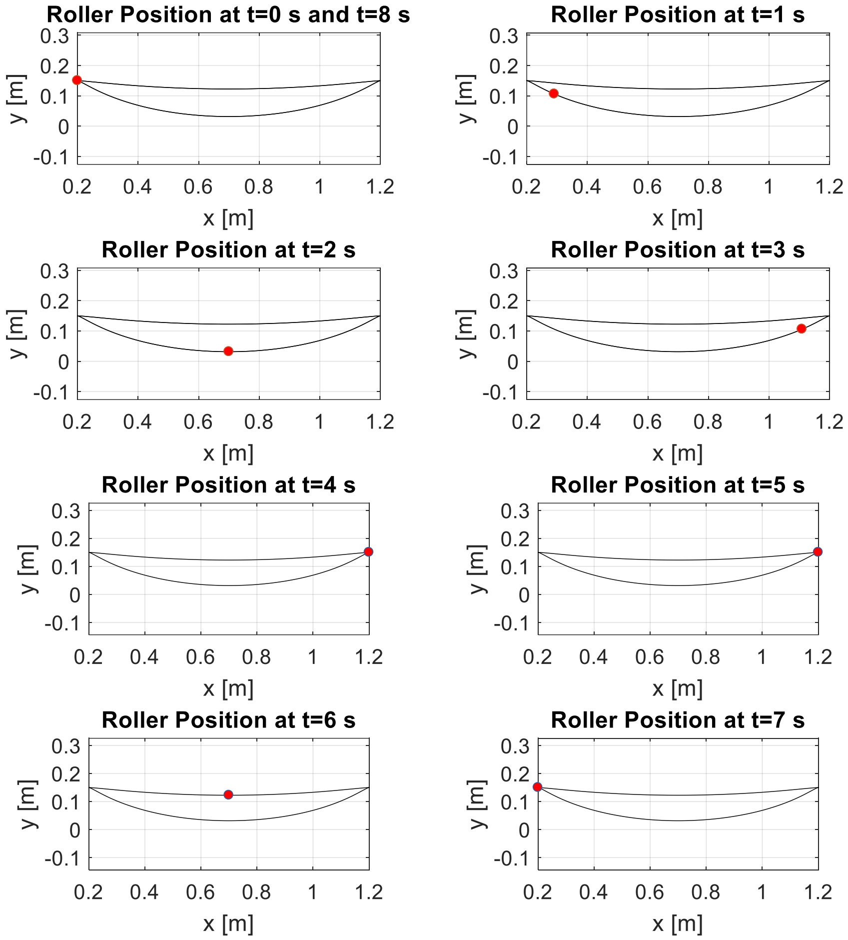

Figure 113: Roller Positions for Different Times for Task-4

In Figure 114, the energy graphs for Task-4 are shown. In Figure 115, the time rate of change of energy graphs are shown for Task-4. In Figure 116, the contributions of links to the total mechanical energy for Task-4 are shown.

As it is seen in Figure 114 and Figure 116, the biggest contributors to the mechanical energy are the springs. However, between the 5th and 7th seconds, the contributions of links 2 and 4 to mechanical energy are higher than the springs. Although links 2, 4, 3 and 5 have the same masses, contributions of links 3 and 5 to the mechanical energy are much smaller than the contributions of links

2 and 4 to the mechanical energy. Recall that, in Task-2, contributions of links 3 and 5 were larger than the contributions of links 2 and 4. This is due to the different velocity profiles of the two tasks. Since kinetic energy is proportional to the square of the velocity, the velocity difference of the links impacts the contributions significantly.

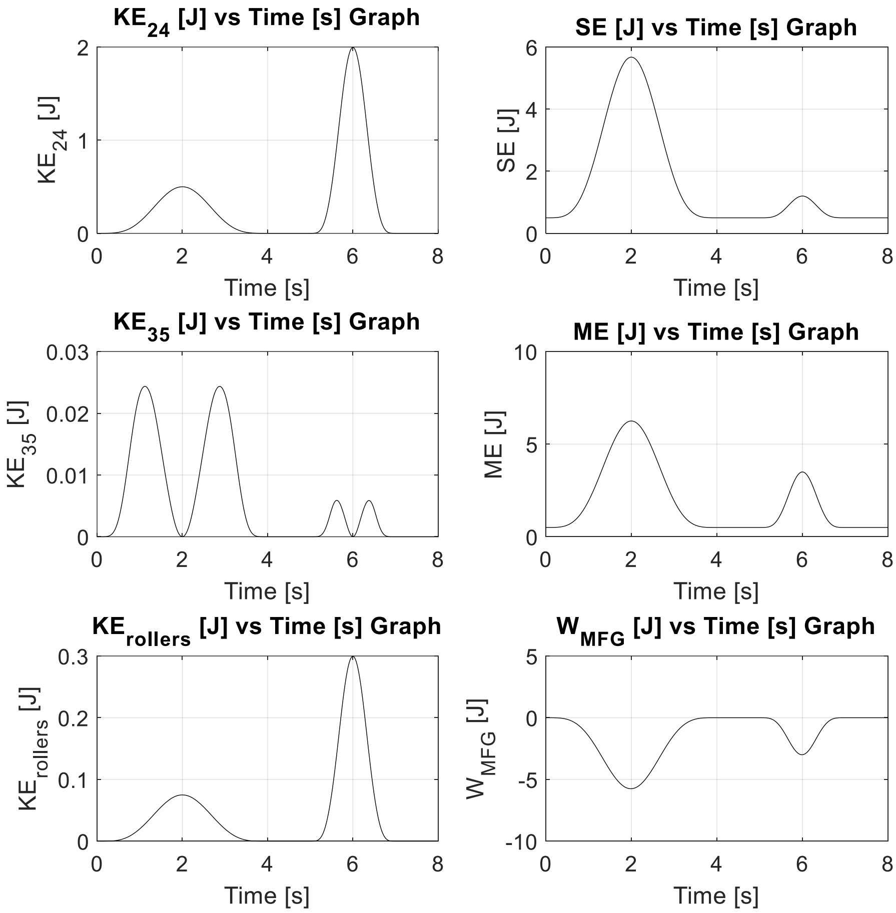

Figure 114: Energy Graphs for Task-4

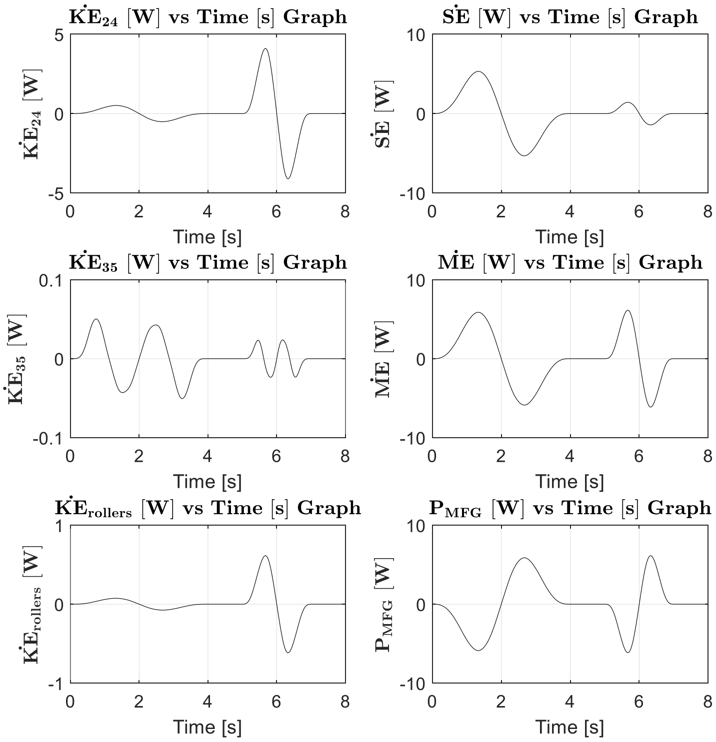

Figure 115: Time Rate of Change of Energy Graphs for Task-4

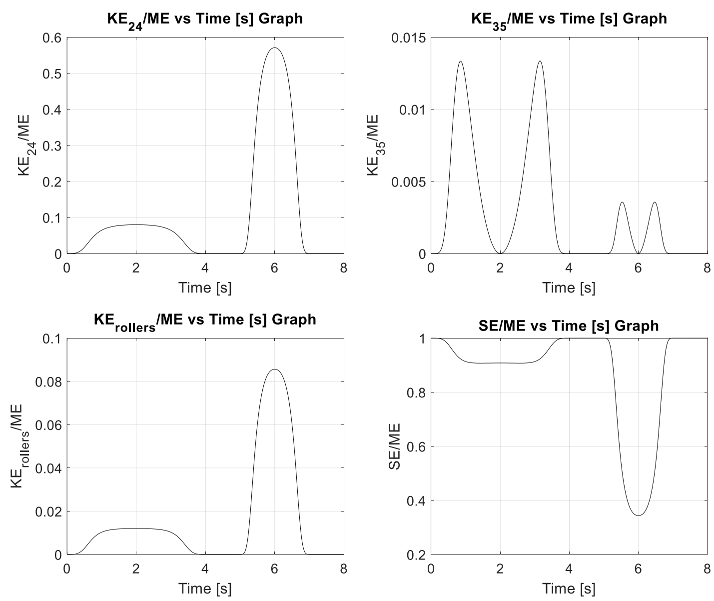

Figure 116: Contributions of Links to Total Mechanical Energy for Task-4

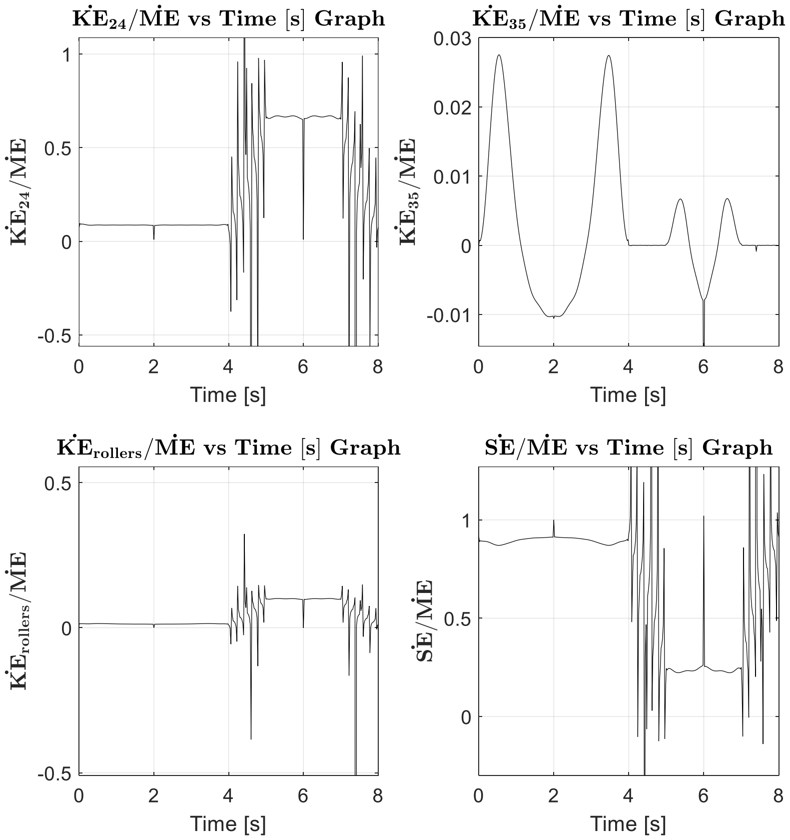

Figure 117: Ratios of the Time Rate of Change of to the Time Rate of Change of the Energies to Total Mechanical Energy for Task-4

In Figure 117, the ratios of the time rate of change of energies to the time rate of change of the total mechanical energy for Task-4 are shown. Note that between the 4th and 5th, and the 7th and 8th seconds, $\dot{ME}$ is zero. Hence, the ratios have peaks at these regions (because of division by 0).

Recall that, $F_{MFG}(t)$ is approximated by a 20th order Fourier series. Between the 4th and 5th, and the 7th and 8th seconds, its value should be zero. But, since it is approximated, there are small oscillations at these time intervals, as it can be seen in Figure 93. That explains the oscillations in the graphs given in Figure 117. Practically, the oscillations of the $F_{MFG}(t)$ do not affect the results. One may take $F_{MFG}(t)$ to be directly as zero in these intervals.

The maximums and minimums of the energies and the time rate of change of energies for Task-4 are presented in Table 15.

Table 15: Presentation of the Results for Task-4

	Unit	Maximum	Minimum	Total Change
ME	Joule	6.249	0.500	5.749
KE_{24}	Joule	1.997	0.000	1.997
KE_{35}	Joule	0.024	0.000	0.024
$KE_{rollers}$	Joule	0.300	0.000	0.300
SE	Joule	5.674	0.500	5.174
P_{MFG}	Watt	6.137	-6.134	12.271
$\dot{KE}_{24}$	Watt	4.102	-4.102	8.204
$\dot{KE}_{35}$	Watt	0.050	-0.051	0.101
$\dot{KE}_{rollers}$	Watt	0.615	-0.615	1.230
$\dot{SE}$	Watt	5.320	-5.320	10.640

5.5.4.1 Effect of Link Masses and Spring Constants

In order to investigate the effects of the link masses and the spring constants on the slot shape, and their contribution to the energies; four different cases will be considered for Task-4:

Task-4, Case-a : The aforementioned design variables for Task-4, i.e.,

$$k = 200 \text{ N/m},\ m_2 = 2 \text{ kg},\ m_3 = 2 \text{ kg}$$

Task-4, Case-b : $k = 800$ N/m, $m_2 = 2$ kg, $m_3 = 2$ kg

Task-4, Case-c : $k = 200$ N/m, $m_2 = 3$ kg, $m_3 = 2$ kg

Task-4, Case-d : $k = 200$ N/m, $m_2 = 2$ kg, $m_3 = 3$ kg

Note that in Case-b, Case-c and Case-d; all other design variables are the same as Case-a. Case-a will not be discussed again, since it has been discussed before.

5.5.4.1.1 Case-b

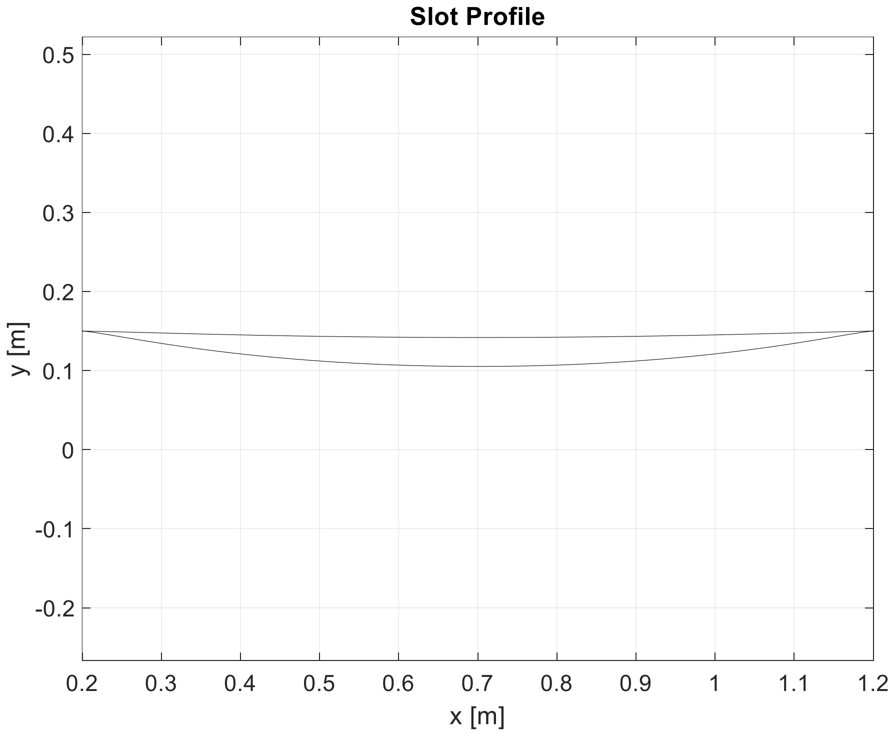

Figure 118: Slot Profile for Case-b

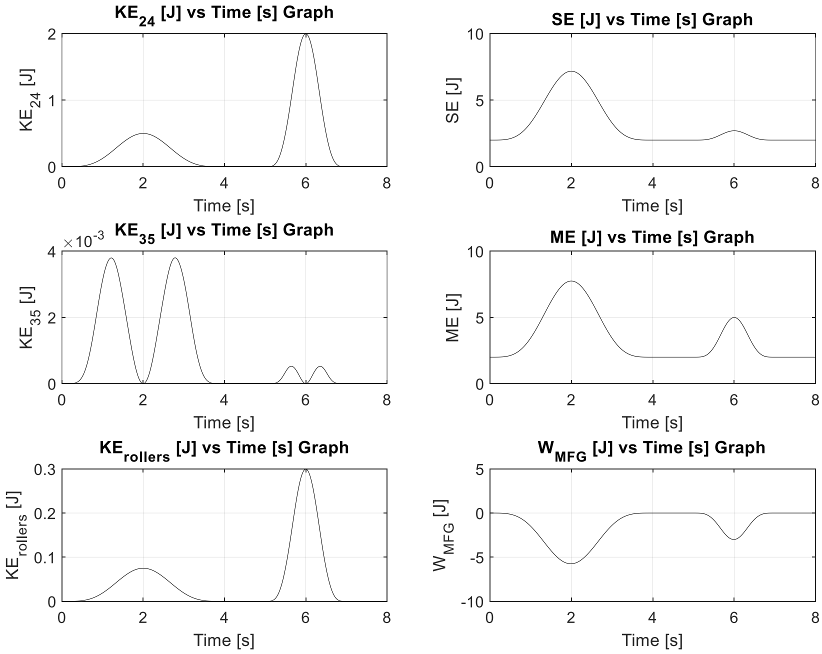

Figure 119: Energy Graphs for Case-b

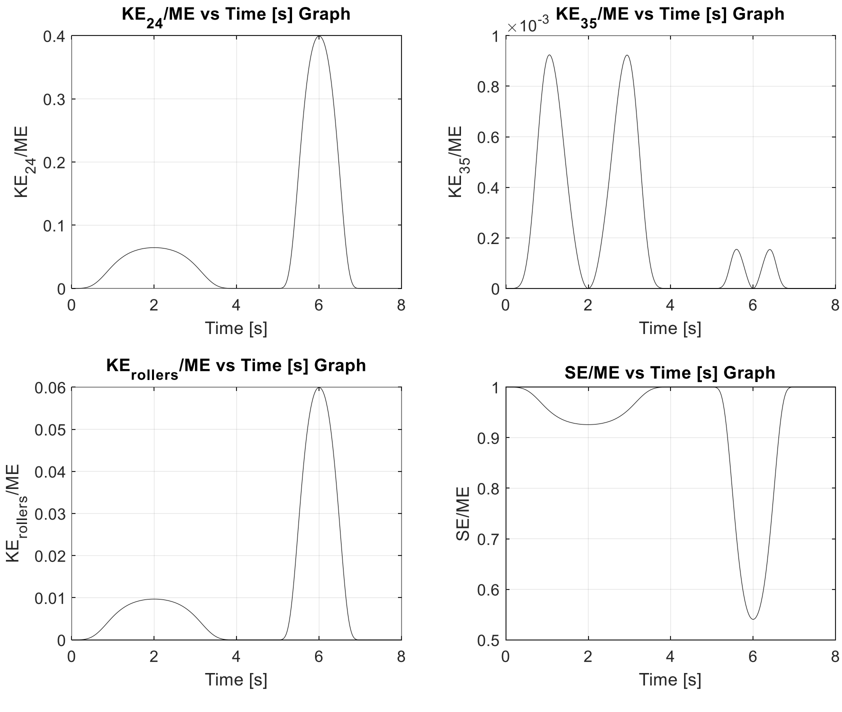

Figure 120: Contributions of Links to Total Mechanical Energy for Case-b

5.5.4.1.2 Case-c

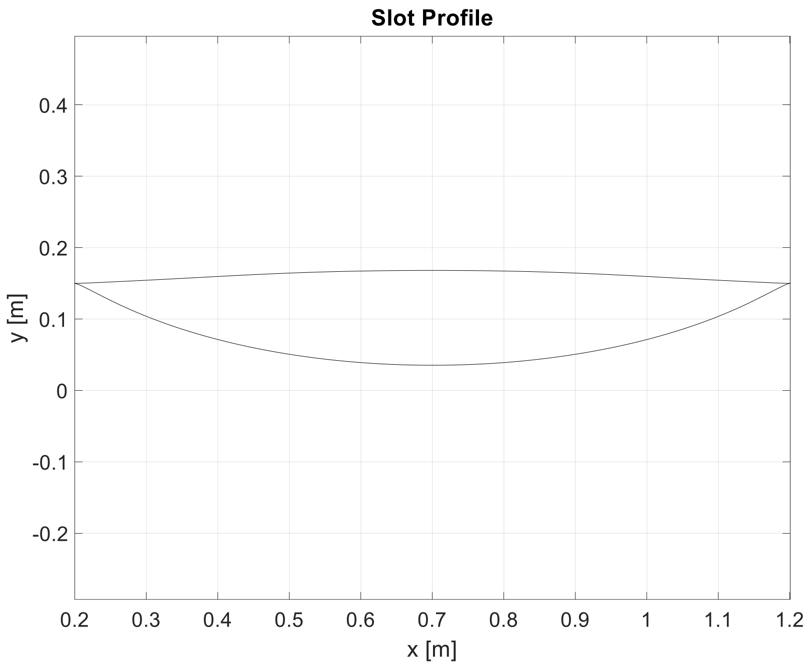

Figure 121: Slot Profile for Case-c

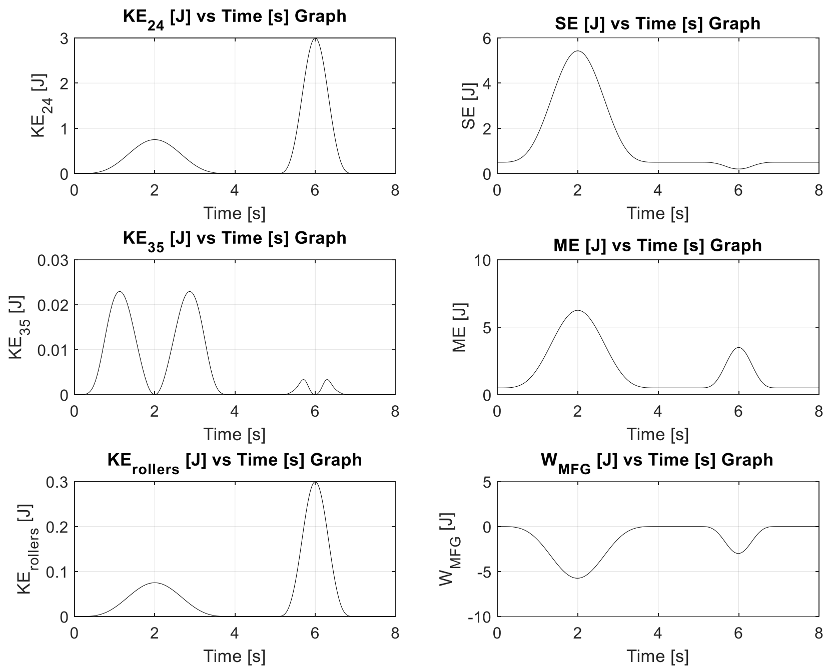

Figure 122: Energy Graphs for Case-c

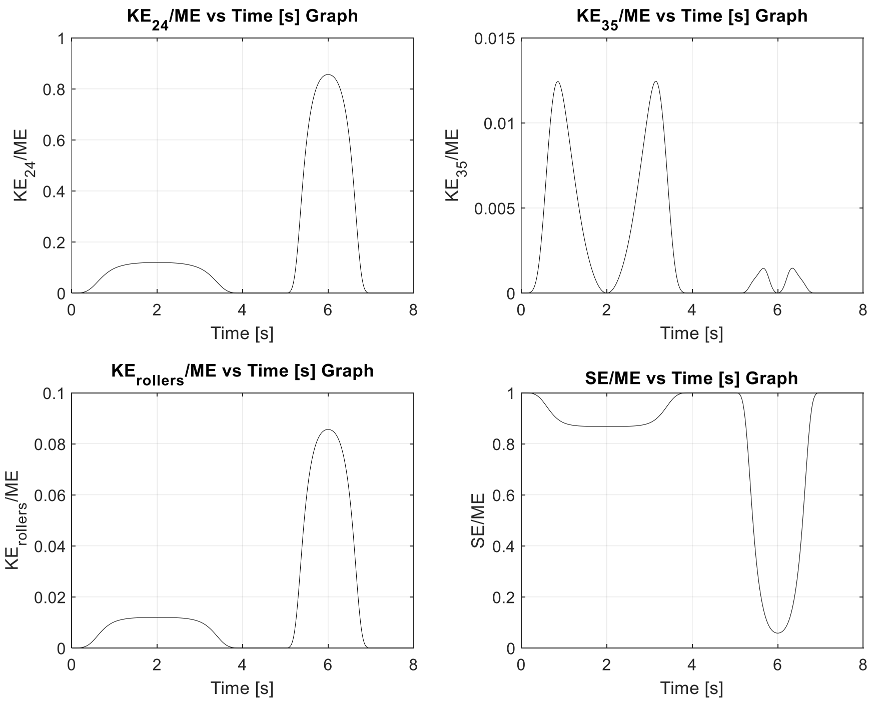

Figure 123: Contributions of Links to Total Mechanical Energy for Case-c

5.5.4.1.3 Case-d

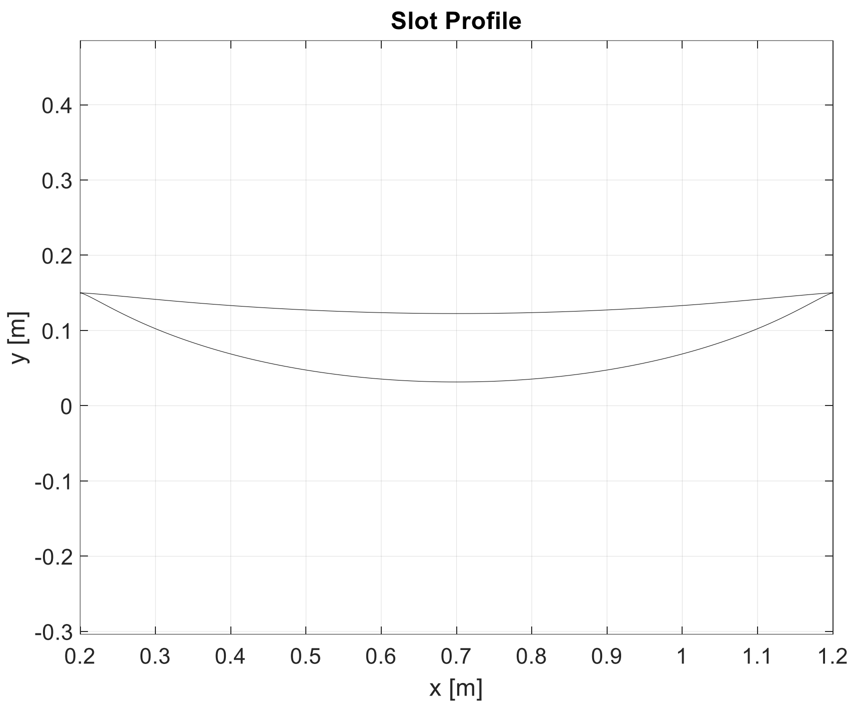

Figure 124: Slot Profile for Case-d

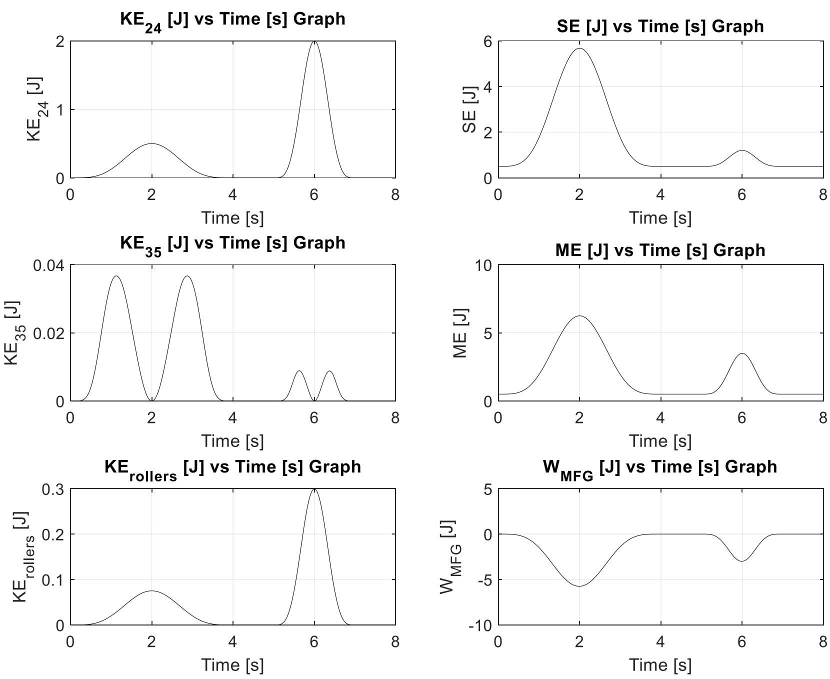

Figure 125: Energy Graphs for Case-d

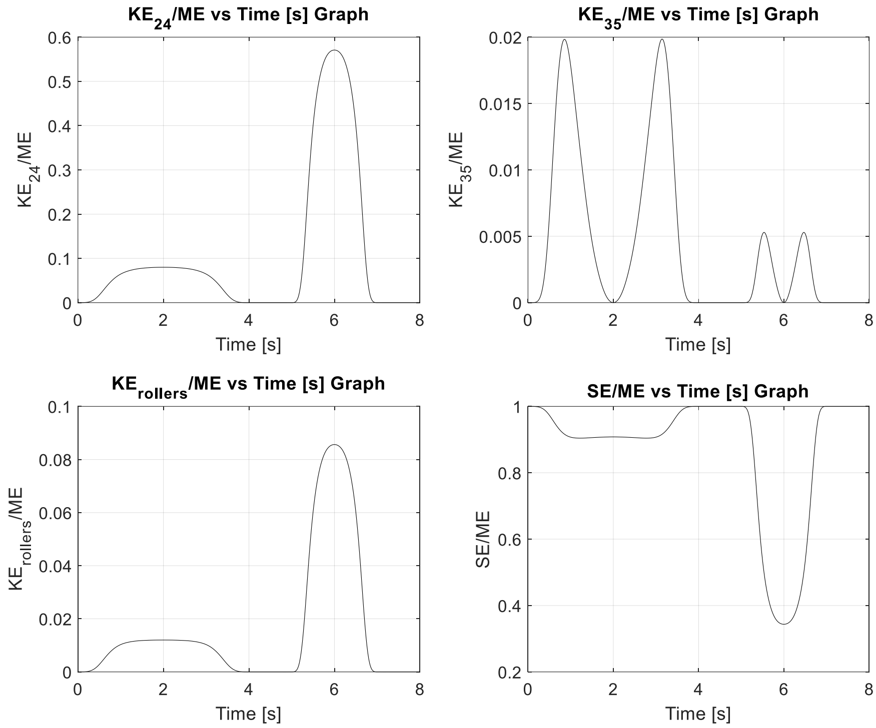

Figure 126: Contributions of Links to Total Mechanical Energy for Case-d

5.5.4.2 Conclusions for Different Cases

Results of the various cases of Task-4 are presented in Figure 111 to Figure 126.

- Increase in the spring constant (as in Case-b) makes the slot shape narrower in the y direction, as it can be seen in Figure 111 and Figure 118. Here, a narrow slot shape implies a slot shape with a smaller "max(y)-min(y)" value, where y is the coordinate of slot in the y axis. An optimum spring constant can be determined by considering ease of manufacturing of the links and the availability of springs in the market. If the slot shape becomes too narrow in the y direction, the upper and lower slots will intersect (which is a problematic result). If the slot shape becomes too wide, then the sizes of links 3 and 5 will become too large.

An increase in the spring constant increases the spring energy and decreases the kinetic energies of links 3 and 5. This decrease is due to a decrease in $\dot{s}_3$ (since slot becomes narrower in y direction). $\dot{s}_2$ or s_2 are not affected by this, as s_2 is input and stays the same. Moreover, the kinetic energies of the rollers and links 2 and 4 also stay the same, since they are related to s_2. The total mechanical energy increases, since the increase in the spring energy is much higher than the decrease in the kinetic energies of links 3 and 5. However, W_{MFG} is not changed, since there is no change in its definition as shown in equation (203).

- An increase in the masses of links 2 and 4 (Case-c), obviously increases the kinetic energies of links 2 and 4. Hence, the contributions of links 2 and 4 to the total mechanical energy increase as it can be seen from Figure 114, Figure 116, Figure 122 and Figure 123. This increase is only due to the mass increase. In other words, $\dot{s}_2$ has no change, thus it has no effect on this energy increase. An increase in the masses of links 2 and 4 changes the slot shape significantly, as it can be seen in Figure 111 and Figure 121.

  Change in slot the shape affects $\dot{s}_3$ (its maximum value is decreased). Hence, the kinetic energies of links 3 and 5 and their contributions to the total mechanical energy decreases. But this decrease is very small, since the contribution of links 3 and 5 were too small initially.

  According to equations (203) and (204), the mechanical energy graph can shift upwards or downwards (as in Case-b), but it cannot change its pattern completely, as long as $\dot{s}_2$ and F_{MFG} that appear in equation (203) do not change (they are the same for all cases presented here). The shift of the mechanical energy graph can be measured with $ME(0)$, which is the initial mechanical energy. Considering equations (204) to (209) along with Figure 114, only the spring energy affects $ME(0)$, since $\dot{s}_2(0)$ and $\dot{s}_3(0)$ are 0. For Case-c and Case-d, since the spring constants stay the same, the mechanical energy graphs do not change. Considering the contributions of links 2 and 4 to the mechanical energy increase at some time interval, especially in between 5th and 7th seconds (and contributions of links 3 and 5 to the mechanical energy decrease very slightly), contribution of springs to the mechanical energy must decrease at the corresponding time intervals. Since the spring constant stays the same, the only free parameter is the deflection of the spring. Hence, $s_3(t)$ changes and this change affects the slot shape.

- An increase in the masses of links 3 and 5 (Case-d), increases the kinetic energies of link 3 and 5. However, since their contributions are too small initially, this increase practically changes nothing. On the other hand, if their contribution was large enough, then their mass increase would affect the energies and the slot shape as shown in Case-c.

CHAPTER 6

CONCLUSIONS

This study examines the dynamic performance improvement of mechanisms by coupling mechanical force generators.

In chapter 1, mechanical force generators are introduced. A literature survey regarding overconstrained mechanisms, balancing of mechanisms, mechanical presses and the efficiency maps of electric motors is presented.

In chapter 2, the parallelogram mechanism is investigated. Since it is an overconstrained mechanism, in order to perform dynamic analysis, one should consider the flexibilities of the links. Another alternative approach is to increase the degree of freedom of the mechanism by 1, by increasing the degree of freedom of an appropriate joint. In this modification, one has free parameters that may be changed at will. In chapter 2, the effects of these free parameters are examined. This comparison is important and gives preliminary information for the following chapters, since the same modification may also be realized for the mechanical force generators. It is expected that, the results of the dynamic analyses of the modified equivalent mechanical force generators are close to the original mechanical force generator. However, the results of the dynamic analyses of the original parallelogram mechanism and the modified parallelogram mechanisms are slightly different. Note that these differences are small enough so that one may use the results of the modified mechanism, rather than the original mechanism.

In chapter 3, the dynamic analysis of the mechanical force generator is performed by utilizing two different methods. The first method is using the dynamic analysis algorithm which is proposed by Soylu in [45]. The second method uses a commercial software, MSC Adams. Different models of the same mechanism are generated by using different joints or contacts. The effect of these different joints and contacts are examined and compared with the algorithm. At the end, the most successful model to describe the mechanism is selected. The results are compared with the results of the algorithm. It is observed that they are consistent with each other.

In chapter 4, five different mechanical press tasks have been considered. Kinematic and dynamic analyses of the press mechanisms have been realized. The force applied by the mechanical force generator is also included in the dynamic analyses and left as a design function. Several different electric motors are chosen and used for the analyses. The efficiency maps of the motors are also considered in the analyses. Required force to be applied by the mechanical force generator that is coupled to the system is determined for various optimization purposes. Mainly two objectives are considered, namely minimizing the maximum power consumption and minimizing the total energy consumption during the task. Maximum power consumption of the press machine is reduced by 60.11%. Hence, it is shown that, a much smaller motor can be used for the same task. For the second objective, total energy consumption during the task is reduced by various amounts. The saving in energy depends on the task and the electric motor type. In tasks that include only inertial and gravitational forces, the reduction in energy consumption is close to 100%, since the mechanical force generator stores all the energy when there is a need for “braking”, and releases it when it is needed. In these analyses, the friction is neglected. Even when the friction is included, one may end up with a significant amount of energy saving. This is due to the fact that, the mechanical force generator acts like a spring with a variable stiffness and a kinetic energy storage device with variable inertia.

Hence, mechanical force generators are much more efficient than regular springs and flywheels.

In chapter 5 in order to determine the slot profile of the mechanical force generator, an iterative algorithm is proposed. Using this algorithm, slot profiles are found for four different cases. Effects of the mass of each link and the spring constant on the slot profile are investigated. Dynamic analysis of the mechanical force generator is performed by using a simpler method than the one presented in [45], and contact surface of the rollers are determined. Some recommendations regarding the practical usage of the mechanical force generator are also made. The slot profile for a rise-dwell-return-dwell task is also determined. Hence, it is possible to observe the resulting slot profile for tasks which include intermittent displacement input.

The main results of this study are listed below:

- Overconstrained mechanisms can be modeled as regular mechanisms by replacing one or more joints with a higher degree of freedom joint(s). These modified regular mechanisms can lead to identical dynamic properties as the original mechanism.
- MFGs can be efficiently used to optimize one (or more than one) dynamic characteristics of an existing machine. For instance, one can minimize the energy consumption of an existing machine. Furthermore, when a suitable MFG is coupled to an existing machine, it is possible to use “smaller and less powerful” actuators to execute a given task.
- MFG acts as a linear spring with a variable stiffness. Masses and inertias of the links of the MFG also contribute to the total mechanical energy. The contributions (to the total mechanical energy) of the link masses, inertias and springs can be adjusted by changing the masses, inertias and spring parameters (spring constant, free length of the spring, etc.) of the MFG. These changes also affect the slot shape of the MFG.

REFERENCES

[1] Free Dictionary, “The Free Dictionary.” [Online]. Available: http://www.thefreedictionary.com/mechanism. [Accessed: 22-Sep-2017].

[2] R. Soylu, “A Mechanical Force Generator and Related Kinematic Chains, ” T.R. Patent WO/2015/069207, Application Number: 2013/13064, PCT/TR2014/000413, 2013.

[3] R. Soylu and H. Mencek, “An Overconstrained, Energy Efficient, Shaking Force Free Mechanical Force Generator and Related Mechanisms - Part 1 : Mechanical Force Generator,” (to be published).

[4] C. Bagci, “Complete Shaking Force and Shaking Moment Balancing of Link Mechanisms Using Balancing Idler Loops,” *J. Mech. Des.*, vol. 104, no. 2, pp. 482–493, 1982.

[5] M. J. French and M. B. Widden, “The spring-and-lever balancing mechanism, George Carwardine and the Anglepoise lamp,” *Proc. Inst. Mech. Eng. Part C J. Mech. Eng. Sci.*, vol. 214, no. 3, pp. 501–508, 2000.

[6] C. M. Gosselin and J. Wang, “Static balancing of spatial six-degree-of-freedom parallel mechanisms with revolute actuators,” *J. Robot. Syst.*, vol. 17, no. 3, pp. 159–170, 2000.

[7] a. Gopalswamy, P. Gupta, and M. Vidyasagar, “A new parallelogram linkage configuration for gravity compensation using torsional springs,” *IEEE Int. Conf. Robot. Autom.*, pp. 664–669, 1992.

[8] G. Brown and A. O. DiGuilio, “Support Apparatus,” 4,208,028, 1980.

[9] T. Rahman, W. Sample, R. Seliktar, M. Alexander, and M. Scavina, “A body-powered functional upper limb orthosis.,” *J. Rehabil. Res. Dev.*, vol. 37, no. 6, pp. 675–680, 2000.

[10] W. D. van Dorsser, R. Barents, B. M. Wisse, and J. L. Herder, “Gravity-Balanced Arm Support With Energy-Free Adjustment,” *J. Med. Device.*,

vol. 1, no. 2, p. 151, 2007.

[11] S. K. Agrawal *et al.*, “Assessment of motion of a swing leg and gait rehabilitation with a gravity balancing exoskeleton,” *IEEE Trans. Neural Syst. Rehabil. Eng.*, vol. 15, no. 1, pp. 410–420, 2007.

[12] D. A. Streit and B. J. Gilmore, “Perfect Spring Equilibrators for Rotatable Bodies,” *J. Mech. Transm. Autom. Des.*, vol. 111, no. December 1989, pp. 451–458, 1989.

[13] Zong-Wei Yang and Chao-Chieh Lan, “An adjustable gravity-balancing mechanism using planar extension and compression springs,” *Mech. Mach. Theory*, vol. 92, pp. 314–329, 2015.

[14] R. H. Nathan, “A Constant Force Generation Mechanism,” *J. Mech. Transm. Autom. Des.*, vol. 107, no. 4, p. 508, 1985.

[15] W. D. van Dorsser, R. Barents, B. M. Wisse, M. Schenk, and J. L. Herder, “Energy-free adjustment of gravity equilibrators by adjusting the spring stiffness,” *Proc. Inst. Mech. Eng. Part C J. Mech. Eng. Sci.*, vol. 222, no. 9, pp. 1839–1846, 2008.

[16] R. Barents, M. Schenk, W. D. van Dorsser, B. M. Wisse, and J. L. Herder, “Spring-to-Spring Balancing as Energy-Free Adjustment Method in Gravity Equilibrators,” *J. Mech. Des.*, vol. 133, no. 6, p. 61010, 2011.

[17] J. L. Herder, “Design of Spring Force Compensation Systems,” *Mech. Mach. Theory*, vol. 33, pp. 151–161, 1998.

[18] Y. Wu and C. Gosselin, “Design of reactionless 3-DOF and 6-DOF parallel manipulators using parallelepiped mechanisms,” *IEEE Trans. Robot.*, vol. 21, no. 5, pp. 821–833, 2005.

[19] R. S. Berkof and G. G. Lowen, “A New Method for Completely Force Balancing Simple Linkages,” *J. Eng. Ind.*, vol. 91, no. 1, p. 21, 1969.

[20] F. R. Tepper and G. G. Lowen, “General Theorems Concerning Full Force Balancing of Planar Linkages by Internal Mass Redistribution,” *J. Eng. Ind.*, vol. 94, no. 3, pp. 789–796, 1972.

[21] G. Feng, “Complete shaking force and shaking moment balancing of 26 types of four-, five- and six-bar linkages with prismatic pairs,” *Mech.*

Mach. Theory, vol. 25, no. 2, pp. 183–192, 1990.

[22] I. S. Kochev, "General method for active balancing of combined shaking moment and torque fluctuations in planar linkages," *Mech. Mach. Theory*, vol. 25, no. 6, pp. 679–687, 1990.

[23] V. Arakelian and S. Briot, "Simultaneous inertia force/moment balancing and torque compensation of slider-crank mechanisms," *Mech. Res. Commun.*, vol. 37, no. 2, pp. 265–269, 2010.

[24] S. Briot and V. Arakelian, "Complete shaking force and shaking moment balancing of in-line four-bar linkages by adding a class-two RRR or RRP Assur group," *Mech. Mach. Theory*, vol. 57, pp. 13–26, 2012.

[25] V. H. Arakelian and M. R. Smith, "Complete shaking force and shaking moment balancing of linkages," *Mech. Mach. Theory,* vol. 34, no. 8, pp. 1141–1153, 1999.

[26] O. Mendoza-Trejo, C. A. Cruz-Villar, R. Peón-Escalante, M. A. Zambrano-Arjona, and F. Peñuñuri, "Synthesis method for the spherical 4R mechanism with minimum center of mass acceleration," *Mech. Mach. Theory*, vol. 93, pp. 53–64, 2015.

[27] H. Chaudhary and S. K. Saha, "Balancing of shaking forces and shaking moments for planar mechanisms using the equimomental systems," *Mech. Mach. Theory*, vol. 43, no. 3, pp. 310–334, 2008.

[28] B. Moore, J. Schicho, and C. M. Gosselin, "Determination of the complete set of shaking force and shaking moment balanced planar four-bar linkages," *Mech. Mach. Theory,* vol. 44, no. 7, pp. 1338–1347, 2009.

[29] V. H. Arakelian and M. R. Smith, "Shaking Force and Shaking Moment Balancing of Mechanisms: A Historical Review With New Examples," *J. Mech. Des.*, vol. 127, no. March 2005, pp. 334–339, 2005.

[30] V. van der Wijk, B. Demeulenaere, C. Gosselin, and J. L. Herder, "Comparative Analysis for Low-Mass and Low-Inertia Dynamic Balancing of Mechanisms," *J. Mech. Robot.*, vol. 4, no. 3, p. 31008, 2012.

[31] C. M. Gosselin, F. Vollmer, G. Côté, and Y. Wu, "Synthesis and design of reactionless three-degree-of-freedom parallel mechanisms," *IEEE Trans. Robot. Autom.*, vol. 20, no. 2, pp. 191–199, 2004.

[32] A. Fattah and S. K. Agrawal, “On the design of reactionless 3-DOF planar parallel mechanisms,” *Mech. Mach. Theory*, vol. 41, no. 1, pp. 70–82, 2006.

[33] V. H. Arakelian and M. R. Smith, “Design of planar 3-DOF 3-RRR reactionless parallel manipulators,” *Mechatronics*, vol. 18, no. 10, pp. 601–606, 2008.

[34] C. Mavroidis and B. Roth, “New and Revised Overconstrained Mechanisms,” *J. Mech. Des.*, vol. 117, no. 1, p. 75, 1995.

[35] G. Gogu, “Mobility of mechanisms: A critical review,” *Mech. Mach. Theory*, vol. 40, no. 9, pp. 1068–1097, 2005.

[36] J. S. Dai, Z. Huang, and H. Lipkin, “Mobility of Overconstrained Parallel Mechanisms,” *J. Mech. Des.*, vol. 128, no. 1, p. 220, 2006.

[37] I. Fernández-Bustos, J. Agirrebeitia, G. Ajuria, and C. Angulo, “A new finite element to represent prismatic joint constraints in mechanisms,” *Finite Elem. Anal. Des.*, vol. 43, no. 1, pp. 36–50, 2006.

[38] R. Avilés, A. Hernández, E. Amezua, and O. Altuzarra, “Kinematic analysis of linkages based in finite elements and the geometric stiffness matrix,” *Mech. Mach. Theory*, vol. 43, no. 8, pp. 964–983, 2008.

[39] M. Wojtyra, “Joint reaction forces in multibody systems with redundant constraints,” *Multibody Syst. Dyn.*, vol. 14, no. 1, pp. 23–46, 2005.

[40] S.-M. Song and X. Gao, “The Mobility Equation and the Solvability of Joint Forces/Torques in Dynamic Analysis,” *J. Mech. Des.*, vol. 114, no. 2, pp. 257–262, Jun. 1992.

[41] J. Frączek and M. Wojtyra, “On the unique solvability of a direct dynamics problem for mechanisms with redundant constraints and Coulomb friction in joints,” *Mech. Mach. Theory*, vol. 46, no. 3, pp. 312–334, 2011.

[42] M. Wojtyra and J. Frączek, “Comparison of Selected Methods of Handling Redundant Constraints in Multibody Systems Simulations,” *J. Comput. Nonlinear Dyn.*, vol. 8, no. 2, p. 21007, 2012.

[43] Y. Xu, W. Liu, J. Yao, and Y. Zhao, “A method for force analysis of the

overconstrained lower mobility parallel mechanism," *Mech. Mach. Theory*, vol. 88, pp. 31–48, 2015.

[44] E. Söylemez, *Mechanisms*. Ankara: Middle East Technical University, 2009.

[45] R. Soylu and H. Mencek, "An Overconstrained, Energy Efficient, Shaking Force Free Mechanical Force Generator and Related Mechanisms - Part 3 : Dynamic Force Analysis," (to be published).

[46] R. Soylu and H. Mencek, "An Overconstrained , Energy Efficient, Shaking Force Free Mechanical Force Generator and Related Mechanisms - Part 2 : Related Kinematic Chains and Applicational Aspects," (to be published).

[47] H. Mencek, "Theoretical and Experimental Dynamic Performance Optimization of Planar Mechanisms Using Adjustment Systems and Mechanical Generators," Middle East Technical University, 2015.

[48] R. Halicioglu, L. C. Dulger, and A. Bozdana, "Mechanisms, classifications, and applications of servo presses: A review with comparisons," *Proc. Inst. Mech. Eng. Part B J. Eng. Manuf.*, vol. 230, no. 7, 2016.

[49] K. Osakada, K. Mori, T. Altan, and P. Groche, "Mechanical servo press technology for metal forming," *CIRP Ann. - Manuf. Technol.*, vol. 60, no. 2, pp. 651–672, 2011.

[50] D. A. Smith, "Mechanical Press Types and Nomenclature," pp. 1–28, 2005.

[51] H. Mäkelt, *Mechanical Presses*. London: Edward Arnold, 1968.

[52] Y. Tamai, T. Inazumi, and K. I. Manabe, "FE forming analysis with nonlinear friction coefficient model considering contact pressure, sliding velocity and sliding length," *J. Mater. Process. Technol.*, vol. 227, pp. 161–168, 2016.

[53] M. Zahálka and J. Staněk, "Options of Advanced Simulations of Crank Presses Loading," *Procedia Eng.*, vol. 100, pp. 891–898, 2015.

[54] S. Subramonian, T. Altan, C. Campbell, and B. Ciocirlan, "Determination

of forces in high speed blanking using FEM and experiments," *J. Mater. Process. Technol.*, vol. 213, no. 12, pp. 2184–2190, 2013.

[55] C.-P. Jiang and C.-C. Chen, "Grain Size Effect on the Springback Behavior of the Microtube in the Press Bending Process," *Mater. Manuf. Process.*, vol. 27, no. 5, pp. 512–518, 2012.

[56] K. Stockman, S. Dereyne, D. Vanhooydonck, W. Symens, J. Lemmens, and W. Deprez, "Iso efficiency contour measurement results for variable speed drives," *19th Int. Conf. Electr. Mach. ICEM 2010*, 2010.

[57] R. Bojoi, E. Armando, M. Pastorelli, and K. Lang, "Efficiency and loss mapping of AC motors using advanced testing tools," *Proc. - 2016 22nd Int. Conf. Electr. Mach. ICEM 2016*, vol. 1, pp. 1043–1049, 2016.

[58] F. Aguilera, P. M. De La Barrera, and C. H. De Angelo, "Induction machine models for efficiency studies in EV design applications," *2012 10th IEEE/IAS Int. Conf. Ind. Appl. INDUSCON 2012*, no. 1, 2012.

[59] A. Mahmoudi, W. L. Soong, G. Pellegrino, and E. Armando, "Efficiency maps of electrical machines," *2015 IEEE Energy Convers. Congr. Expo. ECCE 2015*, no. 2015, pp. 2791–2799, 2015.

[60] MSC, "MSC Adams - Help." MSC.

[61] "Ansys Blog." [Online]. Available: http://www.ansys-blog.com/wp-content/uploads/2013/11/Fig2.png. [Accessed: 22-Sep-2017].

[62] J. C. Lagarias, J. A. Reeds, M. H. Wright, and P. E. Wright, "Convergence Properties of the Nelder--Mead Simplex Method in Low Dimensions," *SIAM J. Optim.*, vol. 9, no. 1, pp. 112–147, 1998.

[63] "Optimizing Nonlinear Functions," 2017. [Online]. Available: https://se.mathworks.com/help/matlab/math/optimizing-nonlinear-functions.html#bsgpq6p-11. [Accessed: 22-Sep-2017].

[64] *DC Motors, Sizes 160 to 630, 31.5 kW to 1610 kW*. Siemens AG, 2008.

[65] *LSK D.C. motors 2 to 750 kW Technical catalogue*. Leroy-Somer, 2014.

APPENDIX

COEFFICIENTS USED IN THE DYNAMICAL ANALYSIS OF THE MFG

c_coef=(F_Su^2)/4 + (m6^2) * s2dd^2 - (F_Su*m3*s3dd)/2 - F_Su*m6*s3dd + ((m3^2)*(s3dd^2))/4 + m3*m6*(s3dd^2) + (m6^2)*(s3dd^2) - ((I6^2)*((tetha6dd)^2))/((r_fr^2)*(sigma_rf^2)) - F_Su*m6*s2dd*cot(tetha_t) + m3*m6*s2dd*s3dd*cot(tetha_t) + (1/4)*(F_Su^2)*((cot(tetha_t))^2) - (1/2)*F_Su*m3*s3dd*((cot(tetha_t))^2) + (1/4)*(m3^2)*(s3dd^2)*((cot(tetha_t))^2) + (F_Su*I6*r6*sigma*tetha6dd*csc(tetha_t))/((r_fr^2)*(sigma_rf^2)) - (I6*m3*r6*s3dd*sigma*tetha6dd*csc(tetha_t))/((r_fr^2)*(sigma_rf^2)) - ((F_Su^2)*(r6^2)*(sigma^2)*((csc(tetha_t))^2))/(4*(r_fr^2)*(sigma_rf^2)) + (F_Su*m3*(r6^2)*s3dd*(sigma^2)*((csc(tetha_t))^2))/(2*(r_fr^2)*(sigma_rf^2)) - ((m3^2)*(r6^2)*(s3dd^2)*(sigma^2)*((csc(tetha_t))^2))/(4*(r_fr^2)*(sigma_rf^2))

b_coef=-F_Su*cos(tetha_t) + m3*s3dd*cos(tetha_t) - (2*I6*r6*sigma*tetha6dd*cot(tetha_t))/((r_fr^2)*(sigma_rf^2)) + 2*m6*s2dd*cos(tetha_t)*cot(tetha_t) - F_Su*cos(tetha_t)*((cot(tetha_t))^2) + m3*s3dd*cos(tetha_t)*((cot(tetha_t))^2) + (F_Su*(r6^2)*(sigma^2)*cot(tetha_t)*csc(tetha_t))/((r_fr^2)*(sigma_rf^2)) - (m3*(r6^2)*s3dd*(sigma^2)*cot(tetha_t)*csc(tetha_t))/((r_fr^2)*(sigma_rf^2)) + 2*m6*s2dd*sin(tetha_t)

a_coef=2*((cos(tetha_t))^2) -
((r6^2)*(sigma^2)*((cot(tetha_t))^2))/((r_fr^2)*(sigma_rf^2)) +
((cos(tetha_t))^2)*((cot(tetha_t))^2) + ((sin(tetha_t))^2)